THERMOLUMINESCENCE TEMPERATURE SENSING: AN INVESTIGATION OF METHODOLOGICAL AND PRACTICAL LIMITATIONS OF THE TECHNIQUE

By

ADAM CARRIGAN COLEMAN

Bachelor of Arts in Physics
Claremont McKenna College
Claremont, California
2008

Master of Science in Physics
San Diego State University
San Diego, California
2012

Submitted to the Faculty of the
Graduate College of the
Oklahoma State University
in partial fulfillment of
the requirements for
the Degree of
DOCTOR OF PHILOSOPHY
May, 2018

THERMOLUMINESCENCE TEMPERATURE SENSING: AN INVESTIGATION OF METHODOLOGICAL AND PRACTICAL LIMITATIONS OF THE TECHNIQUE

Dissertation Approved:

Eduardo G. Yukihara, Ph.D.

Dissertation Adviser

Stephen W.S. McKeever, Ph.D.

John Mintmire, Ph.D.

Don A. Lucca, Ph.D.

ACKNOWLEDGEMENTS

When my math physics instructor, Dr. Eduardo G. Yukihara, invited me to check out his lab I had no idea it would lead me down such a bizarre, yet fascinating research path. I cannot express enough my gratitude for Dr. Yukihara's guidance and mentorship here at OSU. His efforts have provided me focus and conviction in my studies and helped to improve me as a scientist. Thank you, Dr. Yukihara, for your seemingly endless patience with me over the years.

My humble respect to my committee members, Dr. Stephen W.S. McKeever, Dr. John W. Mintmire, and Dr. Don A. Lucca, who took a great deal of time out of their busy schedules to help my advancement and provide guidance to improve this work. I would like to acknowledge Dr. Stephen W. S. McKeever for taking the time to field my questions and provide valuable feedback over the years. It has been invaluable to have you as a resource while Dr. Yukihara was abroad.

It is my pleasure to thank our Defense Threat Reduction Agency (DTRA) project collaborators who have provided both resources and time to help advance the field of TL temperature sensing. My gratitude to Dr. Talghader and his research group at the University of Minnesota for their support in the preparation, testing, and analysis of multiple detonation tests. A large thank you to the group at the NSWC Indian Head EOD facility and Amber Daniels for her invaluable feedback. Thanks to Dr. Nick Glumac and his students at UIUC for allowing us to use their shock tube for material testing. I would like to acknowledge the DTRA who partially supported the work presented here under the contract HDTRA-10-1-0007. Their support provided me the opportunity to visit testing sites, present my work at multiple venues, and focus on research.

I would like to extend a thank you the Physics department staff, with special thanks to both Susan Cantrell and Tammy Austin. Your support has helped me to navigate my Ph.D. and made my teaching life easier in more ways than I can list.

I would like to thank Dr. Carl Johnson and Dr. Von Whitley for their mentorship during my summer internship at Los Alamos National Laboratory. Without Dr. Whitley's assistance, the hydrodynamics simulations presented in this work would not have been possible.

During my tenure at OSU, my lab mates have grown from a group of nerds to a family of nerds. You all, past and present, made working in the lab fun and provided a much-needed support system. Thanks for making the lab a cooperative and fun environment to do science. A special thanks to Tim and Nishan, who have both provided invaluable feedback on many aspects of this project. Tim, thank you for taking the time to help edit this work.

A major thank you to my family, who have provided love, support, and a healthy dose of sarcasm over the years. Thanks for keeping me grounded and providing an ear when I needed to vent during my seemingly endless years in school. I can never thank you enough. To my friends and teammates over the years; APT 681F, Rox, CMS TF & XC, ADMWLKR, the SD Boston crew and many, many more, thanks for keeping it weird.

Name: ADAM CARRIGAN COLEMAN

Data of Degree: MAY, 2018

Title of Study: THERMOLUMINESCENCE TEMPERATURE SENSING: AN INVESTIGATION OF METHODOLOGICAL AND PRACTICAL LIMITATIONS OF THE TECHNIQUE

Major Field: PHYSICS

Scope and Method of Study: This work had three primary goals. The first was to investigate the validity and accuracy of the initial rise method and the two-dimensional deconvolution method in their application to complex Thermoluminescence (TL) curves. The second goal was to use these methods to obtain the trapping parameters of novel temperature sensing TL materials: $Li_2B_4O_7$:Cu,Ag (LBO), MgB_4O_7:Dy,Li (MBO), and $CaSO_4$:Ce,Tb (CSO), and finally to determine the limitations of TL temperature sensing methodology as a diagnostic technique for bio-agent defeat testing. The initial rise method and the two-dimensional deconvolution method were used to reconstruct the trapping center distributions of simulated, realistic, TL curves associated with a variety of trapping center distributions. Trapping center parameter studies were conducted on experimental TL curves for LBO, MBO, and CSO. The limitations of the TL temperature reconstruction technique were studied using numerical simulations and heat transfer methods.

Findings and Conclusions: The results demonstrate that the IRM paired with the trap density method proposed by Van den Eeckhout et al. (2013) and the two-dimensional deconvolution method were sufficient to recover reliable estimates of the input distributions in certain cases. The two-dimensional deconvolution approach was successful in recovering a reasonable estimate for the input distribution of two and three trap systems, provided sufficient constraint data is used. Both methods were found to be sensitive to noise. Trap parameters were obtained for all three TL materials, but only those for MBO were consistent across all methods investigated. Additionally, LBO and CSO were found to show the effects of thermal quenching. The temperature reconstruction method was found to be biased to lower temperatures when applied to samples containing particles with a distribution of thermal histories. The method was also found to be sensitive to the TL material's trapping center parameters when allowing for a thermal gradient within the particle.

TABLE OF CONTENTS

LIST OF TABLES

LIST OF FIGURES

CHAPTER 1

INTRODUCTION

Since the events of September 11, 2001, there has been increased focus on the prevention of terrorism, including the use of chemical and biological weapons. The use of *Bacillus anthracis*, more commonly known as anthrax, as a weapon has seen use in Japan in the 1990s and more recently in the U.S. mail system in 2001 (Nadasi et al., 2007). Although there are many biological agents that are of concern, particular interest is paid to *Bacillus* spores due to their resistance to damage by irradiation, heat, and chemical treatments. Computer modeling and experimental work has shown that spores subjected to high temperatures can produce spore death from both DNA damage and internal pressurization (Kumar et al., 2011; Zhou et al., 2015).

The post-detonation blast wave and resulting heated gases from a High Explosive (HE) provides a method for killing large stockpiles of. Current approaches utilize HEs such as PETN, HMX, or C4, with the capability to rupture stockpile containment and a high temperature fireball for bio-agent inactivation (Milby et al., 2012). However, HEs produce high pressures that can send live bio-agents into the surrounding environment resulting in danger for the public (Levi, 2004). Simulations and shock tube testing have shown that such an approach is efficient, provided the spore cloud is sufficiently close to the HE charge, but it was also found that if the spores are placed too far away (e.g. 3 - 8 times the HE charge radius) then a considerable percentage of the spores survive (Gottiparthi et al., 2014).

To address this issue, the Defense community has undertaken the development of warheads, specialized for bio-agent defeat. The primary kill mechanism of agent-defeat weapons is prolonged exposure to high temperatures. Therefore, it is of interest to characterize the thermal history a biological agent (e.g. spore) would experience within the warhead's resulting fireball for different explosive formulations (Glumac et al., 2005; Lewis and Rumchik, 2009; Lewis, 2012; Lewis et al., 2013; Milby et al., 2012).

Currently, there exists no established experimental technique for obtaining the temperature a free-flowing particle experiences within a detonation fireball. Conventional techniques such as thermocouples have been used to measure temperature in detonations by providing *in situ*, fixed-point temperature measurements (Jetté et al., 2011), but they can disrupt mass and heat flow due to their fixed position (Asay et al., 2005). Optical methods such as pyrometry (Densmore et al., 2011; Glumac et al., 2005; Jetté et al., 2011; Koch et al., 2010), atomic and molecular spectroscopy (Glumac et al., 2005; Koch et al., 2010; Lewis and Rumchik, 2009; Lewis, 2012), and Coherent-Anti-Stokes-Raman Scattering (Kearney et al., 1999) provide fast response times, but prioritize line of sight and give weight to the hottest particles.

To address the downsides of conventional thermometry techniques, particle sensors with new thermometrics have emerged as promising replacements. Approaches and materials range from thermographic phosphors (Bosze et al., 2011; Heyes et al., 2006; Heyes, 2009; Jaque et al., 2013; Wang et al., 2002), luminescent nanoparticles (Gunawidjaja et al., 2011a, b; Myint et al., 2012a, b), morphological changes to nanoparticles in gold island films (Sun et al., 2013), changes to the photoluminescence spectra of ZnO, and Raman shift of TiO_2 nanoparticles (Mishra et al., 2014; Wang and Huang, 2011) to TL materials (Talghader et al., 2016). Data from the thermographic phosphors must be collected *in situ* making their use in a detonation fireball impossible. The other approaches offer the benefits of *ex situ* data collection and small particle

size (micrometer sizes) allowing for rapid thermal response. Furthermore, these techniques have demonstrated sensitivity to temperatures of hundreds of degrees Celsius for timescales as short as one second. However, many of these methods rely on calibration to known temperatures and timescales. The exception is the use of TL particles which require no such calibration, but depend heavily on the underlying material model and temperature profile assumptions.

Thermoluminescence is a widely used technique to investigate exposure to ionizing radiation, defects in crystalline materials, and luminescence dating of geological materials (Chen and McKeever, 1997; Horowitz, 1983; McKeever, 1985). TL dosimetry relies on the creation of charger carrier pairs (electrons, holes) when a TL material is subjected to ionizing radiation. Charge carriers become trapped at metastable energy levels within the band-gap resulting from defects within the crystalline lattice. Heating (typically linear) of an irradiated TL material releases trapped charges giving rise to TL by electron-hole recombination. The plot of luminescence against temperature results in a TL curve characterized by peaks whose intensity and position is related to the trap's charge carrier population and thermal stability, respectively.

Dosimetric analysis concerns itself with the filling of trapping centers as a response to ionizing radiation, whereas the use of TL for thermometry concerns itself with the emptying of previously filled trapping centers as a response to heating. TL as applied to temperature measurements has wide utility in geology and archeology (Aitken and Thompson, 1968; Spencer and Sanderson, 1994; Spencer and Sanderson, 2012), the study of fire damaged concrete (Placido, 1980), and more recently as particle temperature sensors (Mah et al., 2010; Talghader and Mah, 2012; Talghader et al., 2016; Yukihara et al., 2014b; Yukihara et al., 2015).

Particle thermometry with a dosimetric commercial material, LiF:Mg,Ti, has been demonstrated using TL for a high explosive (Mah et al., 2013). Commercial materials are

attractive because of cost, access and extensive literature pertaining to trapping centers (McKeever et al., 1995; Taylor and Lilley, 1978). The majority of LiF:Mg,Ti TL information, however, is contained in TL peaks at low (< 250°C) readout temperatures, reducing the application temperature range (McKeever et al., 1995). Materials with more thermally stable trapping centers are desirable for high explosive temperature sensing. Furthermore concerns over the effect of thermal exposure on defect concentrations exist and have yet to be fully addressed with regards to temperature sensing (Talghader et al., 2016).

With this in mind, new TL materials $Li_2B_4O_7$:Ag,Cu (LBO), MgB_4O_7:Dy,Li (MBO) and $CaSO_4$:Ce,Tb (CSO), collectively referred to as "OSU Materials", were synthesized for temperature sensing at Oklahoma State University (Doull et al., 2014). Initial testing of the OSU materials for particle thermometry was conducted under both laboratory settings (Yukihara et al., 2014b) and in closed chamber detonations at the Naval Surface Warfare Center (NSWC), Indian Head Explosive Ordinance Disposal Technology Division (IHEODTD) (Daniels et al., 2015; Yukihara et al., 2015). In both cases, reconstructed temperatures were found to be consistent with *in situ* thermocouple measurements, validating the use of the OSU materials for temperature sensing as promising. The results did show evidence of "partial heating", which suggests the reconstructed thermal histories were not characteristic of all particles in the sample. There is also the outstanding question of the validity of making comparisons between with thermocouple measurements for agent-defeat testing. Thermocouples are generally more massive than sensor particles making them slow to respond, and their static position will likely see a completely different temperature environment than a sensor particle traveling freely within a blast-wave.

Subsequent results from explosive testing at the DTRA Humble Gingko XIX facility and at the University of Illinois at Urbana-Champaign (UIUC) shock tube facility provided further

questions about the technology (Yukihara et al., 2016). The Humble Gingko test was conducted in a large, two-room facility with 16 collection sites for detonation tests. Thermal history reconstruction was conducted both on site by UoM, and off site by OSU. The analysis results were found to be inconsistent for samples from the same collection site, as well as between the UoM and OSU results. As was the case with the NSWC closed chamber tests, evidence of partial heating was observed in the Humble Gingko XIX results. The large degree of variation in temperatures and evidence of insufficient heating suggests the materials are behaving as expected, rather than failures of the materials and technique. Unlike the closed chamber tests, where the full chamber was heated, the Humble Gingko XIX test was open and allowed for a true free flow of sensor particles, from which we would expect a large degree of variation in thermal histories. This theory was supported by the analysis of individual MBO TL particles within a single sample which found particles with temperature ranging over serval hundreds of degrees as well as several unheated particles (Armstrong, 2017; Yukihara et al., 2016). While these results proved the evidence of particles heated to a distribution of temperatures, no additional work has been conducted to understand the effect of such samples on the thermal history reconstruction method.

One suggestion for the evidence of insufficient heating for the Humble Gingko XIX test was that the samples were simply too large to respond. To investigate this claim, samples of OSU materials sieved to < 35 μm to ensure small particle size, and were used as temperature diagnostics as the UIUC shock tube facility (Yukihara et al., 2016). Two initial shock tube pressures, corresponding to NASA Chemical Equilibrium with Applications (CEA) calculated temperatures of ~650 K and ~850 K, were used. The estimated exposure times for the particles was 2-5 ms based of shockwave velocity. Pre-shot analysis suggested these temperature profiles were well within the application range for all the OSU materials, but the results indicated

insufficient heating for the ~ 650 K shots and a ~ 300 K underestimation of the ~ 850 K shots. It is unknown if the TL particles stayed within the high pressure and high temperature region characterized by the NASA CEA temperatures, and modeling and imaging would be needed to determine this. The characteristic heating timescale for a 35 μm (diameter) particle is < 1 ms, well under the estimated exposure time (2-5 ms). The results from the Humble Ginkgo XIX and UIUC shock tube facility tests suggest the need to determine an accurate method for estimating the response time for TL particles that accounts for the depletion of trapping centers, as well as the need to look into the interaction of TL particles with the post-detonation blast environment. Understanding these concerns is vital in determining the utility of this technology as a viable temperature diagnostic for bio-agent tests.

Another major obstacle in TL particle thermometry is the reliance on a specific TL model. The trapping center parameters govern the thermal stability of a trapped charge, and thus an incorrect TL model would be a source of error in the thermal history reconstruction calculation. Given the lack of reliable trapping center data for the OSU materials a one-dimensional deconvolution, using a distribution of activation energies while assuming both a common frequency factor and first-order kinetics has been used to model TL behavior (Yukihara et al., 2014b). While the parameters obtained describe the overall TL curve well, they serve only as an approximation of the underlying physics of each trapping center. The true kinetics and trap parameters can differ from the deconvolution results and introduce errors into the thermal history calculation.

The initial characterization of LBO, MBO, and CSO for temperature sensing was conducted by Doull et al. (2014), who concluded each material displayed approximately first-order kinetics and suggests many of the TL peaks to be the result of a distribution of overlapping TL peaks. Initial TL modeling studies using traditional TL analysis techniques by Yukihara et al.

(2016) also found evidence of complex peak distributions for the OSU materials. Additionally, to date, no investigation into thermal quenching has been conducted for the OSU materials. There is no direct effect of thermal quenching on the temperature recovery calculation, but it would introduce error into any TL model based on thermally quenched TL curves (Talghader et al., 2016).

Several TL analysis methods are available for the characterization of a TL materials trap parameters (Chen and McKeever, 1997; McKeever, 1985), but their accuracy when applied to a complex curve structure has not been fully determined. Analysis methods such as peak shape analysis (Chen, 1969) and isothermal decay (Randall and Wilkins, 1945a), rely on isolated TL peaks and are, therefore, not applicable to the OSU materials.

Curve fitting, often referred to as Glow Curve De-Convolution (GCDC) in TL literature, relies on *a priori* knowledge of the number of individual peaks (Horowitz and Yossian, 1995), which makes it a useful choice for modeling LiF:Mg,Ti for temperature sensing (Talghader et al., 2016). When the number of TL peaks is not well defined or broad peak structures are present, such as the case with OSU materials, the curve fitting approach is strongly susceptible to user bias which can result in good fit for a single TL curve, but a model with no predictive merit.

Methods that depend on changes to peak positions, such as the various heating rate method (VHRM) (Hoogenstraaten, 1958) depend on isolated TL peaks to a lesser degree than the peak shape method, being applicable to certain peaks of the OSU materials. Furthermore, by studying the changes in total and individual TL peak area as a function of heating rate one can investigate the existence of thermal quenching for the temperature sensing materials.

One promising analysis method for the OSU temperature sensing materials is the application of the initial rise method (IRM) to step-annealed TL curves (McKeever, 1985). The IRM is perhaps the most reliable method, estimating a TL peaks activation energy, E,

independently of the kinetic order and frequency factor, *s*. The IRM is based on the assumption that at the low temperature side of the TL peak the population of trapped charges remains approximately constant ($n \cong n_0$) and, therefore, the TL intensity is proportional to the factor $\exp(-E/kT)$ (Garlick and Gibson, 1948a). This region is linear when one plots ln(*I*) versus 1/*T*, with the slope being the *E*/*k*.

There has been much debate over what constitutes the upper limit of the initial rise region to be considered for IRM analysis with values falling between 5% and 15% of maximum peak intensity, and considerations such as linearity of the ln(*I*) versus 1/*T* plots have been ruled out (Chen and Haber, 1968; Haake, 1957; Kivits and Hagebeuk, 1977). In cases of strongly overlapped peaks, however, it is often difficult, if not impossible, to isolate a fitting region corresponding to a single trapping center. Furthermore, literature approaches the initial rise region problem with a sole focus on the upper limit but ignores the issue of a lower limit. Experimental TL curves include noise which cannot be removed through background subtraction, and therefore influences both the fitting region choice as well the calculated value for *E*.

For cases where highly overlapped TL peaks cannot be isolated, it has been suggested that step-annealing or partial heatings such as those used by the fractional glow technique (FGT) (Gobrecht and Hofmann, 1966), could be used to recover a trapping center distribution (Rudlof et al., 1978; Van den Eeckhout et al., 2013). The FGT is known to perform well, but requires a highly precise heating system, coupled with extensive data analysis. In contrast, the combination of the IRM with step-annealing is easier to implement and requires less post processing. Recent work by Van den Eeckhout et al. (2013) has shown promise in applying the IRM to more complex peaks, such as those comprised of a Gaussian distribution in activation energy (fixed frequency factor) similar to that previously investigated using the FGT by Rudolf

(1978). Neither FGT nor step-annealing have been tested for several overlapping TL peaks, each consisting of its own trap parameter distribution. The situation is more complicated due to the strong overlap of TL peaks of different intensities and the possible presence of peaks associated with *E*-distributions. The IRM validity and accuracy to obtain *E* in realistic cases, i.e., in the presence of *E*-distributions and strongly overlapped TL peaks, still requires further investigation. Even recent studies on this topic have not considered the influence of noise and experimental uncertainties involved in a TL measurement (Kitis et al., 2017; Van den Eeckhout et al., 2013).

Perhaps the main limitation of the IRM is the lack of a reliable method for obtaining a value for *s*. The y-intercept of the linear fit of the ln(*I*) versus 1/*T* dataset can be used to obtain *s* but requires knowledge of the true TL peak positions, which is not possible for highly overlapped TL peaks. The two-dimensional deconvolution method offers a method for determining both *E* and *s* from a set of experimental TL curves which are expressed as a two-dimensional Fredholm integral equation over a set of activation energies and frequency factors (Chen and McKeever, 1997). The two-dimensional integral approach maps a two-dimensional trap parameter space to a two dimensional experimental dataset comprised of the readout temperature and another experimental variable such as the heating rate (Chen and McKeever, 1997), over several orders of magnitude (Larsen, 1999). Whitley et al. (2002) implemented the two-dimensional integral approach proposed by Chen and McKeever (1997) and applied the deconvolution technique to both simulated TL and thermally stimulated conductivity (TSC) curves, and experimental Al_2O_3:C TL/TSC curves obtained at various heating rates, $I_{TSC}(T, \beta)$. Whitley et al. (2002) used heating rates spanning several orders, as suggested by Larsen (1999), and found good agreement between the trap parameters obtained through the two-dimensional deconvolution and the input parameter distributions used for the simulated datasets.

While the demonstration of the two-dimensional deconvolution by Whitley et al. (2002) on a set of simulated TSC curves is promising, the accuracy of the results in the presence of noise was not investigated. The suggestion by Larsen (1999) of using heating rates spanning several orders of magnitudes, to elicit the dramatic changes to the dataset required by the two-dimensional deconvolution approach, suggests that noise could disrupt the fitting process.

This work presents the efforts to characterize the trap parameters for the OSU temperature sensing materials and to determine the limitations of TL temperature sensing as a diagnostic technique for bio-agent defeat testing. The overarching goal of this project is to establish an approach to characterizing novel TL materials for temperature sensing based upon experimental data and to investigate the factors effecting thermal history reconstruction. The TL analysis methods of VHRM, IRM and two-dimensional deconvolution were applied to the OSU materials. The VHRM datasets were used to determine if the materials suffer from thermal quenching. The application of the IRM and two-dimensional deconvolution to highly complex and realistic TL curves has not been fully investigated to date, thus prior to the application the OSU materials both methods were investigated for their validity and accuracy when applied to complex, realistic, TL curves. IRM studies were applied to numerically generated TL curves resulting from a variety of activation energy distributions. The influence of fitting method (unweighted and weighted least squares), noise, and fitting region on the IRM results were analyzed. The two-dimensional deconvolution method focused on more complex TL curves, simulated for various combinations of activation energy and frequency factors distributions. Datasets for each trap parameter distribution were obtained using either a range of heating rates, or a dataset obtained from various pre-heating temperatures (heating after irradiation and prior to readout). A least squares deconvolution algorithm was used to analyze a set of TL curves in an attempt to extract the underlying *E-s* distributions. Also, the results were

investigated with and without noise, as well as using a non-negative least squares algorithm and Tikhonov regularization. The results are compared to those obtained using TL curves measured with various heating rates, as done by Whitley et al. (2002). We concluded with an investigation of conditions that may adversely affect the determination of a correct thermal history. Numerical methods are applied to study the effect of partial heating resulting from temperature distributions both within a single sample, as well as within a particle. Heat transfer methods were used to determine a TL particle's response time to heating event, and a hydrodynamics simulation of the NSWC closed chamber test was used to study the effect on realistic heating conditions on thermal history reconstruction.

Chapter 2 provides the relevant background of TL processes to understand the studies implemented in this work. The traditional analysis methods and thermal quenching are introduced and discussed. The history of TL materials as temperature sensors is summarized and the established materials and methods for thermal history reconstruction are reviewed. In addition, an introduction to heat transfer methods as they pertain to TL temperature sensing is provided.

Chapter 3 discusses the general details of the experimental studies presented in this dissertation, including the irradiation sources, readout equipment and data acquisition methodologies used for the studies. Additionally, the details for the simulation studies are also provided. Data analysis techniques and uncertainty characterization is also introduced.

Chapter 4 presents the studies performed to investigate the validity of the IRM as applied to realistic, simulated, step-annealed TL curves. TL curves were obtained from a variety of trapping center distributions to help understand the applicability of the IRM technique to temperature sensing materials in Chapter 6.

Chapter 5 presents the result of studies conducted to determine the applicability of the two-dimensional deconvolution method to realistic datasets of complex, highly overlapping peak distributions. Studies look at datasets of step-annealed and VHRM TL curves to identify a superior methodology, and to identify possible limitations, for analysis of temperature sensing materials in Chapter 6.

Chapter 6 presented the results of trap parameter characterization of the temperature sensing materials LBO, MBO and CSO. Studies include the IRM, VHRM and the two-dimension deconvolution method. Results of thermal quenching analysis are also provided. Discussions for each materials suitability as a temperature sensing material are presented, also.

Chapter 7 presents a discussion of the limitations and concerns of TL temperature sensing using heat transfer simulations. The results of partial heating studies are represented and a methodology for determining a thermal response time for a TL particle is discussed. The results of a hydrodynamics simulation of the NSWC close chamber test is used to simulate the residual TL curves from both hypothetical, and real (CSO) materials.

Chapter 8 summarizes the results of the previous chapters to address the limitations of the TL temperature sensing and suggest necessary future work.

CHAPTER 2

BACKGROUND

The aim of this chapter is to provide the reader with relevant theoretical background upon which the future chapters will build. To discuss methods for obtaining kinetic parameters, we must first present the theory of thermoluminescence (TL). This allows for an understanding of the role these parameters play in determining the TL peak shape, temperature of the peak, as well as its thermal stability. Then, we present information pertaining to the traditional analysis techniques which will be used in later chapters. We also present a basic background on temperature sensing and thermal diffusion to provide context for later chapters, which include the limitations of TL particle temperature sensors.

2.1 Basic Thermally Stimulated Luminescence Models

Thermoluminescence (TL) and Thermally Stimulated Luminescence (TSL) are terms ascribed to the light emitted from an irradiated semiconductor or insulator (henceforth TL materials), which has been previously irradiated, subjected to heating. Because TL is a transient phenomenon that requires previous excitation (e.g. irradiation) of the material, it should not be confused with blackbody emission which is persistent and does not require irradiation.

The TL phenomenon is best understood through a band gap diagram (Figure 2-1). The energy levels in a crystalline solid combine to form a delocalized energy band, with the electrons filling all these energy bands up to the top most filled band, called valence band, with an energy E_v. The next available energy to an excited electron is the conduction band with energy E_c. The energy difference between the two is referred to as the band gap with a defined energy of E_g =

$E_c - E_v$. Defects in a crystal structure such as impurities (extrinsic) and lattice vacancies (intrinsic) create localized meta-stable energy states within the band gap and are referred to as trapping centers.

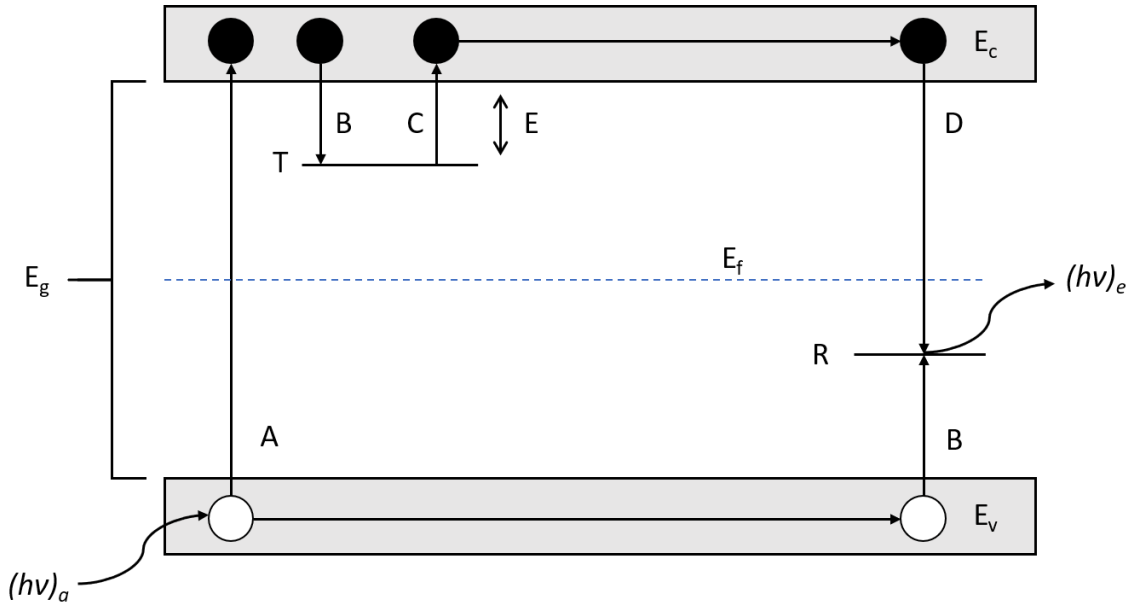

Figure 2-1. Energy band diagram illustrating the valence band, conduction band, Fermi level E_f, and bandgap E_g, as well as electronic transitions for the so-called one-trap, one-recombination center model. Incident radiation is absorbed (A) creating electron-hole pairs; (B) free electrons and holes in the conduction and valance bands are trapped; (C) thermal stimulation results in release of electrons into the conduction band; (D) radiative recombination may occur. Here, T signifies an electron trapping center with energy difference *E* from the conduction band, and R is a recombination center. Adapted from Bos (2006).

Figure 2-1 illustrates a simple band gap model for TL known as the one trap, one recombination (OTOR) center model (Chen and McKeever, 1997). Incident radiation (gamma, x-ray, beta, UV, etc.) provides sufficient energy to ionize electrons in the material creating electron-hole pairs. The charge carriers (electrons and holes) move freely within the bands until either trapping or direct recombination occurs.

The delay between ionization and recombination, as well as the temperature dependence of the phenomenon, dictates the type of luminescence observed. Rapid recombination ($< 10^{-8}$ s) following excitation with little influence of temperature is referred to as

fluorescence. Although longer fluorescence lifetimes have been observed for spin-forbidden transitions; such as the 35 ms lifetime for F-centers in aluminum oxide (Akselrod et al., 2003). Phosphorescence processes are characterized by longer delay times (> 10^{-8} s) and are strongly temperature dependent. TL is a subgroup of phosphorescence processes characterized by delay times of minutes to billions of years (McKeever, 1985).

2.1.1 The First-Order Model

In the case of the one-trap, one-recombination center model, electrons become trapped at the energy level *T* with an energy (trap depth) of $E = E_c - E_T$. In the model presented in Figure 2-1, holes are trapped at R, where R denotes that this center can also be a recombination center. Electrons that become trapped are metastable with a probability of release (per unit time) described by the Arrhenius equation given by:

$$p = s\, exp\left(-\frac{E}{kT}\right), \qquad \textbf{2-1}$$

where *s* is the frequency factor, *E* is the trap depth, *k* is the Boltzmann constant and *T* is the temperature.

If there are *n* trapped electrons, the rate of thermal release of the electrons from the traps is *np*. Assuming the irradiation and storage temperatures of the TL material are small compared *E*/*k*, electrons will remain trapped for extended periods of time or until the temperature is increased, at which point electrons will be released, move through the crystal until they recombine with holes at *R*. Assuming the recombination to be radiative, the resulting luminescence can be measured by a light detection device, such as a photomultiplier tube (PMT).

The TL intensity (per unit time) is proportional to the rate of recombination between electron-hole pairs. Letting n_h be the concentration of holes trapped at *R*, the intensity is proportional to the reduction in trapped holes and can be stated as:

$$I(t) = |dn_h/dt|. \quad \textbf{2-2}$$

We expect the rate at which the hole concentration decreases to depend on the concentration of electrons within the conduction band, the concentration of holes at *R*, and the probability of recombination A_h

$$-\frac{dn_h}{dt} = n_c n_h A_h. \quad \textbf{2-3}$$

The population of trapped electrons decreases with thermal stimulation, but a portion of those electrons that are thermally released can become retrapped with probability $n_c(N-n)A$, where *N* is the number of available electron traps, n_c is the number of electrons in the conduction band, and *A* is the probability of retrapping. Thus, we write the rate of change of trapped electrons as:

$$-\frac{dn}{dt} = np - n_c(N-n)A. \quad \textbf{2-4}$$

Thermally released electrons enter the conduction band and can become retrapped or relax to a recombination center. This behavior is expressed by the following equation:

$$\frac{dn_c}{dt} = np - n_c(N-n)A - n_c n_h A_h. \quad \textbf{2-5}$$

We impose a charge neutrality condition that the total number of electrons in the conduction band and trapped electron population must be equal to the total trapped hole population, $n_c + n = n_h$. Together these coupled rate equations (2-3 to 2-5) and the neutrality condition describe the trap emptying process for which no analytic solution exists without further assumptions.

The rate equations can be simplified by assuming a quasi-equilibrium (QE) condition, wherein the charge carrier concentration in the conduction band is small and quasi-stationary (Chen and McKeever, 1997). Mathematically, the QE assumption is stated as $n_c \ll n, n_h$ and $|dn_c/dt| \ll |dn/dt|, |dn_c/dt|$. Applying the QE assumption to the rate equations gives:

$$I(t) = -\frac{dn}{dt} = nse^{-\frac{E}{kT}}\left(1 - \frac{(N-n)A}{(N-n)A + n_h A_h}\right), \quad \textbf{2-6}$$

where the luminescence intensity is now expressed as a function of the probability of thermal release of an electron multiplied by the probability that retrapping does not occur.

Different assumptions about the rate of retrapping lead to varied orders of kinetics. In the case where retrapping is negligible and recombination dominates $n_h A_h \gg (N-n)A$, the system is said to be governed by first-order kinetics (Randall and Wilkins, 1945b, c), expressed as:

$$I(t) = -\frac{dn}{dt} = nse^{-\frac{E}{kT}}. \quad \textbf{2-7}$$

The recorded TL intensity as a function of heating temperature is called TL curve and is typically obtained using a linear heating ramp expressed as $T = \beta t + T_0$, with a heating rate of $\beta = dT/dt$. Integrating Equation 2-7 for a linear heating produces intensity per unit temperature, known commonly as the Randall-Wilkins (RW) glow curve:

$$I(T) = n_0 \frac{s}{\beta} \exp\left(-\frac{E}{k\,T}\right) \exp\left(-\frac{s}{\beta}\int_{T_0}^{T} exp\left[-\frac{E}{k\,\theta}\right] d\theta\right), \quad \textbf{2-8}$$

where n_0 is the initial trap occupancy. Solutions to the exponential integral can be carried out numerically or by approximation methods (Horowitz and Yossian, 1995). Normalization of Equation 2-8 by n_0 removes the dependence on initial trap occupancy, indicating a linear relationship between intensity and n_0 illustrated in Figure 2-2a. Such behavior is desirable for

both dosimetry and thermometry, as TL peaks will increase with increasing dose (until saturation) and decrease with thermal stimulation.

Figure 2-2b illustrates the effect of trap parameters on the thermal stability of a trapping center. Simulations of RW TL curves for a fixed trap occupancy and activation energy show a shift to lower temperatures with increasing frequency factor (*s*) values, as well as an increase in intensity and narrowing of the peak width, while maintaining constant area.

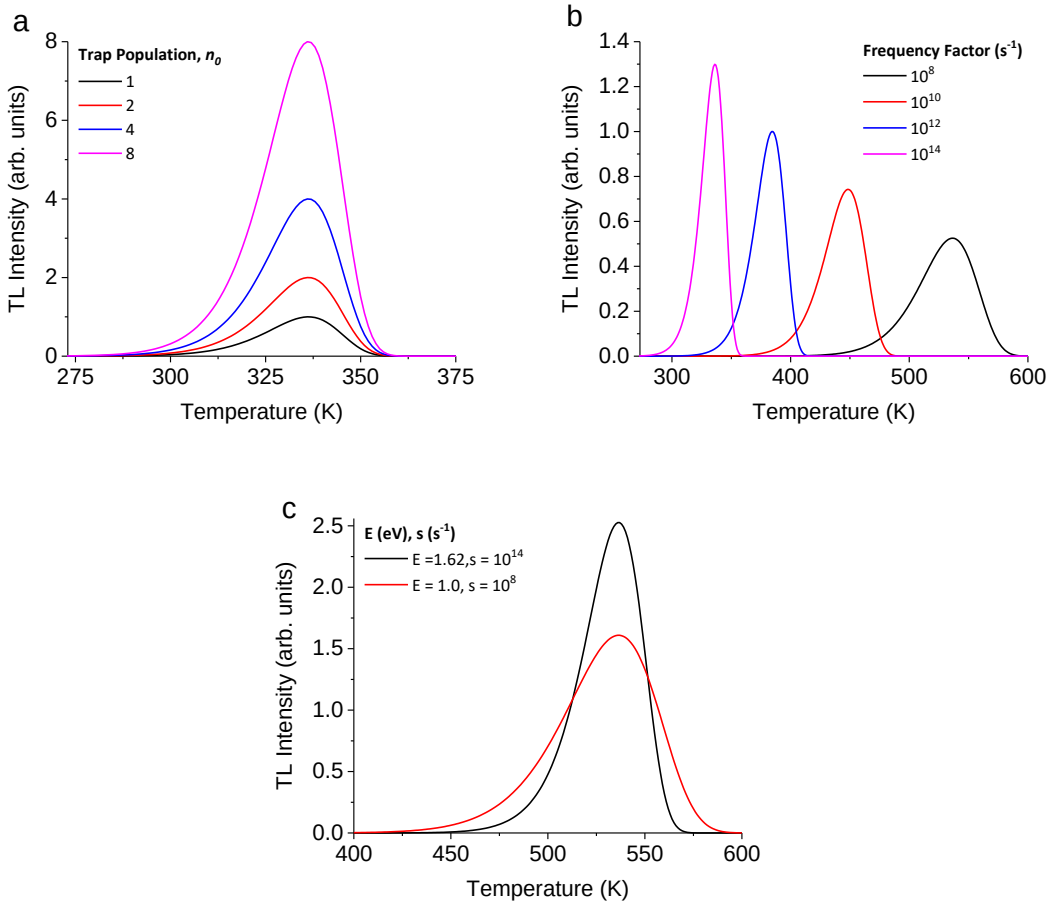

Figure 2-2. Simulated Randall-Wilkins TL curves for: (a) various initial trap occupancy values (*E* = 1.0 eV, *s* = 10^{14} s^{-1}); (b) various frequency factor values (*E* = 1.0 eV, n_0 = 1.0); and (c) T_m = 536 K resulting from two activation energy/frequency factor combinations. Simulations use the exponential integral Ei(x) approximation for the integral in Equation 2-8.

The TL area is proportional to the population of trapped electrons. The same behavior is observed by fixing all values but the activation energy *E*, but in this case increasing *E* values result in higher peak temperatures. There exist no unique combination of frequency factors and

activation energies that correspond to a peak position, but the shape of the TL curve is modified according to the trap parameters (Figure 2-2c). The peak position of a first-order TL curve can be obtained numerically by solving the expression:

$$\frac{\beta E}{kT_m^2} = s \exp\left(-\frac{E}{kT_m}\right), \qquad \textbf{2-9}$$

for the peak position, T_m. Equation 2-9 is obtained by setting the time derivative of Equation 2-8 to zero.

2.1.2 Non-First-Order Behavior

In the event that retrapping dominates, the system is said to be governed by second-order kinetics (Garlick and Gibson, 1948b). The equation for the TL intensity is given by $I(t) = (n^2 s/N) exp(-E/kT)$, resulting in the following expression for a linear heating:

$$I(T) = \left(\frac{n_0^2 s}{N}\right) \exp\left(-\frac{E}{k\,T}\right) \exp\left(1 + \left(\frac{n_0 s}{\beta N}\right) \int_{T_0}^{T} exp\left[-\frac{E}{k\,\theta}\right] d\theta\right)^2, \qquad \textbf{2-10}$$

where *N* is the concentration of available electron traps. Based upon the form of the first- and second-order kinetic equations, a general-order kinetics (GOK) equation for intensity was proposed, $I(t) = (n^b s/N) exp(-E/kT)$ (May and Partridge, 1964). Linear heating gives the following expression for intensity per unit temperature

$$I(T) = s'' n_0 exp\left[-\frac{E}{k\,T}\right] \exp\left(1 + \left((b-1)\frac{s''}{\beta}\right) \int_{T_0}^{T} exp\left[-\frac{E}{k\,\theta}\right] d\theta\right)^{-\frac{b}{b-1}}, \qquad \textbf{2-11}$$

where $s'' = s' n_0 = s n_0 / N$.

The GOK equation is an artificial generalization only and is valid for $b > 1$. With a value of $b = 2$, Equation 2-11 reduces to second-order kinetics. The increase in the kinetic parameter *b* (>1) is supposed to reflect an increase in retrapping. The peak position shifts to lower readout temperatures with increasing dose, and the high temperature side of the TL peak broadens.

Sunta et al. (1998) found that b is not constant and depends on the trap occupancy, $b = n(F'/F) + 1$, where F is defined as the fraction of untrapped charge carriers that recombine, and *F'* is the derivative of F as a function of *n*. Such a conclusion makes the use of the GOK expression (Equation 2-11) for analyses unwise, if one's goal is to obtain realistic trap parameters.

Figure 2-3a demonstrates the effect of increasing *b*, compared to first and second-order TL curves. Unlike the first-order-kinetic case, the effect of varying the initial trap population results in a non-linear behavior, as normalization to initial trap occupancy fails to remove the intensity dependence on trap carrier population, as observed by the exponential dependence on n_0 in Equation 2-10 and s'' in Equation 2-11. The result of varying the initial trap population can be seen for the case of second-order kinetics in Figure 2-3b, where an increase in n_0 leads to a peak shift to lower readout temperatures and a non-linear increase in intensity.

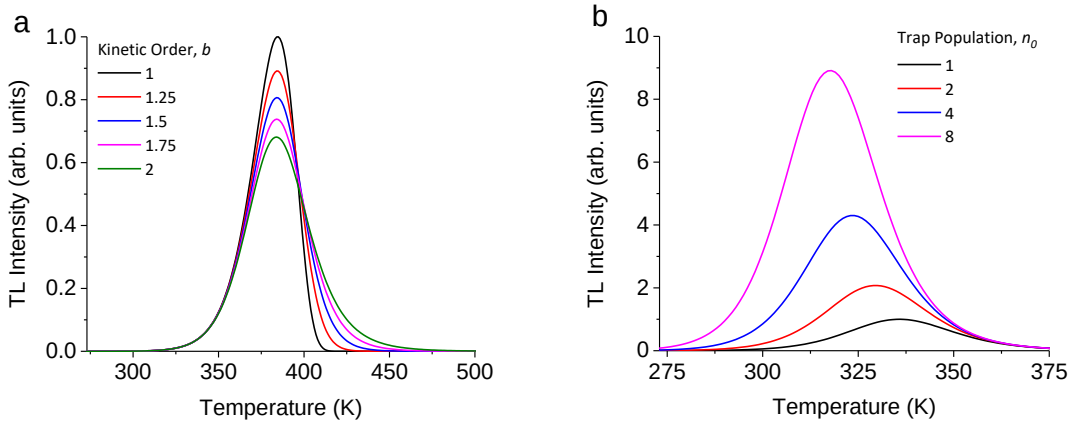

Figure 2-3. (a) Simulations of TL glow curves using the first-order (n_0 = 1, E = 1.0 eV, s = 10^{14} s^{-1}) and second-order TL curve (n_0 = 1, N = 1, E = 1.0 eV, s'' = 10^{14} $s^{-1}m^3$). (b) Simulations of the second-order TL curve (N = 1, E = 1.0 eV, s'' = 10^{14} $s^{-1}m^3$) for various values of n_0.

2.1.3 On the Validity of Higher-Order Kinetics

Although non-first-order kinetic models exist, in which retrapping occurs and influences the TL peak shape and position, only in rare cases have they been supported by experimental

data. Many authors have suggested the presence of higher-order kinetics based on individual TL peak characteristics determined by the peak shape analysis methods (Kitis et al., 2008), or curve fitting using general-order or second-order expressions. Sunta (2015) suggests that many authors cite shifts of the TL peak position with pre-heating to increasing temperatures (step-annealing) as evidence of higher-order kinetics, when they might be equally indication of the presence of multiple overlapping first-order peaks. Sunta et al. (2005) concluded that the glow peaks of real materials do not behave in an analogous manner to non-first-order glow peaks, behaving more closely to first-order kinetics.

A quick comparison of the first-order TL function (Equation 2-8) and the general-order function (Equation 2-11) shows that an increase in the initial occupancy results in a direct change in the peak position. Therefore, one may easily check for the presence of higher-order kinetics through the collection of several TL curves at various doses. If the peak positions are dose independent, then first-order kinetics are present. Even in cases where shifts are found, one must also consider the possibility of trap competition and sensitization (McKeever, 1985).

If a material is determined to have higher-order kinetics by peak shape method or curve fitting, but the peak behavior is dose independent, then the TL curve is more likely associated with a superposition of closely overlap first-order TL peaks, e.g. trapping centers characterized by an activation energy distribution (*E*-distribution).

2.1.4 Distributions in Trapping Parameters

We have suggested that often broad TL peaks are mischaracterized as general-order kinetics instead of a superposition of several closely overlapping first-order TL peaks. The assumption is that the environment surrounding the defect will vary throughout the TL material (crystal, polymer, glass, etc.) as a result of local random variations in bond length and angle which in turn effect the potential (Van den Eeckhout et al., 2013).

Figure 2-4 depicts a band gap diagram with three common distributions: Gaussian, exponential, and uniform. Here trap depths are still measured as the difference between the energy level of the trapped charge and the conduction band energy, while the number of trapping centers, *N*, available at that level is represented by the length of the black bar.

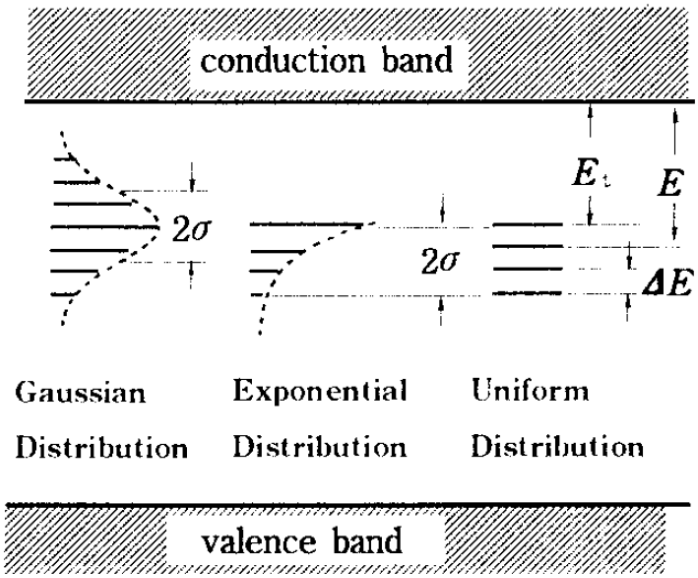

Figure 2-4. Band gap diagram depicting a trapping center distribution. After Sakurai and Gartia (1997).

Initially, the concept of a continuous distribution of activation energies was suggested by Medlin (1961) to explain phosphorescent decay curves using a Gaussian distribution in energy for results that did not follow first or second-order kinetics. Since then, many cases of continuous distributions of activation energy have been seen in a range of materials, including quasi-disorder semiconductors (Bosacchi et al., 1973), polystyrene (Pender and Fleming, 1977a, b), and quartz (Hornyak et al., 1992). Sakurai and Gartia (1997) initially found evidence for an exponential activation energy distribution, but later discovered indirectly through analysis of glass samples their previous result was really the high energy tail of a Gaussian distribution

(Sakurai et al., 2001). The presence of a continuous distribution in activation energy is typically found in highly disordered materials such as polymers and glasses, but evidence of a Gaussian distribution (FWHM = 0.158 eV) was found in the commercial material TLD-400 (CaF_2:Mn) using isothermal decay data (Hornyak and Franklin, 1988).

In prior works mentioned in this section, the continuous nature of the trap distribution was determined using a multilevel trapping model allowing for retrapping (Hornyak and Franklin, 1988; Sakurai et al., 2001). In contrast, we will proceed under the assumption of first-order kinetics as to allow for the superposition principle for first-order TL peaks (Bull et al., 1986b). The following subsections provide the mathematical background to describe TL curves that result from various distributions in activation energy and a multinormal distribution in activation energy and frequency factor.

Activation Energy Distribution

Equation 2-8 can be further generalized for an *E*-distribution by (Agersnap Larsen et al., 1999; Chen and McKeever, 1997; Hornyak and Chen, 1989):

$$I(T) = \int_0^\infty g(E_t) RW(E_t, s)\, dE_t, \qquad \textbf{2-12}$$

where $g(E_t)$ is a normalized trap distribution, often expressed as $N(E_t)f_0(E_t)$ where $N(E_t)$ is the available trap distribution and $f_0(E_t)$ is the initial fraction of filled traps, and s is a fixed (assumed known) frequency factor.

In this work, we focus on three distribution types in activation energy *E* (seen in Figure 2-5a): discrete, Gaussian, and uniform. The discrete *E*-distribution is given by the Dirac delta function $g(E_t) = \delta(E_t - E_0)$, for which Equation 2-12 reduces to Equation 2-8 when $E_t = E_0$.

The Gaussian *E*-distribution with a mean value μ_E and standard deviation of σ_E is given by $g(E_t) = \frac{1}{\sqrt{2\pi}\sigma_E} exp\left(-\frac{(E_t-\mu_E)^2}{2\sigma_E^2}\right)$, with a TL intensity given by (Hornyak and Chen, 1989):

$$I(T) = \frac{n_0}{\sqrt{2\pi}\sigma_E} \int_0^{\infty} e^{-\frac{(E_t-\mu_E)^2}{2\sigma_E^2}} exp\left(-\frac{E_t}{kT} - \frac{s}{\beta}\int_{T_0}^{T} e^{-E_t/kT'}\right) dE_t. \qquad \textbf{2-13}$$

The uniform distribution is expressed by a constant value $g(E_t) = 1/\Delta E$ for E_t values in a range $\Delta E = E_B - E_A$. The expression for TL resulting from such a distribution is expressed as (Hornyak and Chen, 1989):

$$I(T) = \frac{n_0 s}{\Delta E} \int_{E_A}^{E_B} exp\left(-\frac{E_t}{kT} - \frac{s}{\beta}\int_{T_0}^{T} e^{-E_t/kT'}\right) dE_t. \qquad \textbf{2-14}$$

Figure 2-5 shows discrete, Gaussian, and uniform trap distributions (Figure 2-5a) and the associated TL peaks (Figure 2-5b). TL peaks associated with Gaussian and uniform *E*-distributions are more symmetrical than the first-order TL peak (discrete *E*-distribution). As mentioned before, this is often taken (erroneously) as an indicator of higher-order kinetic processes. The rectangular distribution is used to represent the problem of highly overlapped TL peaks with comparable intensities.

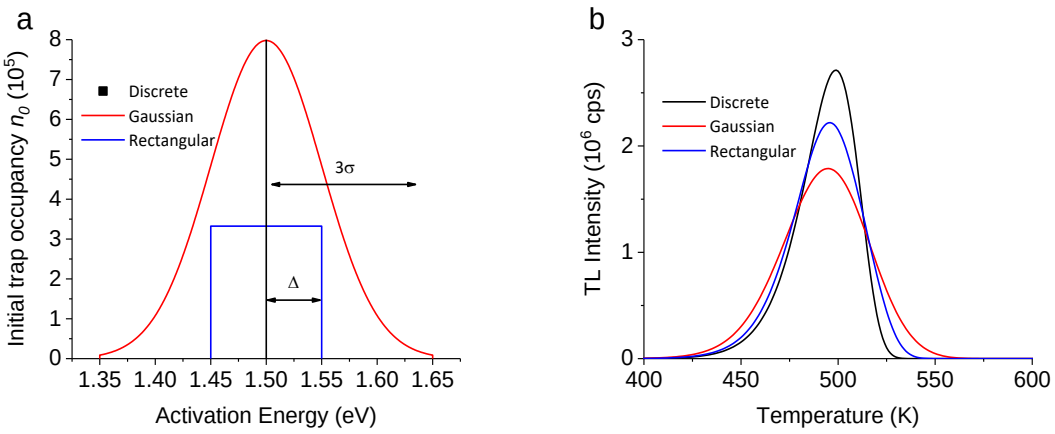

Figure 2-5. (a) Discrete, Gaussian, and uniform *E*-distributions and (b) resultant TL peaks. All TL curves are calculated using $s = 10^{14}$ s^{-1} and a 1 K/s heating rate. A total of 300 and 301 individual TL peaks were used to simulate the Gaussian and uniform respectively.

Distribution in Activation Energy and Frequency Factor

Whitley et al. (2002) assumed the same variations in the crystal lattice that gave rise to a random distribution in activation energy for a single trapping center also produced a random distribution of frequency factors. Under these conditions the trapping center distribution is well described by the probability density function of a two-dimensional multivariate normal distribution, also known as the bivariate normal distribution. The probability density function of the bivariate normal distribution is defined as (Gut, 2009):

$$f(x_1, x_2) = \frac{1}{2\pi\sigma_1\sigma_2\sqrt{1-\rho^2}} \times \exp\left(-\frac{1}{2(1-\rho^2)}\left[\left(\frac{x_1-\mu_1}{\sigma_1}\right)^2 - 2\rho\left(\frac{x_1-\mu_1}{\sigma_1}\right)\left(\frac{x_2-\mu_2}{\sigma_2}\right) + \left(\frac{x_2-\mu_2}{\sigma_2}\right)^2\right]\right), \quad \textbf{2-15}$$

where $\rho = \sigma_{12}/\sigma_1\sigma_2$, and σ_{12} is the covarance. If both variables are independent of each other, then $\rho = 0$, and the probability density function simplifies to

$$f(x_1, x_2) = \frac{1}{2\pi\sigma_1\sigma_2} \exp\left(-\frac{1}{2}\left[\left(\frac{x_1 - \mu_1}{\sigma_1}\right)^2 + \left(\frac{x_2 - \mu_2}{\sigma_2}\right)^2\right]\right). \quad \textbf{2-16}$$

For a bivariate normal distribution of traps in both activation energy and log frequency factor space, $\log s$, we transform the one-dimensional Fredholm integral expression in Equation 2-12 to a two-dimensional Fredholm integral expression as

$$I(T) = \int_{E_0}^{E_f} \int_{s_0}^{s_f} g(E_t, s_t) RW(E_t, s_t) dE_t ds_t\,, \quad \textbf{2-17}$$

where $g(E_t, s_t)$ is the probability density function for the trapping center

$$g(E_t, \log s_t) = \frac{1}{2\pi\sigma_E\sigma_{\log s}} exp\left(-\frac{(E_t - \mu_E)^2}{2\sigma_E^2} - \frac{\left(\log s_t - \mu_{\log s}\right)^2}{2\sigma_{\log s}^2}\right). \quad \textbf{2-18}$$

2.1.5 Other Considerations

Having discussed the basic models for TL it is important to understand material and experimental conditions that affect the ability to recover the parameters of the TL model. Many analysis methods, such as those to be discussed later, rely upon an undistorted TL peak to recover descriptive trap parameters.

Thermal fading and low temperature phosphorescence are two major concerns for traps with low thermal stability. The mean time of an electron in a trapping center is exponentially dependent on the temperature (McKeever, 1985):

$$\tau = s^{-1} e^{E/kT}. \quad \textbf{2-19}$$

Shallow trapping centers, defined as having a short lifetime at room temperature, will lead to phosphorescence and distort the low temperature part of the TL peaks during TL curve acquisition. Additionally, traps that are thermally unstable at room temperature will fade during storage and during the delay between irradiation and data acquisition.

Thermal lag between material temperature and heat source can lead to a distortion and shift in peak positions. This effect is generally the result of attempts to heat a large amount of material corresponding to a larger thermal mass, or insufficient contact between the sample material, sample holder and heat source. High heating rates that outpace the thermal conductivity of the sample and the sample holder will also lead to thermal lag. When investigating trap parameters, care must be taken to reduce the effect of thermal lag as multiple analysis methods rely on accurate peak position to recover activation energy.

There exist many other concerns that we have not yet discussed. These include, but are not limited to, recombination as a result of the tunneling process, localized transitions, and temperature dependence of the frequency factor (McKeever, 1985). The TL models and analysis presented in this work did not involve any of these complications and, therefore, we proceed without a thorough discussion of them, but point out that when choosing materials for TL temperature sensing one must be aware of their effects.

2.1.6 Non-Radiative Recombination

Thus far, we have only considered cases where thermal release results in a radiative recombination, but this is not always the case. TL peaks occurring at higher readout temperatures can sometimes experience reduced intensity and a distortion of peak shape. This effect has been seen in multiple TL materials including quartz (Wintle, 1975) and α-Al_2O_3:C (Akselrod et al., 1998a; Akselrod et al., 1998b). This high temperature effect is commonly referred to as thermal quenching and is a result of a temperature dependent reduction in luminescence efficiency of the luminescence centers.

The luminescence efficiency is defined as η and is expressed as a ratio of the probability of a radiative recombination Γ_r, over the total probabily of recombination (Chen and McKeever, 1997):

$$\eta = \frac{\Gamma_{\mathrm{r}}}{\Gamma_{\mathrm{r}} + \Gamma_{\mathrm{nr}}}, \qquad \textbf{2-20}$$

where Γ_{nr} is the probability of a non-radiative recombination. If thermal quenching is not present, then there is no probability of a non-radiative recombination and the luminescence efficiency is equal to one. In the case where $\Gamma_{\mathrm{nr}} \neq 0$, we must consider the situations that give rise to a non-radiative recombination.

First, we will consider the Mott-Seitz model and refer the reader to the OTOR model (Figure 2-1). Following the thermal excitation of the electron to the conduction band and the electronic transition to the recombination center (R, also known as luminescence center), the electron is in an excited state as illustrated by the configuration coordinate diagram (Figure 2-6). The transition from the excited state E_e to the ground state E_g produces luminescence. If, however, the electron absorbs an additional energy, W, while in the excited state by phonon interaction (lattice vibrations), the electron can transition to the ground state level and relax to the lowest energy state E_g without the emission of light (via phonon emission) (Bøtter-Jensen et al., 2003).

The probability for a non-radiative recombination is given as $\Gamma_{nr} = \Gamma_0 \exp(-W/kT)$ where Γ_0 is a non-zero constant. Plugging in the expression for Γ_{nr} and normalizing Equation 2-20 by Γ_r gives a luminescence efficiency of

$$\eta(T) = \frac{1}{1 + (\Gamma_0/\Gamma_r)\, exp(-W/kT)}, \qquad \textbf{2-21}$$

where the ratio Γ_0/Γ_r is typically expressed as a pre-exponential factor c.

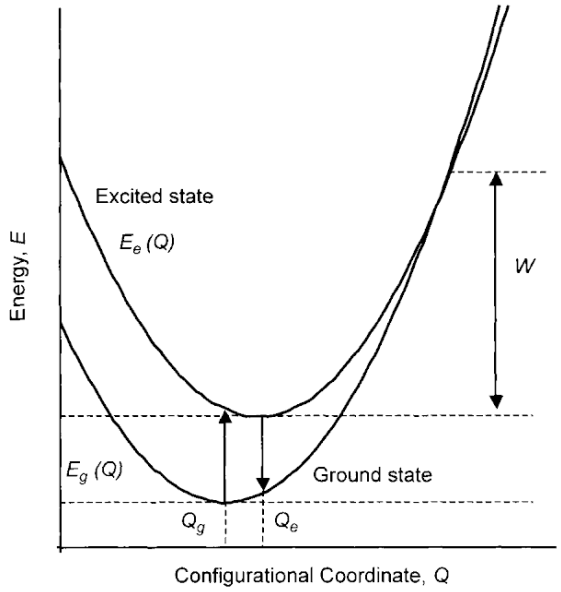

Figure 2-6. Configuration coordinate diagram for the luminescence center. After Bøtter-Jensen et al. (2003).

Just as electrons have a probability of thermal release during heating, holes can also become thermally freed from (under the OTOR mode) the luminescence center with a probably of $p_h = s_h \exp(-E_h/kT)$. If the freeded holes recombine non-radiatively with trapped electrons within the lattice, then the number of available holes for radiative recombination is decreased, resulting in a temperature dependent decrease in luminescence. Under the Schön-Klasens model, the probability for non-radiative recombination is equal to the probability of thermal release of a hole from the luminescence center and, therefore, the efficiency function takes the same function form, with W now representing the activation energy for the hole (McKeever, 1985):

$$\eta = \frac{1}{1 + c\ exp(-W/kT)}. \qquad \textbf{2-22}$$

Figure 2-7 shows the results of thermal quenching on a simulated glow curve obtained by numerically solving the rate equations for a system with two electron trapping centers, one sufficiently deep such that it is thermally disconnected, and a single recombination center.

Figure 2-7a illustrates how the quenching function (Equation 2-22) reduces the overall intensity of the peak, distorts the shape of the peak, and shifts the peak to a lower readout temperature.

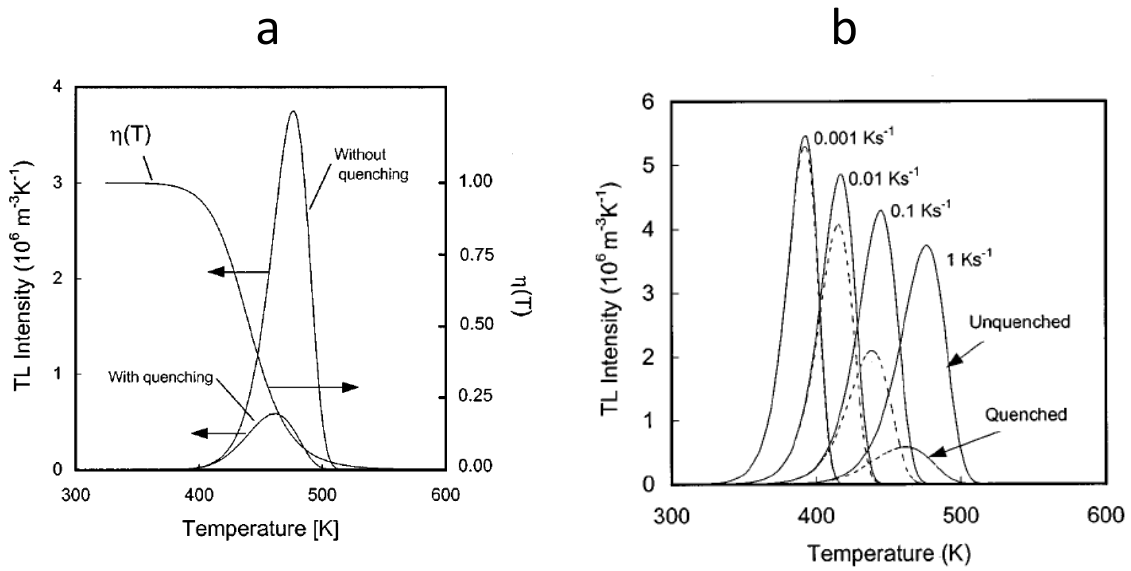

Figure 2-7. Effect of thermal quenching on (a) a single simulated TL curve and (b) a set of TL curves collected at various heating rates. Simulations used *W* = 1.05 eV and a pre-exponential factor *c* = 10^{12}. The TL curve was obtained using an activation energy of 1.25 eV and a frequency factor of 10^{13}s^{-1}. After Akselrod et al. (1998a).

Figure 2-7b shows how the quenching function affects TL curves obtained at different heating rates. As discussed before, increasing the heating rate shifts the TL peak position to higher temperatures, while reducing the intensity and broadening the peak to conserve the area (McKeever, 1985). In this case, the effect of the quenching function becomes greater as the peak position moves to higher temperatures. As a result, the area is no longer conserved, which provides one with an experimental consideration for determining the presence of thermal quenching in a material.

Having discussed the basics of TL and some of the factors that contribute to the collection of TL curve, we now discuss methods to recover trapping parameters.

2.2 ***Thermoluminescence Analysis Methods***

Knowledge of the kinetic order and trapping parameters allows for an understanding of how a TL curve behaves under the influence of irradiation and heating. Multiple analysis methods, both experimental and computational, are available for investigating a TL material's trapping parameters. In this section, we provide a description of the analysis methods implemented in this project to investigate the materials produced at OSU.

2.2.1 Initial Rise Method

The IRM is an attractive approach to determine the activation energy of isolated TL peaks, due in part to its ease of application and validity for all kinetic orders. The method relies on the assumption that, in the initial portion of a TL peak (low readout temperature side), the trap occupancy (electron, hole, etc.) is approximately constant. Inspection of Equation 2-7 for the case of $n \cong n_0$ leads to the approximation of the initial rise in luminescence as exponential (Garlick and Gibson, 1948b)

$$I(T) \propto C_0 \, exp(-E/kT). \qquad \textbf{2-23}$$

A plot of $ln\, I(t)\ vs\ 1/T$ produces a linear trend with a slope of $-E/k$, allowing for the determination of the activation energy. To convince oneself of the IRM's independence of kinetic order, consider the integral $\int_{T_0}^{T} \exp\left(-\frac{E}{k\,\theta}\right) d\theta$ in the initial rise limit, $T \cong T_0$, which reduces to zero simplifying each TL curve expression to Equation 2-23.

If the initial rise region under investigation behaves according to first-order kinetics, is well isolated, and is known to belong to the peak of interest located at a readout temperature T_m, then the frequency factor is calculated as

$$s = \beta E/kT_m^2 \cdot exp(E/kT_m), \qquad \textbf{2-24}$$

where β is the heating rate (K/s), and k is the Boltzmann constant. Equating the derivative of Equation 2-8 to zero results in a transcendental equation (in temperature) that allows for the determination of the peak's position T_m. Through algebraic manipulation, the same expression yields Equation 2-24 allowing for the determination of s.

Two major assumptions have been made in the current discussion of the IRM. The first is that we know the correct interval to apply the method; and second that the initial rise region of interest belongs to the peak we wish to investigate.

It is attractive to choose a data set that produces the best linear fit to determine the region to be fitted. This approach, however, leads to errors in the calculated activation energy and, therefore, the frequency factor as well (Chen and Haber, 1968; Haake, 1957). Computer simulations have previously been used to show that a critical temperature corresponding to 5 – 15% of the max peak intensity resulted in the smallest deviation of the calculated value for *E* from the input value (Chen and Haber, 1968; Kivits and Hagebeuk, 1977).

The choice of an upper limit of 5 – 15% ensures the analysis region obeys the initial rise condition, $n \cong n_0$, but minimal discussion is aviable regarding the lower limit for experimental data, which is of concern when dealing with systematic noise. Christodoulides (1985) found that researchers were using upper limits as high as 50% of the max peak intensity for TL curves with poor signal to noise ratios. Christodoulides (1985) developed a correction function for the IRM activation energy obtained from a region bounded by a minimum (α_1) and maximum (α_2) percent of the max peak intensity, which allows for the freedom to avoid high noise regions of an isolated TL curve. A small survey of published activation energies obtained from the IRM was found to require corrections between 1% to a 25% increase in energy. Singh et al. (1988) extended this work to TL curves with general order kinetics, but neither correction method has been applied to TL curves with overlapping peaks. Assuming we have established the

appropriate range to apply the IRM, we must ensure the initial rise region is isolated to the peak of interest. In cases of strongly overlapped peaks, however, it is often difficult, if not impossible, to isolate a fitting region corresponding to a single trapping center. Generally, TL curves are composed of multiple, often overlapping, TL peaks.

To ensure the initial rise region of a TL peak has been cleared, a step-annealing approach is employed (McKeever, 1980). Step-annealing is the refinement of previous attempts to use thermal cleaning to resolve peaks and their activation energies (Nicholas and Woods, 1964) and a method known as the fractional glow curve technique (FGCT) which uses series of controlled partial heating and cooling cycles to resolve peak structures (Gobrecht and Hofmann, 1966).

Step-annealing works by heating an irradiated TL material to a temperature below the maximum readout temperature, cooling to room temperature, then heating to the maximum readout temperature. The process is repeated, increasing the pre-heating temperature (T_{stop}) by (2 – 5) °C every step. The result is a sequential depletion of the low temperature TL structures to aid in isolation of the initial rise region of higher temperature TL peaks. A plot of the peak position T_m, as a function of annealing temperature T_{stop}, referred to as a $T_m - T_{stop}$ plot, can be used resolve peak position and to infer information pertaining to kinetic order. Additionally, the use of step-annealing technique with $T_m - T_{stop}$ data has been successful in the guidance of other analysis techniques such as curve fitting (McKeever, 1980).

Figure 2-8 illustrates how $T_m - T_{stop}$ varies for first and second-order kinetics according to different TL peak spacing. Though this method is accurate to ~5 K resolution of peak position it is only effective for resolving the most prominent TL peaks. Low intensity peaks can be obscured by their larger intensity neighbors.

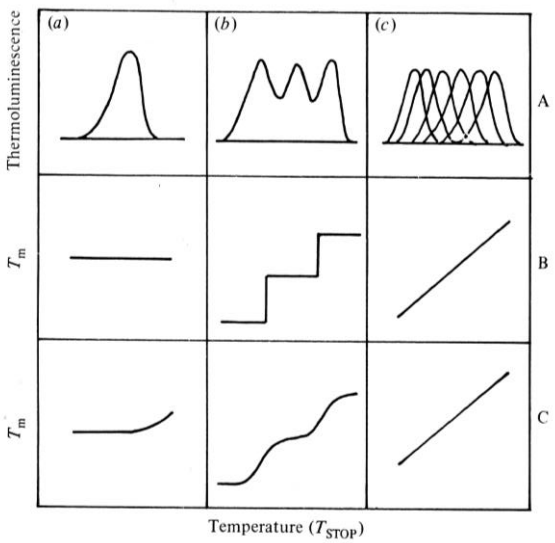

Figure 2-8. Row A indicates the TL peak configuration while Rows B and C show the resulting T_m-T_{stop} plots for the first and second-order kinetics respectively. After McKeever (1980).

The step-annealing method suggested by McKeever (1980) works well for cases where the annealing procedure fully separates the initial rise region from lower temperature peaks, but often, data is found to be closer in behavior to those in Row B columns (b) and (c) of Figure 2-8.

The previously mentioned factional glow curve technique (FGT) offers a more sophisticated and precise method for obtaining the underlying trap distribution of a TL material with poorly resolved peaks than the step-annealing procedure alone. The FGT purposed by Gobrecht and Hofmann (1966) applies the IRM to TL curves collected during successively increasing linear heating and cooling cycles see in Figure 2-9. Work by Rudlof et al. (1978) applied the FGT to highly complex TL curves obtained from uniform and Gaussian distributions in either activation energy or frequency factor and found poor agreement between the trap parameters obtained by the FGT and the simulation values at the low side of the respective distribution.

Chruścińska (1994) developed new method for obtaining an activation energy from a FGT dataset which took into account the activation energies of both the heating and cooling cycles. This approach accurately reconstructed simulation inputs and reduced the issues seen by Rudlof et al. (1978), but the FGT still sees very little use in publications presenting material trap parameters.

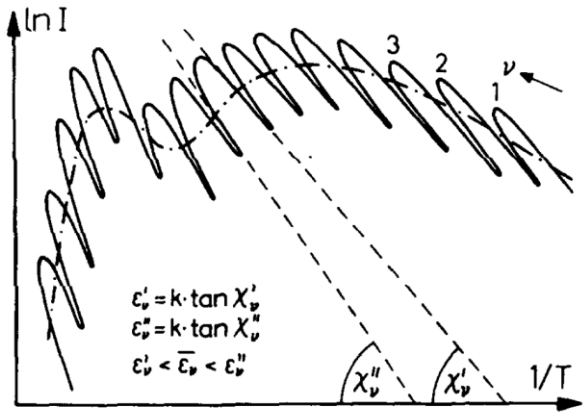

Figure 2-9. Fractional glow curves shown as natural log of intensity versus inverse temperature. Curves were obtained from iterative linear heating and cooling of a TL material. Here v is the heating-cooling cycle. Adapted from Gobrecht and Hofmann (1966).

The success of the FGCT is highly dependent on the experimental system. Insufficient thermal contact between the material and heater or thermal gradients within the material itself can produce large values of thermal lag which introduce large errors in the recovered parameters (Kitis et al., 2000). Additionally, any inconsistencies in the programed heating rate, such as overheating and overcooling will also introduce errors in the calculation of trap parameters therefore producing a need for a highly accurate temperature control system (Lyamayev, 2006).

Van den Eeckhout et al. (2013) suggested an alternative method from FGT for obtaining a trap distribution using just the linear heating rates from the step-annealing procedure. In this method, activation energies are computed using the IRM as previously suggested and the

depletion of the TL curve area between successive heatings, see Figure 2-10, is used to weight the contribution of that given activation energy to the distribution as is the case in the FGT.

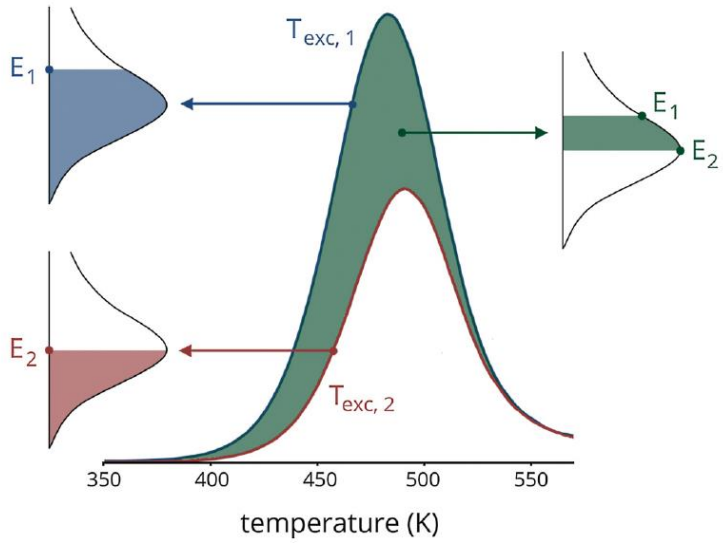

Figure 2-10. For a TL peak that is the result of a superposition of Gaussian distribution TL peaks, the difference in area between two step-annealed curves is proportional to the change in trap population. Here T_{exc} is the excitation temperature (or preheat temperature) and *E* is activation energy. After Van den Eeckhout et al. (2013).

Van den Eeckhout et al. (2013) tested the method on TL curves obtained from both Gaussian and uniform distributions in activation energy. They found the IRM to provide a good estimate to the lower side of the energy distribution when looking at just the first step-annealed curve, but provided no further efforts to demonstrate the full distribution could be recovered.

The IRM validity and accuracy to obtain *E* in realistic cases, i.e., in the presence of *E*-distributions and strongly overlapped TL peaks, still requires further investigation. Even recent studies on this topic have not considered the influence of noise and experimental uncertainties involved in a TL measurement (Kitis et al., 2017; Van den Eeckhout et al., 2013).

2.2.2 Various Heating Rate Method

TL curves are generally collected using a linear heating function, $T(t) = T_0 + \beta t$. The effect of increasing a heating rate, while keeping all other parameters equal, is to shift the TL peak to a higher readout temperature, while reducing maximum peak intensity and increasing the peak width to maintain total area. This is a result of the decrease in the amount of time the sample remains at a given temperature, thereby reducing the integrated intensity per degree readout temperature, as illustrated by the unquenched curves in Figure 2-7b.

A relationship between the peak position T_m and the heating rate β can be expressed by a manipulation of Equation 2-24:

$$\beta = (sk/E)T_m^2 exp(-E/kT_m), \qquad \textbf{2-25}$$

where an increase in the heating rate must be met by an increase in $T_m^2 exp(-E/kT_m)$, and therefore an increase in peak position. Theoretically, it is possible to extract the activation energy from this transcendental equation. In practice, however, the only parameters available are the heating rate and peak position, thereby requiring knowledge of the frequency factor. Under the assumption that the frequency factor is not temperature dependent, Equation 2-25 can be written for two heating rates as $\beta_1$and β_2 for $\beta_1 \neq \beta_2$. The calculation of β_1/β_2 removes the dependence of the activation energy's calculation on the frequency factor (Bohun, 1954; Booth, 1954; Parfiabovitch, 1954). Simplifying β_1/β_2 yields the following expression for the activation energy:

$$E = \left(k \frac{T_{m,1}T_{m,2}}{(T_{m,1} - T_{m,2})}\right) ln\left[\left(\frac{\beta_1}{\beta_2}\right)\left(\frac{T_{m,2}}{T_{m,1}}\right)^2\right]. \qquad \textbf{2-26}$$

This approach can be extended for the case of several heating rates by the following manipulation of Equation 2-25 (Hoogenstraaten, 1958),

$$\frac{T_m^2}{\beta} = s\frac{E}{k}exp\left(\frac{E}{kT_m}\right), \quad \textbf{2-27}$$

$$ln\left(\frac{T_m^2}{\beta}\right) = ln\left(\frac{E}{sk}\right) + \frac{E}{k}\frac{1}{T_m}, \quad \textbf{2-28}$$

allowing for a linear trend between $ln(T_m^2/\beta)$ and $1/T_m$ with a slope of E/k. The activation energy is obtained from the slope of a linear fit and in turn used to calculate the frequency factor from the *y*-intercept $ln(E/sk)$.

The VHRM has been shown to be applicable for any first-order TL peak obtained using a monotonically increasing heating rate function and to be a good approximation for non-first-order kinetics process (Chen and Winer, 1970). As with the IRM, the VHRM approach favors only the most prominent peaks and can be affected by thermal lag which becomes more apparent at higher heating rates. Furthermore, this method assumes a tracking of a singular peak position and not that of a TL peak resulting from a distribution of closely grouped trapping centers. In such a case, the VHRM will resolve an effective trapping parameter set responsible for the peak shift, but fail to characterize the individual components within the distribution.

2.2.3 Peak Fitting

Previously we have discussed experimental methods to investigate a TL material's trapping centers. These methods have focused on an analysis of regions of a TL peak or its change in position when varying experimental factors such as annealing temperature or heating rate. With aid of computational software, it is possible to analyze a single TL curve by peak fitting or deconvolution to obtain individual TL peak parameters (*E*, *s*, T_m). Nevertheless, special attention must be paid to data collection, as errors introduced at this point will lead to errors in analysis (Chen and McKeever, 1997). Curve fitting requires the knowledge of the number of TL

peaks, for which $T_m - T_{stop}$ may be useful, and looks to represent the TL curve as a superposition of TL curves expressed as:

$$I(T) = \sum_{i=0}^{\nu} \alpha_i f_i(T), \qquad \textbf{2-29}$$

where ν represents the number of TL peaks, α_i weights the solution, and $f_i(T)$ is the function choosen to represent the TL curve from which trapping parameters can be extracted (Chen and McKeever, 1997). For this reason, peak fitting is often referred to as "Glow Curve De-Convolution" or GCDC as TL curve is represented as a deconvolution of individual glow curves.

Many functions beyond the first, second, and general-order formulas presented here can be used in place of $f_i(T)$, having been tested through the GLOCANIN project and discussed by others (Chen and Pagonis, 2011). There are freely available programs such as GlowFit (Puchalska and Bilski, 2006), also. Other models such as the asymmetrical Weibull distribution (c = 16) have shown to have accurately represent TL curves (Pagonis et al., 2001)

$$I(T) = 2.713\, I_m \left(\frac{T - T_m}{b} + 0.996\right)^{15} exp\left(-\frac{T - T_m}{b} + 0.996\right)^{16}. \qquad \textbf{2-30}$$

It should be noted that superposition principle for multilevel interacting trapping centers is only valid for first-order kinetics (Bull et al., 1986b). Non-first-order behavior assumes retrapping cannot be ignored and allows for the possibility for interaction between trapping centers, making the use of curve fitting with non-first-order expressions suspect.

2.2.4 Deconvolution

An alternative to the traditional methods mentioned above and curve fitting is deconvolution. The difference between this method and that of the GCDC method presented in the prior section is the GCDC typically relies on non-linear least square fitting methods while this section focusses on the tradition interpretation of a deconvolution. This method makes no

assumptions on the number of underlying trapping centers and can be constrained to a set of experimental TL curves. Based on Bull et al. (1986a), it was suggested that an experimental TL curve can be expressed as a two-dimensional Fredholm integral equation over a set of activation energies and frequency factors (Chen and McKeever, 1997). The two-dimensional integral approach maps a two dimensional trap parameter space to a two dimensional experimental dataset comprised of the readout temperature and another experimental variable such as the heating rate (Chen and McKeever, 1997), over several orders of magnitude (Larsen, 1999) and is expressed as:

$$I(T,\beta) = \int_{E_0}^{E_f} \int_{s_0}^{s_f} g(E_t, s_t) F(E_t, s_t, T, \beta) dE_t ds_t \,, \qquad \textbf{2-31}$$

where β is a range of heating rates and $F(E_t, s_t, T, \beta)$ represents the user's choice function for a TL curve (typically Randall-Wilkins).

The solution the two-dimensional expression is not straightforward and as a result initial work proceeded with a simplification to one-dimension expression which requires one to restrict one of the trap parameters, typically the frequency factor. A more physical choice of *s* can be made by repeating the deconvolution multiple times for different fixed frequency factors and selecting the value which reduces a figure of merit parameter such as chi-squared (Chen and McKeever, 1997).

This method can be further refined by carrying out the deconvolution over a range of fixed frequency factors for a set of preheated TL curves (Yukihara et al., 2014b). By fixing the frequency factor to a realistic value, the superposition principle can be presented as an integration over a distribution of trapping centers, $g(E_t)$, with an initial occupancy dependent on the activation energy (Agersnap Larsen et al., 1999; Chen and McKeever, 1997; Hornyak and Chen, 1989)

$$I(T) = \int_0^{\infty} g(E_t) RW(E_t, s, T, \beta)\, dE_t, \qquad \textbf{2-32}$$

where the frequency factor s, is now fixed and the dataset $I(T)$ is now a single curve collected at a single heating rate. Larsen (1999) applied the one-dimensional deconvolution analysis to TSC curves of α-Al_2O_3:C, where the TSC curves were expressed as a superposition of first-order peaks with a distribution of activation energies and a common frequency factor assumed to be 10^{13} s^{-1}. More recently, the one-dimensional deconvolution approach was also applied to temperature sensing materials with some success (Yukihara et al., 2014b). The limitation of this approach is that all TL peaks must have the same (or very similar) frequency factor, which may not be the case. As a result, an incorrect choice of frequency factor will bias the activation energy results.

Whitley et al. (2002) implemented the two-dimensional integral approach initially proposed by Chen and McKeever (1997) to both simulated (no noise) and experimental Al_2O_3:C TSC curves obtained at three heating rates 0.001, 0.01, and 0.1 K/s. Whitley et al. (2002) found good agreement between the trap parameters obtained through the two-dimensional deconvolution and the input parameter distributions used for the simulated datasets as shown in Figure 2-11. Analysis of the experimental Al_2O_3:C TSC curves indicated the low temperature peak to be comprised of six trapping centers and with the high temperature peak comprised of a single trapping center.

While the demonstration of the two-dimensional deconvolution by Whitley et al. (2002) on a set of simulated TSC curves is promising, the accuracy of the results in the presence of noise was not investigated. The suggestion by Larsen (1999) of using heating rates spanning several orders of magnitudes, to elicit the dramatic changes to the dataset required by the two-dimensional deconvolution approach, suggests that noise could disrupt the fitting process.

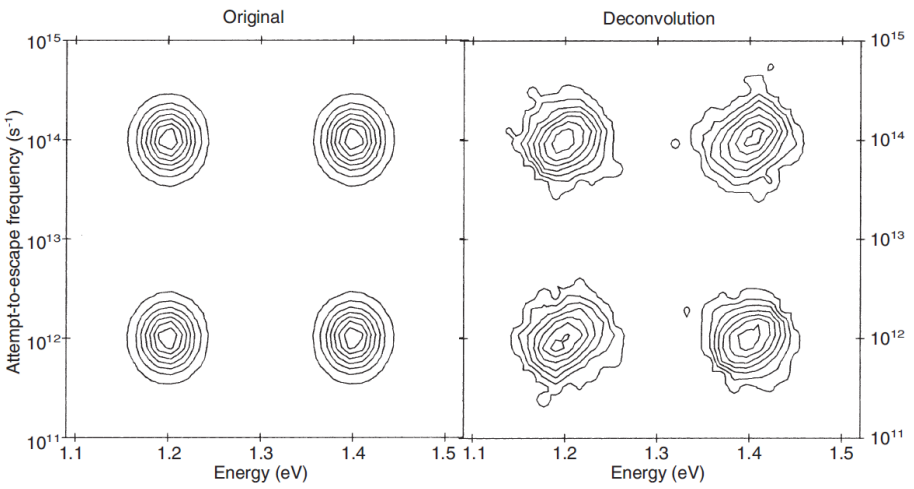

Figure 2-11. Contour plots of the simulation input parameters used to generate TSC curves and the trap parameter distributions obtained from two-dimensional deconvolution. After Whitley et al. (2002).

The only requirement for the application of the two-dimensional deconvolution is that the variation of an experimental parameter produces a significant change in the resulting experimental curve. Instead of using different heating rates, one can also use TL curves obtained after the material has been irradiated and subjected to a pre-heating to various temperatures. Since the rate with each the TL peaks are depleted depends on both *E* and *s*, these sets of curves provide the constraint necessary to solve the two-dimensional deconvolution problem.

If we fix the heating rate β and instead vary the preheat treatment, we must find a new functional form for F. Let ψ represent the preheating temperature profile, and $\phi(E_t, s_t, \psi)$ the fractional depletion of the trapping center (E_t, s_t) resulting from the preheating. Equation 2-8 states that any change in the initial trap population results in a proportional reduction in curve intensity. Therefore, the decrease in the TL peak after preheating is directly proportional to the decrease in the trapped population due to the preheating. The function F is modified to reflect the dependence on ψ resulting in:

$$I(T,\psi) = \int_{E_0}^{E_f} \int_{s_0}^{s_f} g(E_t, s_t)[\phi(E_t, s_t, \psi) RW(E_t, s_t, T, \beta)] dE_t ds_t, \qquad \textbf{2-33}$$

where the experimental curve $I(T,\psi)$ reflects intensity, changes resulting from readout temperature and variations caused by the preheating, instead of the heating rate.

2.2.5 Thermal Quenching

The analysis methods discussed in this section assumed the TL curve of interest is not effected by thermal quenching which can lead to an underestimation in calculated activation energies (Subedi et al., 2010). To use TL curves for analysis, one must first establish if thermal quenching is present and, if necessary, correct the TL curves prior to analysis.

The total luminescence for a single TL peak is given by $I(T) = (1/\beta)\int_0^\infty I_{TL}(T)\,dT = \eta \cdot n_0$ (Nanjundaswamy et al., 2002) where β is the heating rate, η is the luminescence efficiency and n_0 is the initial trap occupancy (TL area). If the factor η is independent of heating temperature (constant), the total luminescence (TL curve area) will be independent of heating rate for the same trap occupancy. If η is dependent on heating temperature, a reduction in TL area will be observed for increasing heating rates. An example of thermal quenching was previously shown in Figure 2-7, and shows a noticeable reduction in area as well as a distortion of each peak's shape for higher heating rates.

To determine the existence of thermal quenching, a dataset of TL curves is obtained for a large range of heating rates. Each TL curve is used to obtain individual TL peak area as a function of heating rate using GCDC. Plots of individual peak area (typically normalized to the lowest heating rate) as a function of heating rate are used to determine if the area deviates from the expected constant behavior as a function of temperature. If quenching is determined to be present for the material, then efforts to obtain the quenching parameters in Equation 2-20 are made so that the quenched curve can be corrected.

Now, we will discuss two methods for obtaining the quenching parameters *c* and *W* of the efficiency factor η defined previously in Equation 2-22. The calculation of parameters utilizes indirect methods such as modeling changes in intensity with heating rate (Kitis et al., 1994), or fitting the ratio of peak areas (Subedi et al., 2011).

The first method proposes modeling the maximum peak position as a function of heating rate given by $T_m = \alpha_1 \beta^{\gamma_1}$ where α_1 and γ_1 are obtained by curve fitting (Kitis et al., 1994). Figure 2-12a illustrates this approach for simulated data. The normalized TL response (peak intensity) will decrease according to Equation 2-22, which with a substitution of T_m for *T* can be expressed in terms of heating rate as,

$$\eta(\beta) = \frac{1}{1 + c\ exp(-W/k(\alpha_1 \beta^{\gamma_1}))}, \quad \textbf{2-34}$$

where α_1 and γ_1 were previously obtained. A fit of the normalized intensity as a function of heating rate using Equation 2-34 will yield values for c and W, illustrated in Figure 2-12b.

Subedi et al. (2010) states the relationship between an individual TL peaks quenched, and unquenched area is expressed as

$$\eta(T_{mq}, \beta) = \frac{A(\beta)}{A(\beta_l)} \eta(T_{mq}, \beta_l), \quad \textbf{2-35}$$

where T_{mq} is the quenched peak position and β_l is the lowest heating rate. Since unquenched data is typically unavailable, the use of the factor $\eta(T_{mq}, \beta_l)$ is introduced to scale the results accordingly, but the authors do not suggest a method for obtaining this factor when unquenched data is unavailable. The area for TL peaks in multipeak TL curves is obtained using GCDC. This method has been used to obtain thermal quenching parameters for natural and synthetic quartz (Subedi et al., 2011), where the lowest temperature peak can be obtained as unquenched using sufficiently slow heating rates.

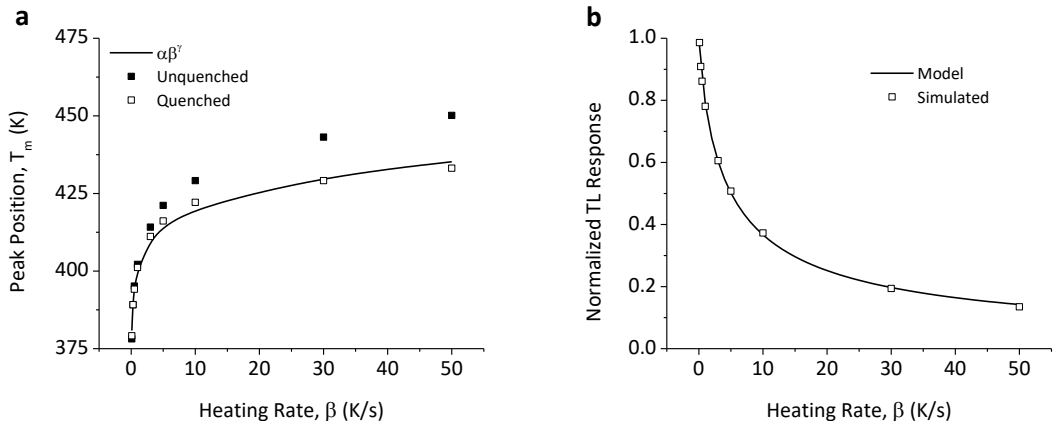

Figure 2-12. (a) Peak position for unquenched (black) and quenched (open) fit by the trend line given by $\alpha\beta^{\gamma}$. (b) Normalized TL response of the quenched TL curves with a trend line given by Equation 2-34 ($c = 1.3\times10^{16}$, $W = 1.32$ eV).

Aşlar et al. (2017) developed an algorithm for determining the corrective factor, $f = 1/\eta(T_{mq}, \beta_l)$, for materials where the lowest heating rate does not produce an unquenched TL peak. A series of TL curves are collected over a range of heating rates and fit using GCDC to obtain individual peak areas. A plot of $\eta(T_{mq})$ is constructed and fit using Equation 2-35 and an assumed value of f. The quenched dataset is corrected using the obtained quenching function $\eta(T_{mq})$ and the evaluated using GCDC to obtain a goodness of fit parameter. This process is repeated for a range of values of f with the value that produces the lowest goodness of fit parameters deemed the correct correction value. Similar methods using a Monte-Carlo approach have also been suggested (Mandowski et al., 2010).

2.3 TL for Temperature Sensing

Thus far, the discussion of both TL and analysis methods has not differentiated between techniques used in dosimetry and those used in temperature sensing. TL has many applications beyond radiation dosimetry, including use for dating of archaeological and geological samples (Chen and McKeever, 1997). The effects of thermal exposure have also been used to estimate the closest orbital distance (perihelion) to the sun of meteorites (Benoit et al., 1991).

Additionally, various applications of TL as a thermometric for thermal history reconstruction have been seen, including in cases of fire-damaged sandstone (Spencer and Sanderson, 1994), biological agent defeat testing (Talghader et al., 2016), and thermochronometry (King et al., 2016). In this section, we will cover the requirements of an ideal temperature sensing material and the approaches to obtaining temperature from a material exposed to a heating event. This section will outline the initial attempts at the use of TL as a thermometric as well as presenting the more recent efforts to the harsh environments of agent defeat testing.

2.3.1 Thermal Exposure Method

Spencer and Sanderson (1994) were the first to attempt the use of TL to obtain the thermal history of a material following a dynamic heating event. The theory behind temperature sensing relies on taking advantage of the fact that each individual trapping center has its own thermal stability for a given temperature exposure, expressed previously as Equation 2-19. For materials where an increase in peak position results in an increase in thermal stability, an exposure to a thermal event, such as an isothermal profile, will result in preferential depletion of the lower temperature peaks (less stable centers) and leave the higher temperature peaks partially depleted or unaffected. Following an exposure to a heating event, the remaining charge carrier population can be recovered in the form of a residual TL curve.

Spencer and Sanderson (1994) suggested a correlation between a so-called thermal exposure metric and the half-maximum position of the lowest temperature TL peak, $T_{1/2}$. The thermal exposure metric is expressed as a proportionality:

$$\text{thermal exposure} \propto \int_0^{t_f} T(t) \cdot \log(t)\, dt, \qquad \textbf{2-36}$$

where $T(t)$ is the functional form of the temperature experienced by a TL material and t is the duration of exposure. Plots of $T_{1/2}$ as a function of thermal exposure are characterized by a linear trend. The linear trend acts much like a dose response calibration curve from which one can determine a thermal exposure value from an arbitrary value of $T_{1/2}$.

Testing of the thermal exposure methodology under dynamic temperature conditions was first seen for sandstone exposed to fire fueled by various sources to ensure different heating profiles. Thermocouple readings were used to obtain the functional temperature profile, $T(t)$, seen in Figure 2-13a at various depths within a sandstone slab. Following exposure to the fire, cores were removed from the slab and used to obtain TL measurements and the position of $T_{1/2}$. Figure 2-13b shows a plot of $T_{1/2}$ versus thermal exposure with the linear trend line.

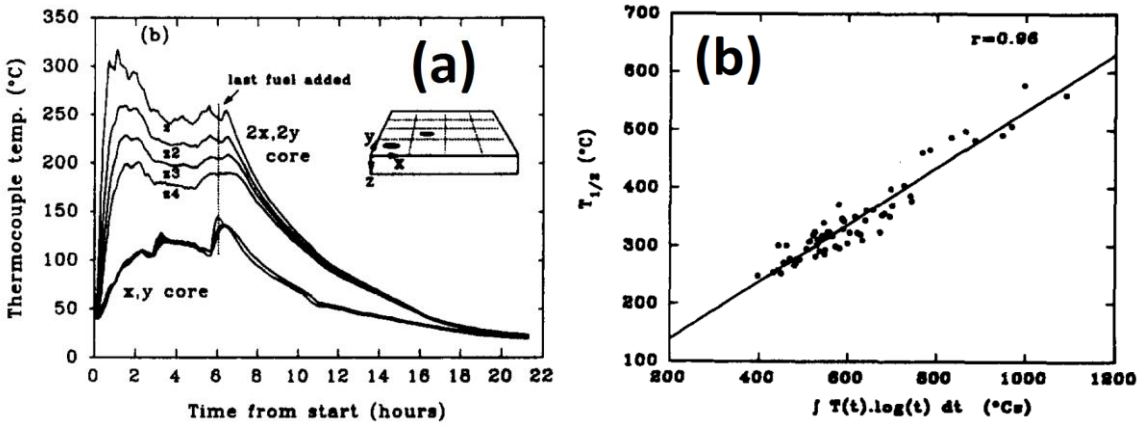

Figure 2-13. (a) Thermocouple data from a peat fire and (b) $T_{1/2}$ results shown with thermal exposure values. Data reflects simulated data. Adapted from Spencer and Sanderson (1994).

The thermal exposure methodology offers the advantage of a look up table from which one can easily obtain a temperature function. While this approach may be useful for certain applications, it requires a large experimental effort to obtain a calibration curve for every possible temperature function one might encounter. Additionally, the authors of this approach suggest limitations because of systematic errors (e.g. thermal lag during TL curve collection) in

correctly obtaining the value for $T_{1/2}$, which can be seen by the clustering behavior in Figure 2-13b. We have found no discussion on the uniqueness of the calibration data nor its validity in application to extreme temperature events such as high temperatures (>1000 K) for short timescales (<1s). This method also suffers from one major limitation, which is how to apply it to TL curve data ($T_{1/2}$ values) where the temperature function is completely unknown and no prior calibration data exists.

2.3.2 Full Curve Methods

Overview

In the previous section, we presented the thermal exposure method for mapping thermal exposure to changes in the TL curve, but this method is limited in its use for materials that have experienced unique or unknown temperature profiles. The "defense community" has an interest in improving the efficacy of its biological agent defeat weapons (Milby et al., 2012) but lacked the capability to obtain the thermal history experienced by a free flowing particle (e.g. *Bacillus anthracis* commonly known as anthrax) within the fireball. Carrera et al. (2007) found *Bacillus anthracis* spores to be ellipsoidal in geometry with an average length of ~1.5 µm and average diameter of ~0.85 µm. TL materials, when in powder form, can in principle be prepared to within an order of magnitude in size and can be collected and analyzed *ex situ* and, therefore, are a promising temperature diagnostic tool (Talghader et al., 2016).

A new method for temperature determination was needed for particles placed within a blast environment as a result of the uniqueness of the thermal profile and the need to have a more reliable TL metric than the half-max peak position, $T_{1/2}$, suggested by Spencer and Sanderson (1994). Two different, but similar methods were developed by groups at Oklahoma

State University (Yukihara et al., 2015), and University of Minnesota (Mah et al., 2010), which reflected the TL materials used for temperature sensing.

Both groups follow a similar methodology. Prior to thermal exposure (e.g. explosion) the TL material is given a dose of ionizing radiation to populate trapping centers. The material is then exposed to a temperature event and collected afterwards along with any material generated during the test (e.g. soot, metal, wood, etc.). A control sample is maintained free of heat exposure and is modeled as a superposition of first-order TL peaks. A temperature profile is assumed (exponential decay or uniform) and a set of TL curves is simulated for a range of temperatures and exposure times. A comparison between the computer-generated and the post-heating experimental curves is made using a defined metric. The heating parameters (temperature and timescale) of the computer-generated curve which best represents the experimental curve are taken to represent the so-called “thermal history”.

While the approaches between the OSU and UoM groups are similar, there are some differences. Firstly, UoM uses the commercial material, LiF:Mg,Ti, while OSU uses novel materials developed primarily for temperature sensing. As a result, the TL models for LiF:Mg,Ti are well known, while those for the OSU materials must be modeled under a restrictive approach using one dimensional deconvolution (Equation 2-32). Secondly, the UoM assumes a different heating profile than OSU. The UoM approach assumes the particle’s temperature jumps to a maximum value, T_{max}, followed by an exponential decrease to room temperature. The duration of time between the jump to T_{max} and return to room temperature is the heating time, $t_{cooling}$. OSU assumes the particle’s temperature jumps to a maximum value and remains constant through the duration of the heating. To obtain the best temperature profile, T_{max} and $t_{cooling}$, UoM applies a random search method of the temperature-time space, while OSU assumes an order of magnitude timescale of the heating and searches for temperatures at the

timescale that best describe the experimental data. The timescale assumption made by OSU is based on the result that the TL curve is sensitive to linear changes in temperature and exponential changes in heating duration. As of this writing, no attempt to validate either temperature profile as been made, but results for both approaches have shown to be consistent with *in situ* static thermocouple measurements for closed-chamber explosive testing (Yukihara et al., 2015). This current work focuses on the use of the OSU approach and as a result all future discussion will be limited to the OSU methodology and materials.

Thermal History Reconstruction

The recovery of an accurate thermal history relies on three main factors: TL model, trap depletion model, and temperature reconstruction algorithm. Acquisition of accurate trap parameters for a TL model was previously discussed in Section 2.2. Here, we focus on how to model trap depletion and how to obtain a characteristic temperature from experimental curves.

The OSU approach uses a control sample modeled as a superposition of first-order TL peaks using Equation 2-32. Techniques laid out by Yukihara et al. (2014b) are used to obtain the optimal frequency factor for the material under investigation. First, a dataset of TL curves obtained following a preheating sequence were obtained from a control sample of the material of interest. Next, the experimental dataset was fit using the one-dimensional deconvolution method for various assumed frequency factor values. The frequency factor value that resulted in the best figure of merit was chosen as the optimal value for the material. The control sample is prepared (synthesized and irradiated) at the same time as the heated material, so the effects of temperature during transit and storage can be monitored and separated from the actual test results. Having established a TL model, efforts must be focused on simulating the depletion of individual trapping centers because of the heating event.

Simulated heating is conducted using the first-order TL curve expression and a depletion factor, $\phi(E, s, \psi(t))$:

$$\frac{n}{n_0} = \phi\big(E, s, \psi(t)\big) = \exp\left(-s \int_0^t e^{-E/k\psi(t')}\, dt'\right), \quad \textbf{2-37}$$

where $\psi(t)$ is the temperature function experienced by the particle. Generally, TL materials have multiple trapping centers which contribute to the TL intensity. Thus, the total intensity, following a preheating, is expressed as a summation over N trapping centers,

$$I(T) \propto \sum_i^N \phi\big(E_i, s_i, \psi(t)\big)\, n_{0,i} s e^{-E_i/kT} \exp\left(-\frac{s_i}{\beta}\int_{T_0}^{T} e^{-E_i/k\theta}\, d\theta\right), \quad \textbf{2-38}$$

where θ is the integration variable representing temperature. The form of the depletion factor ϕ varies according to the heating function $\psi(t)$. The following expressions are examples of the depletion factor for: uniform ($\psi_u = T_{hold}\tau$), linear ($\psi_{lin} = T_0 + \beta t$), and exponential decay ($\psi_{exp} = T_0 + (T_{max} - T_0)e^{-t/\tau_c}$) heating profiles:

$$\phi_{const} = \exp\big(-s\tau e^{-E_i/kT_{hold}}\big), \quad \textbf{2-39}$$

$$\phi_{linear} = \exp\left(-\frac{s}{\beta}\int_{T_0}^{T_{max}} e^{-E_i/k\theta}\, d\theta\right), \quad \textbf{2-40}$$

$$\phi_{exp} = \exp\left(-s\int_0^{t_f} exp\left(-\frac{E_i}{k\,\psi_{exp}(T_{max}, T_0, t, \tau_c)}\right) dt\right), \quad \textbf{2-41}$$

where integrations for the linear and exponential profiles must be solved numerically. For uniform heating, T_{hold} is the hold temperature for a duration τ. For linear heating, T_{max} is the maximum heating temperature, β is the heating rate, and T_0 is the initial material temperature. For exponential cooling, T_{max} and T_0 are defined in the same manner as the linear case, but τ_c is the decay constant and t is time expressed in terms of the decay constant. Figure 2-14 illustrates the effect of constant heating for increasing T_{hold} (often referred to as T_{ph} the pre-heat temperature) values assuming a heating duration of 0.1s.

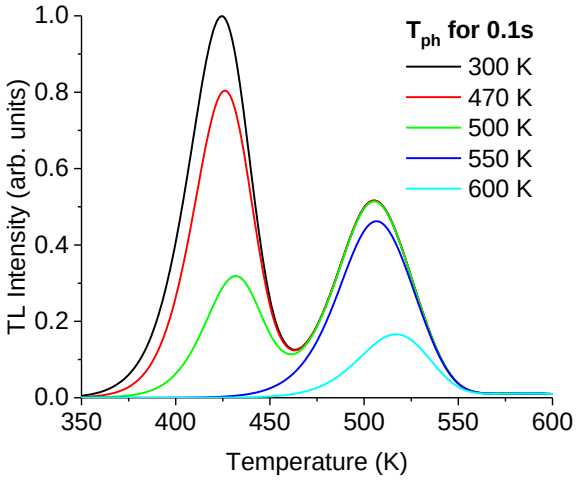

Figure 2-14. Simulated heating of LBO for a constant heating of 0.1 seconds. The black trace (300 K) indicates the control sample heated to room temperature. After Yukihara et al. (2015).

Simulated heated curves are calculated from the TL model for the heating function of interest. The simulated TL curves (y_{sim}) are compared to the experimentally heated TL curves (y_{exp}) using the parameter η (Yukihara et al., 2014b):

$$\eta = \frac{n}{\sqrt{\sum_i^n \left(y_{i,sim} - y_{i,exp}\right)^2}}. \qquad \textbf{2-42}$$

The value of η is maximized when there is good agreement between simulated and experimental TL curves. For the heating profiles discussed above, η is a function of two variables and, therefore, the result is a two-dimensional solution space (Figure 2-15a). As a result of probability of trap depletion depending on the Arrhenius expression ($p = se^{-E/kT}$), the solution space does not provide a unique solution, but rather a band of solutions that requires *a priori* knowledge of heating duration to isolate temperature (Figure 2-15b).

In the case where the heating duration is conducted under controlled settings and the time scale is known, this is not an issue, but more dynamic settings such as an explosion can introduce uncertainties in the temperature determination. For OSU materials, it has been shown that temperature dominates the trap emptying process and the user need only have

knowledge of the order of magnitude of heating duration (Yukihara et al., 2015). Nevertheless, with a more accurate model and a better understanding of the factors that affect temperature determination, the certainty of the thermal history reconstruction can be improved.

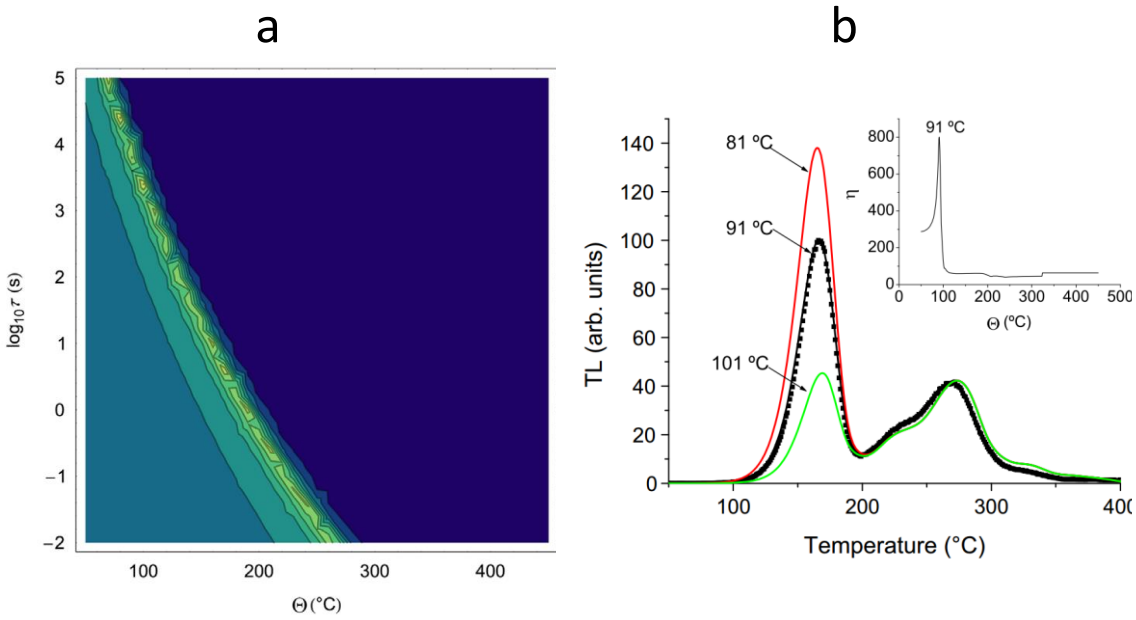

Figure 2-15. Contour plot of η (Equation 2-42) for LBO held at 100 °C/2h where θ is the hold temperature and τ is the duration in seconds. Comparison between simulated TL curves (τ=7200 s) for various hold temperatures, with inset showing a horizontal slice of the η at $\log_{10}\tau$ =3.85. After Yukihara et al. (2014b).

2.3.3 Temperature Sensing Materials

Dosimetric materials should be tissue equivalent ideally and have an isolated TL peak (200 – 250) °C that is thermally stable but unaffected by blackbody emission (McKeever, 1985). TL materials have different requirements based upon experimental conditions. Several materials have been identified as candidates for temperature sensing applications and can be grouped as either known, "established" dosimetric materials, such as those that were pursued by researchers at the UoM, or "novel" materials, such as those there were developed and optimized for temperature sensing applications by researchers at OSU.

Mg_2SiO_4:Tb,Co (magnesium orthosilicate), developed for OSL dosimetry (Mittani et al., 2008), was used to demonstrate the viability of temperature sensing using TL particles (Mah et al., 2010), but its sensitivity to light makes it impractical for use in agent defeat testing. The same group made use of a common OSL dosimetric material, α-Al_2O_3:C, to verify the survivability and recoverability of TL sensors particles in dentation tests using various explosive shot sizes. Mah et al. (2013) found no difference between the TL of Al_2O_3:C control and test samples following exposure to UV irradiation. This test was important in providing a proof of concept for the use of TL materials as robust sensors but did not provide any thermal analysis. Although Al_2O_3:Cis a highly sensitive TL material with high temperature peaks, it exhibits strong light sensitivity with known phototransfer thermoluminescence (PTTL) peaks (Colyott et al., 1996), and thermal quenching (Akselrod et al., 1998a), making accurate TL kinetic parameter determination difficult and thermal history reconstruction impossible.

While the mentioned studies demonstrated the possibility of TL particles to work as temperature sensors, additional material characteristics are needed to be useful diagnostic tools for agent defeat testing. The requirements for a TL particle temperature sensor are discussed by both Doull et al. (2014) and Talghader et al. (2016) are summarized again here:

1. TL from the materials must be bright since material collected post agent-defeat testing is often composed of post-detonation products (wood, metal, dirt, HE product, etc.) and may only have a few gains of TL material.
2. The TL curve for each material should consist of multiple peaks spread over a wide readout temperature range to allow for sensitivity to a broader range of thermal events.
3. Materials should be insensitive to room light, as they will be exposed during the preparation for and collection after agent defeat testing.

4. TL peaks should be stable at room temperature over typical timescales for irradiation, collection, and laboratory TL readout for both control and tested samples.
5. TL kinetics should be first-order to allow for the application of traditional characterization methods and for the application of the superposition principle during trap depletion modeling.

In addition to characteristic (2) above, it is not only desirable to have TL peaks across a wide readout temperature range, but to also have peak positions at temperatures well beyond those desired for dosimetric purposes (e.g. T_m > 300°C). Such a need is motivated by the fact that temperatures within explosives can reach beyond 3000 K (Milby et al., 2012), sufficient even at short timescales to fully deplete all trapping centers of traditional TL materials.

Although the exact thermal history of a particle within a post-detonation fireball is unknown, and is the primary motivation of the present research, materials with higher temperature peaks extend the upper temperature limit (for a set timescale) and are useful in setting a lower temperature bound for the explosive event in the case all trapping centers are depopulated. It is also useful to have materials with TL emission in the UV region, as to allow for the removal of blackbody radiation using optical filters.

Higher temperature TL peaks present an additional problem to thermal history reconstruction due to thermal quenching (Talghader et al., 2016). The specifics of thermal quenching were previously discussed (Section 2.1.5) and can be explained simply as a reduction in luminescence as a result of an increase of non-radiative recombination with the increase in temperature (McKeever, 1985). Thermal quenching does not effect the depopulation of trapped charge carriers, only the mechanism by which they recombine. Therefore, this phenomenon does not effect thermal history reconstruction directly. Thermal quenching does distort the TL curve shape and peak position leading to incorrect calculations of kinetic parameters when

analysis methods are applied to TL curves that are not corrected using the correct quenching function.

With these considerations in mind, three materials, $Li_2B_4O_7$:Cu,Ag (LBO), MgB_4O_7:Dy,Li (MBO), and $CaSO_4$:Ce,Tb (CSO), were developed at OSU for use in temperature sensing (Doull et al., 2014; Yukihara et al., 2016). The materials of interest show TL curves which are dose independent or which show only a slight shift in peak with dose; some even shift to higher temperatures with dose (Doull et al., 2014; Yukihara et al., 2003).

One commercial material LiF:Mg,Ti was identified and investigated for use in temperature sensing within a detonation fireball (Talghader and Mah, 2012; Wang et al., 2013). Work has been conducted to identify other TL materials as possible temperature sensors, one example being MgB_4O_7:Nd (Souza et al., 2015), but this work will focus on the OSU-developed materials (LBO, MBO, and CSO).

Figure 2-16 shows the typical TL curves of the OSU materials, illustrating high intensity and TL emission across a wide range of readout temperatures. Unlike LiF:Mg,Ti, new materials developed at OSU have not been fully characterized, yet. Previous work has identified emission regions and characterized dose response (linear < 10 Gy, supra-linear >10 Gy) and found minimal change in peak position with dose evidence for close to first-order kinetics (Doull et al., 2014).

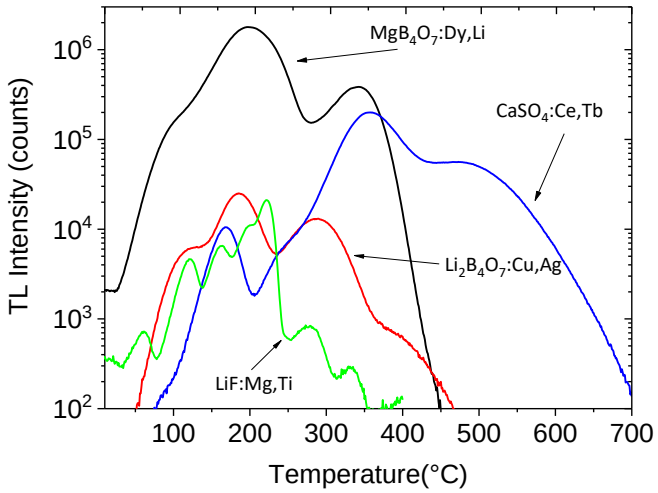

Figure 2-16. Representative TL curves of TL materials developed at OSU for temperature sensing, with LiF:Mg,Ti provided for reference.

LiF:Mg,Ti

LiF:Mg,Ti is one of the most widely used dosimetric materials. Since its introduction in the 1960s, LiF:Mg,Ti has been the subject of hundreds of publications; which have been thoroughly discussed by others (Chen and McKeever, 1997; McKeever, 1985; McKeever et al., 1995). Therefore, we will only present a brief summary on matters important to temperature sensing here.

The TL curve of LiF:Mg,Ti is characterized by four prominent TL peaks stable at room temperature (numbered as 2-5). In addition to these, there is a low-temperature peak (unstable at room temperature) and multiple low-intensity high-temperature TL peaks. The TL emission of LiF:Mg,Ti is a broad, Gaussian-like band ranging over several hundred nanometers, with a maximum at 412 nm. The main dosimetric peak is commonly referred to as “peak 5”. The defect responsible for peak 5 is a trimer comprised of three dipoles (Mg_{Li}^{+}–V_{Li}^{-}) (McKeever, 1985). The concentration of this defect is maximized by a pre-irradiation annealing procedure: 1 h at 400 °C then 24 h at 80 °C. Variations in the pre-irradiation annealing result in large changes

to the TL sensitivity and curve shape. Furthermore, the heating during the TL measurement changes the defect concentration and, therefore, the material must be reset before re-use.

The TL peaks for LiF:Mg,Ti are generally considered to be first-order (Taylor and Lilley, 1978), although there has been debate over the possibility of non-first-order behavior for peak 5 (Kathuria and Sunta, 1979, 1982; Lilley and Taylor, 1981; Lilley and McKeever, 1983). Additionally, there has been evidence that peak 5 is actually the superposition of two peaks; referred to as peak 5a and peak 5b (Weizman et al., 1999). Variations from batch to batch make it difficult to present a definitive set of trap parameters for LiF:Mg,Ti, but a good resource is found in Table 1 by Taylor and Lilley (1978). It should also be noted that peak 5 is commonly found to have a frequency factor above 10^{20} s^{-1}, 8-10 orders of magnitude above the lattice vibration frequency and is a source of additional debate over the underlying TL model and true trap parameters (McKeever et al., 1995).

Ultimately, these complexities are ignored by those who use it as a TL temperature sensor. The well-defined, first-order TL peaks make LiF:Mg,Ti a desirable material for temperature sensing as it is easy to model, but the lack of high temperature TL peaks (T_m > 300 °C) limits the temperature range over which this sensor is useful. Calculations using a constant heating for 1 ms suggest an applicable range of 450 K to 750 K. Works that have used LiF:Mg,Ti have solely relied on curve fitting to obtain the trap parameters, claiming batch to batch variation would disallow the use of published values (Mah, 2017). The values, however, have not been verified by other methods such as IRM and the values for peaks 3 and 4 are not in agreement with published values by Taylor and Lilley (1978). Furthermore, the effect of the heating event on the defect concentration and ultimately the TL curve have been addressed as possible sources of source of error when attempting to recover a thermal history (Talghader et al., 2016).

MB_4O_7:Dy,Li

The use of magnesium borate (MgB_4O_7) as a host lattice has been of interest for dosimetry due to its tissue equivalency (Z_{eff} = 8.4) and utility for neutron and gamma dosimetry (McKeever et al., 1995). Originally, the material was doped with either Dy or Tm (Prokić, 1980), and was found to be between 6 – 15 times more sensitive than LiF:Mg,Ti depending on the PMT sensitivity (McKeever et al., 1995). In the process of searching for a temperature sensing material, Doull et al. (2014) found that by co-doping Dy with Li (0.1% and 1% respectively) the TL and radioluminescence (RL) intensities were approximately doubled, but their results were only ~3 times more sensitive than LiF:Mg,Ti, suggesting a need for optimization.

TL emission of MBO:$Dy_{0.1\%}$,$Li_{1\%}$ is characterized by two Dy^{3+} emission peaks in the visible band found at 480 nm and 574 nm and is consistent with values in literature for MBO:Dy (Doull et al., 2014). The TL of MBO is characterized by two main peaks (Figure 2-16), but TL from MBO:Dy has shown a different TL curve both in position and number of peaks (Barbina et al., 1982). While a model for the underlying TL mechanism has been proposed for MBO:Dy,Li (Yukihara et al., 2014a), there have been minimal efforts to characterize its TL behavior. Dose response of MBO:Dy,Li (0.5 Gy to 500 Gy) showed only a slight decrease in TL peak position (~20 K) for the main peak, suggesting approximately first-order kinetics. For second order kinetics, the effect of increasing dose (Figure 2-3b) demonstrates a drastic change in peak position with a doubling in trap occupancy (proportional to dose). The second TL peak of MBO:Dy,Li showed a small increase to higher temperatures with increasing dose and an increase in relative intensity. This finding was suggested to be the result of competition. The main TL peaks for MBO were found to be stable at room temperature, but sensitive to room light exposure (~40 % in 3 h) and exposure to light during experiments and preparation must be limited.

No effort has been undertaken to characterize the trap parameters of MBO:Dy,Li and only one reference is available for MBO:Dy. Souza et al. (1993) applied curve fitting to step-annealed data from MBO:Dy and determined the two main TL peaks were comprised of 11 first-order TL peaks. For use in temperature sensing, Yukihara et al. (2014b) applied a one dimensional deconvolution approach assuming a common frequency factor of $s = 10^{14}$ s^{-1} and found activation energy values between 1.1 eV and 2 eV.

The increased sensitivity of MBO:Dy,Li makes it a useful material for temperature sensing, as a signal can be measured even if only a few grains of material are present in a sample and fading can be minimized in a controlled experimental environment. Additionally, MBO:Dy,Li has an applicable temperature range 550 K to 850 K for a 1 ms constant heating, comparable to that for LiF:Mg,Ti. The largest drawback to the use of MBO:Dy,Li is its reliance on a possibly incorrect TL model, which may produce inaccurate thermal histories.

LiB_4O_7:Cu,Ag

The first use of LiB_4O_7 (LBO) was published by Schulman et al. (1965) who doped the lithium borate host with manganese to serve as a tissue equivalent dosimetric material (Z_{eff} = 7.4). Efforts to improve the sensitivity of the material led to the use of new dopants, including a co-doping with Cu and Ag (0.02%) (Takenaga et al., 1977). The use of Cu,Ag as co-dopants was deemed less favorable as a dosimetric material, but the use of LBO:Cu,Ag recently regained use as a temperature sensor with concentrations of 0.3% (Doull et al., 2014). Its use in test environments shows an improved formulation with a higher Cu content with 0.4% and Ag with a concentration of 0.1% (Yukihara et al., 2014b; Yukihara et al., 2015). For a detailed discussion of the effect of dopant concentrations and material synthesis methods for LBO:Cu,Ag, we refer to Doull et al. (2013); (Doull et al., 2014) and Wang et al. (2013). Additionally, we suggest the work

by Pekpak et al. (2011) on LBO with Cu, Ag, and In in singly, doubly and triply doped concentrations.

Doull et al. (2014) found the TL emission of LBO:Cu,Ag to show a single broad band at ~370 nm from Cu^{+}, associated with the main TL peak (~200 °C in Figure 2-16). A second emission band was expected from Ag^{+} near ~272 nm (Ignatovych et al., 2012), but was not observed due to poor instrument sensitivity at that wavelength. TL curves for LBO:Cu,Ag are characterized by a three-peak structure. The first TL peak is not used, as it fades in under 24 h (Doull et al., 2014). Dose response was found to produce a small shift (<25 K) of the main TL peak to a lower temperatures and a strong change to the TL structure of the high temperature peak (Doull et al., 2014). Doull et al. (2014) suggested this behavior was the result of sensitization from a decrease in trap competition at higher doses.

There is little literature on the trap parameters and their kinetic order, perhaps, due to the lack of popularity of LBO:Cu,Ag as a dosimetric material. Table 2-1 summarizes the available trap parameter literature for LBO:Cu,Ag for a range of dopant concentrations. Results for peak 2 point towards an activation energy near 1.2 eV while the results for peak 3 indicate activation energy between 1.3 and 1.34 eV, but no common frequency factor was found for either peak. None of the studies in Table 2-1 looked at LBO:Cu,Ag in powder form. Only one study was found that used a methodology other than GCDC for obtaining trap parameters. In general, the TL peaks were found to obey approximately first-order kinetics, but with a range in activation energies and frequency factors. Although trap parameters are available in literature, the step-annealing results, found by Doull et al. (2014), suggest a complicated system of peaks that is not easily described by 2-3 TL peaks. Therefore, TL modeling for LBO:Cu,Ag in temperature sensing followed the same one dimensional deconvolution procedure used for MBO:Dy,Li (Yukihara et

al., 2014b). LBO has a similar applicable temperature range to MBO of 550 K to 850 K for a 1 ms constant heating, but does not suffer from the light induced fading.

Table 2-1. Table of trap parameters for LBO:Cu,Ag found in literature. All results were obtained using a 1 K/s heating rate, except Romet et al. (2016) which used 10 K/s.

Source Form (Cu%,Ag%)	Peak 2				Peak 3			
	T_m (K)	b	E (eV)	s (s^{-1})	T_m (K)	b	E (eV)	s (s^{-1})
Romet et al. (2016) Crystal (0.5%, 0.5%)	420	1	1.14	9.53×10^{11}	480	1	-	-
Rawat et al. (2012) Crystal (0.25%, 0.25%)	440	1.09	1.25	1.3×10^{13}	515	1.07	1.34	4.08×10^{11}
Rawat et al. (2012) Crystal (0.25%, 0.25%)	-		-	-	509	1	1.34	5×10^{11}
Patra et al. (2013) Crystal (0.25%, 0.25%)	433	1	1.2	1.7×10^{13}	503	1	1.3	1.6×10^{12}
Hemam et al. (2016) Nanoparticles (3%, 1%)	450	1.36	1.08	8.1×10^{10}	523	1.81	1.5	1.88×10^{13}

$CaSO_4$:Tb,Ce

Unlike the previous materials, $CaSO_4$:Ce,Tb (CSO) is a relatively new material for both temperature sensing and dosimetry. Although Tb and Ce have been used to study the energy transfer process in CaS_4O:Ce,Tb (Sanaye et al., 2003), the majority of literature focuses on calcium sulfate doped with either Dy and Mn, which are highly sensitive dosimetric materials (McKeever et al., 1995). The work by Doull et al. (2014), summarized below, is the only TL characterization study of the material to date.

TL emission of CSO:Ce,Tb shows several line emissions for Tb^{3+} and a double-band Ce^{3+} emission at 306 nm and 324 nm. TL curves were obtained using an optical filter to select the Ce^{3+} emission and, therefore, curve comparisons will be made with CSO:Ce. The TL curve for CSO:Ce,Tb developed for temperature sensing is characterized by a complicated peak structure (Figure 2-16). The TL curve presented for temperature sensing by Doull et al. (2014) does not resemble the results found in literature for CSO:Ce,Tb (Sanaye et al., 2003), or for CSO:Ce

(Lapraz et al., 2002), but some similarities can be identified for the low temperature TL peak (T_m ~ 150°C) and the high temperature structure.

Dose response showed a small shift of the main TL peak to higher temperatures as well as an increase in sensitivity for the higher temperature structure. The dose response results coupled with step-annealing behavior suggest approximate first-order kinetics, with the high temperature peak behavior due to competition of a series of overlapping TL peaks. Results also showed negligible fading in both dark storage (1 week) and in light exposure (room light, 3 h), making this material well suited for temperature sensing. The curve structure produces an applicable temperature range between 570 K and 975 K (1 ms constant heating), allowing it to reach higher temperatures (or longer exposures) than other materials within this section.

2.3.4 Limitations

Although the use of TL materials as a particle temperature sensor has been presented as a robust technology (Talghader et al., 2016), it is not without limitations. Here we address some of the major limitations of TL temperature sensing and suggest an in-depth read of the Defense Threat Reduction Agency (DTRA) project report for a full scope of the development of the technology (Yukihara et al., 2016). Although the full curve approach offers benefits over the thermal exposure method, it still requires an assumption of the temperature function and approximate heating duration, making the recovery of the true thermal history intractable (Talghader et al., 2016). Despite this limitation the use of TL temperature sensors have demonstrated success in laboratory testing (Yukihara et al., 2014b) and closed chamber detonations (Yukihara et al., 2015). Additionally, the accuracy of the temperature reconstruction is fully dependent on an accurate TL model which correctly predicts trap population and TL curve behavior following the exposure to a temperature event. We have discussed in the

previous sections the inadequacy of the models used, which makes the improvement of the underlying TL models a priority.

To date, the measure of success for TL temperature sensors has been measured by consistency with *in situ* thermocouple measurements (Daniels et al., 2015; Yukihara et al., 2015). While this comparison provides valuable feedback, ultimately, the sensor particles are supposed to track the thermal history of a free-flowing particle, making the comparison with a static diagnostic measurement a point of concern.

Furthermore, individual samples collected following a detonation event are comprised of several individual particles, all of which could experience a unique thermal history. By collecting the TL of the whole sample, one would expect to average the luminescence and, therefore, obtain an averaged thermal history of the material. Results from both closed chamber testing (Yukihara et al., 2015) and open chamber testing at the DTRA Humble Gingko XIX facility conducted in 2014 (Yukihara et al., 2016) showed evidence of "partial heating" which suggests the sample contains a distribution of thermal histories. This could be the result of a single particle heated non-uniformly or several individual particles exposed to different temperature profiles. A particle-by-particle analysis of MBO:Dy,Li from the Humble Gingko test (2014) confirmed the latter hypothesis and showed that a typical sample used for thermal history reconstruction contained multiple thermal histories (Armstrong, 2017). For the particular sample analyzed in the study, it was found that the maximum temperature of individual particles ranged over several hundreds of degrees, including a large number of unheated (no difference from control) particles.

In addition to the issues mentioned, there has been debate over the response time of the particles themselves to temperature events. Although individual TL particles are small (<100 μm), results from the DTRA Humble Gingko XIX for samples of MBO and CSO showed evidence

of insufficient heating, which indicates the temperature exposure (time or temperature) was insufficient to cause a significant depletion of the TL curve area to obtain a temperature. These tests utilized a 5 lb. pentolite charge, which produced high temperatures as registered by *in situ* thermocouple measurements. Additionally, a series of shock-tube tests (system details found in Brown (2007)) were conducted using OSU materials sieved below 35 μm to reduce the thermal mass of the sensor. For samples where sufficient heating occurred (>10% total TL depletion), the results (for a 2-5 ms heating) still indicated temperatures well below the NASA CEA (Chemical Equilibrium with Applications) simulation predictions (Gordon and McBride, 1994; Yukihara et al., 2016).

2.4 Transient Heating of a Spherical Particle

The exact geometry of TL particles used in temperature sensing is unknown, but SEM imaging of LBO, MBO and CSO by (Doull et al., 2014) suggests particles and aggregates vary greatly in size and shape. We will treat individual particles (or single aggregates) as spherical particles characterized by a length dimension corresponding to the sphere's diameter.

2.4.1 Heat Conduction in TL Studies

The effect of heat transfer on TL materials has long been a concern with regards to the accuracy of the trap parameters obtained from traditional analysis methods that rely on peak position, such as the VHRM. Chvoj (1977) modeled the effect of a 40 K linear gradient on the TL curve of a 0.1 cm sample of NaCl:Mg, and found the TL curve to broaden and the peak position to shift to higher temperatures as a result of the thermal gradient. Gotlib et al. (1984) expanded on this approach by modeling the thermal gradient within a sample by solving the one-dimensional heat transfer equation and investigating the effect of various sample parameters on the TL peak position and intensity. Betts et al. (1993) found that the exchange gas within the

heating chamber also effects the TL curve, so a more comprehensive model of the heat exchange is needed.

Piters and Bos (1994) proposed a one-dimensional system consisting of the heating element, TL material, and exchange gas and used LiF:Mg,Ti to model the effect of non-ideal heat transfer on kinetic parameters. His model ignored the material thickness, and, then imposed a linear gradient based on the temperature differences between the heating element and the exchange gas. Along the gradient, a total of 60 "sample particles" were used to simulate the total TL curve from the entire sample.

As the use of TL materials has increase in popularity, the need for quicker readout systems, and therefore faster heating rates, has been seen. To maintain throughput, new methods such a clamped heating by a heated gas (Kumar et al., 2005), or jet impingement have been implemented (Cohen et al., 2014; Rozenfeld et al., 2011). All references presented up to this point have treated the heating of TL material to be one-dimensional, and only Piters and Bos (1994) suggested the total TL curve be represented by a superposition of TL curves obtained from positions within the bulk crystal. The jet impingement heating system shown in Figure 2-17a is much more complex and requires a two-dimensional hydrodynamics simulation to model. Rozenfeld et al. (2011) modeled the temperature distribution and gas flow for the system in Figure 2-17a for a LiF:Mg,Ti crystal (~ 900 µm thick).

Figure 2-17b shows the system behavior at a simulation time of 1 s. They found it took ~ 15 s and ~ 30 s for the crystal temperature to reach the gas temperature when using a linear and step (uniform) heating respectively. Also, they found the contribution of radiative heat flux to be less than an order of magnitude of that of convection and did not include this effect in their simulations. TL curves were simulated using a TL model for LiF:Mg,Ti using a first-order TL model simulated at discrete timesteps using an adjusted heating rate for each step of $\beta =$

$[T(\Delta t + t) - T(t)]/\Delta t$. It is not clear from this work if the total TL curve was obtained as a summation of the TL signal from all computational cells. Additionally, it is suggested the radial temperature dependence is negligible, indicating the TL curve simulation assumes the sample to be one-dimensional.

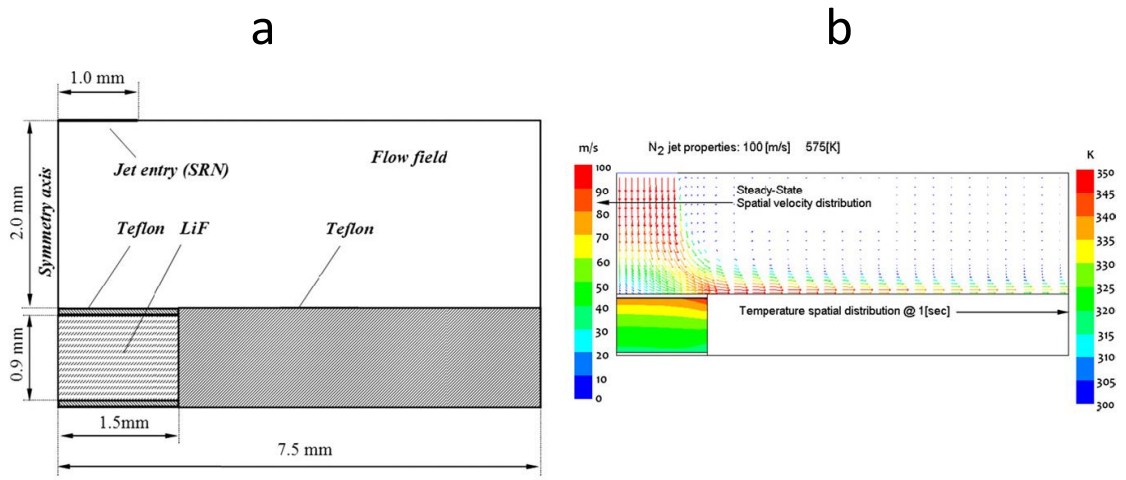

Figure 2-17. (a) System design and (b) simulated flow field results at 1 s simulation time for a N_2 gas with a velocity of 100 m/s heated to 575 K. After Rozenfeld et al. (2011).

The works presented in this subsection are related to the TL curve obtained during the collection process, but can easily be extended to model the trap depopulation for temperature sensing. The work by Piters and Bos (1994) and by Rozenfeld et al. (2011) set the groundwork for an approach for using heat transfer to model the heating of a multidimensional TL particle the effects on the residual TL curve.

2.4.2 Thin Films

Heat conduction within TL materials is the result of lattice vibrations by phonons scattering with other phonons, impurities, charges, and material boundaries (Kittel, 2004). Under traditional macroscale heat transfer theory, the boundary consideration plays a negligible role, but if the mean free path of a phonon in the material is larger than one or more of the material dimensions (e.g. ~ 1 µm in room temperature diamond), a microscale treatment is

needed (Majumdar, 1993). Due to limitations of SEM imagery, is it not possible to determine the thickness of typical TL particles used in temperature sensing (see Fig. 2c in Doull et al., 2014), we will assume the thickness of some particles to be > 1 µm. Heat transfer of particles below this size (~ 1 µm or less) should be treated using phonon transport methods (Majumdar, 1993; Mazumder and Majumdar, 2001). Particles of this size will typically be thermally cleaned (no residual TL signal) in all the temperature profiles of interests and will not contribute to the analysis curves used in the thermal history reconstruction. As such, we will assume that all particles of interests are sufficiently large in dimension to be treated with a macroscopic heat transfer approach.

2.4.3 Convective Heat Transfer

Our system is comprised of a single TL particle placed within a heated gas or fluid. Heat transfer between the local gas and the surface of the particle is governed by convective heat transfer, while the surface temperature is diffused through the material via conduction. Convective heat transfer between the local gas and the particle's surface expressed as (Crowe et al., 2011):

$$\dot{Q}_c = hA(T - T_\infty), \tag{2-43}$$

where T is the particle's surface temperature, T_∞ is the surrounding gas temperature, and h is the heat transfer coefficient. The value for h can be obtained from the *Nusselt* number as $Nu = hL/k_c$ where L is the characteristic length in the boundary layer (measured from surface of particle) and k_c is the thermal conductivity of the local gas or fluid. Equation 2-43 can be expressed in terms of the *Nusselt* number as

$$\dot{Q}_c = Nu\pi D k_c(T - T_\infty), \tag{2-44}$$

where *D* is the diameter of the particle. In cases where there exists a relative flow with respect to the particle, the rate of heat transfer increases due to forced convection, and it becomes

possible that thermal gradients within the particle can be ignored. The Biot number (*Bi*) is defined as, $Bi = L_c h/k_p$, where k_p is the particle's thermal conductivity and L_c is the characteristic length, defined as the ratio of the volume to surface area. When $Bi < 0.1$, it is assumed that thermal gradients within the particle are negligible and the temperature within the particle is treated as uniform under the lumped capacitance approach (Crowe et al., 2011). In this case, convective heat transfer is considered as the primary mean of energy exchange. Thus, the particle's surface temperature is taken as the temperature of the entire particle. Under these assumptions, we see an increase in the *Nusselt* number given by the *Ranz-Marshall correlation* for spheres (Ranz and Marshall, 1952):

$$Nu = 2 + 0.6Re_r^{\frac{1}{2}}Pr^{\frac{1}{3}}, \qquad \textbf{2-45}$$

where Re is the Reynolds number and Pr is the Prandtl number. The Reynolds number is defined as $Re = uL/\nu$, where u is the velocity of the gas with respect to the particle, L is the characteristic particle size (e.g. diameter), and ν is the kinematic velocity of the fluid. The Prandtl number is defined as $Pr = \nu/\alpha$, where α is the thermal diffusivity of the local gas. The expression for heat transfer for the sensors particle becomes (Crowe et al., 2011),

$$\frac{dT}{dt} = \frac{Nu}{2}\frac{1}{\tau_t}(T - T_\infty), \qquad \textbf{2-46}$$

using the adjusted value for Nu, and where the thermal response time is $\tau_t = \frac{c_p \rho_p D^2}{12\, k_c}$ where c_p and ρ_p are the particle specific heat capacity and density respectively and D is the particle diameter. Equation 2-46 is easily solved analytically for a steady-state system (e.g. Newton's Law of cooling) or using a finite difference approach for time-dependent boundary conditions.

2.4.4 Conductive Heat Transfer

If the value for $Bi > 0$, then we must consider the thermal gradients within the particle. Under this assumption the particle surface temperature, obtained via the convective heat transfer in Equation 2-43, is propagated through the particle as if the particle were placed in a heat bath. As such, the temperature within a particle as a function of time is expressed by the function $u(r, \theta, \phi, t)$, which can be used to model the heat diffusion through the particle as (Yunus and Afshin, 2011):

$$\frac{\partial u}{\partial t} = -\alpha \nabla^2 u, \qquad \textbf{2-47}$$

where t is time, α is the thermal diffusivity of the material. The value of α is obtained from the expression, $\alpha = k/\rho c$, where k is the thermal conductivity, ρ is the density, and c is the specific heat capacity of the particle. For a spherical system, Equation 2-47 becomes:

$$\frac{1}{\alpha}\frac{\partial u}{\partial t} = \frac{1}{r^2}\frac{\partial}{\partial r}\left(r^2 \frac{\partial u}{\partial r}\right) + \frac{1}{r^2 \sin^2\theta}\left(\frac{\partial^2 u}{\partial \phi^2}\right) + \frac{1}{r^2 \sin\theta}\frac{\partial}{\partial \theta}\left(\sin\theta \frac{\partial u}{\partial \theta}\right). \qquad \textbf{2-48}$$

We assume the particle to be homogeneous and the boundary temperatures to have no angle dependence. Therefore, $\frac{\partial}{\partial \theta} = 0$ and $\frac{\partial^2 u}{\partial \phi^2} = 0$, and the problem is reduced to a one-dimensional system (Ã–zisik and Özışık, 1993):

$$\frac{\partial u}{\partial t} = \alpha\left(\frac{1}{r^2}\frac{\partial}{\partial r}\left(r^2 \frac{\partial u}{\partial r}\right)\right) = \alpha\left(\frac{d^2 u}{dr^2} + \frac{2}{r}\frac{du}{dr}\right). \qquad \textbf{2-49}$$

The analytic solution to this problem is well known and is expressed as

$$u(r,t) = u_r + \frac{2R[u_0 - u_r]}{\pi}\sum_{n=1}^{\infty}\frac{(-1)^{n+1}}{n}\, e^{-\lambda_1^2 \alpha t}\, \frac{\sin(\lambda_n r)}{r}, \qquad \textbf{2-50}$$

where *R* is the radius of the particle, λ_n is a constant $\lambda_n = n\pi/R$, u_0 is the initial temperature of the particle, and u_r is the temperature at the boundary $u(r = R, t)$. The characteristic heating timescale is expressed in terms of the particle size and thermal diffusivity as ($n = 1$):

$$\tau = \frac{1}{\lambda_1^2 \alpha} = \frac{R^2}{\pi^2 \alpha}. \quad \textbf{2-51}$$

For the case of particle heating, the value τ corresponds to the time it takes for the particle temperature to reach ~63% (1-1/e) of the surrounding environment (gas, liquid, etc.) temperature. Toshiaki (2000) defined an alternate characteristic timescale that corresponds to the time required for a spherical particle to reach a uniform temperature as;

$$t_{g3} = \frac{5R^2}{\pi^2 \alpha}, \quad \textbf{2-52}$$

based on the time it takes the term $e^{-\lambda_1^2 \alpha t} = 0.0067$. The time constant t_{g3} corresponds to the time required for the particle to reach ~99.3% (1-1/e^5) of the surrounding environment temperature.

Equation 2-50 is useful to obtain solutions to the radial distribution within a particle, but is discontinuous at the center of the particle and not suited for problems with time-dependent boundary conditions. Therefore, we move to a finite difference approach but will verify and make comparisons to the analytic solution when appropriate.

To apply finite difference methods, first, we must discretize the problem both in time and spatial domains. We discretize the one-dimensional particle uniformly along the radius outward from the center such that $r_i = i\Delta r$ from $i = 0, 1, 2, \ldots n$, where n is the number of cells (or "sub-particles" as they will often be referred to). For a given particle size, $R = D/2$ (radius), the special mesh resolution is given by $\Delta r = R/(n-1)$. We employ the explicit Forward in Time Central in Space (FTCS) method over the more stable implicit Crank-Nicolson method (Ã–zisik and Özışık, 1993), as the FTCS algorithm is faster and easily stabilized assuming the stability condition $\frac{\alpha \Delta t}{\Delta r^2} < \frac{1}{2}$ is met. Thus, the discretization in the time domain must have a spacing $\Delta t \leq \frac{\Delta r^2}{2\alpha}$.

To find a solution to Equation 2-49, we apply a Taylor series expansion at each special position, $u(r_i + \Delta r)$ and $u(r_i - \Delta r)$ which we will call u_{i+1} and u_{i-1},

$$u_{i+1} = u_i + \Delta r \left.\frac{du}{dr}\right|_{r_i} + \left.\frac{\Delta r^2}{2!}\frac{d^2u}{dr^2}\right|_{r_i} + \left.\frac{\Delta r^3}{3!}\frac{d^3u}{dr^3}\right|_{r_i} + \cdots,$$

$$u_{i-1} = u_i - \Delta r \left.\frac{du}{dr}\right|_{r_i} + \left.\frac{\Delta r^2}{2!}\frac{d^2u}{dr^2}\right|_{r_i} - \left.\frac{\Delta r^3}{3!}\frac{d^3u}{dr^3}\right|_{r_i} + \cdots, \quad \textbf{2-53}$$

and by subtracting u_{i-1} from u_{i+1},

$$u_{i+1} - u_{i-1} = 2\Delta r \left.\frac{du}{dr}\right|_{r_i} + \left.\frac{2\,\Delta r^3}{3!}\frac{d^3u}{dr^3}\right|_{r_i} + \cdots \quad \textbf{2-54}$$

and solving for first-order spatial derivative:

$$\left.\frac{du}{dr}\right|_{r_i} = \frac{u_{i+1} - u_{i-1}}{2\Delta r} + O(\Delta r^2). \quad \textbf{2-55}$$

We dropped terms of (Δr^2) assuming the choice of Δr to be sufficiently small. Equation 2-55 approximates the spatial derivative at position u_i as an average over cells both forward and backwards in space, hence the "centered in space" of the FTCS method.

Now, we move to obtain an approximation for the second-order derivative in Equation 2-49. If we add u_{i+1} and u_{i-1} instead of subtracting, we have

$$u_{i+1} + u_{i-1} = 2u_i + \Delta r^2 \left.\frac{d^2u}{dr^2}\right|_{r_i} + \cdots, \quad \textbf{2-56}$$

which gives,

$$\left.\frac{d^2u}{dr^2}\right|_{r_i} = \frac{u_{i+1} + u_{i-1} - 2u_i}{\Delta r^2}, \quad \textbf{2-57}$$

having again neglected terms of $O(\Delta r^2)$ and above. Now, we have expressions that allow us to discretize both spatial derivatives in Equation 2-49, leaving only the time derivative. To do so, we Taylor expand the time derivative forward in time and drop terms of $O(\Delta t^2)$ and above:

$$\left.\frac{du}{dt}\right|_{t_{j+1},r_i} = \frac{u_i^{j+1} - u_i^j}{\Delta t}. \quad \textbf{2-58}$$

Inserting Equations (2-55, 2-57, and 2-58) into Equation 2-49 and noting that we have previously defined $r = i\Delta r$ gives the following expression:

$$\frac{u_i^{j+1} - u_i^j}{\Delta t} = \alpha\left(\frac{u_{i+1}^j + u_{i-1}^j - 2u_i^j}{\Delta r^2} + \frac{2}{i\Delta r}\frac{u_{i+1}^j - u_{i-1}^j}{2\Delta r}\right), \quad \textbf{2-59}$$

which we can further simplify to:

$$u_i^{j+1} = u_i^j + \frac{\alpha\Delta t}{\Delta r^2}\left(u_{i+1}^j + u_{i-1}^j - 2u_i^j + \frac{u_{i+1}^j - u_{i-1}^j}{i}\right). \quad \textbf{2-60}$$

This expression is only valid for the interior cells, $i > 0$, as the term $\frac{u_{i+1}^j - u_{i-1}^j}{i}$ will go to infinity at the center of the particle ($i = 0$). As the same equation cannot be used for the entire particle, we must consider three regions of interest: the center of the particle ($r = 0$), the interior of the particle ($0 < r < R$), and the boundary of the particle and gas ($r = R$). To obtain a solution for the center of the particle, we follow the approach by Ã–zisik and Özışık (1993) and apply L'Hospital's rule to Equation 2-49 for the $\frac{1}{r}\frac{du}{dr}$ term:

$$\frac{1}{r}\frac{du}{dr} = \frac{\frac{d}{dr}\left(\frac{du}{dr}\right)}{\frac{d}{dr}(r)} = \frac{d^2u}{dr^2}, \quad \textbf{2-61}$$

thereby removing the $1/r$ complication. Expression (2-49) for the center of the particle is now:

$$\frac{du}{dt} = \alpha\left(\frac{d^2u}{dr^2} + 2\frac{d^2u}{dr^2}\right) \rightarrow \frac{u_i^{j+1} - u_i^j}{\Delta t} = 3\alpha\left(\frac{d^2u}{dr^2}\right)\Big|_{r=0}. \quad \textbf{2-62}$$

The second order derivative in space is treated with a first-order approach, wherein the Taylor series expansion is again given by:

$$u(r + \Delta r) = u(r) + \Delta r\left.\frac{du}{dr}\right|_{r_i} + \frac{\Delta r^2}{2!}\left.\frac{d^2u}{dr^2}\right|_{r_i} + \frac{\Delta r^3}{3!}\left.\frac{d^3u}{dr^3}\right|_{r_i} + \cdots, \quad \textbf{2-63}$$

where $r = r_0 = 0$ and $r + \Delta r = r_1$, which simplifies to,

$$u_1 = u_0 + \Delta r \frac{du}{dr}\bigg|_{r_0} + \frac{\Delta r^2}{2!}\frac{d^2u}{dr^2}\bigg|_{r_0} + \frac{\Delta r^3}{3!}\frac{d^3u}{dr^3}\bigg|_{r_0} + \cdots, \quad \textbf{2-64}$$

allowing for us to obtain an expression in terms of the second-order derivative:

$$\frac{\Delta r^2}{2!}\frac{d^2u}{dr^2}\bigg|_{r_0} = u_1 - u_0 - \Delta r \frac{du}{dr}\bigg|_{r_0} - \frac{\Delta r^3}{3!}\frac{d^3u}{dr^3}\bigg|_{r_0} + \cdots. \quad \textbf{2-65}$$

Solving for the second-order derivatives after dropping higher-order terms gives:

$$\frac{d^2u}{dr^2}\bigg|_{r_0} = 2\frac{u_1 - u_0}{\Delta r^2}. \quad \textbf{2-66}$$

Equation 2-49 for the center of the particle becomes:

$$u_0^{j+1} = u_o^j + 6\frac{\alpha \Delta t}{\Delta r^2}(u_1^j - u_0^j). \quad \textbf{2-67}$$

Equations 2-60 and 2-67 allow for the numerical solution to the system up to the particle's boundary $0 \leq i < R$.

At this point, we choose to restrict the system such that the particle cannot transfer heat back to the gas. This is achieved by enforcing the following boundary condition $u_n^j = T_{enviro}^j$, which constrains the surface of the particle to have the same temperature as the surrounding environment (e.g. local gas temperature). The FTCS solution is then easily obtained by iteration over the temporal and spatial domains as shown in Figure 2-18.

```
for j in range(nsteps):                                    \ Time step loop
   u[-1] = T_hot                                           \ Boundary Condition
   for i in range(nx-1):                                   \ Spatial loop
      if i == 0:                                           \ Center Temperature
         u[i] = u_1[i] + dt*((6 * a)/(dx2)) * (u_1[i+1] - u_1[i])
      if i > 0:                                            \ Interior Temperature
         p1 = (1/dx2)* u_1[i-1] - (1/(i * dx2))*u_1[i-1]
         p2 = (1/dx2)* u_1[i+1] + (1/(i * dx2))*u_1[i+1]
         p3 = (2 / dx2) * u_1[i]
         u[i] = u_1[i] + (dt*a)*(p1 + p2 - p3)
   u_1, u = u, u_1                                         \ Set current T to old T
```

Figure 2-18. Pseudo Python code to solve the spherical one-dimensional heat equation. Here u_1 is the radial temperature profile at the prior time step and u is temperature at the current time step. Iterations over the index *j* are in time while those in *i* are in the spatial domain.

2.4.5 Radiative Heat Transfer

In addition to the heat exchange between the particle and the gas by convection, the particle can lose heat to the surrounding by radiation. The heating of a TL particle produces light resulting from both blackbody radiation and the recombination of thermally released charge carrier pairs. The loss of heat by the particle as a result of blackbody radiation is given by (Ã–zisik and Özışık, 1993),

$$\dot{Q}_r = \epsilon\sigma A\left(T_{surface}^4 - T_{gas}^4\right), \qquad \textbf{2-68}$$

where $\sigma = 5.6697 \times 10^{-8}\ [W/m^2K^4]$ is the Stefan-Boltzmann constant, A is the particle's surface area, and ϵ is the fluid/gas emissivity. For purposes of this work, we will ignore the effect of radiative heat loss based on the results by Tanguay (2009), who modeled the temperature of a single aluminum particle placed within a nitromethane charge. The results looked at the differences in total energy transfer when including and excluding the radiative heat transfer term and found ~0.2% difference. Jet impingement studies by Rozenfeld et al. (2011) also showed the contribution of the radiative heat flux term to be negligible in their simulations.

CHAPTER 3

MATERIALS AND METHODS

3.1 Materials

Three different TL materials were used for the studies: $Li_2B_4O_7:Cu_{0.4\%},Ag_{0.1\%}$ (LBO), $MgB_4O_7:Dy_{0.1\%},Li_{1\%}$ (MBO) and $CaSO_4:Ce_{0.2\%},Tb_{0.2\%}$ (CSO). The samples were synthesized at OSU according to Doull et al. (2014) for agent-defeat tests at the Naval Surface Warfare Center Indian Head Division (NSWC-IHEODTD) in 2012 (henceforth "NSWC-2012"), closed chamber agent-defeat tests in 2013 (henceforth "NSWC-2013"), and for open chamber agent-defeat tests at the Humble Gingko XIXB test facility at the Kirkland Air Force Base in 2014 (henceforth "NM").

Following synthesis, the samples were divided into "control", "testing" and "non-irradiated control" groups. For the TL analyses, we used material from the "non-irradiated control" group, which means the material was stored in the laboratory and not previously exposed to radiation (except for laboratory background) or heat (except for room temperature).

The materials prepared for the NSWC test were sieved (Dual Manufacturing Co.) to select specific grain sizes; LBO between 53µm and 75 µm, MBO and CSO below 125 µm. MBO was the only material from the Humble Gingko XIXB tests investigated in this work and was sieved to < 75 µm. It should be noted that individual particles for the OSU materials are typically ~10 µm and are known to aggregate.

3.2 TL Measurements

TL was measured using a Risø reader TL/OSL-DA-15 (Risø National Laboratory, Denmark) in the presence of N_2 gas. The TL was detected by a bialkali photomultiplier tube (PMT) (model 9235QB, Electron Tubes Inc.). Optical filters optimized for the main emission of each material were placed in front of the PMT: 5 mm Hoya U-330 (Hoya Corporation) for the Cu^+ emission line at 370 nm for LBO, 6 mm Schott BG-39 (Schott AG) for Dy^{3+} emission lines at 480 nm and 574 nm for MBO, and 7.5 mm Hoya U-340 (Hoya Corporation) for Ce^+ emission lines at 306 nm and 324 nm for CSO. Samples were placed in stainless steel sample cups for irradiation, heating, and TL measurement within the Risø reader.

3.3 Irradiations

Irradiations were conducted in the Risø reader using a $^{90}Sr/^{90}Y$ beta source with a dose rate ~0.1 Gy/s. Heating rates and profiles vary according to the method of analysis and are mentioned in the result sections.

3.4 TL Analysis Methods

3.4.1 Various Heating Rates Method

Data Collection

Samples were pre-heated in the Risø reader to clean them of residual signals, irradiated, and allowed to sit for 2 min to allow the charge carrier population to reach an equilibrium state. Following the pause, the sample was heated linearly from room temperature to a temperature sufficient to record the main TL peaks of the respective material, using heating rates between 0.1 K/s and 10 K/s. Following the TL readout, a single background curve was obtained using a 1 K/s heating rate. This process was repeated for a total of three aliquots for each material. The

amount of material used in each measurement varied and is mentioned in the respective result sections. The integration time of the TL curves was chosen such that they are in counts per degree (e.g. 5 K/s heating rate uses counts per 0.2 s to give results in counts per K) and, therefore, the datasets require no additional normalization prior to analysis.

Data Analysis

The VHRM was applied as described in Section 2.2.2. The TL curves were corrected for the background. The background curve corresponding to 1 K/s was scaled to account for the different integration times and subtracted point by point. This approach was introduced to save time by not having to collect background curves at the lower heating rates such as 0.1 K/s and is not expected to have any effect on the peak position. TL peak maximum positions, T_m, were obtained from the background subtracted data using the *PeakDectect* function within the *Mathematica 11* software environment.

Datasets of $\ln\left(\frac{T_m^2}{\beta}\right)$ *versus* T_m^{-1} were constructed for each peak. A trend line was obtained for each peak using an unweighted linear least squares (LLS) fitting. The activation energy for each peak was obtained via the following expression, $E = -k_B \times slope$. The frequency factor was calculated from the y-intercept and the calculated activation energy using the formula $y_{intercept} = \ln(E/sk_B)$.

3.4.2 Initial Rise Method

Data Collection

Step-annealed data for IRM was obtained using the following sequence:

1. Irradiation
2. 120 s pause

3. Linear ramp to T_{stop} at 1 K/s
4. Cool to room temperature, T_{room}
5. 120 s – 180 s pause at T_{room}
6. Linear ramp to T_{max} at 1 K/s
7. Repeat steps 1 – 5 increasing T_{stop} by steps of 5 K until $T_{stop} = T_{max}$.

Following the steps 1-6, an additional TL curve was obtained at 1 K/s to estimate the system's background. TL curves obtained in step 5 make up the step-annealed dataset for IRM analysis. The T_{stop} values are material dependent and are mentioned in the respective result sections.

Data Analysis

A computer routine was written to automatically apply the IRM to background-subtracted TL curves. The main problem was to automatically choose the fitting region of ln(*I*) *versus* 1/*T*.

The minimum temperature, T_{min}, for the fitting region should be such that the signal is distinct from the PMT background noise. We chose, therefore, temperatures that satisfy the criteria $I > \overline{I_n} + 3\sigma_n$, where $\overline{I_n}$ and σ_n represent the mean and standard deviation of the first n data points of the background TL curve and I is the background subtracted TL curve. The background subtraction was conducted by subtracting the single background curve from each step-annealed TL curve. This approach is shown in Figure 3-1.

The maximum temperature used in the analysis, T_{max}, should be such that the concentration of trapped charged remains approximately constant, *i.e.*, $n \sim n_0$, where n_0 is the concentration of trapped charges at the beginning of the measurement. As discussed in the introduction, the choice of T_{max} has been debated in the literature, but the discussion rarely applies here because of the strong overlap of TL peaks resulting from discrete trapping center distributions or the existence of distributions (uniform or Gaussian) of activation energies.

For this reason, we investigated three approaches:

(i) **Fixed region method:** We chose T_{max} as the temperature in which the TL intensity reaches 5% of the first TL peak observed, as traditionally discussed in the literature, even though that applies only to a single TL peak associated with a discrete *E*-distribution. We also analyzed in one situation (single TL peak associated with discrete distribution) how the results vary with the chosen percentage.

(ii) **Search method.** We chose a fitting region that minimized the uncertainty in *E*, *i.e.* the temperature interval that most properly describes a straight line in the ln(*I*) versus 1/*T* graph (Figure 3-2). This fitting region was obtained by scanning all fitting region possibilities between T_{min} and the temperature corresponding to the peak maximum, with a minimum number of fitted points $n > 5$.

(iii) ***E*-histogram method.** We calculated the histogram of *E*-values obtained in (ii) for various fitting regions of each TL curve, to see if this information can provide an estimation on the reliability of the results.

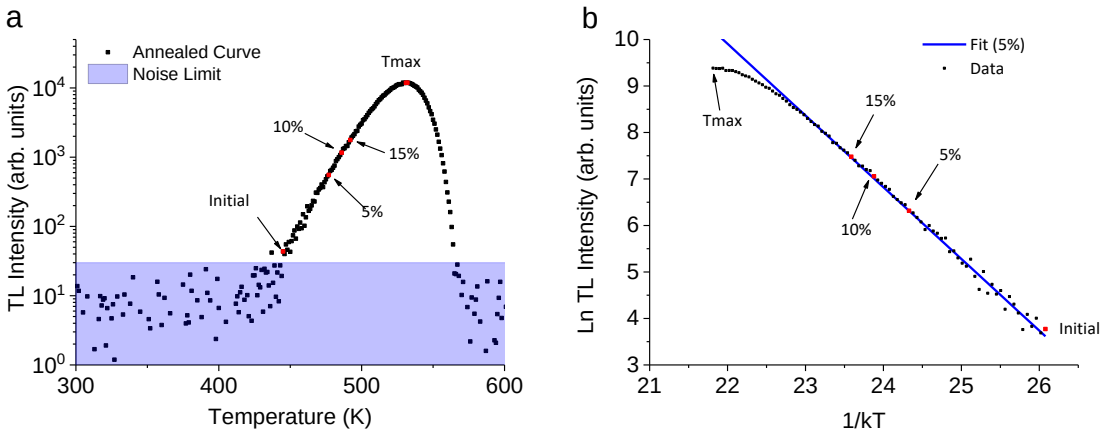

Figure 3-1. Illustration of the IRM analysis following approach (i) for a single simulated TL peak with discrete *E*-distributions ($n_0 = 10^6$, $E = 1.6$ eV, $s = 10^{14}$ s^{-1}). Noise is Poisson distributed about the TL intensity. (a) Noise limit (shaded blue) and relevant points of interest (red points) prior to transformation to the typical Arrhenius plot in (b). Here the blue line is the result of a linear fit of IR data between the initial and 5% data points.

Figure 3-2 illustrates approach (ii) for two simulated TL peaks, with Poisson noise, associated with discrete *E*-distributions ($E_1 = 1.45$ eV and $E_2 = 1.6$ eV). After the first peak maximum and T_{min} are identified, the search region is established (blue data points in Figure 3-2a). Linear fits are performed on subsets of this region by varying the initial data point and the number of points used in the fit. Figure 3-2b shows a plot of the χ^2_{red} as a function of the fitting region (given by the initial index of the point in the y-axis and the number of points used in the fitting in the x-axis), where the red dot indicates the parameters that result in the minimum χ^2_{red} (green data points in Figure 3-2a). This corresponds to intensities between 0.15 – 3 % of the first TL peak and $E = 1.44$ eV, essentially identical to the input value $E_1 = 1.45$ eV for the first TL peak.

Figure 3-3 illustrates the results obtained using approach (iii) applied to simulated TL curves for $T_{stop} = 483$ K (same curve as in Figure 3-2a) and for $T_{stop} = 503$ K (for which the first TL peak is strongly depleted); the input *E* values are shown in red vertical lines. In the first case (Figure 3-3a), the histogram shows a sharp peak coinciding with the input value of the first TL peak ($E_1 = 1.45$ eV), despite the second TL peak being dominant. In the second case (Figure

3-3a), the histogram indicates the presence of two distinct *E*-distributions, but the histogram peak values strongly underestimate the input values E_1 = 1.45 eV and E_2 = 1.60 eV.

These results suggest that the *E*-histogram can be a useful diagnostic tool to identify the presence of more than one distribution, and, therefore, indicate the possible underestimation of *E*, although it does not provide accurate estimations of *E*.

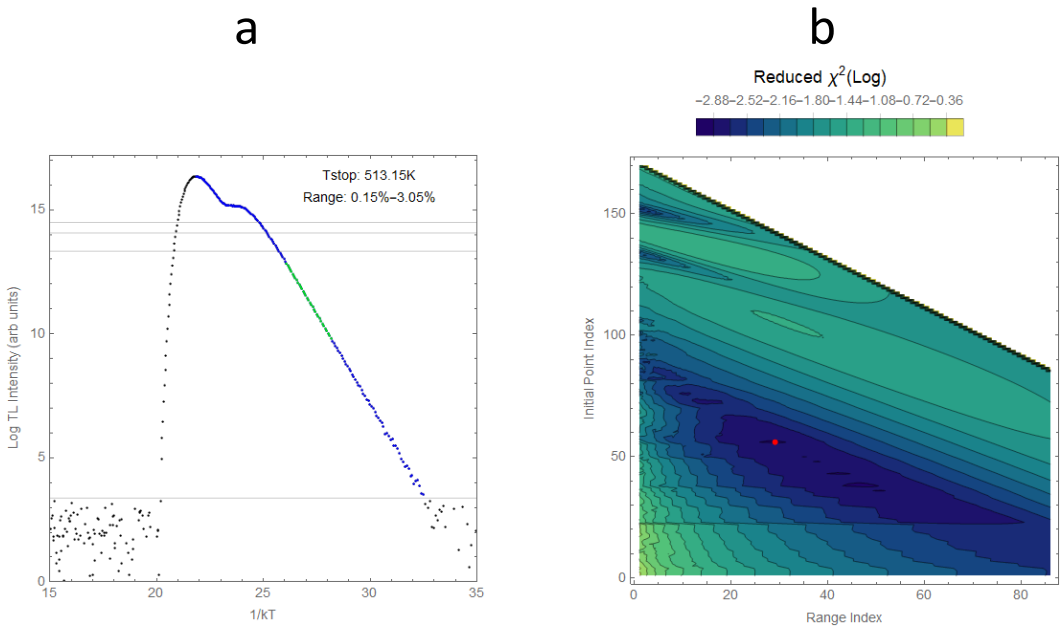

Figure 3-2. Demonstration of approach (ii) applied to a two TL peaks associated with discrete *E*-distributions (E_1 = 1.45 eV and E_2 = 1.6 eV), both with $s = 10^{14}$ s^{-1}. (a) Arrhenius plot for a temperature of 483 K with the horizontal lines indicating the 3σ background, 5 %, 10 % and 15 % of I(T_m). (b) Contour plot of the reduced χ^2 fitting metric as a function of the search region range (number of data points) and starting index, the red dot indicates the minimum reduced χ^2 value.

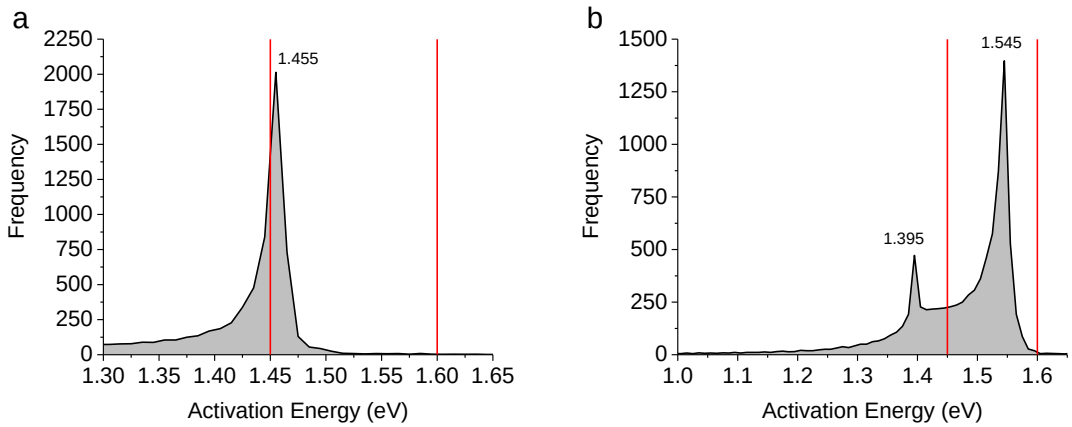

Figure 3-3. *E*-histograms obtained by applying the search method to TL curves for (a) T_{stop} = 483 K and (b) T_{stop} = 503 K. Vertical red lines indicate the actual activation energies used in the simulations.

Other considerations

Additional steps were undertaken to automate the IRM analysis. Curves presenting negligible TL signal ($I_{max} < 10^3$ cps) were not analyzed. Due to high noise and size of the data sets, the TL peak maximums were determined numerically by smoothing (low pass filter) and differentiation.

Attempts to recover the underlying *E*-distributions were conducted following a similar approach to those proposed by Van den Eeckhout et al. (2013) and Gobrecht and Hofmann (1966). Each *E* value obtained for each step-annealed curve is weighted according to the corresponding depletion in TL curve area and binned to obtain the "trap density. Weights are obtained as $w_j = |Total(TL_{i+1}) - Total\ (TL_i)|$, where the subscript *i* indicates the annealed curve number, and *j* indicates the bin number ($n_j = n_i - 1$). For constructing the trap density graphs, each weight was assigned to the mean value between the two adjacent activation energies, $E_j = Mean(E_{i+1}, E_i)$. In this approach, activation energies obtained in regions in which there is a larger decrease in the intensity of the TL curve with T_{stop} have a larger weight,

therefore providing information on the underlying *E*-distribution. The linear fit in the IRM for experimental data was performed using an un-weighted LLS method.

3.4.3 Thermal Quenching

Data Acquisition

This study uses the same background subtracted data that was collected for the VHRM analysis in Section 3.4.1.

Data Analysis

The thermal quenching analysis presented in this work is focused on qualitative analysis of the TL curve behavior as a function of heating rate. Thus, only two methods, whole curve analysis and TL model analysis were implemented to determine if, at all, thermal quenching effects the materials studied.

The total TL curve area for each rate was obtained by summing all positive intensity values of the background subtracted TL curves. Each area was normalized to the lowest heating rate area. Normalized TL areas are then plotted as a function of heating rate to see if a deviation from unity is observed.

Additionally, a TL model for each material was obtained using the one-dimensional deconvolution method discussed in the next section. The trapping parameters obtained from the one-dimensional deconvolution were used to simulate the TL curves for the same heating rates used in the VHRM study. Plots of both the simulated dataset and the experimental dataset were used to compare the heating rate behavior.

3.4.4 One and Two-dimensional Deconvolution

Data Collection

The step-annealed datasets for analysis by deconvolution were obtained following an exposure to an extended hold temperature, T_{hold}. A single aliquot of each OSU material of a few grains was prepared and placed in the Risø reader for data collection according to the following sequence:

1. Irradiation (~10 Gy)
2. Linear ramp to T_{hold} at 20 K/s
3. Maintain T_{hold} for 300 seconds (5 min)
4. Linear ramp to T_{max} at 1 K/s
5. Repeat steps 1 – 4 increasing T_{hold} by steps of 10 K.

Experimental datasets utilized in this work were previously presented by Yukihara et al. (2014b), which were used to obtain trap parameters for the OSU materials using a one-dimensional deconvolution approach.

One-dimensional Deconvolution

We begin by assuming that the experimental dataset $I(T)$ can be modeled by the following expression:

$$I(T) = \sum_i g(E_i) K(E_i, s, T, \beta), \qquad \textbf{3-1}$$

where K is the kernel, comprised of basis functions $\phi(E_i) RW(E_i, s, T, \beta)$ with unknown weights $g(E_i)$. Here, the frequency factor and heating rate are known and the values for T are those used in data collection. When applied to the novel TL temperature sensing materials (MBO, LBO, and CSO) we will use the value of $s = 10^{14} s^{-1}$ suggested by Yukihara et al. (2014b).

Equation 3-1 can be expressed as a linear matrix equation, $b = Ax$ where b is the experimental dataset and A represents the kernel. The kernel is expressed as a matrix

$$\sum_i K(E_i, s, T, \beta) = \begin{bmatrix} K(E_1, s, T_1, \beta) & \dots & K(E_p, s, T_1, \beta) \\ \vdots & \ddots & \vdots \\ K(E_1, s, T_N, \beta) & \dots & K(E_p, s, T_N, \beta) \end{bmatrix}, \quad \textbf{3-2}$$

where the experimental dataset had N datapoints collected at a heating rate of β. The matrix has p rows which represent the number of activation energies used in the deconvolution. The solution for the weights $x = g(E_i)$ are obtained through the miniziation of $\|Ax - b\|_2$ subject to the non-negative least-squares (NNLS) condition $x \geq 0$ (Lawson and Hanson, 1974), to ensure physical solutions to the system. The solution for the weights is obtained through a custom written Mathematica script which employs the algorithm by Lawson and Hanson (1974).

Two-Dimensional Deconvolution

We begin by assuming that the simulated experimental dataset $I_\theta(T, \theta)$, or $I_\beta(T, \beta)$, can be modeled by the following expression:

$$I_\theta(T, \theta) = \sum_i \sum_j g(E_i, s_j) K(E_i, s_j, \theta, \tau, T, \beta), \quad \textbf{3-3}$$

where K is the kernel, comprised of basis functions $\phi(E_i, s_j, \theta, \tau) RW(E_i, s_j, T, \beta)$ with unknown weights $g(E_i, s_j)$. When performing the analysis, the values of T, θ, β and τ are fixed to the values used to obtain the simulated dataset; additionally, when analyzing β-datasets we set $\phi(E_i, s_j, \theta, \tau) = 1$, i.e., we assume that no thermal depletion of the trapping centers occurred at the start of the TL measurement. Equation 3-3 can be expressed as a linear matrix equation, $b = Ax$, where b is the experimental dataset and A represents the kernel. Equation 3-3 represents an ill-posed problem given that Fredholm equations of the first kind are known to be ill-posed (Hansen, 1992), and the system contains noise (Van Beek et al., 2003). Therefore,

we may only obtain an approximate solution $x \to \tilde{x}$ through the minimization of $\|Ax - b\|_2$ where $\|\cdot\|$ is the Euclidean norm.

For conciseness, we focus on the formulation of the matrix problem for the case of the θ-dataset with the knowledge that these methods can be directly used for the β-dataset. We begin by defining the constraint set (simulated experimental data) in vector form:

$$y = vec[I(T,\theta)] = \begin{bmatrix} I(T_1,\theta_1) \\ I(T_2,\theta_1) \\ I(T_3,\theta_1) \\ \vdots \\ I(T_N,\theta_1) \\ I(T_1,\theta_2) \\ I(T_2,\theta_2) \\ \vdots \\ (T_N,\theta_2) \\ \vdots \\ I(T_1,\theta_M) \\ \vdots \\ I(T_N,\theta_M) \end{bmatrix}, \quad \textbf{3-4}$$

where N is the number of data points for a given TL curve whose index corresponds to readout temperatures in T, and M corresponds to the number of hold temperatures utilized in the simulation, giving the vector y a length of $N \times M$. Next, we linearize the two-dimensional solution space matrix $g(E_i, s_j)$ to a vector x for p activation energies, and q frequency factors

$$x = vec\left[\sum_i \sum_j g(E_i, s_j)\right] = \begin{bmatrix} g(E_1,s_1) \\ g(E_2,s_1) \\ g(E_3,s_1) \\ \vdots \\ g(E_p,s_1) \\ g(E_1,s_2) \\ g(E_2,s_2) \\ \vdots \\ g(E_p,s_2) \\ \vdots \\ g(E_1,s_q) \\ \vdots \\ g(E_p,s_q) \end{bmatrix}, \quad \textbf{3-5}$$

for a solution vector of length $p \times q$. Finally, we express the kernel matrix as,

$$\sum_i \sum_j K\left(E_i, s_j, \theta, \tau, T, \beta\right) = \begin{bmatrix} K(E_1, s_1, \theta_1, T_1) & \dots & K\left(E_p, s_q, \theta_1, T_1\right) \\ \vdots & \ddots & \vdots \\ K(E_1, s_1, \theta_M, T_N) & \dots & K\left(E_p, s_q, \theta_M, T_N\right) \end{bmatrix}, \quad \textbf{3-6}$$

where each element, $K\left(E_i, s_j, \theta, \tau, T, \beta\right)$, represents an individual TL curve of length N obtained from the single trapping center (E_i, s_j) following a preheating at temperature θ for a time τ. Therefore, the kernel is a two-dimensional matrix with dimensions of $[N \times M, p \times q]$.

The introduction of Poisson noise coupled with background subtraction produces uncertainty for each data point within the simulated dataset. Therefore, we must adjust the problem description to a weighted least squares formulism. Let $V_{[N\times M, N\times M]}$ be a diagonal matrix of weights corresponding to the uncertainties in the dataset vector, y. The weighted sum of squares is expressed as $Q = \sum v_i\left(y_i - K_i^T x\right)^2$ or as matrices $(y - Kx)^T V (y - Kx)$ (Lawson and Hanson, 1974), which has a solution:

$$x = (K^T V K)^{-1} K^T V y, \quad \textbf{3-7}$$

which is simply $min\|Ax - B\|_2$ for $A = K^T V K$ and $B = K^T V y$.

As the problem is ill-posed, we must provide additional information or constraints to ensure a unique and stable solution (Van Beek et al., 2003). We further restrict the solution to be positive, as negative trapping center occupancies are non-physical and, therefore, subject the problem to the condition $x \geq 0$, known as the non-negative least-squares (NNLS) problem (Lawson and Hanson, 1974). We obtained the solution numerically within the *Python* programming environment using the *scipy.optimize.nnls(A,B)* function.

In addition to NNLS we will also implement Tikhonov regularization subjected to a NNLS constraint. Tikhonov regularization seeks to minimize the argument (Hansen, 1992),

$$\|Ax - B\|_2 + \lambda^2 \|Lx\|_2, \quad \textbf{3-8}$$

where λ is the regularization parameter which weighs the effect of the is the regularization matrix L on the minimization problem. By choosing L to be the identity matrix, we give

preference to solutions with smaller norms, and, theoretically, allow finer resolutions for the kernel to produce distribution behavior. The determination of the optimal λ value is achieved by obtaining the location of the corner of the log-log plot of solution norm $\|x\|_2$ and residual norm $\|Ax - B\|_2$ known as the L-Curve (Hansen, 1992).

For the experimental datasets collected by Yukihara et al. (2014b) and described in the data collection subsection of the Section 3.4.4, we must make an adjustment to the kernel in Equation 3-3 to reflect the experimental conditions. Prior to the 5 min hold, the sample is heated from room temperature to a set hold temperature using a 20 K/s linear heating rate. Thus, the basis functions for the experimental dataset are given by

$$\phi_{linear}(E_i, s_j, \beta', T_{hold})\phi_{const}(E_i, s_j, T_{hold}, \tau)RW(E_i, s_j, T, \beta), \quad \textbf{3-9}$$

where ϕ_{linear} is the linear depletion function defined in Equation 2-40 with β' equal to 20 K/s, and ϕ_{const} is the constant heating depletion function in Equation 2-39.

3.5 Simulation Methods

3.5.1 Calculations

All calculations were performed using built in functions in *Mathematica 11*. For faster computation, the integrals were re-written using the exponential integrals $Ei(x) = \int_{-z}^{\infty} \frac{e^{-t}}{t} dt$, as in:

$$-\frac{s}{\beta}\int_{T_0}^{T_{stop}} e^{\frac{E_t}{k\Theta}} d\Theta = Te^{-\frac{E_t}{kT_{stop}}} + \frac{E_t}{k} Ei\left(-\frac{E_t}{kT_{stop}}\right). \quad \textbf{3-10}$$

3.5.2 IRM Datasets

TL curves for Gaussian and uniform *E*-distributions were generated using a summation approximation to the integral in Equations 2-13 and 2-14. The separation between activation

energies (bin width), δE, was chosen to be sufficiently small, resulting in the following expressions for the TL intensity from a uniform *E*-distribution:

$$I(T) = \sum_{i=1}^{N_E} n_{0,i} RW(E_i, s_i, T), \qquad \textbf{3-11}$$

where N_E is the total number of trapping centers. Each individual TL peak is weighed by $n_{0,i} = n_0/N_E$, where n_0 is the total initial trap occupancy. In the Gaussian *E*-distribution, case we have:

$$I(T, \mu_E, \sigma_E) = \sum_{i=1}^{N_E} \left[\left(\frac{n_0 \delta E}{\sqrt{2\pi}\sigma_E} \right) exp\left(-\frac{(E_i - \mu_E)^2}{2\sigma_E^2} \right) \right] RW(E_i, s_i, T), \qquad \textbf{3-12}$$

where the term within square brackets represents a Gaussian *E*-distribution of mean energy μ_E and full-width at half-maximum FWHM = $2\sqrt{2ln2}\sigma_E$. The discretised Gaussian was evaluated over the interval, $\mu_E \pm 3\sigma_E$, representing 99.7% of the distribution. The spacing in activation energies is considered to be sufficiently small to make such an approximation in the case that $\delta E \ll kT$ for an ideal TL curve without noise (Rudlof et al., 1978).

Simulation of Step-annealed TL Curves

To simulate the TL curves obtained using step-annealing to a maximum temperature T_{stop}, the original trapping center population for each energy bin $n_{0,i}$ was multiplied by a depletion factor also derived for first-order kinetics, given by:

$$\Phi_i(E_i, s_i, T_{stop}) = \frac{n_i}{n_0} = \exp\left(-\frac{s_i}{\beta} \int_{T_0}^{T_{stop}} e^{\frac{E_i}{k\Theta}} d\Theta \right). \qquad \textbf{3-13}$$

For a single trapping center (*E*, *s*), pre-heating to a maximum temperature, T_{stop}, using a heating rate β produces a TL curve simply described by $\Phi(T_{stop})RW(E, s, T)$. Therefore, the resulting TL curves previously obtained in Equations 3-11 and 3-12 are easily modified to describe the TL curves for uniform and Gaussian *E*-distributions after a preheat:

$$I(T) = \frac{1}{N_E \delta E} \sum_{i=1}^{N_E} n_{0,i} \Phi_i\left(E_i, s_i, T_{stop}\right) RW(E_i, s_i, T), \quad \textbf{3-14}$$

$$I(T) = \frac{\Delta E_G}{N_E \delta E} \left(\frac{1}{\sqrt{2\pi}\sigma_E}\right) \sum_{i=1}^{N_E} exp\left(-\frac{(E_i - \mu_E)^2}{2\sigma_E^2}\right) \Phi_i\left(E_i, s_i, T_{stop}\right) n_{0,i} RW(E_i, s_i, T). \quad \textbf{3-15}$$

Figure 3-4a-c illustrates the procedure for two TL peaks associated with discrete distributions, pre-heated to 422 K at 1 K/s.

Introduction of Noise to the Data

To simulate realistic conditions, noise was added to the simulated TL curves. Poisson noise is only one source of variability in the TL curves, whose intensity is influenced by other factors (e.g. heating temperature). Therefore, here, the Poisson noise was multiplied by a factor α, estimated based on experimental TL curves, to mimic the variability in the experimental curves.

To determine the factor α, TL curves for $Li_2B_4O_7$:Cu,Ag, MgB_4O_7:Dy,Li and $CaSO_4$:Ce,Tb (Yukihara et al., 2014b) were fitted with an arbitrary *E*-distribution assuming a fixed frequency factor $s = 10^{14}$ s^{-1} and bin separation δE = 0.03 eV, as described by Yukihara et al. (2014b). Based on that, we calculated the reduced chi-square χ^2_{red} for the fit, given by:

$$\chi^2_{red} = \frac{1}{f} \sum_{i=1}^{i=n} \left(\frac{y_i - y_{i,exp}}{\sigma_i}\right)^2, \quad \textbf{3-16}$$

where σ_i are the estimated uncertainties of the data points in the TL curve. If the uncertainties in the TL curve are properly estimated and the model is correct, $\chi^2_{red} = 1$. For the experimental curves, however, if one assumes uncertainty is only due to Poisson noise and, therefore, equal to $\sqrt{y_i}$, then $\chi^2_{red} > 1$, indicating that the uncertainties are underestimated. Then, we estimated that the Poisson uncertainties must be increased by a factor between ~2.8 and ~4.2 (depending on the material) to obtain $\chi^2_{red} = 1$. Note that this is a standard method of

estimating the uncertainties in the data based on distribution of the experimental values around the fitted curve (Dobaczewski et al., 2014).

Taking that into account, the experimental curves were simulated as follows:

(i) The TL curve was calculated

(ii) A constant value simulating the PMT background I_{BG} = 100 counts per second (cps) was added to the curves

(iii) An error ε was added to each data point following a normal distribution with standard deviation equal to $\alpha\sqrt{y_i}$. (The Poisson approaches a normal distribution for large number of counts.)

Additionally, a background curve was simulated as a normal distribution with a mean value 100 cps and standard deviation $\sqrt{100}$ cps. The mean value of the background curve was used for background subtraction, valid if the background does not include a blackbody radiation component.

Figure 3-4 shows the simulated TL curve, simulated background, and background subtracted TL curve used in the analyses.

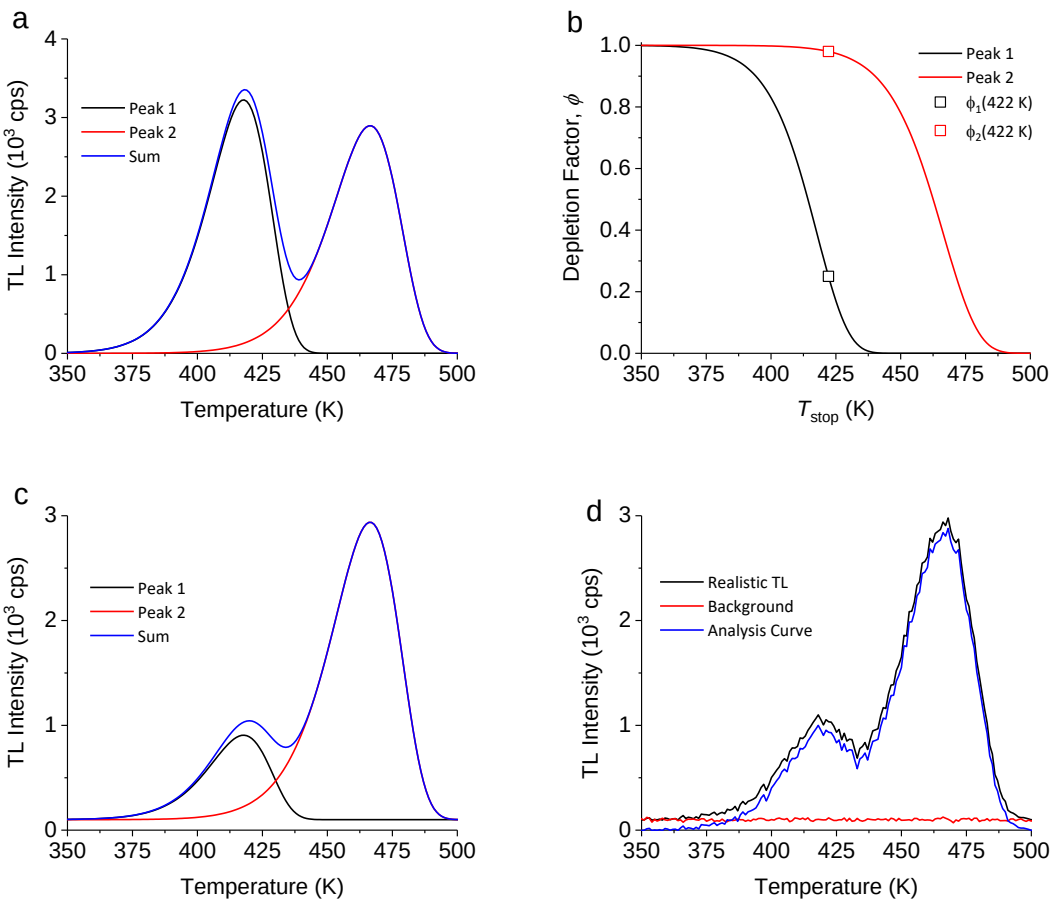

Figure 3-4. (a) Simulated composite peaks, (b) computed depletion curves, (c) TL curve after T_{stop} = 422 K (c), and (d) simulated TL curve with noise, before and after subtraction of the constant background.

Simulated Scenarios

Based on the procedure described in the previous sections, the scenarios presented in Table 3-1 were simulated. These can be divided into: single distributions (D1, G1, U1) and overlapped TL peaks (D2, G2, U2).

Table 3-1. Simulation sets used in this study. For discrete *E*-distributions, E_1 and E_2 correspond to the single trap parameters for peaks 1 and 2, respectively. For the distributions, E_i represents the mean value of the distributions, and the width represents either the full width (uniform distribution) or FWHM (Gaussian distribution) for each TL peak. ΔE represents the spacing between successive activation energies within a given distribution. For the Gaussian and uniform *E*-distributions, ΔE = 1.0 meV.

Set	Type	ID	N	Peaks	E_1(eV)	s_1 (s^{-1})	E_2 (eV)	s_2 (s^{-1})	Width (eV)
1	Discrete	D1	1	1	1.5	10^{14}	-	-	-
1	Gaussian	G1	300	1	1.5	10^{14}	-	-	0.3
1	Uniform	U1	301	1	1.5	10^{14}	-	-	1.0
2	Discrete	D2	2	2	1.05	10^{8}	1.8	10^{14}	-
2	Gaussian	G2	600	2	1.5	10^{14}	1.75	10^{14}	0.3, 0.3
2	Uniform	U2	602	2	1.45	10^{14}	1.65	10^{14}	1.0, 1.0

IRM Analysis of Simulated Data

Background subtracted analysis curves underwent a similar analysis as experimental TL curves presented in Section 3.4.2. The linear fit in the simulated IRM data was performed using both a weighted and unweighted LLS method, where the weights for a linear regression are defined as $w_i = 1/\sigma_i^2$ and σ_i is the estimated uncertainty for the i^{th} data point. To obtain σ_i, we began by estimating the uncertainty of a step-annealed TL curve to be the result of Poisson noise, and therefore $\sigma_{TL,i} = \sqrt{TL_i}$. Then, we estimated the uncertainty for the background curve, σ_{BG}, as the standard deviation of the mean. Following typical background subtraction, the uncertainty for the i^{th} data point is calculated as $\sigma_i = \sqrt{{\sigma_{TL,i}}^2 + {\sigma_{BG}}^2}$. The final uncertainty of ln(*I*) was computed by error propagation (Taylor, 1997) as $\sigma_{\ln I,i} = \sigma_i / I(T_i)$.

3.5.3 One-dimensional Deconvolution Datasets

The single trapping center case can be generalized to that of a Gaussian $g(E_t)$ or multinomial distribution $g(E_t, s_t)$. The TL expression for a Gaussian distribution of initial trap occupancies over a range of activation energies with a common frequency factor, s, can be

obtained by making the substitution of $g(E_t) \rightarrow \frac{1}{\sqrt{2\pi}\sigma_E} exp\left(-\frac{(E_t-\mu_E)^2}{2\sigma_E^2}\right)$ in Equation 2-12 (Hornyak and Chen, 1989):

$$I(T) = \frac{1}{\sqrt{2\pi}\sigma_E}\int_0^\infty e^{-\frac{(E_t-\mu_E)^2}{2\sigma_E^2}} RW(E_t, s, T, \beta)\, dE_t, \qquad \textbf{3-17}$$

where μ_E is the mean activation energy and σ_E is the standard deviation of the activation energy. For a multinomial distribution of traps in both activation energy and log frequency factor space, $\log s$, we use the multivariate normal expression for the trap parameter distribution,

$$g(E_t, \log s_t) = \frac{1}{2\pi\sigma_E\sigma_{\log s}} exp\left(-\frac{(E_t-\mu_E)^2}{2\sigma_E^2} - \frac{\left(\log s_t - \mu_{\log s}\right)^2}{2\sigma_{\log s}^2}\right), \qquad \textbf{3-18}$$

where we have assumed the covariance matrix off diagonal values to be 0. Substitution of Equation 3-18 into Equation 2-12 requires the addition of a second integration which results in the following expression for an experimental TL curve (previously seen as Equation 2-31)

$$I(T) = \frac{1}{2\pi\sigma_E\sigma_{\log s}}\int_0^\infty\int_0^\infty e^{\left(-\frac{(E_t-\mu_E)^2}{2\sigma_E^2} - \frac{\left(\log s_t-\mu_{\log s}\right)^2}{2\sigma_{\log s}^2}\right)} RW(E_t, \log s\,, T, \beta) dE_t d\log s\,. \qquad \textbf{3-19}$$

TL curves were simulated numerically using *Mathematica* (version 11.1.0.0, Wolfram Research Inc.) and a discrete approach through the replacement of the integrals in Equation 3-19 with summations over discrete steps in parameter space. For this study, we used distributions in *E* and *log s* instead of *E* and *s*. As a result, Equation 3-18 becomes

$$g(E_t, \log s_t) = \frac{1}{2\pi\sigma_E\sigma_{\log s}} exp\left(-\frac{(E_t-\mu_E)^2}{2\sigma_E^2} - \frac{\left(\log s_t - \mu_{\log s}\right)^2}{2\sigma_{\log s}^2}\right). \qquad \textbf{3-20}$$

For a multinomial distribution in *E* and *log s*, the resultant discretization of Equation 3-19 is:

$$I(T) = \frac{1}{2\pi\sigma_E\sigma_{\log s}}\sum_i\sum_j e^{\left(-\frac{(E_i-\mu_E)^2}{2\sigma_E^2}-\frac{\left(\log s_j-\mu_{\log s}\right)^2}{2\sigma_{\log s}^2}\right)} \times \phi(E_i, 10^{\log s_j}, \theta, \tau)\, RW\left(E_i, 10^{\log s_j}, T, \beta\right), \quad \textbf{3-21}$$

where $\phi(E_i, 10^{\log s_j}, \theta, \tau)$ is set equal to 1 when simulating varied heating rate datasets (no pre-heating).

Noise was introduced by randomly sampling a Poisson distribution centered about a mean value equal to $TL_{exp,i} = I(T_i) + I_{dc}$, where $I(T_i)$ is the intensity at the readout temperature T_i and I_{dc} is dark count of the system. We set I_{dc} to be 100 counts per second and scale it according to the variations in integration time that result from changes in the heating rate. For each simulated TL curve, we simulated a background curve, $I_{bg,i}$, where each intensity is randomly sampled *n* data points from a Poisson distribution about a mean value of I_{dc}.

The experimental curves used in the analysis follow the usual TL procedure, where the TL intensity was obtained by subtracting an average background from the experimental TL signal: $y_i = TL_{exp,i} - \langle I_{bg}\rangle$. We estimated the uncertainty the i^{th} data point in the background subtracted curve to be Poisson, $\sigma_{TL,i} = \sqrt{TL_{exp,i}}$ and the uncertainty in the background curve to be the standard deviation of the mean such that $\sigma_{bg} = \sigma(I_{bg})/\sqrt{n}$. The total uncertainty of the i^{th} data point in the analysis curve, y_i is calculated as $\sigma_{y,i} = \sqrt{\sigma_{TL,i}^2 + \sigma_{bg}^2}$.

Figure 3-5 exemplifies the simulated curves for two discrete trapping centers (E_1 = 1.2 eV, s_1 = 10^{14} s^{-1}, E_2 = 1.4 eV, s_2 = 10^{12} s^{-1}), where Figure 3-5a shows the depletion factors of each trapping center as a function of pre-heating (temperature fixed at θ for 300 s), and Figure 3-5b shows the resultant TL curves.

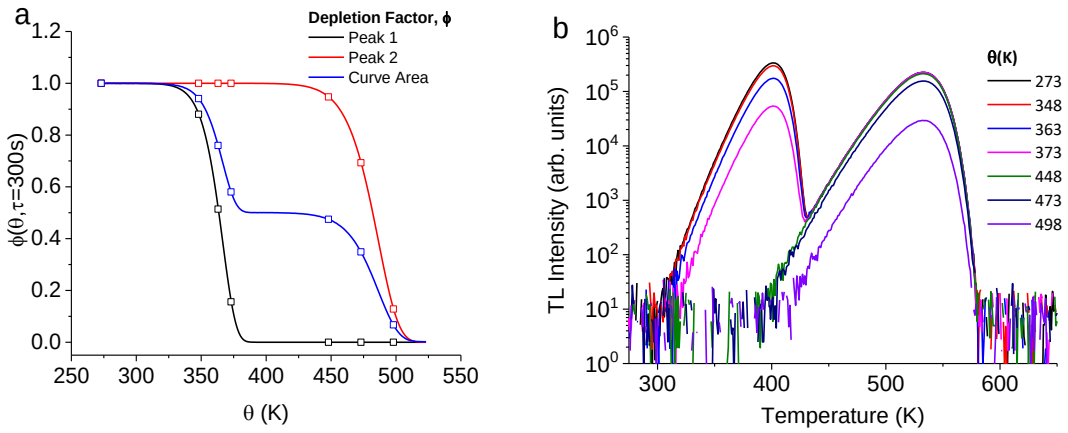

Figure 3-5. (a) Depletion curves for both discrete TL peaks and the corresponding curve area depletion and (b) residual TL following the preheating profiles indicated by the depletion figure as open squares. The data were generated assuming the samples were held at a temperature θ for 300 s.

Simulation Input Parameters

Single TL peaks are obtained from input distributions that are centered about a mean activation energy and a mean $\log s$ value. The distributions for each TL peak simulated in this work are presented in Table 3-2. Each individual TL peak in Table 3-2 was simulated for a range of input values equal to $\mu \pm 3\sigma$ and with a spacing ($\Delta E = E_{i+1} - E_i, \Delta \log s = \log s_{i+1} - \log s_i$) which results in total number of $N = N_E \times N_{\log s}$ peaks.

Table 3-2. Input parameters for each of the four TL peaks in the simulated TL curves.

Peak	μ_E (eV)	FWHM (eV)	μ_s (log s)	FWHM (log s)	$N_{centers}$
A	1.2	0.059	12	0.59	3721
B	1.2	0.059	14	0.59	3721
C	1.4	0.059	12	0.59	3721
D	1.4	0.059	14	0.59	3721

Simulated TL curves are comprised of different combinations of the individual peaks in Table 3-2, which are used to simulate sets of TL curves resulting from changes to hold temperatures, "θ-datasets" and heating rate "β-datasets". All β-datasets are simulated using the same seven heating rates in the range (0.1 – 10) K/s, whereas the input hold temperatures are changed to reflect the thermal stability for each peak configuration. The choice of hold

temperatures is up to the user and is discussed in more detail in the following section, but we always use the same 300 s hold duration (5 min).

Reconstruction of Input Distribution

Background subtracted analysis curves undergo the same two-dimensional deconvolution analysis as experimental TL curves, presented in Section 3.4.4.

3.6 Particle Heating Simulations

3.6.1 Modeling Multiple Thermal Histories

The residual TL from a particle subjected to a heating profile $T(t)$ and assumed to be heated uniformly over the particle volume was previously shown in Equation 2-38. Typically, TL curves collected from detonation test samples in laboratory are the result of the TL from multiple particles, expressed as:

$$I_{total}(T) = \sum_{j}^{m}\sum_{i}^{n} \phi_j(E_i, s_i, T_j(t)) \times RW(n_{0,i}, E_i, s_i, T, \beta), \qquad \textbf{3-22}$$

where I_{total} is the summation of the TL intensity from m individual particles and $RW(\ldots)$ is the Randall-Wilkins TL curve (Equation 2-8). Each trapping center from each particle is depleted by a unique depletion factor, $\phi_j(\ldots)$, which reflects the temperature function, $T_j(t)$, for that individual particle.

To understand the effect that a sample comprised of particles with multiple thermal histories has on the temperature reconstruction process, we consider a theoretical TL material characterized by a 3-trap system (1.35, 1.55, 1.75 eV) with a common frequency factor of s = 10^{12} s^{-1}. Equation 3-22 is used to simulate the residual TL from mixtures of two different thermal profiles, and a thermal history is determined following the method provided in Section 2.3.2.

To observe the effect of a more realistic dataset, a single distribution of temperature profiles was considered using data from Armstrong (2017). This work looked at the maximum temperature of 42 individual MBO particles that displayed residual TL following exposure to an agent-defeat test. Thermal history recovery assumed an exponential decay temperature profile with a time constant of $\tau = 50\ ms$. We obtained the maximum temperatures from Figure 5.11 of Armstrong (2017), reproduced in Figure 3-6a.

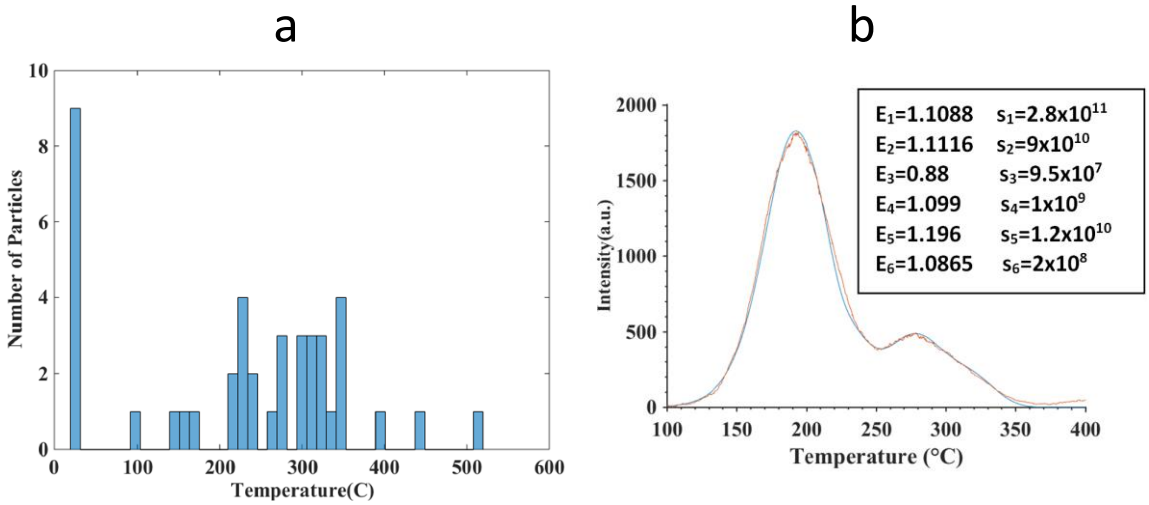

Figure 3-6. (a) Distribution of maximum temperatures of MBO particles exposed to an agent-defeat test and (b) TL model used for MBO assuming first-order kinetics obtained via curve fitting. Figures after from Armstrong (2017).

Temperatures were obtained via an online digitizer (Rohatgi, 2018), and rounded to the nearest 5 K. We assumed the total thermal exposure time to be 1 second with a decay constant of 50 ms. We simulated the residual TL of the MBO particle using Equation 3-22 and relied on the same trap parameters used by Armstrong (2017) for MBO (Figure 3-6b). The heating function was assumed to be of the form

$$T(t) = T_0 + (T_{max} - T_0)\exp(-t/\tau), \qquad \textbf{3-23}$$

which was used in the calculation of the depletion factor.

3.6.2 Modeling Transient Particle Heating

Modeling of transient particle heating assumes the material is characterized by a thermal diffusivity constant equal to that of CSO, $\alpha = 1.55 \times 10^{-7}\ m^2/s$, (Kontogeorgos et al., 2011) such that the model behavior mimics that of a typical TL sensor. TL particles were modeled as 25-, 50- and 100-μm particles to reflect typical particle sizes in detonation testing and to capture the effect of scaling the particle size.

As a first approximation, we modeled the particle heating under highly constrained conditions. First, we assumed the particle is sufficiently small such that the surface area available for heat transfer by convection is small and that the particle moves with the local gas or fluid (Kumar et al., 2011), and therefore there are no relative velocity effects such as forced convection. Along the same line of reasoning we assumed the value of the Biot number to be *Bi* > 0.1. Other simulations for 100-μm Al particles placed within a HE charge were shown to have values near threshold (*Bi* ~ 0.2) during the main heating regime (Tanguay, 2009). Second, we assumed a one-way heat exchange from the gas/fluid to the particle and assume heat loss (convective or radiative) to be negligible. Finally, we assumed any imposed boundary conditions at the radius of the particle to be equivalent to the surface temperatures that would be obtained from the convective heat transfer, Equation 2-43, and therefore forgo the need to obtain the value for the heat transfer coefficient h.

As previously indicated, particles are assumed to be spherical and homogenous. Additionally, the temperature at the particle's radius is assumed to have spherical symmetry. Thus, the radial temperature distribution is obtained from Equations 2-60 and 2-67. In all cases, the particle is assumed to be initially at or near room temperature,

$$u(r, t = 0) = u_i^{j=0} = 292K. \qquad \textbf{3-24}$$

Dirichlet boundary conditions are applied at the particle's radius at each time step ensuring the temperature at the edge of the particle is equal to the surrounding gas:

$$u(r,t) = T_{gas}(t),$$
$$u_{i=n}^{j} = T^{j}, \quad \textbf{3-25}$$

for $t \geq 1$ & $j \geq 1$. The radial temperature of the particle is obtained iteratively by looping over space and time as illustrated in Figure 2-18 and exported at each time step.

Residual TL Curve

In the previous section, we obtained the temperature at a given radius as a function of time. We assumed each radial node ($r_i = i\Delta r$) to represent an individual "sub-particle" from which we can obtain the entire TL signal (assuming no internal light absorption). Assuming no previous heating of the particle, the total TL curve from a single particle can be expressed as a summation of the TL from each sub-particle multiplied by a geometric factor:

$$TL_{total} = \left(TL_0 \times \frac{4}{3}\pi\Delta r^3\right) + \sum_{i=1}^{n} TL_i \times \left(4\pi r_i^2 \Delta r\right), \quad \textbf{3-26}$$

where TL_0 refers to the TL curve from the center sub-particle and TL_i refers to all other TL sub-particles. The geometric factors weight the TL signal at a radial position by the amount of material located in the 3D spherical geometry. Thus, the center particle is weighted by its volume as it is a single particle, while the other particles are weighted by their "shell contribution" which is their surface area times the shell width.

The depletion of trapped charges of a given sub-particle follows Equation 3-22, but with the assumption that the heating function $T(t)$ can be expressed as a series of a constant heating profiles (Figure 3-7). We choose a constant heating approximation as the depletion factor, previously seen as Equation 2-39. Additionally, if we choose a sufficiently short time interval, we

can easily approximate very complex heating functions in a computationally efficient way. Figure 3-7 shows the example of this approach for an arbitrary exponential decay heating function.

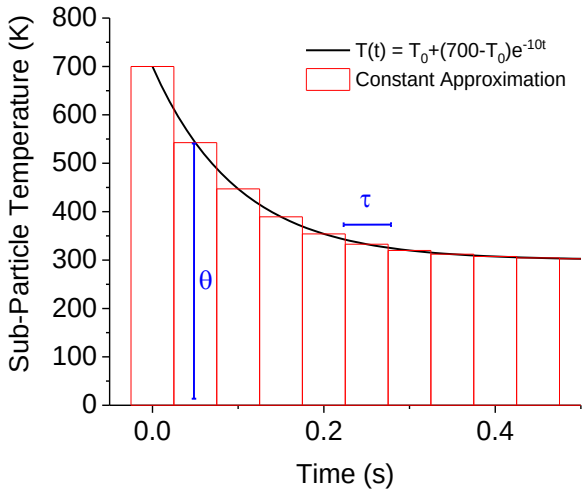

Figure 3-7. Exponential decay heating function and the constant heating approximation assuming a heating interval of 0.05 s for which θ(t) = T(t).

For individual particle heating, the temperature of a given sub-particle at location $r_i = i\Delta r$ at time $t = j\Delta t$ is given by u_i^j. Thus, the depletion factor for this sub-particle is given by $\phi_i\left(E, s, u_i^j, \Delta t\right)$, where we have made the substitution of $\theta = u_i^j$ and $\tau = \Delta t$. Each sub-particle is heated for a total of n_t time steps, and thus, the full depletion factor of the i^{th} sub-particle calculated as the product of the individual depletion factors taken over the full simulation run time:

$$\Phi_{\mathrm{i}}(E, s) = \prod_{j=0}^{n_t} \phi_i\left(E, s, u_i^j, \Delta t\right). \qquad \textbf{3-27}$$

The residual TL from a single sub-particle (not weighted by geometric factors) is given by:

$$I_i(T) = \sum_{k=1}^{N} \Phi(E_k, s_k) \times RW\left(n_{0,k}, E_k, s_k, T, \beta\right), \qquad \textbf{3-28}$$

where the material is characterized by N trapping centers.

3.6.3 Blast Environment Simulations

Computer simulations were undertaken to model the blast environment experienced by free-flowing particles during the NSWC-2015 tests (Daniels et al., 2015; Yukihara et al., 2015) using the Los Alamos National Laboratory (LANL) FLAG hydrodynamics code (Burton, 2007). The experimental testing conducted at NSWC Indian Head is detailed by Daniels et al. (2015) and is summarized in this section for convenience. TL sensor particles were placed within a cylindrical steel chamber with a volume of 243 L and a diameter of 23 inches (58.42 cm) (Figure 3-8a). A package of TL particles was suspended 6 inches (15.24 cm) from a cylindrical High Explosive (HE) charge (r = 1.9cm, L = 2.6 cm) which was placed at the center of the chamber.

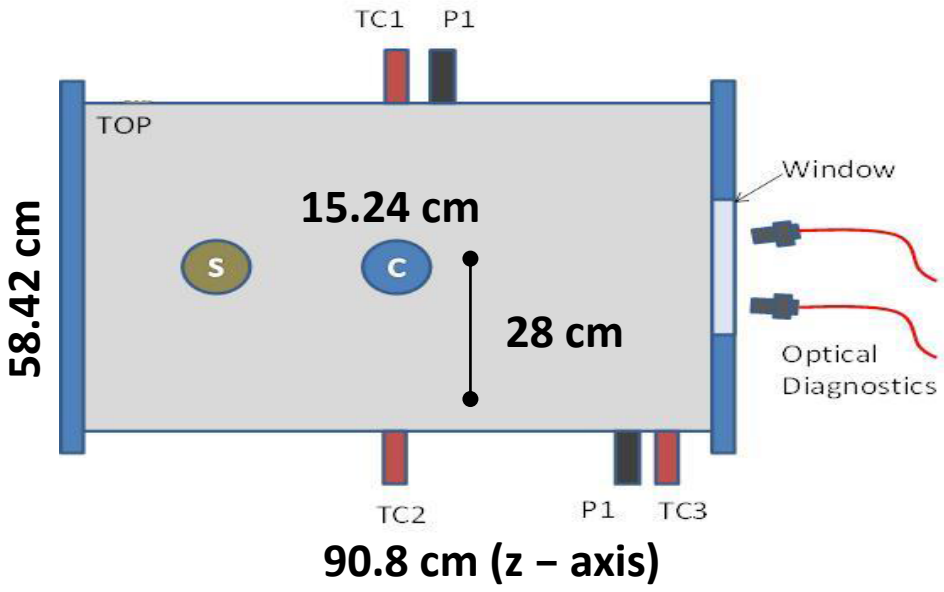

Figure 3-8. Diagram of the NSWC cylindrical chamber (bombproof). Adopted from Daniels et al. (2015).

Figure 3-9 shows the problem geometry used in the FLAG simulations. The axial symmetry of the problem was used to reduce the cylindrical chamber to a two-dimensional rectangular problem. The HE charge, LPBX, was modeled as PBX 9501 (95% HMX and 5% binder

by weight) with a Jones-Wilkins-Lee (JWL) equation of state (EOS). The use of PBX 9501 was suggested by Daniels et al. (2015), as it closely resembles the real high explosive used in the test, and the exact formulation of the charge is restricted. Only the top left quadrant of the chamber in Figure 3-8 was modeled and is shown in Figure 3-9 as a 45.5 cm x 30.5 cm rectangle with a computational mesh size of 0.1 cm and reflective boundary conditions at the wall interfaces.

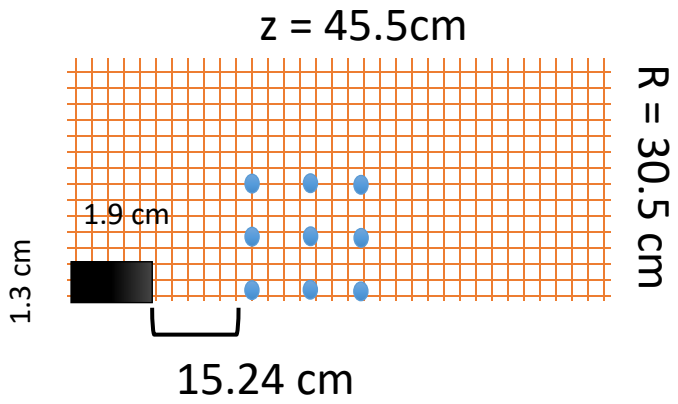

Figure 3-9. Schematic of the two-dimensional simulation geometry implemented in FLAG for the NSWC bombproof. Blue dots represented approximate locations of the tracer particles while the black rectangle approximated the charge position.

The empty chamber volume was modeled as air with a SESAME tabular equation of state (Crockett, 2018). A total of nine tracer particles were placed within the air mesh with approximate locations indicated in Figure 3-9 with exact locations provided in Table 3-3. Tracer particles ("tracers") are used to track system variables such as temperature, pressure, and velocity of a designated computational cell which can move freely with the local gas. Tracers were programmed to output the desired system variables every ten time-steps.

To model two and three-dimensional systems, the spatial domain was discretized with a multi-dimensional grid often referred to as a "mesh". Due to the turbulent nature of a typical detonation, simulation mesh elements can overlap, termed "mesh tangling", and causes the simulation to terminate (Danczyk and Suresh, 2012). Efforts can be made to "untangle" the

mesh by re-mapping the mesh (Burton, 2007), but cases of extreme turbulence cannot be overcome. We were able to run the simulations for approximately ~ 1 ms in simulation time before mesh tangling ended the simulation run.

As a first approximation, the tracer temperature is treated as the surface temperature of the TL particle and, therefore, the approach outlined in Section 3.6.2 can be used to obtain the radial temperature profile within the particle. Prior to the calculation of the radial temperature profile the time-temperature data of the tracers was interpolated. This is necessary as the outputs from the tracers occur every ten time-steps, but the steps themselves are not uniform in length because of the FLAG simulation's need to maintain computational stability. Interpolation was carried out in Python using the built in one-dimensional interpolation function *scipy.interpolate.interp1d*. Then, the resulting interpolated function was used to recalculate the temperature time profile of the tracer using uniform time steps of $\Delta t = \frac{dr^2}{4\,\alpha}$.

Table 3-3. Initial tracer positions in the air mesh.

	Tracer Number								
Position	**1**	**2**	**3**	**4**	**5**	**6**	**7**	**8**	**9**
Radial (cm)	0.05	10	20	0.05	10	20	0.05	10	20
Z-Axis (cm)	15.24	15.24	15.24	20.24	20.24	20.24	35.24	35.24	35.24

CHAPTER 4

THE VALIDITY AND ACCURACY OF THE INITIAL RISE METHOD

Independent of kinetic order, the IRM is a powerful analysis technique for determining the activation energy of a TL peak. Step-annealing allows the IRM to be used for TL curves with moderately overlapping TL peaks, but an in-depth investigation of the IRM and step-annealing approach for strongly overlapped peaks with noise has not been conducted. Novel TL materials for temperature sensing (Section 2.3.3) show a complex curve structure in their step-annealed datasets (Doull et al., 2014). Therefore, the objective of this phase of the work was to investigate the validity and accuracy of the IRM through analysis of realistically simulated TL curves with strongly overlapped TL peaks.

The IRM was used to analyze simulated step-annealed TL curves resulting from a variety of activation energy trapping center distributions (Table 3-1). Steps were taken to recreate a typical experimental dataset including the addition of noise to the step-annealed TL curves and conducting background subtraction prior to IRM analysis. Various aspects of the IRM were investigated, including the effect of noise, weighted versus unweighted LLS fitting, and the initial rise analysis region. Attempts to reconstruct the input trap distributions were conducted using the method purposed by Van den Eeckhout et al. (2013). Also, we present a new technique for scanning the initial rise region for possible contamination of overlapping TL peaks and for calculating activation energies.

4.1 Initial Investigations

4.1.1 Influence of the Linear Least Squares Method

Before dealing with realistic cases, we investigated the influence of the LLS fitting method (weighted *versus* unweighted) for two overlapping TL peaks associated with discrete *E*-distributions. The IRM was applied only to T_{max} corresponding to 5% of I_{max}. For the unweighted LLS fits, all data points were considered as having the same weight. For the weighted LLS fits, the reciprocal of the variance of each data point was used as the weight.

Figure 4-1 illustrates the IRM results. Figure 4-1a shows the E-T_{stop} plots for unweighted (black points) and weighted LLS fit (red points); horizontal lines indicate to the activation energies used in the simulations. The weighted fit leads to smaller fitting uncertainties and more clear plateau regions in the *E versus* T_{stop} graphs (Figure 4-1a), as compared to the unweighted results. As the low temperature TL peak is depleted, however, the weighted LLS fits produces a "dip" in *E* for T_{stop} in the transition region between the two TL peaks (blue box in Figure 4-1a). Similar underestimations in *E* were also observed in simulations by Kitis et al. (2017) which do not include noise in the TL data.

The resulting "Van den Eeckhout distributions" (Figure 4-1b) indicate the presence of two distinct trapping centers regardless of the LLS fit used, although the weighted LLS fit seems to slightly under-estimate the activation energies in comparison to the unweighted results. Nevertheless, the differences between the center of the recovered *E*-distributions and the input values are less than 2%.

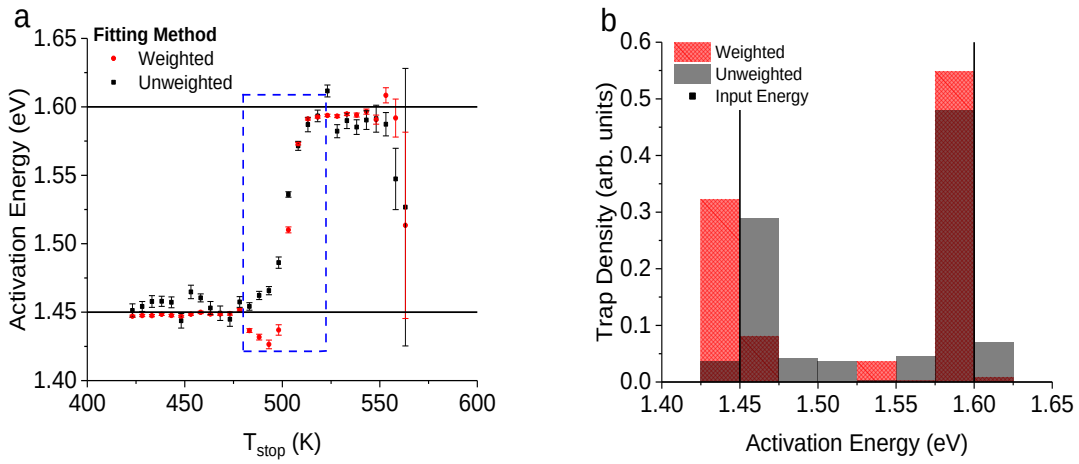

Figure 4-1. (a) IRM results for a TL curve consisting of two first-order TL peaks characterized by E = 1.45 and 1.6 eV with ratio n_{01}:n_{02} = 1:2 and s = 10^{14} s^{-1} as a function of T_{stop}, and (b) trap density recovered using the method by Van den Eeckhout et al. (2013).

Figure 4-2 shows the IRM results applied to step-annealed TL curves for a single Gaussian E-distribution. E-T_{stop} plots (Figure 4-2a), indicate (again) that the weighted LLS fit produces more consistent E values with lower uncertainty as compared to unweighted fitting.

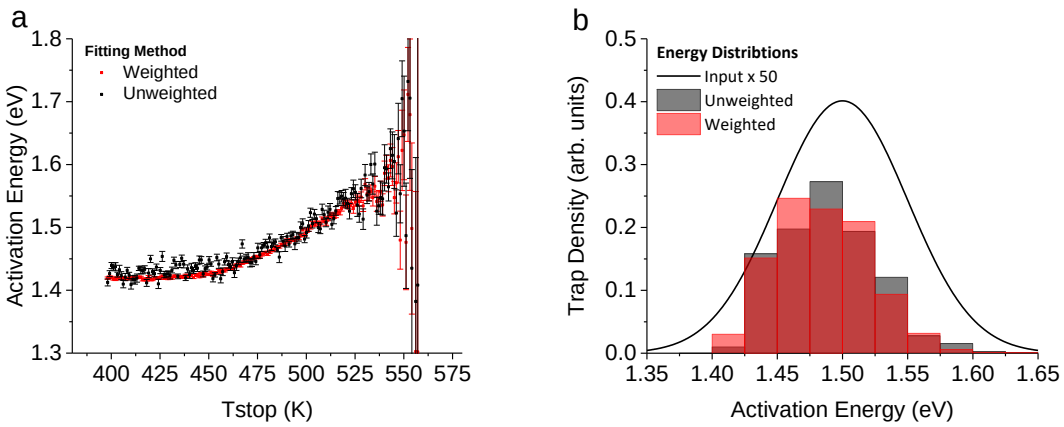

Figure 4-2. IRM results for a single TL peak from a Gaussian E-distribution characterized μ = 1.5 eV, FWHM = 0.12 and s = 10^{14} s^{-1}.

Figure 4-2b shows the corresponding "Van den Eeckhout distribution" of activation energies for this case. The weighted LLS fit results indicate a bias towards lower activation energies, as compared with the unweighted results and the simulation inputs (black trace).

While the consistency and reduced uncertainty obtained with the weighted fit for both cases studied are attractive, the weighted LLS fit consistently underestimated the activation energies. This is caused by the fact that high intensity points have reduced uncertainties (*i.e.* higher weights), therefore forcing a reduction in the slope of the ln(I) *versus* 1/*T* fit of the IRM.

4.1.2 Effect of Noise

To determine the effect of noise on the results, step-annealed TL curves were simulated for a single Gaussian *E*-distribution with Poisson noise. Figure 4-3a shows the normalized TL curves for the same T_{stop} with three different initial occupancies. By increasing the TL intensity, a clear reduction in the low temperature TL noise is observed.

The effect of increasing the Poisson noise by the factor α (see Section 3.5) was investigated for $n_0 = 10^8$ ($I_{max} \sim 10^6$ cps, 1 K/s). Figure 4-3b compares the cases of zero noise ($\alpha = 0$), Poisson noise ($\alpha = 1$) and three times Poisson noise ($\alpha = 3$) for the TL curves after the same T_{stop}. The horizontal lines in Figure 4-3b denote 5% of the maximum intensity and the noise limit ($3\sigma_{BG}$), corresponding to the IRM fitting region. By increasing α, we see an increase in noise within the initial rise fitting region.

Step-annealed curves were obtained for the cases presented in Figure 4-3 and analyzed using a fixed fitting region up to T_{max} corresponding to 5 % of I_{max}, with results presented in the form of E-T_{stop} and "trap density" distributions in Figure 4-4. With α constant, decreasing n_0 increases the fluctuations in the E-T_{stop} plot (Figure 4-4a), resulting in broader *E*-distributions and a decrease in the mean *E* values (Figure 4-4b).

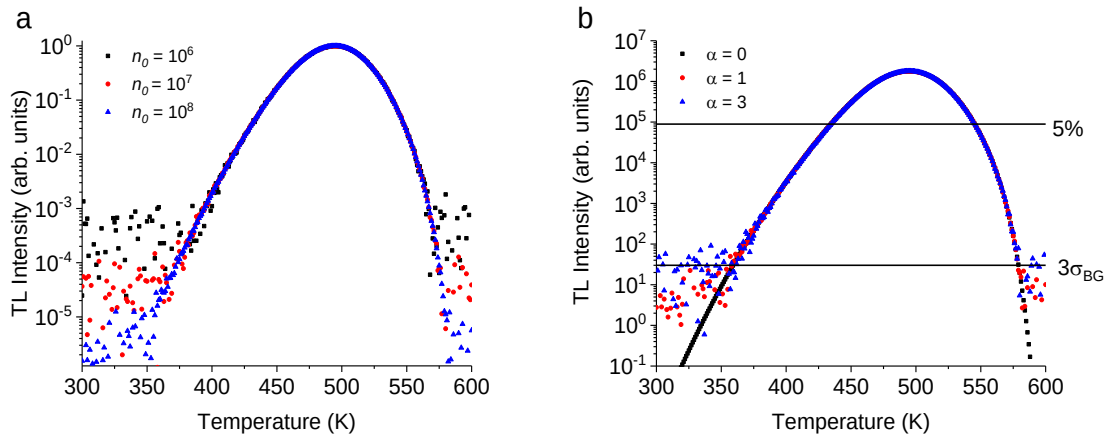

Figure 4-3. (a) Normalized background subtracted step-annealed (T_{stop} = 398 K) TL curves for three different initial occupancies and α = 1 (only Poisson noise); (b) background subtracted step-annealed (T_{stop} = 398 K) TL curves for three different noise levels.

In contrast, keeping n_0 constant and increasing α leads to a small increase in the fluctuations of *E* (Figure 4-4c). The trap density distributions are essentially identical (Figure 4-4d).

These results suggest that the initial occupancy, i.e. the maximum TL intensity, has a larger effect on the IRM result than the degree of noise α. This is probably because varying α does not change the relative intensity of the TL curves with respect to the constant background signal, whereas decreasing the TL signal means that a larger portion of the TL peak "sinks" below the constant background signal, forcing the use of a portion of the TL curve that does not satisfy the initial rise condition.

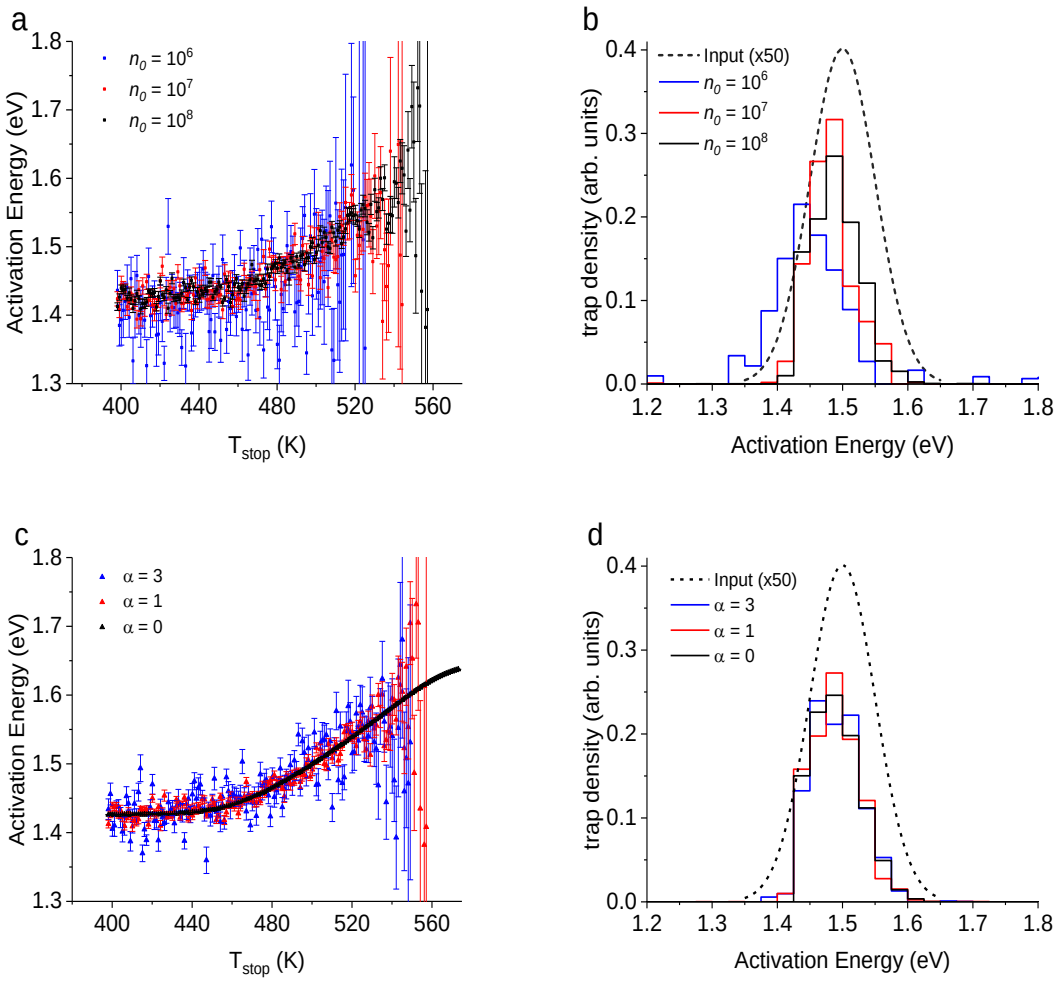

Figure 4-4. *E*-T_{stop} from IRM analysis of (a) fixed α varied n_0 and the resulting (b) "Van den Eeckhout distributions" with corresponding plots for fixed n_0 (c) *E*-T_{stop} plots and (d) "Van den Eeckhout distributions".

The results above demonstrate that the TL intensity has a stronger influence in the results than the noise parameter α. Because of that, we only need to consider variations in initial occupancy when dicussing the effect of noise on the results. Therefore, we proceeded using a fixed noise parameter of $\alpha = 1$ (Poisson noise) and initial occupancies of $n_0 = 10^8$ (I_{max}~10^6 counts per second).

4.2 IRM Accuracy for Single TL Peaks

Figure 4-5 shows the step-annealed curves of the three single TL peaks presented in Table 3-1 (simulation sets D1, G1 and U1). Simulations for the discrete *E*-distributions used a 5 K T_{stop} step size; whereas for the Gaussian and uniform *E*-distributions, we used a 1 K T_{stop} step size for better resolution. The data in Figure 4-5b and Figure 4-5c exemplifies the TL peak symmetry and temperature shift with pre-heating, which again can be interpreted erroneously as non-first-order kinetics. The IRM results are presented in Figure 4-6 and discussed in the following subsections.

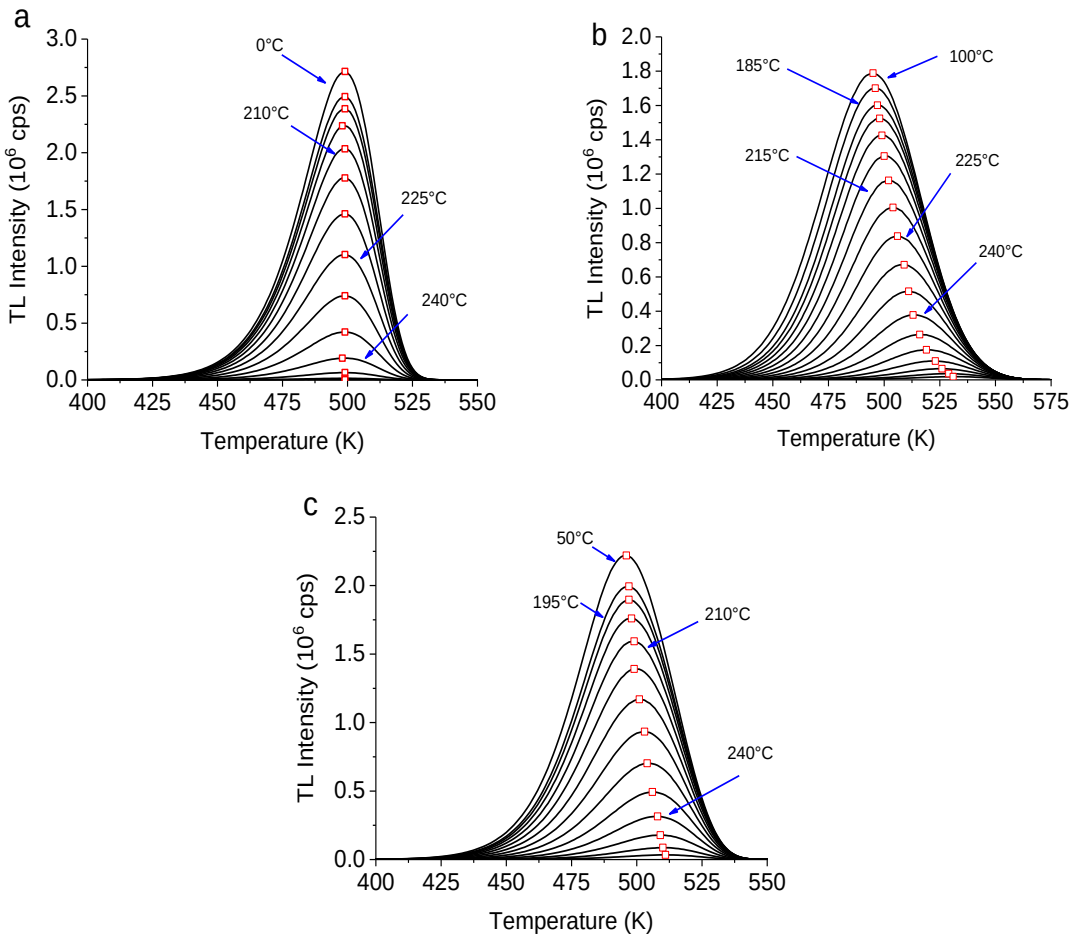

Figure 4-5. Representative step-annealed TL curves obtained from a single (a) discrete (D-1), (b) Gaussian (G1), and (c) uniform (U1) *E*-distributions. Peak maxima are indicated by red data points. Distribution details are found in Table 3-2.

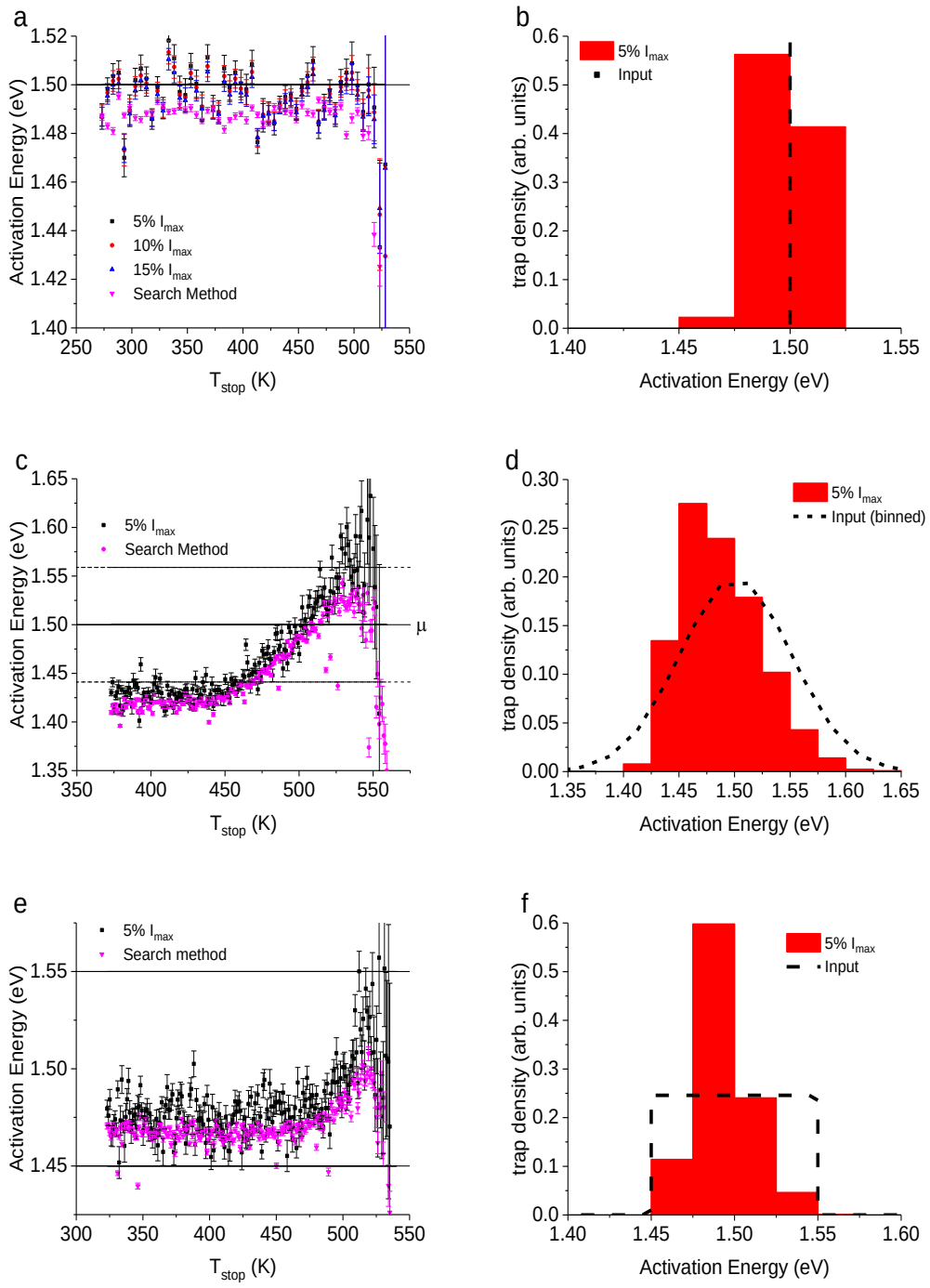

Figure 4-6. IRM results for: (a) and (b) single discrete *E*-distribution with *E* = 1.5 eV (set D1 in Table 3-2); (c) and (d) single TL peak associated with a Gaussian distribution (set G1 in Table 3-2); (e) and (f) single TL peak associated with a uniform distribution (set U1 in Table 3-2). The graphs on the left are the *E*-T_{stop} plots, and the graphs on the right are the trap density graphs. Analyses were performed using unweighted LLS fittings.

4.2.1 Single Discrete Activation Energy Distribution

The E-T_{stop} plots for a single discrete E-distribution (Figure 4-6a) indicate a single E value. Unweighted results (Figure 4-6a) show similar energies regardless of the fitted region. Whereas, weighted results showed a decrease in E with increase in the fitted region of up to 15 % (results not shown). For high T_{stop} values, E becomes underestimated due to the decrease in TL intensity and in the signal-to-background ratio, as discussed in Section 4.1.2. The E-T_{stop} plots for the search method are also slightly underestimated in comparison to the fixed region method.

The trap density distributions (Figure 4-6b) indicate a narrow E-distribution using unweighted LLS fitting. Weighted LLS fitting leads also to a small underestimation of E (results no shown), as discussed previously.

From now on, we will consider only IRM results obtained using a fixed fitting method (with T_{max} corresponding to 5% of I_{max}) and the search method (Section 3.4.2). The results for 10% and 15% of I_{max} do not provide new insights beyond what has already been discussed.

4.2.2 Single Gaussian Activation Energy Distribution

Figure 4-6b shows the E-T_{stop} plot for the single Gaussian E-distribution. The solid horizontal line indicates the mean E value μ, and the dashed lines indicate the values corresponding to one half the distribution's FWHM from the mean E value. The graph shows an initial constant E value below the lower FWHM line for low T_{stop} values for which negligible curve depletion has occurred. Once depletion begins (450 K - 475 K), E values steadily increase with increasing with T_{stop} to the upper FWHM line above μ. At high T_{stop} values (>575 K), the TL peak intensity decreases, with an increase in fitting uncertainty and decrease in E due to the lower signal-to-background ratio.

The trap density distribution (Figure 4-6c) is consistent with the input distribution (in grey), but with a tendency to underestimate *E*. The maximum of the distribution was between 1.45 eV – 1.50 eV, in comparison to input value μ = 1.5 eV.

4.2.3 Single Uniform Activation Energy Distribution

Figure 4-6e shows the E-T_{stop} plot for the single TL peak resulting from a uniform *E*-distribution, the horizontal lines representing the limit *E* values of the distribution. *E* remains constant with increasing T_{stop} until ~ 475 K, increasing for higher T_{stop} values. The *E* values are distributed over a narrower range than the uniform *E*-distribution, indicated by the horizontal lines.

The trap density distribution (Figure 4-6f) fails to recover the input *E*-distribution for both the unweighted (Figure 4-6f) and weighted (results not shown) LLS fittings, resulting in *E*-distributions peaked at ~1.475 – 1.5 eV. The mean *E* value slightly underestimates the center of the *E*-distribution.

4.3 IRM Accuracy for Strongly Overlapped TL Peaks

Figure 4-7 shows the step-annealed curves of the *E*-distributions D2, G2 and U2 (Table 3-1). The blue and red lines Figure 4-7a represent the individual component TL peaks, 1.05 eV and 1.8 eV respectively. Red data points in Figure 4-7 indicate the lowest peak maximum as determined by the automated IRM. Curves corresponding to T_{stop} temperatures 239 °C, in Figure 4-7b and 220 °C in Figure 4-7c are characteristic cases where a low temperature peak presents as a shoulder in front of the dominate TL peak. All simulations were performed using a 1 K T_{stop} step-size. The IRM results are presented in Figure 4-8 and discussed in the following subsections.

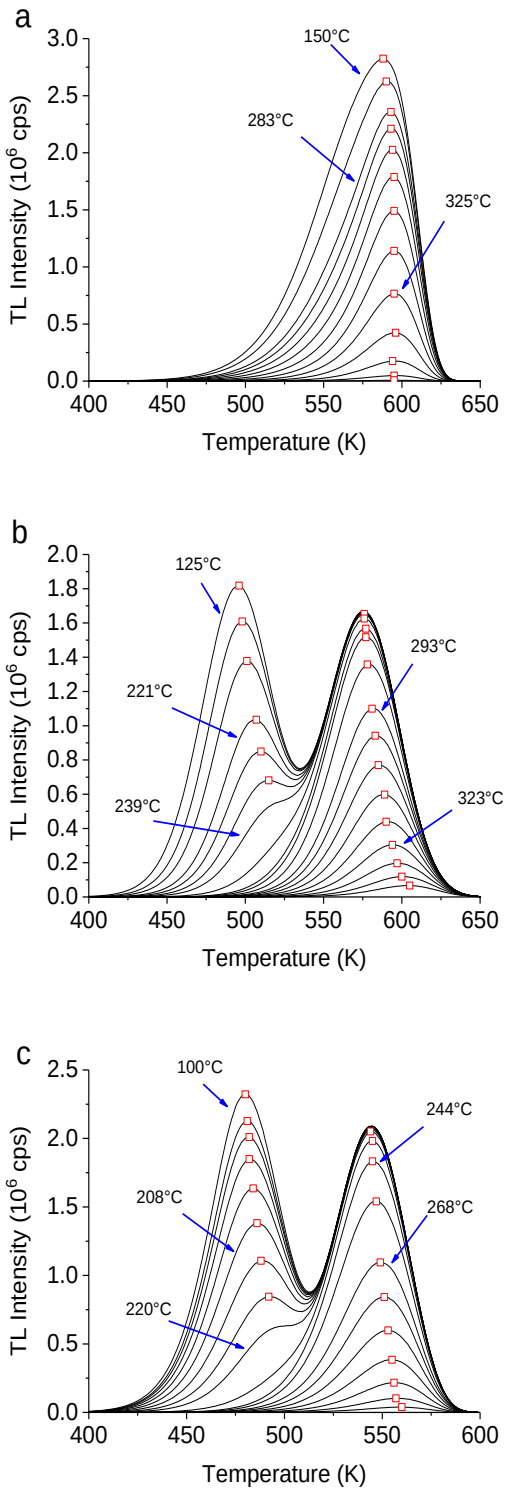

Figure 4-7. Representative step-annealed TL curves associated with: (a) discrete (D2), (b) Gaussian (G2) and (c) uniform (U2) *E*-distributions. Peak maximums are indicated by red data points. Distribution parameters are found in Table 3-2.

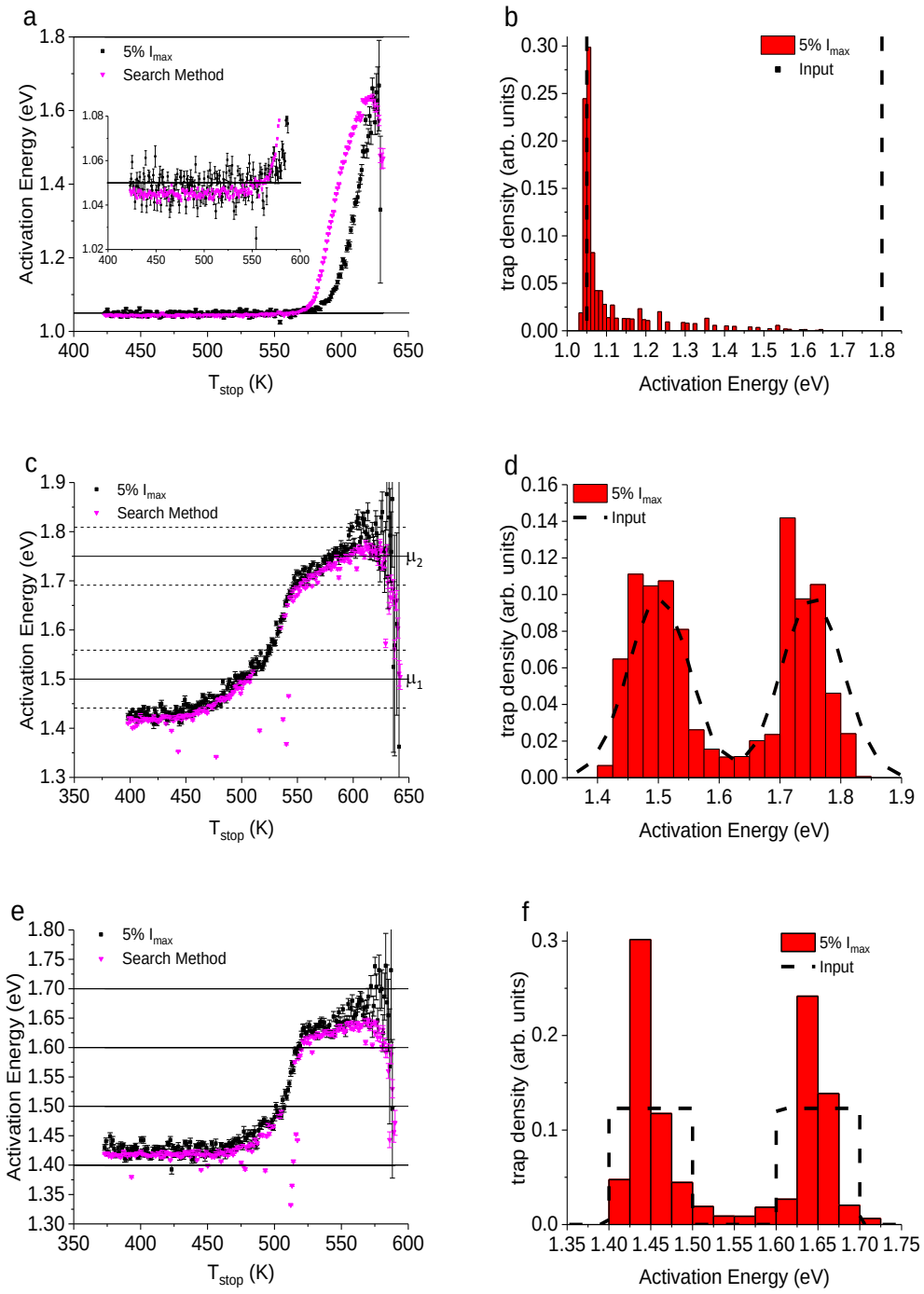

Figure 4-8. IRM results for two strongly overlapping TL peaks associated with: (a) and (b) discrete *E*-distributions (set D2 in Table 3-1); (c) and (d) Gaussian *E*-distributions (set G2 in Table 3-1); and (e) and (f) uniform *E*-distributions (set U2 in Table 3-1). *E*-T_{stop} plots are shown for (a) unweighted and (b) unweighted fits. The graphs on the left are the *E*-T_{stop} plots, and the graphs on the right are the "Van den Eeckhout distributions". Analyses were performed using unweighted LLS fittings.

4.3.1 Two Discrete Activation Energy Distributions

Figure 4-8 presents the IRM results for two overlapped TL peaks associated with discrete *E*-distributions. Despite the two peaks being separated by ~50 K (see Figure 4-7a), the parameters were chosen to produce two highly-overlapped TL peaks, where the low temperature peak is present even after high T_{stop} temperatures.

The high temperature TL peak did not affect the initial rise of the lower temperature peak, despite the high degree overlap. Both the unweighted (Figure 4-8b) and weighted results (not shown) show a plateau in the E-T_{stop} plot, with E rising quickly for T_{stop} > 575 K. As was the case with the single peak associated with discrete distribution, the unweighted results (Figure 4-8b) are distributed about the input energy producing a better estimate for the input energy as compared to the weighted results, which underestimate the input E_1 = 1.05 eV.

E never achieves the value of the second peak (E_2 = 1.8 eV). This is due to the strong peak overlap, as well as the low signal-to-background ratio once the 1.05 eV peak is fully depleted, which leads to an underestimation of E.

These observations are also substantiated by the trap density distribution in Figure 4-8b. A narrow distribution is seen around the input value for the first TL peak (E_1 = 1.05 eV), but there is no indication of a second distribution at 1.8 eV, except for the long tail toward high energy of the distribution centered at 1.05 eV.

Figure 4-9 shows the histogram of E values obtained by the search method (unweighted fit) for two T_{stop} values within the rising region (>575 K) of the E-T_{stop} plot (Figure 4-8a). They both show the presence of two or more activation energies, indicating that any IRM results obtained from the initial rise region of these curves are not typical of a single curve and, therefore, are not reliable. This is the only indication that the results in Figure 4-8a and b require further investigations.

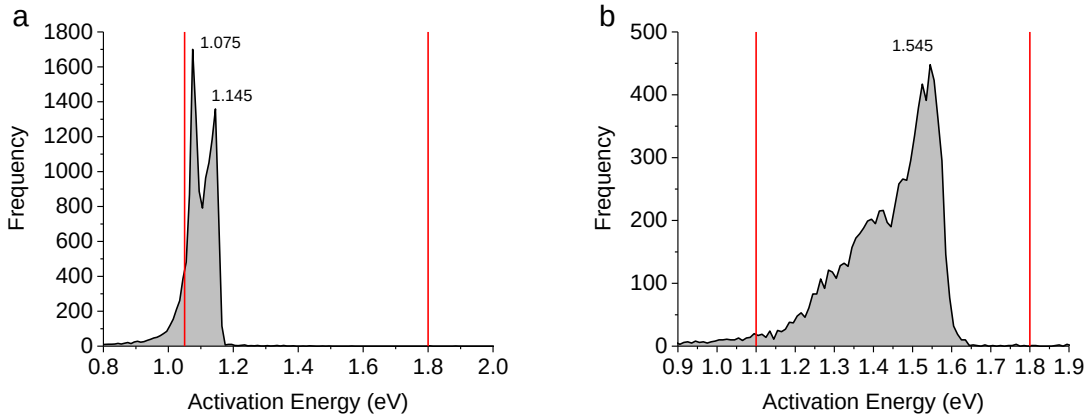

Figure 4-9. Histogram of *E* values during the search method for: (a) T_{stop} = 584 K and (b) T_{stop} = 610 K. Red vertical lines indicate simulation input energies.

4.3.2 Two Gaussian Activation Energy Distributions

The E-T_{stop} plots for the Gaussian E-distributions are more complex than in the previous cases (Figure 4-8b). E is initially constant, but it starts to increase with T_{stop}, as observed previously for a single Gaussian (see Figure 4-6b). The trend becomes increasingly steeper until T_{stop} ~550 K, at which point a transition in the E-T_{stop} plot is seen, indicating that the results are related to a second TL peak. Results for the search method are unreliable for T_{stop} ~ 515 – 550 K, due to the low signal-to-background ratio.

The recovered trap density distributions (Figure 4-8d) show good agreement with the Gaussian input E-distributions, but neither LLS fitting methods (unweighted and weighted) were able to fully resolve the low end (1.3 – 1.4 eV) and high end (1.85 – 1.9 eV) of the input E-distribution. Figure 4-8d, however, shows the unweighted fitting approach accurately resolved the overlapping region.

The E-histogram for step-annealed curves corresponding to T_{stop} in the 508 K to 540 K range are similar to that presented in Figure 3-3b and, therefore, are not repeated. This is a transition region; wherein, the first TL peak is no longer identifiable as a distinguishable peak, appearing as a low temperature “shoulder” of the high temperature peak. The E-histogram

results for the transition region show two peaks as in Figure 3-3b, indicating the presence of either two distinct peaks or two distributions. The peaks from the *E*-histogram for the transition region of the two Gaussian activation energy distribution are not intended to obtain the mean values of the distributions as they strongly underestimate the mean input *E* values by ~0.3 eV or more as was found for the discrete case in Figure 4-9a. The *E*-histograms provide a diagnostic tool to identify the presence of multiple discrete peaks or distributions contributing to the initial rise region of a given curve, thus allowing for discrimination of results with a high degree of TL peak overlap where step-annealing has not fully removed the low temperature TL peaks.

4.3.3 Two Uniform Activation Energy Distributions

The E-T_{stop} plot for the uniform *E*-distributions (Figure 4-8e) shows that the calculated *E* values fall within the limits of the input *E*-distributions, except for T_{stop} in the 500 – 520 K range, where we observe the transition between the two TL peaks. Unweighted LLS fitting results were again more accurate than weighted fitting results (not shown).

The E-T_{stop} plots span a large portion of the input *E*-distributions observed in the trap density distributions (Figure 4-8f). Although *E* values are found over the input range, the shape of the trap density distribution is not uniform, appearing more characteristic of multiple peaks associated with discrete or Gaussian *E*-distributions.

As in the previous Section, we calculated the histograms of *E* values for the TL curves in the transition region, T_{stop} ~ 500 – 520 K, of the overlapping TL peaks. The results are similar to those observed for the Gaussian distribution, again indicating the presence of two peaks or distributions in the initial rise region. The peaks in the *E*-histograms were at *E* values ~0.2 eV lower than the centers of the uniform distributions.

4.4 Discussion

The data presented here attempts to provide a more comprehensive understanding of the advantages and limitations of the IRM as applied to step-annealed curves. Whereas much has been discussed on the IRM, there is much less focus on the results obtained from experimental curves and on the effect of noise on step-annealed curves. While the addition of Poisson noise increased the variability in IRM activation energies and the fitting errors, it did not significantly affect the reliably of the traditional 5% method unless applied to TL curves with low intensity (high noise). However, we did find the addition of noise does place some limitations on the IRM when dealing with highly overlapped TL peaks.

We conclude that unweighted LLS fitting leads to smaller underestimation of the E values than weighted LLS. Weighted LLS fitting gives more importance to parts of the TL curve with higher intensity, for which the deviation from the initial rise condition $n \cong n_0$ increases, leading to stronger underestimation of E.

As the TL intensity decreases, there is an increased underestimation of E due to the reduced signal-to-background ratio. This leads to an increased discrepancy between the trap density distributions and the input E-distributions (Figure 4-4). This finding is important for TL curves characterized by multiple peaks of varying intensities, suggesting that one should try to use variable doses when attempting to obtain IRM results for individual peaks, always using a dose that optimizes the intensity for the peak of interest. Without such optimization, the step-annealing results in both removal of the shallow peaks from the initial rise region and a decrease in intensity of the deeper peaks. The low signal-to-background ratio leads then to an underestimation of E.

We observed this effect in peaks associated with the high-energy tail of the Gaussian and uniform *E*-distributions, which are highly overlapped and found to have low intensity when isolated by step-annealing.

Trap density distributions were found to be reliable for resolving the *E*-distribution for cases where large changes in the TL curve area were observed with step-annealing temperatures. It cannot, however, clearly resolve the lower and higher end of the distributions, being limited to ~FHWM of the distribution. Also, it slightly underestimates the center of the *E*-distributions. This is particularly problematic for uniform *E*-distributions.

While the search method proved to be less reliable than the traditional 5% T_{max} approach, it has been shown that the *E*-histograms obtained using the search method can help identify the presence of multiple distributions, although the peaks observed strongly underestimate the center of the *E*-distributions.

One should note that there are other factors that have not been considered in this study. For example, random fluctuations in the heating rate are assumed to be treated using the factor α, here, but systematic errors have not been considered. One must assume that the user will take every feasible step to minimize that, such as using slow heating rates, small amounts of material, and possibly some heat paste to improve the thermal contact during the TL measurements.

CHAPTER 5

DECONVOLUTION OF STEP-ANNEALED TL CURVES IN E AND S PARAMETER SPACE

The objective of this work is to evaluate the feasibility of finding the activation energy and frequency factor of first-order components of a TL curve using two-dimensional deconvolution of datasets of simulated, realistic TL curves obtained by step-annealing or varying heating rates.

TL curves were simulated from various combinations of the multinormal trapping center distributions in activation energy and Log frequency factor (Table 3-2). Two different dataset types were simulated (Section 3.5) to constrain the two-dimensional deconvolution method: "θ-dataset" (step-annealing) and "β-dataset" (varied heating rates). Reconstruction of the input parameters distributions from the constraining datasets were obtained using the non-negative least squares (NNLS) algorithm.

We investigated the effects of noise to see the limitations of this method to experimental data and to compare the results with prior simulation attempts by Whitley et al. (2002) for simulated, noiseless, TSC curves. Also, we investigated the effect of different regularization methods, system uncertainties, and the constraining dataset size on the results.

5.1 E-s Deconvolution Based on Step-annealed TL curves

Prior to applying the deconvolution procedure to the simulated datasets, it is important to demonstrate the method, as well as to understand the effect choices of regularization, resolution (kernel properties), and signal-to-noise ratio (S/N) on the results. We begin by applying the deconvolution procedure to the simple case of two discrete trapping centers with

E_1 = 1.2 eV, $\log s_1$= 14, E_2 = 1.4 eV, and $\log s_2$ = 12. Equation 2-39 was used to obtain the depletion factor values, $\phi(\theta, \tau)$, for each trapping center for a hold time of 300 s (Figure 5-1a). Then, Equation 3-21 was used to obtain the TL curves for the two peak system for each preheating condition and normalized to the unheated case, $\phi(273\ K, 300s)$, to determine the change in total luminescence (area under TL curve, blue trace in Figure 5-1a). A total of seven hold temperatures of interest were selected (open points in Figure 5-1a) and used to simulate the experimental (without noise) curves (Figure 5-1b).

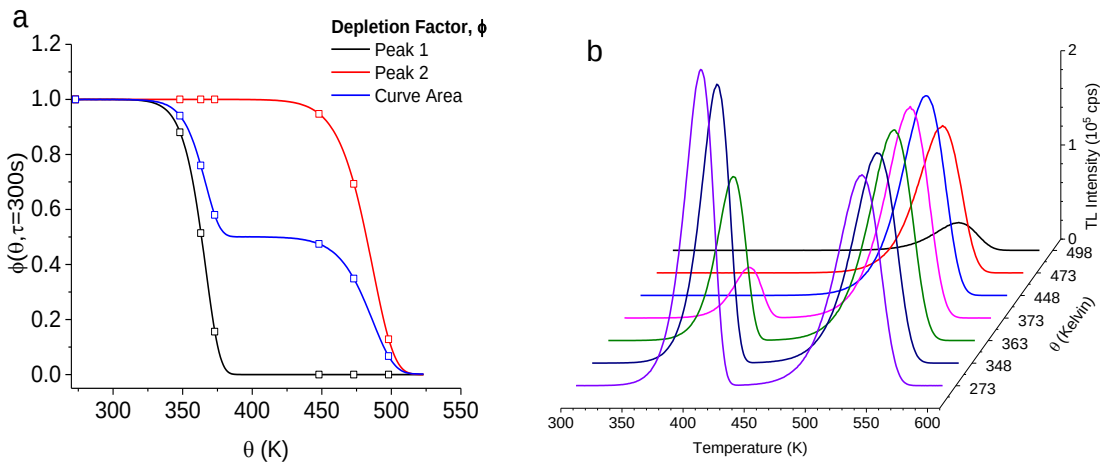

Figure 5-1. (a) Depletion curves were obtained for each trapping center (black and red traces) as well curve area depletion (blue trace), as a function of hold temperature. (b) Background subtracted analysis curves.

Following the calculation of the dataset vector, y, and the corresponding matrix of weights, V, the kernel, K, is obtained using activation energies between 1.0 eV and 1.6 eV, and frequency factors between log s = 10 – 16 (with s in s^{-1}), with spacings of ΔE = 0.025 eV and Δlog s = 0.25, visualized as black points in Figure 5-2a. Combinations of trap parameters that result in a TL peak maximum outside of the input readout temperature (blue patch in Figure 5-2a) are excluded from the kernel to expedite computation time. The computation of the NNLS solution provides the weights $g(E, s)$ (red in Figure 5-2a), which correspond to the red component TL peaks in Figure 5-2b.

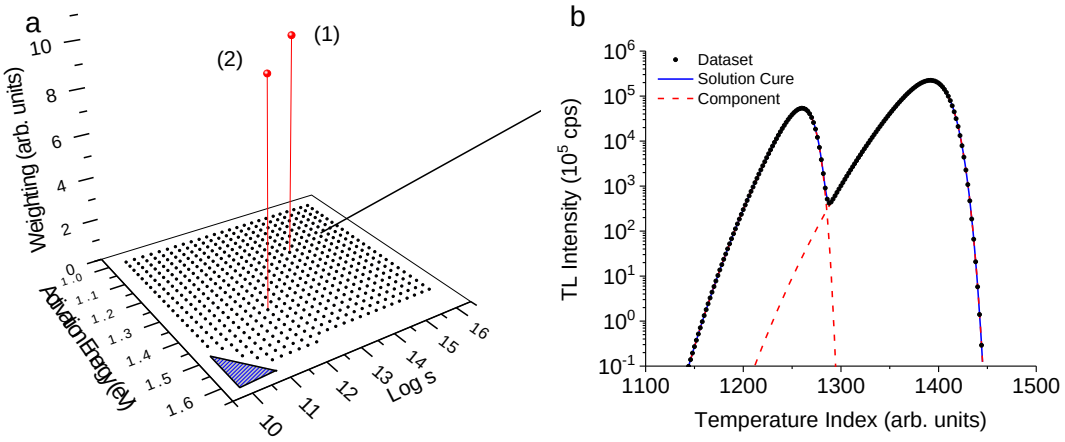

Figure 5-2. (a) Visualization of the planning matrix (black data points) and NNLS solution (red data points). The numbers indicate the trap parameters for the first and second TL peaks. The blue patch reflects simulated *E-log s* combinations that produce TL peaks outside the temperature axis. (b) Comparison between the NNLS solution and the dataset.

The results (Figure 5-2a) shown two main peaks at (1) E = 1.2 eV, $s = 10^{14}$ s^{-1} and (2) E = 1.4 eV, $s = 10^{12}$ s^{-1}, which agrees with simulation input values. This is, of course, just for illustration purposes, because for two discrete first-order TL peaks, curve fitting is obviously preferable.

To demonstrate that TL curves obtained after various pre-heatings serve as a suitable dataset to recover the *E-s* distributions, we simulated the case of a 4 trap *E-s* distributions, without noise. These conditions are intentionally similar to those used by Whitley et al. (2002) to demonstrate the equivalency of *E-s* deconvolution proposed here to those based on TL curves obtained using different heating rates. The input distribution (Figure 5-3a) was simulated for hold temperatures of 273, 355, 375, 405, 420, 440, and 490 K for a hold time of 300 s. (The same dataset with noise added is shown in Figure 5-11a).

Figure 5-3 compares the results with the input distribution for the 4-peak system. The number of peaks and the centers of each distribution (Figure 5-3b) agree with the input distribution (Figure 5-3a), but the deconvolution fails to reproduce the circular symmetry of the input contours. This comes as a result of the differences in bin sizes ΔE and $\Delta \log s$ used for the

deconvolution (one order of magnitude larger than those used for the input distributions, for the simulation of the TL peaks).

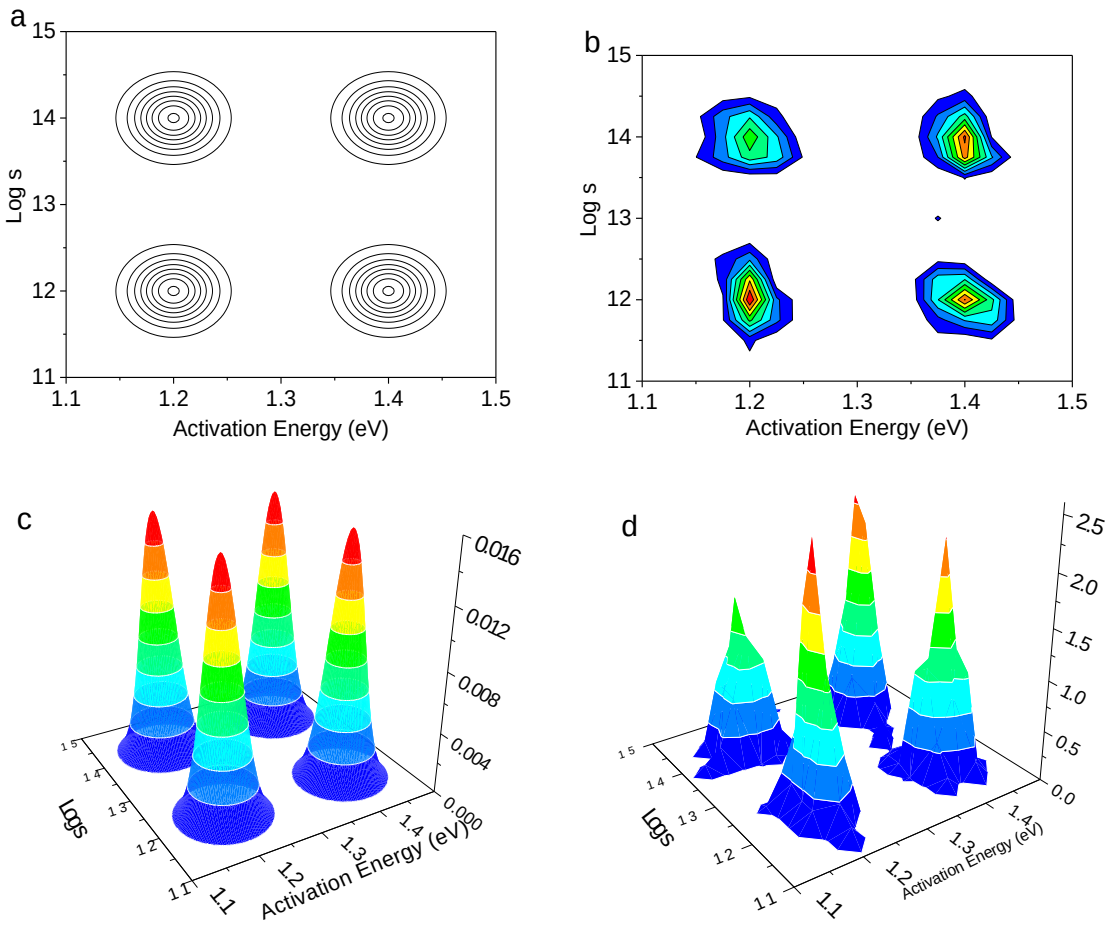

Figure 5-3.(a) and (c) Input distributions and (b) and (d) deconvolution results for a 4-trap system. Contours use a maximum of 8 levels with a minimum threshold of 10% the max value.

5.2 Influence of Deconvolution Procedure and Noise

Efforts to understand the effects of various regularization techniques and Poisson noise were undertaken prior to a full analysis of more complicated curve structures. Within this section, we consider simulated datasets obtained from the input parameters from the combination of the B and C peaks in Table 3-2. Figure 5-4 shows the input distributions and corresponding annealed TL curves without noise. This case was chosen because of the minimal overlap between the two TL peaks. TL curves were simulated for 7 hold temperatures between

273 K and 498 K for a duration of 300 s. Simulations were done both with and without noise for various initial trap occupancies ($\propto I(T)$), to study how the addition of various signal-to-noise ratios (S/N) effect the deconvolution results. Noise was added to TL curves as in Section 3.5.3. Unless otherwise stated, all simulations were carried out using initial occupancies of 10^7 per peak resulting in TL intensities of ~10^5 counts per second for 1 K/s heating rate.

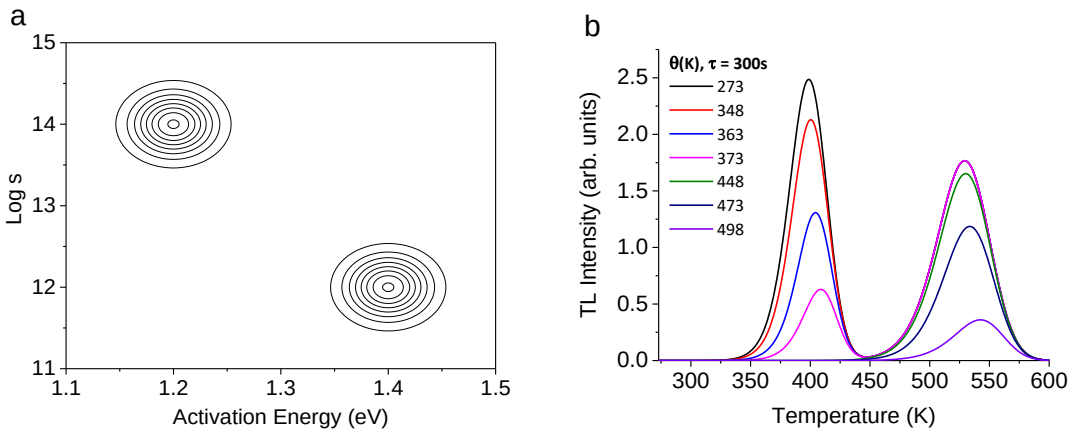

Figure 5-4. (a) Input distribution and (b) simulated annealed curves used to constrain the two-dimensional deconvolution. Curves were obtained for a range of temperatures, θ, for a hold time, τ, of 300 s.

5.2.1 Regularization Method

The two-dimensional deconvolution method was applied to the noiseless, simulated dataset presented in Figure 5-4b using the LLS method, as well as the NNLS, and the Tikhonov with NNLS regularization techniques. The results of the deconvolutions using these different methods are presented in Figure 5-5.

The results for the LLS method in Figure 5-5a are characterized by both positive and negative trap occupancies. As negative trap occupancies are non-physical, we must enforce the nonnegative constraints used for the NNLS and Tikhonov methods. Both the NNLS (Figure 5-5b) and the Tikhonov (Figure 5-5c) regularization methods are characterized by a two-peak structure similar to the input distribution in Figure 5-4a. The Tikhonov results are superior to the

NNLS results, as indicated by the symmetrical structure of the distribution as well as the approximately equal occupancies between the two peaks.

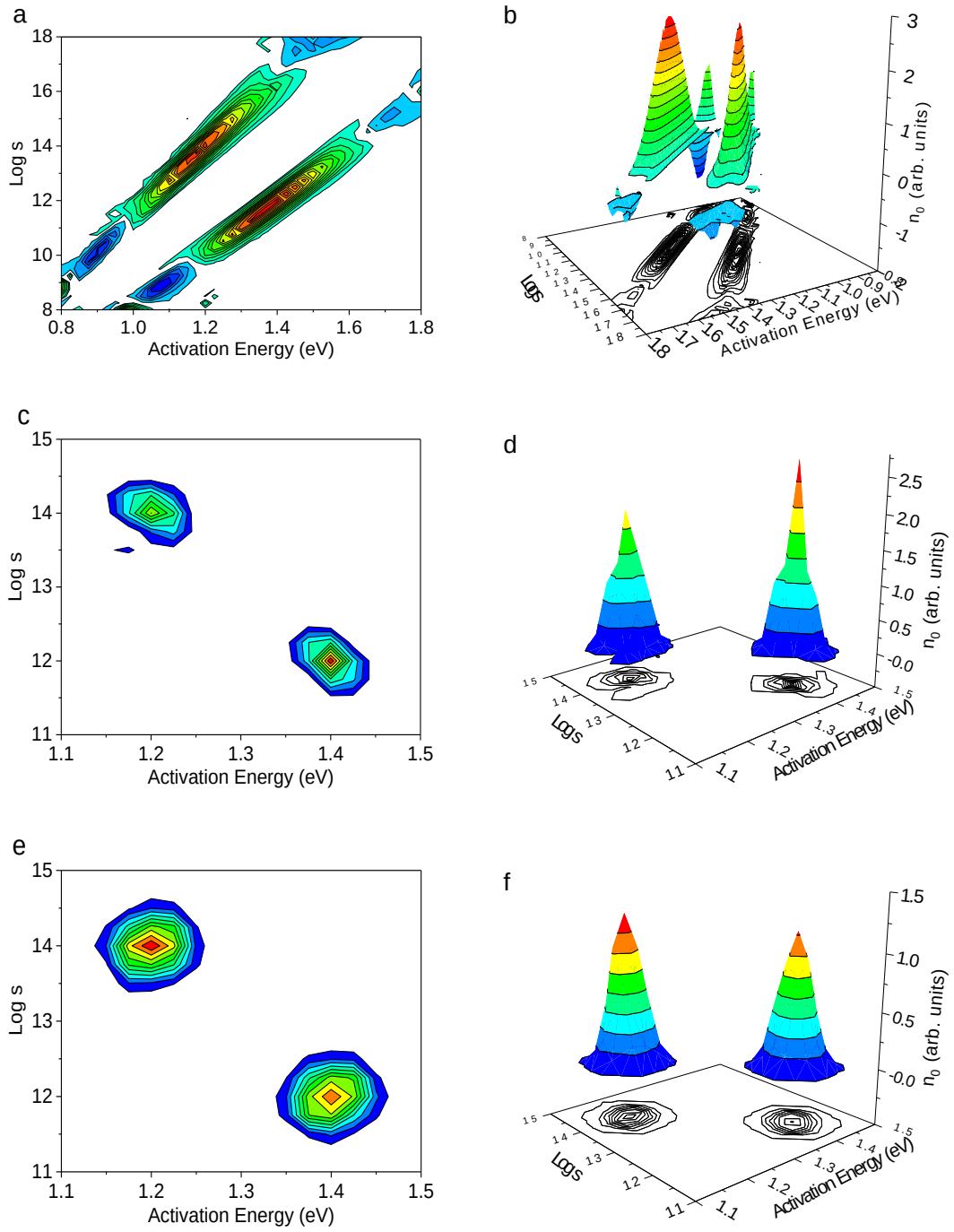

Figure 5-5. Contour plots of two-dimensional deconvolution obtained using (a) LLS method, (b) NNLS method and (c) Tikhonov method with NNLS. All deconvolutions were performed using a kernel resolution of 0.025 eV and log *s* = 0.25 over a range of 0.8-1.8 eV and log *s* = 8-18, with *s* in s^{-1}. Contour values in (b) and (c) are limited to values above 10% max occupancy, with the contour values in (a) spanning both positive and negative values.

5.2.2 Effect of Noise on the Regularization Method

Figure 5-6 shows the deconvolution results for curves simulated from the input parameters in Figure 5-4a using the NNLS method and Tikhonov regularization techniques in the presence of noise. Fitted curves for the NNLS method and Tikhonov technique are presented in Figure 5-6a-c along with the component TL peaks with the respective models in Figure 5-6c-d. A comparison of the results in Figure 5-6c-d with the noiseless data in Figure 5-5b-c shows a failure of both methods to accurately replicate the input distribution (Figure 5-4a) when there is noise in the data, despite accurately reproducing the dataset. The NNLS method results, in Figure 5-6c, show a grouping of trap parameters centered about the input mean parameter values, but multiple low intensity peaks are present within each grouping. The Tikhonov technique results, in Figure 5-6d, are similar to that of the NNLS with the exception of a low intensity, long-banded result for peak with E = 1.4 (eV) and $\log s$ = 12. The type of "diagonal bands" seen in Figure 5-6d appear because these combinations of E-s values lead to the same peak position (just different peak widths). The banded solution was observed for multiple datasets analyzed using the Tikhonov technique and, therefore, we proceed using only the NNLS technique.

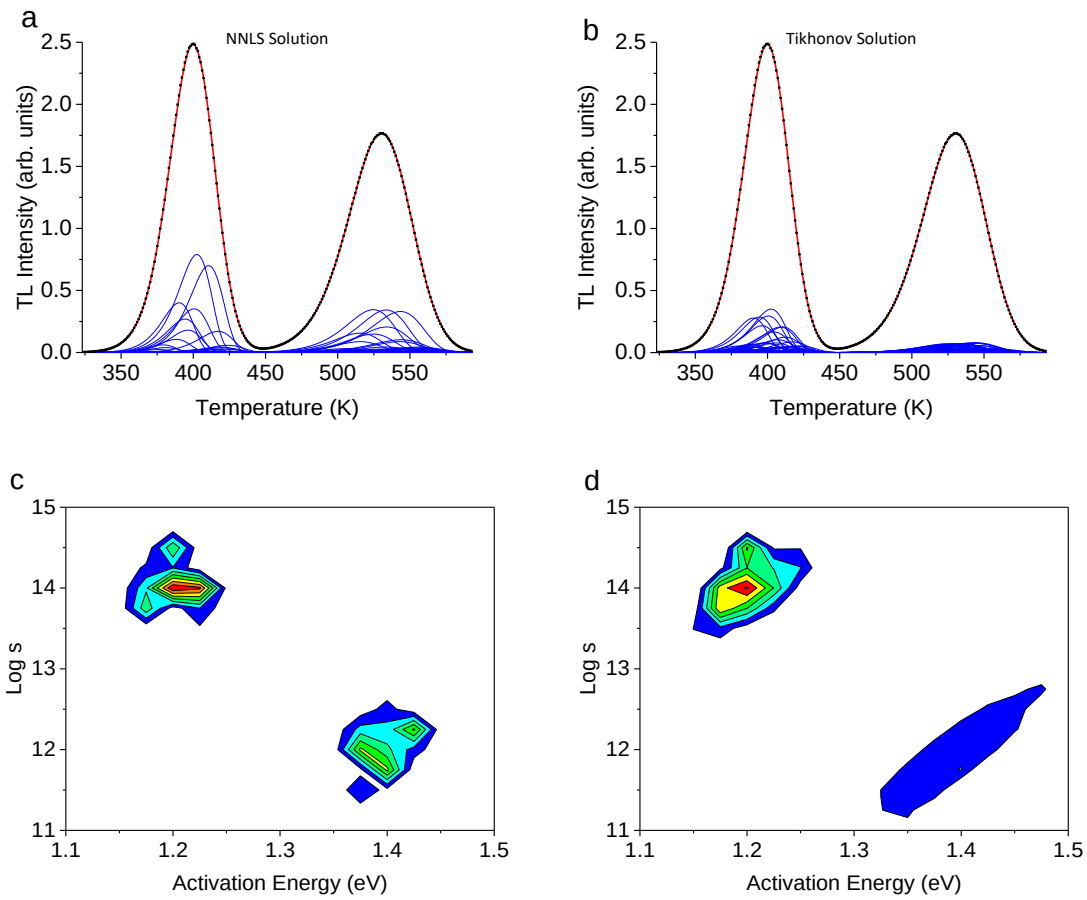

Figure 5-6. Two-dimensional deconvolution results for the input distribution in Figure 5-4a, obtained using the (a) NNLS method and the (b) Tikhonov method using a kernel resolution of 0.025 eV and 0.25 log *s* over a range of *E* = 0.8-1.8 eV and log *s* = 8-18. Only contours values above the 10% max value are shown.

5.2.3 Statistical Variability

To study the effect of the statistical variability of the noise on the results, the input distribution from Figure 5-4a was used to simulate three different datasets with random noise, all with the same input occupancies. Figure 5-7 shows the results of the two-dimensional deconvolution analysis using the NNLS method applied to each of the three datasets. All results in Figure 5-7 display both the r-squared metric,

$$R^2 = 1 - \frac{\sum(y_i - f_i)^2}{\sum(y_i - \bar{y})^2}, \qquad \textbf{5-1}$$

and the reduced chi-squared fitting metric (Press et al., 1993),

$$\chi_r^2 = \frac{1}{n-m}\sum_i \frac{\left(y_i - f_i\right)^2}{\sigma_i^2}, \qquad \textbf{5-2}$$

where *y* is the dataset, $\bar{y}$ is the average value of the dataset, f is the model obtained from the deconvolution, *n* is the number of data points in the summation, m is the number of free parameters and σ is the uncertainty of the dataset. Both metrics show consistently good fits across all three datasets. The deconvolution results show a similar distribution centered around the mean input parameters from Figure 5-4a, but significant variations between each distribution are noticeable, such as the peak located at *E* = 1.45 eV and $\log s$ = 13 in Figure 5-7b. These variations are due to the deconvolution attempting to fit the small changes in each TL curve resulting from the Poisson noise. To account for the random variations between individual datasets, all future results are obtained as an arithmetic average of the results of three datasets.

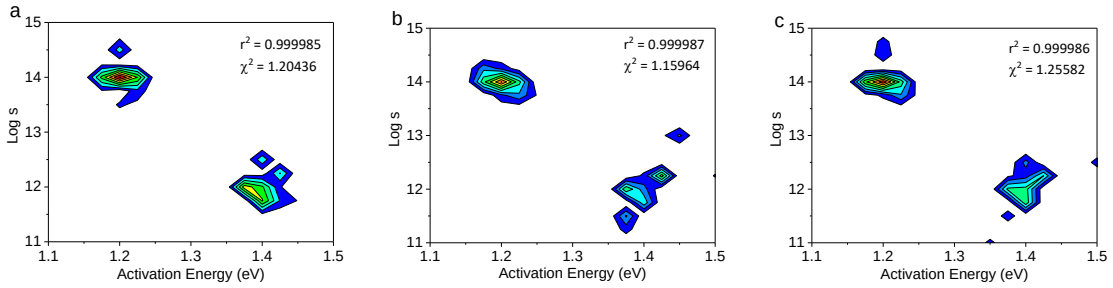

Figure 5-7. *E-log s* distribution (with *s* in s^{-1}) results obtained from three different simulated datasets all with the same input set. The minimum contour value shown is 10% of the maximum contour value of figure.

5.2.4 Effect of Signal-to-Noise Ratio

In Section 3.5.3, we estimated the uncertainty for an individual intensity data point to be $\sigma_{y,i} = \sqrt{\sigma_{TL,i}^2 + \sigma_{bg}^2}$ which allows for the increase and decrease of the (S/N) by increasing or decreasing the initial trap occupancy. Using the input parameters in Figure 5-4a, three datasets

were obtained for three different initial occupancies of 10^5, 10^7, and 10^9 per peak. Figure 5-8 shows representative curves from each dataset with the largest S/N ratio occurring for the largest peak occupancy.

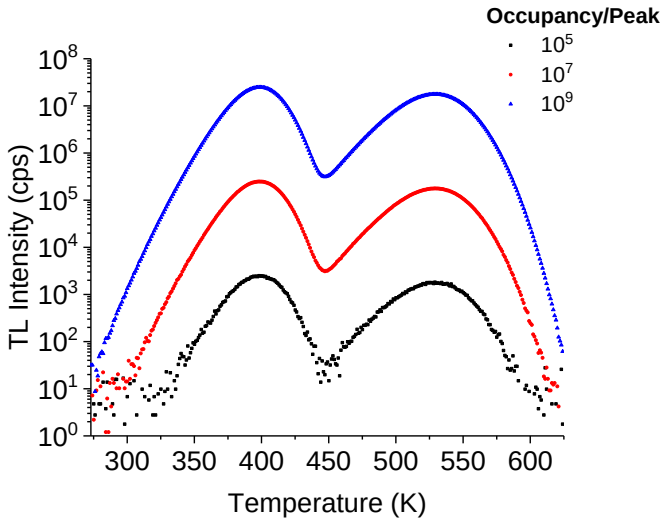

Figure 5-8. Representative TL curves for three different datasets each using similar input distribution with only the total area per peak changed between sets.

Trap parameter distributions obtained following the two-dimensional deconvolution procedure for the varied intensity TL peaks are provided in Figure 5-9. TL peak intensity was changed by varying the individual trapping center distribution size, n_0 (Equation 3-12) . The reliability of the deconvolution deteriorates significantly when the noise is increased (i.e., TL intensity is decreased) (Figure 5-9a). Also, we observe many individual peaks in Figure 5-9a, indicating the decrease in the S/N ratio modifies the TL curve structure in a significant way, which suggests that the deconvolution attempts to "fit the noise". If the noise is reduced by increasing the initial TL intensity, the results become more accurate (Figure 5-9c).

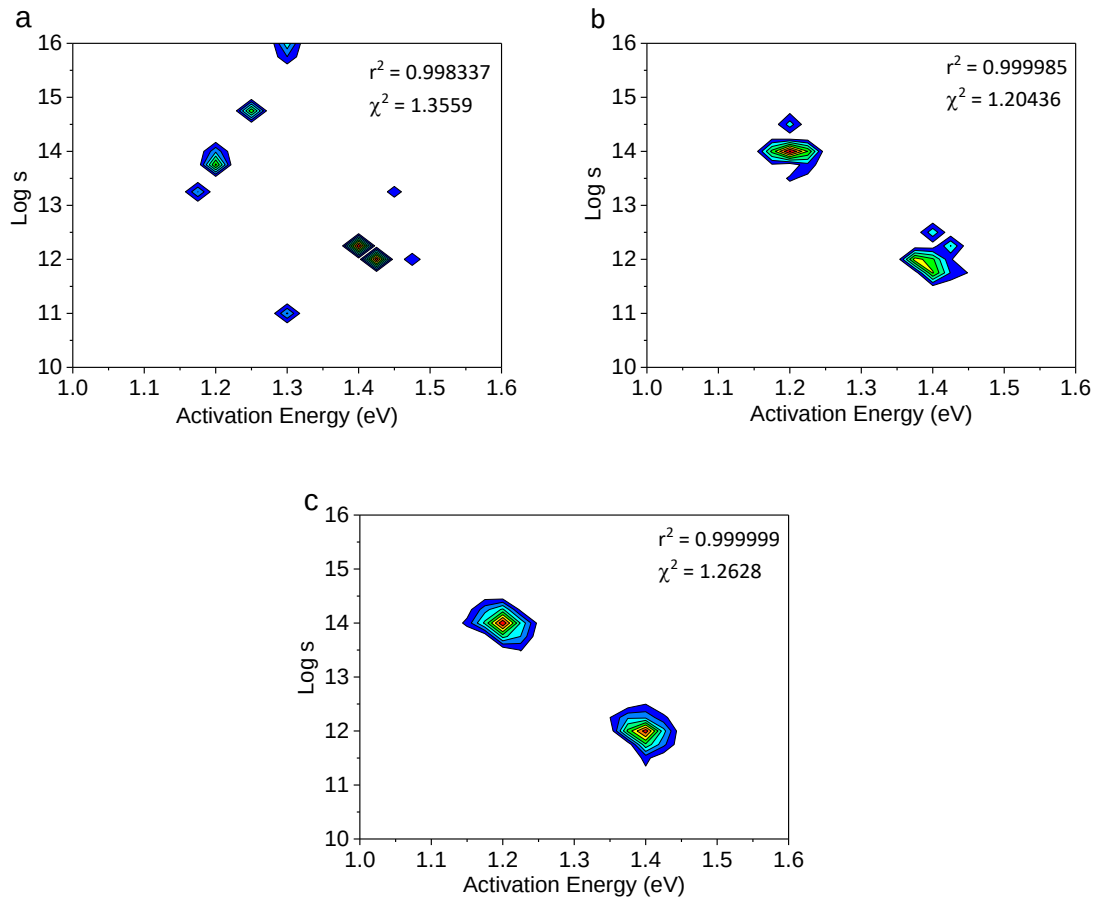

Figure 5-9. *E*-log *s* distribution (with *s* in s^{-1}) results obtained from three different simulated datasets with three different trapping center distribution sizes (a) 10^5, (b) 10^7 and (c) 10^9. The minimum contour value shown is 1% of the maximum contour value of each figure. Results represent those obtained from the deconvolution of a single dataset.

The dependence of the deconvolution results on the S/N is related to the depletion of trapping centers during the preheating, which results in corresponding reductions in TL intensity, thereby decreasing the S/N. For a large initial occupancy, the fractional reduction in occupancy produced by a preheating still produces curves with good S/N ratio. If the initial occupancy is low (i.e. low dose, or small sample size), then the preheated curves are too noisy to be useful as additional constrain in the deconvolution procedure.

Therefore, every attempt should be made to reduce the noise. Here, we have chosen to simulate curves with initial occupancies of 10^7 per peak as they correspond to maximum

simulated TL intensities on the order of $10^5 – 10^6$ counts per second when using a 1 K/s heating rate. Such intensities are characteristic to those found in literature, without being so large as to approximate the noiseless cases already presented.

5.2.5 Resolution Effects

The performance of the NNLS method for three different kernel resolutions (coarse, intermediate, and fine) are shown in Figure 5-10a for the input distribution and dataset presented in Figure 5-4a.

For coarse kernel resolution [ΔE = 0.5 eV, $\Delta \log s$ = 0.5], the method indicates multiple large peak distributions which do not agree with the input distribution (Figure 5-10a). Figure 5-10b shows the results of the intermediate kernel resolution [ΔE = 0.025 eV, $\Delta \log s$ = 0.25], which are similar to the input distribution. Figure 5-10c shows the results of the fine kernel resolution [ΔE = 0.01 eV, $\Delta \log s$ = 0.1], characterized by many individual trapping centers instead of distributions located about the input means.

The choice of kernel resolution seems to be critical to the accuracy of the results and, therefore, it is difficult to evaluate the reliability of the method for unknown distributions. A comparison of the intermediate and fine resolution fitting metrics (Figure 5-10) shows nearly identical figure of merit values, despite the noticeable differences in the resulting trap parameter distribution. Typically, the implementation of the Tikhonov technique would prove useful for the fine resolution, but the results for the fine resolution case were characterized by the same long diagonal banded solutions previously discussed in Figure 5-6b (results not shown). For the purposes of this work, we will focus on the intermediate resolution, as it provided the best results. In later sections, we will discuss the predictive performance of the

deconvolution models through comparisons with additional simulated datasets obtained for a range of heating profiles.

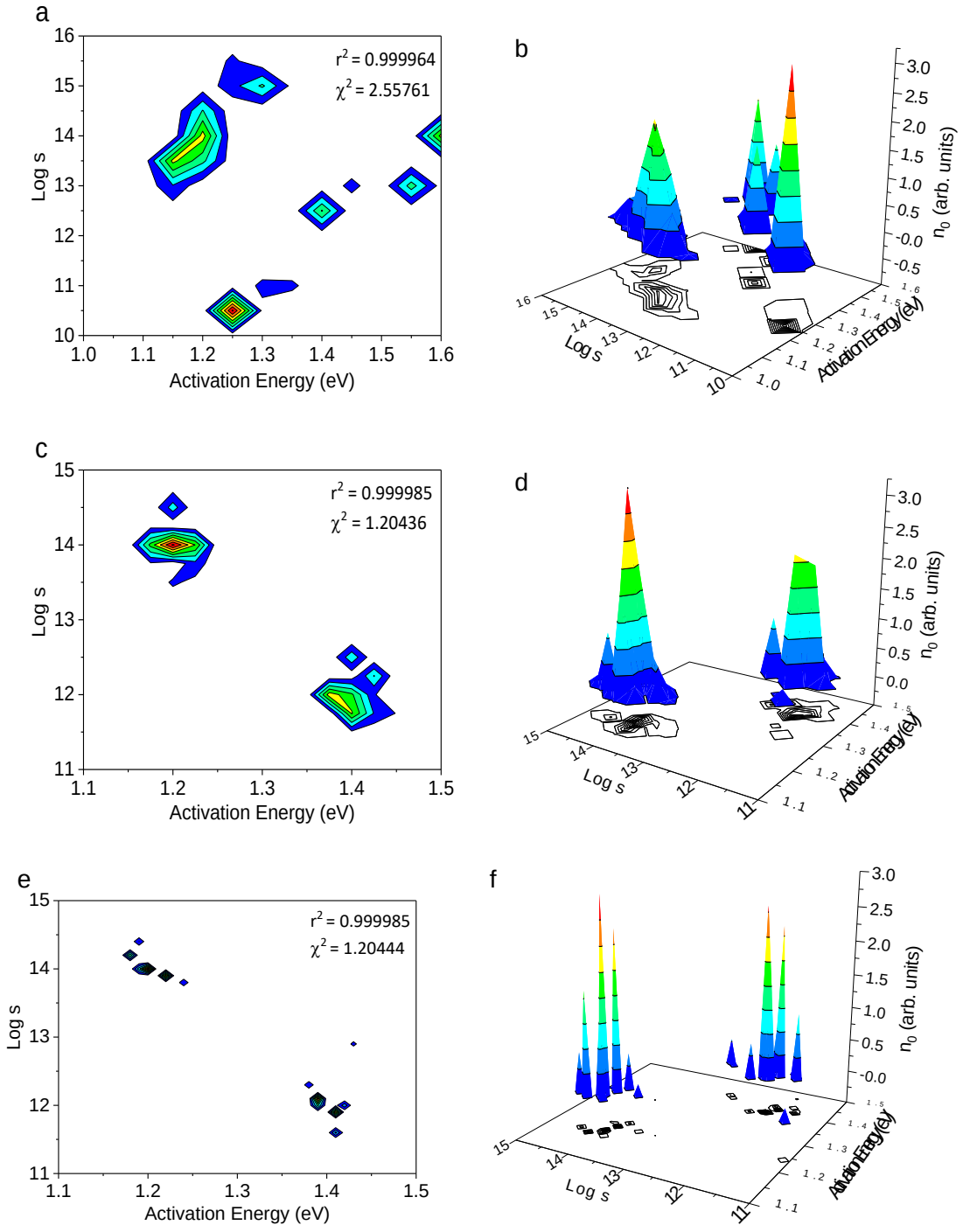

Figure 5-10. NNLS results of noise added TL curves using (a) coarse [ΔE = 0.5 eV, $\Delta \log s$ = 0.5], (b) intermediate [ΔE = 0.025 eV, $\Delta \log s$ = 0.25], and (c) fine [ΔE = 0.01 eV, $\Delta \log s$ = 0.1] kernel resolutions.

5.3 Comparison Between Deconvolution Methods

Datasets were simulated for a four-trap parameter distribution (to be referred to as the four-trap system) comprised of peaks A-D (Table 3-2). The datasets were used to compare the deconvolution method results for datasets obtained from varying the hold temperature, θ-dataset, to datasets obtained from varying the heating rate (β-dataset). Three unique datasets were simulated for the four-trap system for both the step-annealing and heating rate methods (Figure 5-11). The deconvolution of each dataset was completed using the intermediate resolution of ΔE = 0.025 eV, $\Delta \log s$ = 0.25 across values of E = 0.8 – 1.8 eV and $\log s$ = 8 – 18 for a total of 1681 curves within the kernel. The number of curves used in the kernel was reduced slightly to remove curves with TL peak maxima outside the readout temperature (*x*-axis) range.

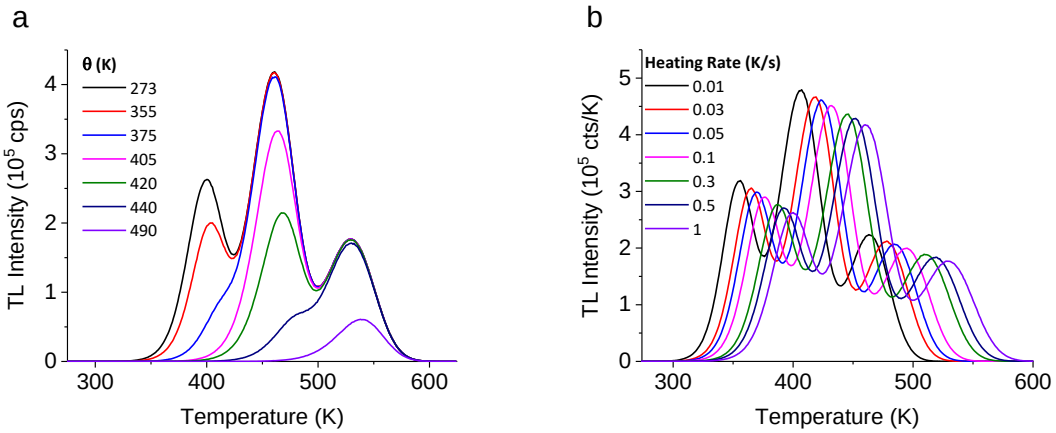

Figure 5-11. Four trap distribution datasets for the (a) step-annealing and (b) heating rate method.

The results for both dataset types are compared with the input distributions in Figure 5-12. The addition of noise and background curve has a large effect on the quality of the deconvolution, as compared to the noiseless results in Figure 5-3. We see the presence of a larger number of peaks, indicating an attempt by the deconvolution procedure to fit the noise.

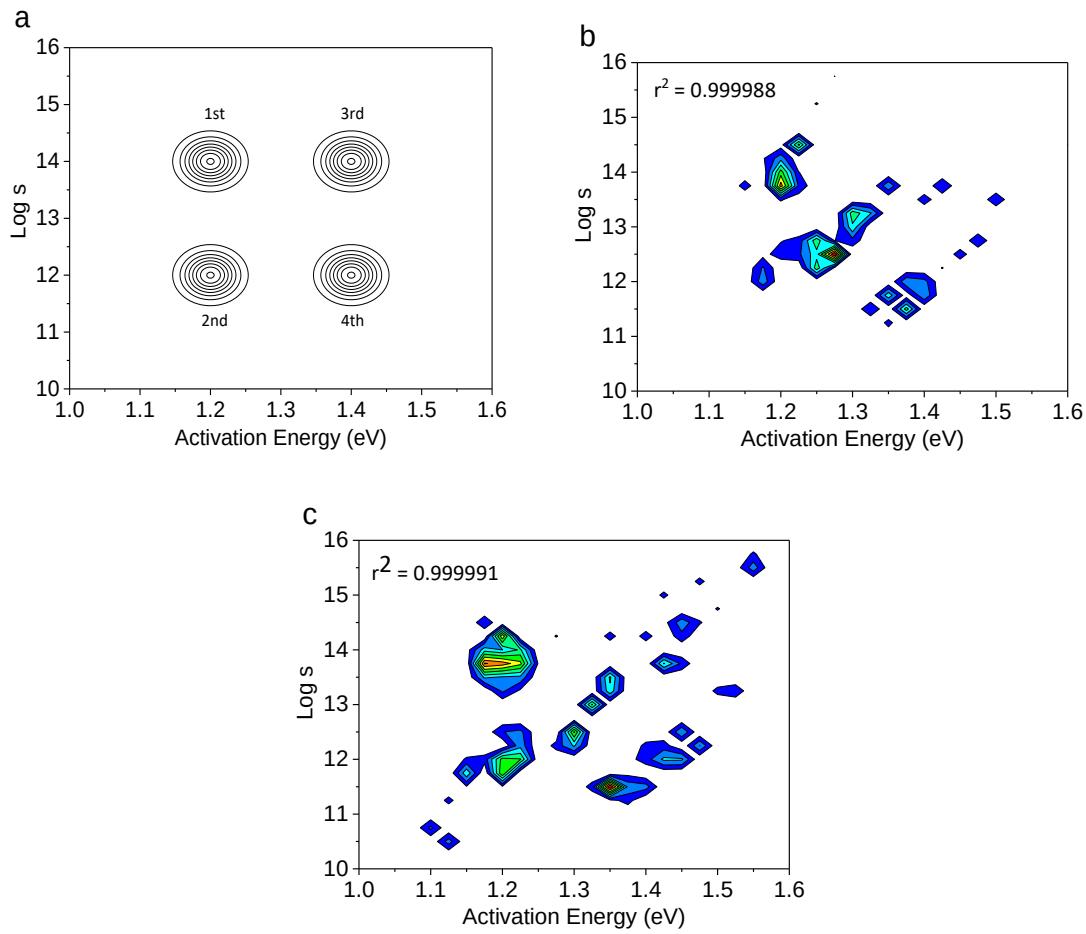

Figure 5-12. (a) Input distributions and corresponding deconvolution results for the four peak (b) θ- and (c) β-datasets. Input distributions are annotated with text to indicate the relative positions of the peak maximums. All contours are comprised of 8 levels with a range of 10% max contour value.

To see how the number of peaks effects the deconvolution results, datasets for a three-trap parameter distribution (to be referred to as the three-trap case/system) comprised of peaks B-D (Table 3-2) were simulated for each method (θ or β) (Figure 5-13). The deconvolution results for the three trap system datasets are shown Figure 5-14.

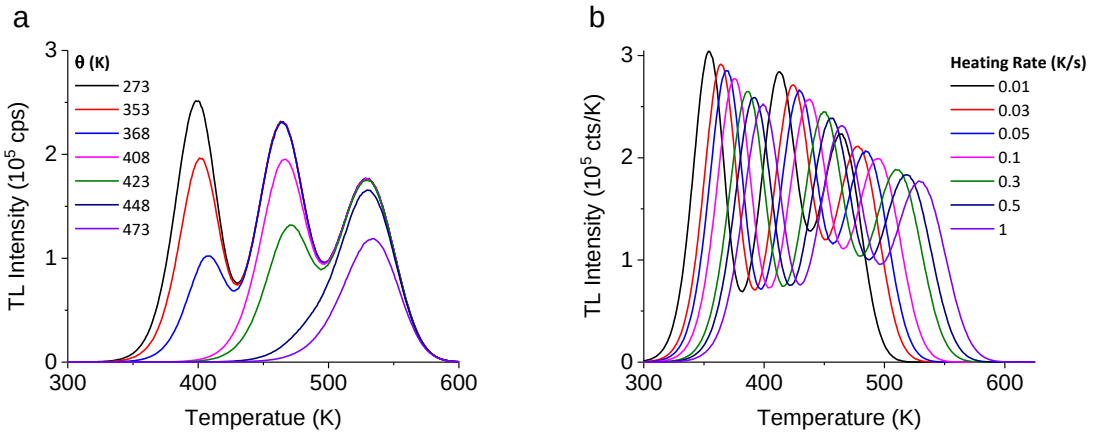

Figure 5-13. Three trap background subtracted datasets for the (a) step annealing and (b) heating rate method.

Figure 5-14 shows the deconvolution results for the three-trap datasets in Figure 5-13. The deconvolution of the θ-dataset in Figure 5-14b shows a three-peak structure positioned at similar trap parameter locations to those in the input distribution in Figure 5-14a, but with multiple spurious peaks. The deconvolution of the β-dataset (Figure 5-14c) shows two main peaks located at *E* = 1.2 eV, $\log s$= 14, and *E* = 1.5 eV, $\log s$ ~15, with many discrete peaks which correspond to the low temperature TL peaks, suggesting the varied heating rate approach does not perform well when the simulated TL curves contain noise.

The results in Figure 5-12 and Figure 5-14 show that there is a negligible difference between the θ- and β-methods. The three-trap system shows better agreement between deconvolution results and simulation input for the θ-dataset (Figure 5-14), whereas both methods fail for the 4-trap system (Figure 5-12). Also, it should be noted that the r-squared value for all the average results presented in Figure 5-12 and Figure 5-14 are $r^2 \sim 0.9999$, suggesting that simply producing a good figure of merit value is insufficient to accurately reproduce the input values. This would indicate that additional curves are required to adequately constrain the deconvolution with the addition of noise.

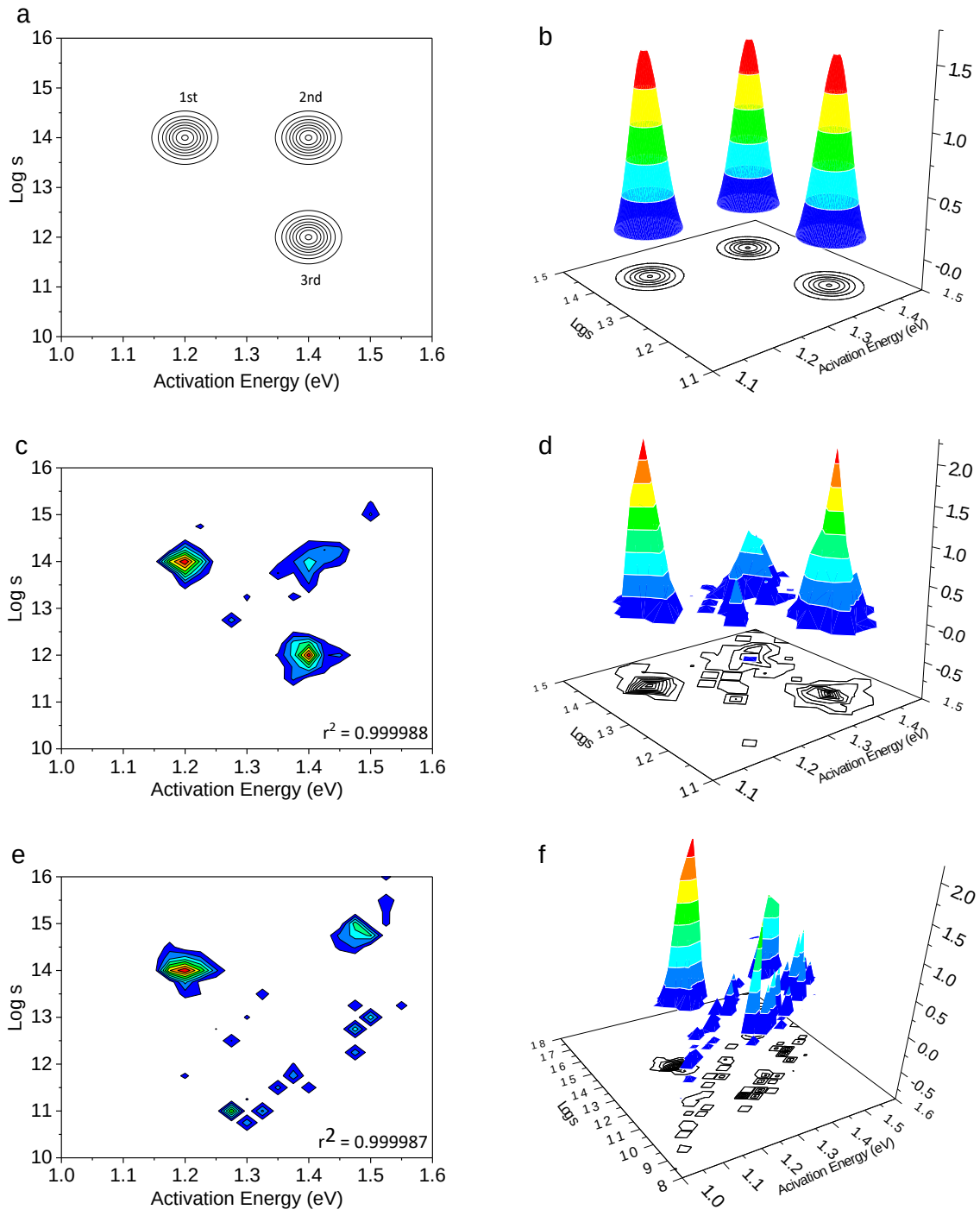

Figure 5-14. (a-b) Input distribution and corresponding deconvolution results obtained using (c-d) θ- and (e-f) β-datasets. Input distributions are annotated with text to indicate the relative positions of the peak maximums. All contours are comprised of 8 levels with a range of 10% of the max contour value.

5.4 Extrapolation of the Deconvolution Results

Although the deconvolution solutions presented, for example, in Figure 5-14, are successful (r-squared value) in describing the constraint dataset, it is not clear if these solutions can predict the rate of thermal decay of the TL signal for a wider range of timescales. This is, of course, of interest for applications, since the parameters obtained in laboratory must be extrapolated to very short or very long timescales (Yukihara et al., 2017).

To investigate this issue, we simulated TL curves and analyzed them using the deconvolution procedures presented here. Then, we simulated the TL curves that would be produced for heating to wider heating conditions [temperatures between 400 K and 1000 K, $\Delta\theta$ =10 K, and for hold times, τ, of -3 to 3 log seconds ($\Delta\tau$ =0.1)] and compared the results with those based on the input distributions. For each heating profile, a comparison between the "experimental" and model TL curves was made using the reduced chi-squared metric previously defined in Equation 5-2. Values of χ_r^2 equal to unity suggest a very good fit with values >1 signifying either a poor fit due to an incorrect model choice or an incorrect estimation of uncertainty. Values of $\chi_r^2 < 1$ are typically the result of an overfitting or an overestimation of the uncertainty. Intensities considered to fall below the background (mean background plus five times the background uncertainty) were not used in the calculation of the χ_r^2 results. We will refer to the group of "experimental" and model curves as "validation curves" throughout the remainder of this study. In the following subsections, we will consider both the 3- and 4-trap system cases just as we did in Section 5.3.

5.4.1 Extrapolation of θ-datasets

"Experimental" datasets for the 4-Peak (Figure 5-12a) and 3-Peak (Figure 5-14a) distributions were simulated for hold temperatures between 400 K and 1000 K and hold times

between $\tau = -3$ and $\tau = 3$. The simulated experimental datasets were compared with datasets simulated using the two-dimensional deconvolution model (extrapolated) for the θ-*datasets* for the 4- and 3-trap systems. Figure 5-12b and Figure 5-14b respectively, using the reduced chi-squared metric Equation 5-2.

Contour plots of the reduced chi-squared metric as a function of temperature profile are shown in Figure 5-15. The hashed grey regions in Figure 5-15 correspond to heating profiles that produce curves for either the extrapolated model or the simulated experimental curves with maximum intensities below system noise (mean plus five times the standard deviation of the background signal).

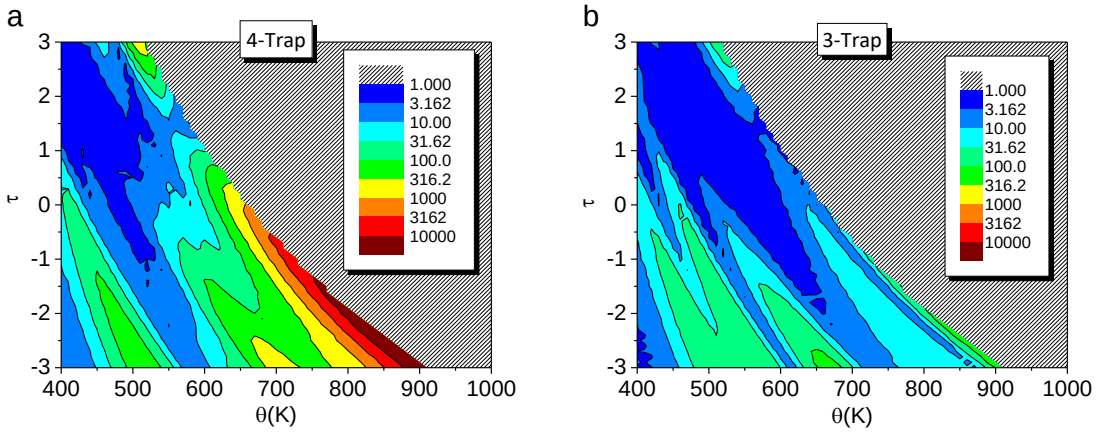

Figure 5-15. Contour plots of the reduced chi-squared metric for the (a) 4-trap and (b) 3-trap distributions using models obtained using the two-dimensional deconvolution results for the θ-datasets. The same contour levels are used for both plots to show comparison between the 4- and 3-peak performance.

The dark blue regions ($1 < \chi_r^2 < 3.162$) in Figure 5-15 represent areas of "best agreement" between the model and experimental simulations. We observe a larger region of dark blue for the 3-trap case (Figure 5-15b) as compared to the 4-trap case (Figure 5-15a), with both regions concentrated at heating parameters of low temperature and long timescale (>1 s) and extending along a diagonal to higher temperature and shorter timescale heating parameters. The validation curves corresponding to the heating parameters ($\theta <$

$500K, \tau \sim 2.46$) used to simulate the *θ-datasets*, from which the model was obtained, demonstrate the "best agreement" ($\chi_r^2 < 3.162$), but both the 3- and 4-trap cases in Figure 5-15 show that at shorter timescales the agreement between the model and experimental curves becomes increasingly poor. We observe regions of "poor agreement" in Figure 5-15, found along diagonal bands mainly for hold times below 1 second or along the transition to full curve depletion (hashed grey region).

To understand the presence of the high χ_r^2 diagonal bands in Figure 5-15b, we selected the band structures in Figure 5-16a ($55 < \chi_r^2 < 10{,}000$) and plotted the corresponding extrapolated curves in Figure 5-16b. The results in Figure 5-16a show that the bands correspond to the start (Figure 5-16b, 1) or end (Figure 5-16b, 4) of a TL peak's depletion. Due to the high overlap of the TL peaks, we also observed that the bands in Figure 5-16a correspond to heating profiles that produce both the full depletion of low temperature TL peaks and the start of the depletion of a higher temperature TL peak. The overlapping regions are the most complex and therefore require additional attention.

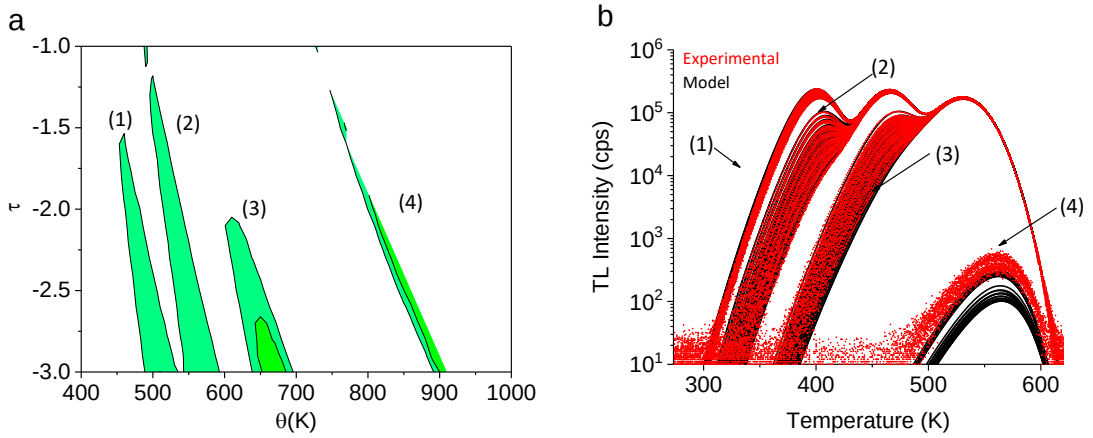

Figure 5-16. (a) Contour plot of the reduced chi-squared metric shown in Figure 5-15b (three trap system) for values between 55 and 10,000 and (b) the associated TL curves. Heating parameters that produce the numbered diagonal bands in plot (a) correspond to the numbered groups of curves in plot (b).

Let θ_c, τ_c be the critical hold temperature and hold duration that produce the largest reduced chi-squared value for the 4- and 3-trap cases. Figure 5-17 shows a plot of all hold temperatures for the single hold duration, τ_c. In Figure 5-17, we observe mismatches between the deconvolution model and simulated experimental curves occur at two places in the thermal annealing: (1) depletion of a lower temperature TL shoulder, and (2) depletion of the highest temperature TL peak. Additionally, we see evidence of the model having a poor estimate of the thermal stability of the underling trap structure, as evidenced by the model either depleting faster or slower than the experimental curve in Figure 5-17a. For both the 3- and 4-trap system results in Figure 5-17 we observe poor agreement for higher hold temperature, which was also found in the contour plots in Figure 5-15.

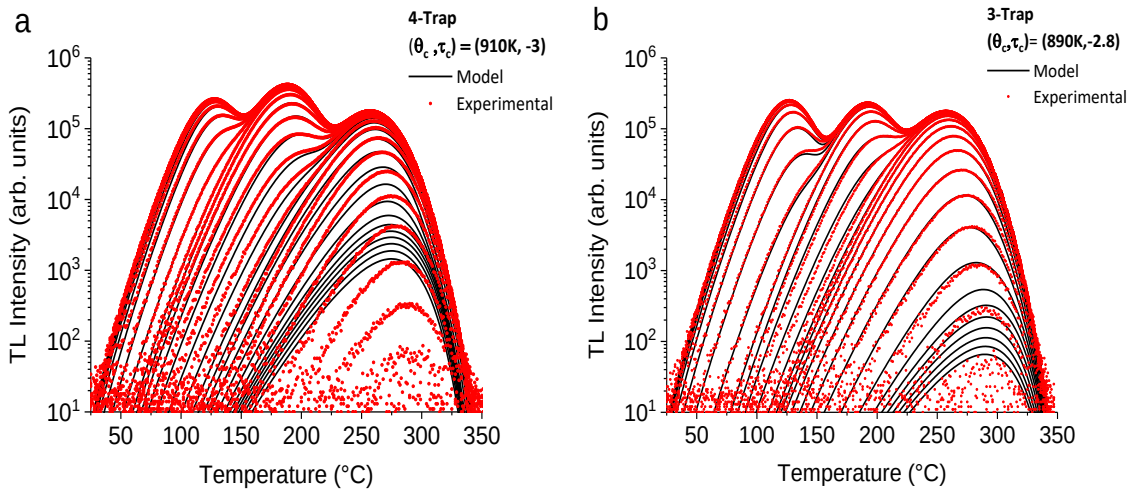

Figure 5-17. Validation curves for the (a) 4-trap and (b) 3-trap cases. Validation curves are plotted for the range of hold temperatures that correspond to the hold duration (τ_c) that resulted in the largest reduced χ^2 value. Every other annealed curve is shown for visual clarity.

5.4.2 Extrapolation of β-Datasets

Simulated experimental datasets were compared with datasets simulated using the two-dimensional deconvolution models obtained from *β-Datasets* for the 4-trap (Figure 5-12c) and 3-trap (Figure 5-14c) systems using the reduced chi-squared metric. The comparison results for

both the 3- and 4-trap cases (Figure 5-18) show large areas of poor agreement between the simulated experimental and model curves for heating profiles with both short heating durations (<1 s) and high hold temperatures (>550 K). The best agreement between the β-*datasets* model and the simulated experimental curves is found for all timescales at lower hold temperatures (<500 K) and longer heating times (~100 s) for hold temperatures below 600 K. Unlike the results for the θ-datasets in Figure 5-15, we do not see major differences from the 4-peak to the 3-peak cases in Figure 5-18. Additionally, the band-like structures in Figure 5-15 that differentiated peak depletion are not found in Figure 5-18.

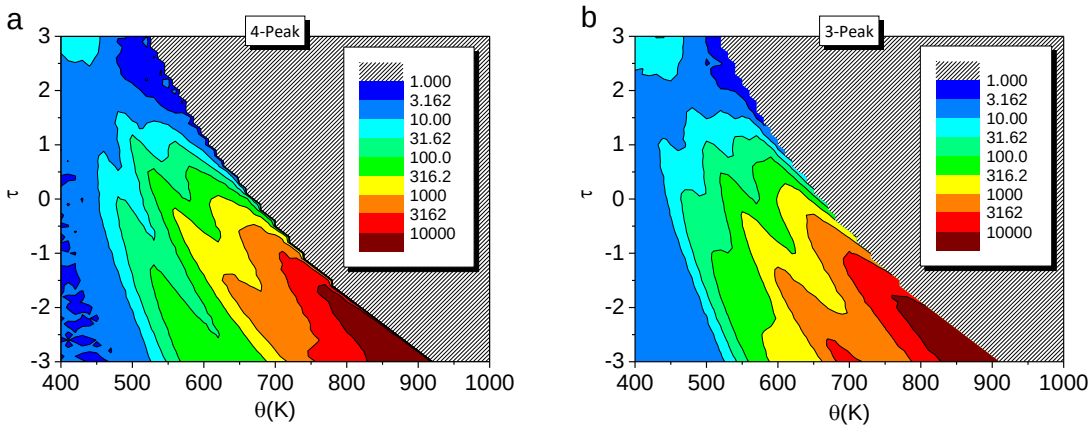

Figure 5-18. Contour plots of the reduced chi-squared metric for the (a) 4-trap and (b) 3-trap distributions using models obtained two-dimensional deconvolution results for the β-datasets.

The heating parameters (τ_c and θ_c) corresponding to the maximum χ^2_{red} value were obtained for both the 3- and 4-peak cases. The curves that correspond to τ_c are plotted in Figure 5-19. The curves visually confirm the poor performance of the deconvolution model at higher hold temperatures which appear to be the result as a non-sequential depletion of the high temperature TL peaks.

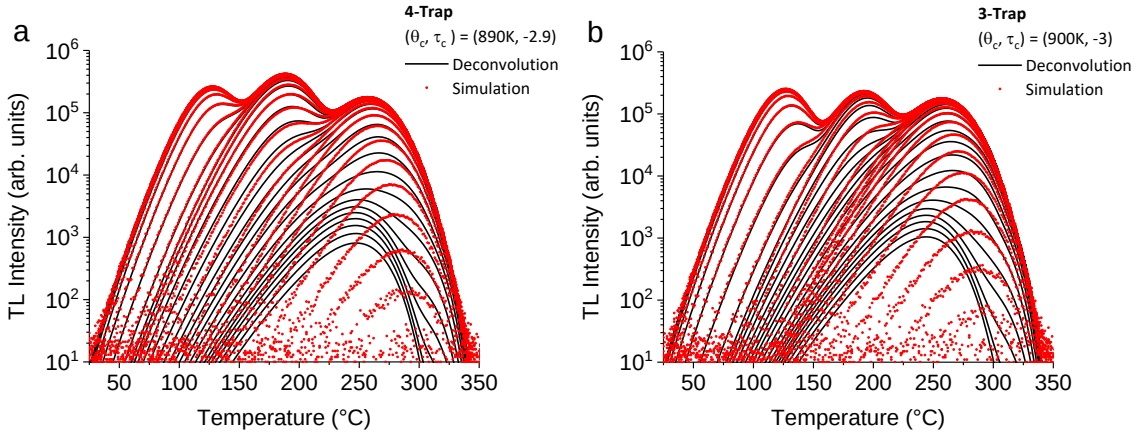

Figure 5-19. TL curves for the (a) 4-trap and (b) 3-trap distributions. Curves are plotted for the range of hold temperatures that correspond to the hold duration (τ_c) that resulted in the largest reduced χ^2 value. Every other annealed curve is shown for visual clarity.

The results, in Figure 5-19b, are used to obtain peak position as a function of hold temperature (Figure 5-20). Similar to a T_m-T_{stop} plot, we expect the peak position to increase as the hold temperature rises and lower temperature TL peaks are thermally removed. Figure 5-20 shows the peak position behavior of the datasets in Figure 5-19a. If the deconvolution model correctly approximates the simulation input, we expect a match in peak position, but Figure 5-20 shows a deviation between the models for hold temperatures above ~875 K for a duration of 1 ms ($\tau_c = -3$). This non-sequential depletion found in the boxed region of Figure 5-20 occurs when TL peaks with higher peak maximum positions are less thermally stable for a given hold temperature then TL peaks with lower peak maximum positions.

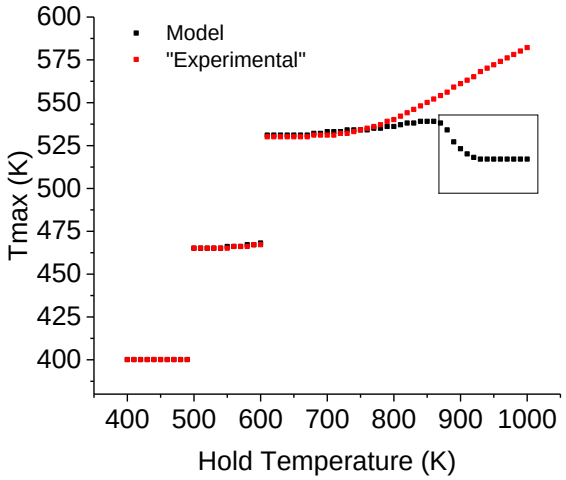

Figure 5-20. Peak maximum locations for the curves in Figure 5-19b as a function of hold temperature.

To understand the depletion behavior found in Figure 5-19b and Figure 5-20, the trap parameter distributions were obtained for each hold temperature at the critical hold time of 1 ms. Figure 5-21a shows the trap parameter distribution (parameters and trap population) for the hold temperature of 900 K for 1 ms and Figure 5-21b shows corresponding component TL curves. Two groupings of trapping centers are observed Figure 5-21a; one corresponding to a trapping center with *E* ~1.3 eV with a peak maximum of ~544 K and the other belonging to a trapping center with *E* ~0.9 eV with peak maximums of ~510 K, which correspond to the plateau in the boxed region in Figure 5-20.

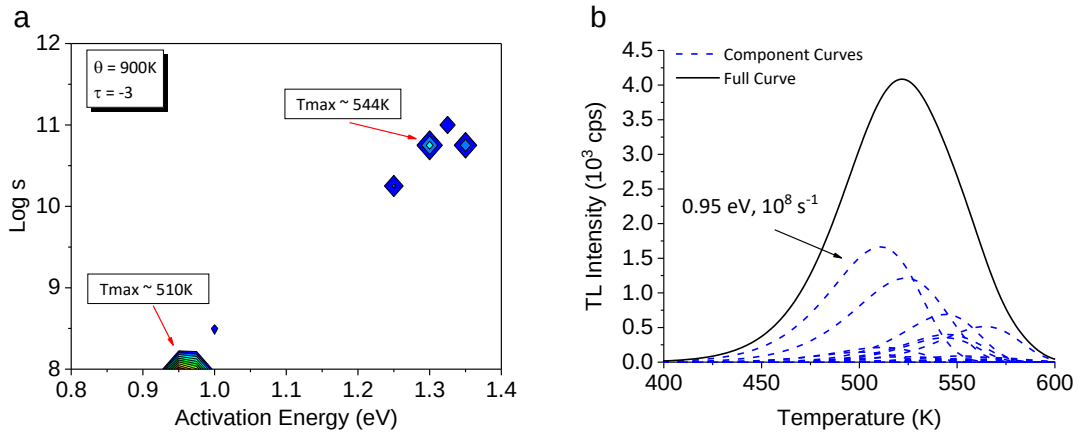

Figure 5-21. (a) Trap parameter distribution of the two-dimensional deconvolution model for a hold duration of 1 ms at a temperature of 900 K and (b) the corresponding component TL curves.

The lifetime of a trapped electron is characterized by the trapping center's kinetic parameters and the temperature of the material (McKeever, 1985),

$$\tau_{[E,s]} = s^{-1} \exp\left(\frac{E}{k\,\theta}\right). \qquad \textbf{5-3}$$

The lifetimes for the ~510 K peak and the ~544 K peak for a hold temperature of 900 K are $\tau_{[0.95,10^8]} = 2$ ms and $\tau_{[1.3,10^{10.75}]} = 0.34$ ms respectively. For a hold temperature of 900 K, the high temperature TL peak (~544 K) is less thermally stable than the low temperature peak (~510 K) and will experience significant depletion of the initial trap population for the 1 ms heating duration results shown in Figure 5-21.

The results in Figure 5-19b are characteristic of the extrapolated curve set which produced the highest chi-squared value in Figure 5-18b. If we instead look at the lifetimes for the hold temperatures in Figure 5-18b that correspond to the lower chi-squared values (400 – 600 K, $\tau = 2$), we find that the higher temperature peak (~ 544 K) has a longer lifetime than the lower temperature peak (~510 K) indicating it is more thermally stable over this range of hold temperatures. In fact, for all hold temperatures below ~ 642 K, the higher temperature TL peak has a longer lifetime than the lower temperature TL peak.

The results in Figure 5-18b suggest that the deconvolution model performs best (lower chi-squared values) when the heating parameters (hold time, hold temperature) closely match those used in the constraining dataset. By using heating parameters that vary greatly from those used to obtain the deconvolution model, we are able to gain insight into the accuracy of those results.

5.5 Improving the Solutions by Increasing the Dataset Size

The r-squared values for the 3-trap cases in Figure 5-12 and Figure 5-14 suggest the two-dimensional deconvolution method for both the θ- and the β-datasets works well, but a comparison of the deconvolution results with the input parameters as well as the extrapolated datasets suggest the opposite. We have previously shown that, in the absence of noise (Figure 5-3) or with low noise contribution (high S/N) (Figure 5-9c), the distribution obtained by deconvolution of a θ-dataset visually resembles the simulation input distribution. Additionally, Whitley et al. (2002) demonstrated the two-dimensional deconvolution method without noise for a β-dataset. Minimizing the impact of noise on the deconvolution method seems to be the key to obtaining results that better approximate the simulation input parameters. A simple increase in peak intensity through an increase in dose is one such method, but this approach might be limited due to experimental concerns. For the case that noise cannot be minimized, the use of additional distinct TL curves to the dataset can be used to further constrain the deconvolution approach.

Whitley et al. (2002) suggested the use of multiple heating rates spanning several orders of magnitude, such as those implemented in their study of 0.001 K/s, 0.01 K/s, and 0.1 K/s. To include additional heating rates requires one to go to faster heating rates, risking thermal lag, or to use heating rates that are not separated by orders of magnitude and, therefore, do not

produce datasets with enough variability to constrain the fit. In contrast to the heating rate approach, the step-annealing approach can include a large number of curves separated by small temperature increments as long as the curves belong to a region of hold temperatures that produce large changes in total TL curve area (Figure 5-1a).

In this section, we consider the performance of the deconvolution method when using larger θ-dataset for the 3- and 4-trap cases previously investigated and evaluate the results using the extrapolation approach presented in Section 5.4.

The trap parameter distributions for the 3- and 4-trap cases were used to simulate new datasets for the heating parameters defined in Table 5-1. The resulting datasets are shown in Figure 5-22 alongside the previously investigated 7 curve datasets. A smaller step size of 5 K was used for the 4-trap case instead of the 10 K to capture the more complex curve behavior resulting from the overlap of two Gaussian peaks.

Table 5-1. Parameters used to simulate larger constraining datasets. Three unique datasets were simulated for each input distribution. Trap parameter values for peaks A-D are found in Table 3-2.

Input Distribution	Hold Temperatures, θ(K)	Hold Time (s)	Dataset Size
3-trap (B, C, D)	273, 323 – 533 (10 K steps)	300	22 curves
4-trap (A-D)	273, 348 – 498 (5 K steps)	300	33 curves

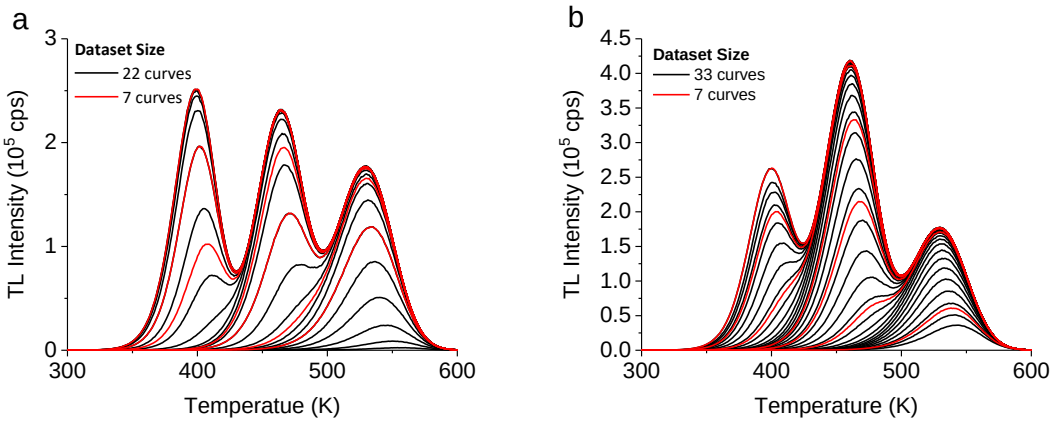

Figure 5-22. Comparison between simulated datasets obtained for the smaller (red trace) and larger datasets (black trace) for the (a) 3-trap and (b) 4-trap cases.

Figure 5-23 shows the deconvolution results for the datasets presented Figure 5-22. The results for the 3-trap case (Figure 5-23a) show three distinct peaks with roughly the same initial occupancy. These peaks are better defined than those found in the 7-curve dataset results (Figure 5-14b). The 4-trap case (Figure 5-23b) shows the presence of multiple individual peak distributions corresponding to the 1st, 2nd and 4th trapping center distribution in stark contrast to the results in Figure 5-14c. While the results for the 4-trap case are promising, they fail to fully capture the input distribution as the noiseless case results did (Figure 5-3), suggesting the need for additional annealing temperatures or a reduction in noise to fully resolve the highly overlapped nature of the 2nd and 3rd peaks. As expected, the increase in dataset size further constrains the resulting underlying model to explain more of the curve behavior. Additionally, the results suggest that the increase in the size of the dataset reduces the effect of the added noise and background (Figure 5-23).

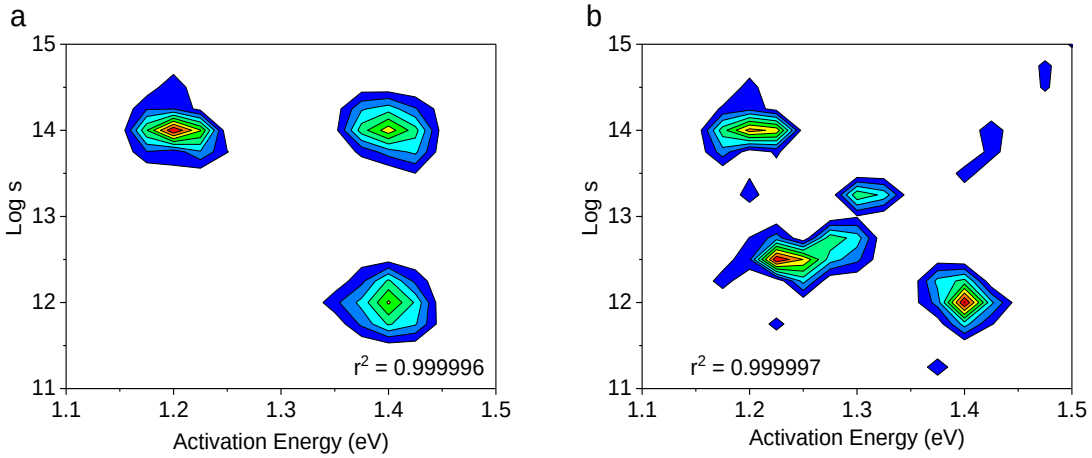

Figure 5-23. Deconvolution results for the (a) 3-trap case with 22 curves and the (b) 4-trap case with 33 curves. The contour threshold was set at 10% of max component with 8 levels.

The visual improvement of the deconvolution results presented in Figure 5-23 does not necessarily imply the obtained model is a good approximation of the simulation input. Extrapolated curves for the models in Figure 5-23 were obtained as previously discussed

(Section 5.4). Figure 5-24 shows reduced chi-square contours obtained for the validation curves for hold times between 10^{-3}-10^{3} for hold temperatures between 400 K and 1000 K.

Results for the 3-trap case (Figure 5-24a) display no distinct structure with the deconvolution model performing worse for heating profiles characterized by short duration heating for temperatures at ~500 K and ~900 K. When fewer curves were used, we previously found a 3-band structure in the results, Figure 5-15b, with the overall results characterized by higher reduced chi-squared values. Only a small isolated region for longer duration heating's corresponded to the lowest contour region (<3.162) in Figure 5-15b, while most of the chi-squared values in Figure 5-24a are within the lowest region (<2.371) and span all timescales simulated. These results suggest the increase in dataset size resulted in a significant improvement in the performance of the deconvolution model's ability to accurately predict the simulated materials response to temperature exposure.

The results for the 4-trap case in Figure 5-24b show a general improvement to the smaller dataset results in Figure 5-15a, based on the scale used to obtain the contour plots, but the presence of multiple bands of high reduced chi-squared values for the shorter duration heating's (<1s) shows the shortcomings of the model. The band extending diagonally up and to the left from the θ-axis at 700 K corresponds to the depletion of the middle peak structure comprised of the 2nd and 3rd trapping center distributions. This is to be expected as Figure 5-23b shows the 2nd trapping center distribution shifted from its simulation input of E = 1.2 eV, $\log s$ = 12 while there exist no structure directly corresponding with the 3rd trapping center distribution used in the simulation.

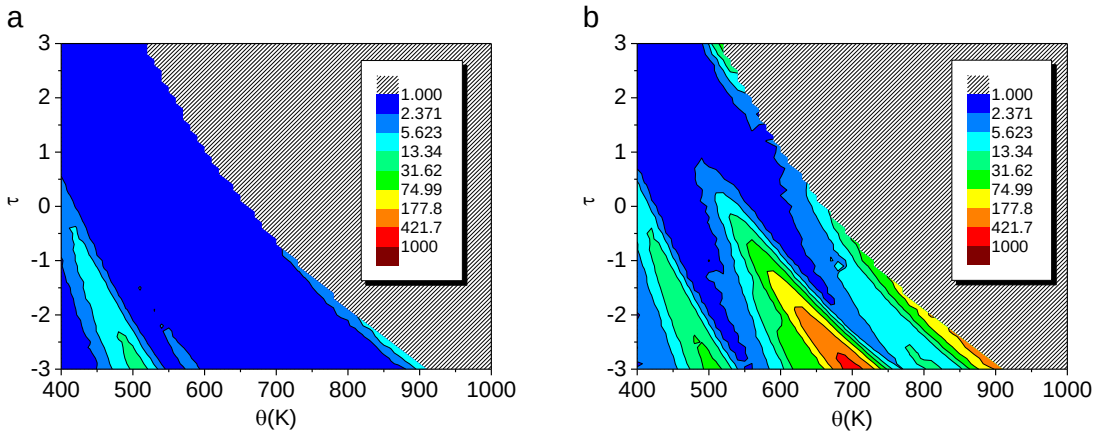

Figure 5-24. Contour plots of the reduced chi-squared metric for the (a) 3-trap and (b) 4-trap distributions using models obtained two-dimensional deconvolution results for the larger sized θ-datasets. The same contour levels are used for both plots to show comparison between the 3- and 4-trap performance but are lower than those previously used in Figure 5-15.

For each plot in Figure 5-24, the hold time corresponding to the highest reduced chi-square value was obtained. All extrapolation curves (400 K – 1000 K) corresponding to that hold time are shown in Figure 5-25. The 3-trap case (Figure 5-24a) shows no major differences between the simulated experimental curves and those obtained via the deconvolution model results (Figure 5-23a). Small differences are observed for the highest hold temperatures highlighted by the slight differences for the final few curves (T_m ~300 °C) where the background noise contribution is high.

The 4-trap case (Figure 5-25b) shows clear differences between the deconvolution model and the simulation input for hold temperatures spanning the depletion of the middle peak structure as well as the depletion of the final peak (T_m ~ 300 °C). The differences found for the increased size dataset are much smaller than those previously found for the smaller dataset validation curves (Figure 5-17a), again suggesting the increase in dataset size has a profound improvement on the model performance.

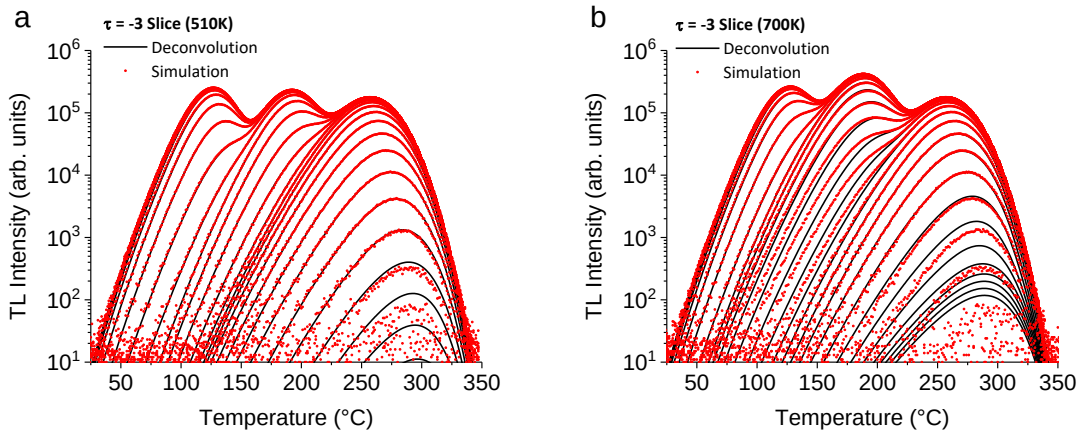

Figure 5-25. Extrapolation curves for the (a) 3-trap and (b) 4-trap distributions. TL curves are plotted for the range of hold temperatures that correspond to the hold duration (τ_c) that resulted in the largest reduced χ^2 value. Every other annealed curve is shown for visual clarity.

5.6 VHRM and IRM Results

The two-dimensional deconvolution method presented in this work is just one of many experimental techniques available for use when attempting to characterize a given TL materials trapping center parameters. Two such techniques, the IRM and VHRM can be directly applied to the θ- and β-datasets (respectively) already presented in this work.

β-datasets corresponding to the three- and four-trap parameter distribution systems were simulated for seven heating rates between 0.01 K/s and 1.0 K/s for the two input distributions shown in Figure 5-26c,d. Plots of the $\log \beta/T$ versus $1000/T$ are shown in Figure 5-26a,b along with the resulting linear fits. Three peaks positions were identifiable for both the three- and four-trap cases. The results of the VHRM analysis are shown as data points overlaying the input distributions in Figure 5-26c,d. The VHRM is limited in its applicability, since it requires well resolved and isolated peaks, but the curves are the result of both distribution and overlapping distributions. For the case of the three-trap system, the results agree moderately with the trap distribution averages for peaks 1 and 3 and less well for peak 2. The percent

differences between the VHRM activation energies and input energy averages were found to be 4.8, 3.6 and 1.4% for peaks 1-3 while the *log s* percent differences were 0.4%, 13.3%, and 12.1%.

For the case of the four-trap system, the results are harder to analyze, as the analysis of peak 2 corresponding to the overlap of trap distributions two and three. Therefore, we will only discuss the results for peaks 1 and 3. The result for the VHRM for peak 1 agree well with percent differences between input and analysis of 4.8% and 0.2% for *E* and *log s* respectively, while peak three has percent differences of 2.9% and 16.7% for *E* and *log s* respectively. The higher percent difference for the 3rd peak (4th trapping center) is the result of overlap with the 2nd trapping center.

The results of the VHRM suggest this analysis technique is moderately successful at approximating the mean input values when applied to TL peaks resulting from isolated distributions. When the method is applied to overlapping peaks such as peak 2 for the three-trap case, the trap parameter results are in poor agreement with the input distribution mean values.

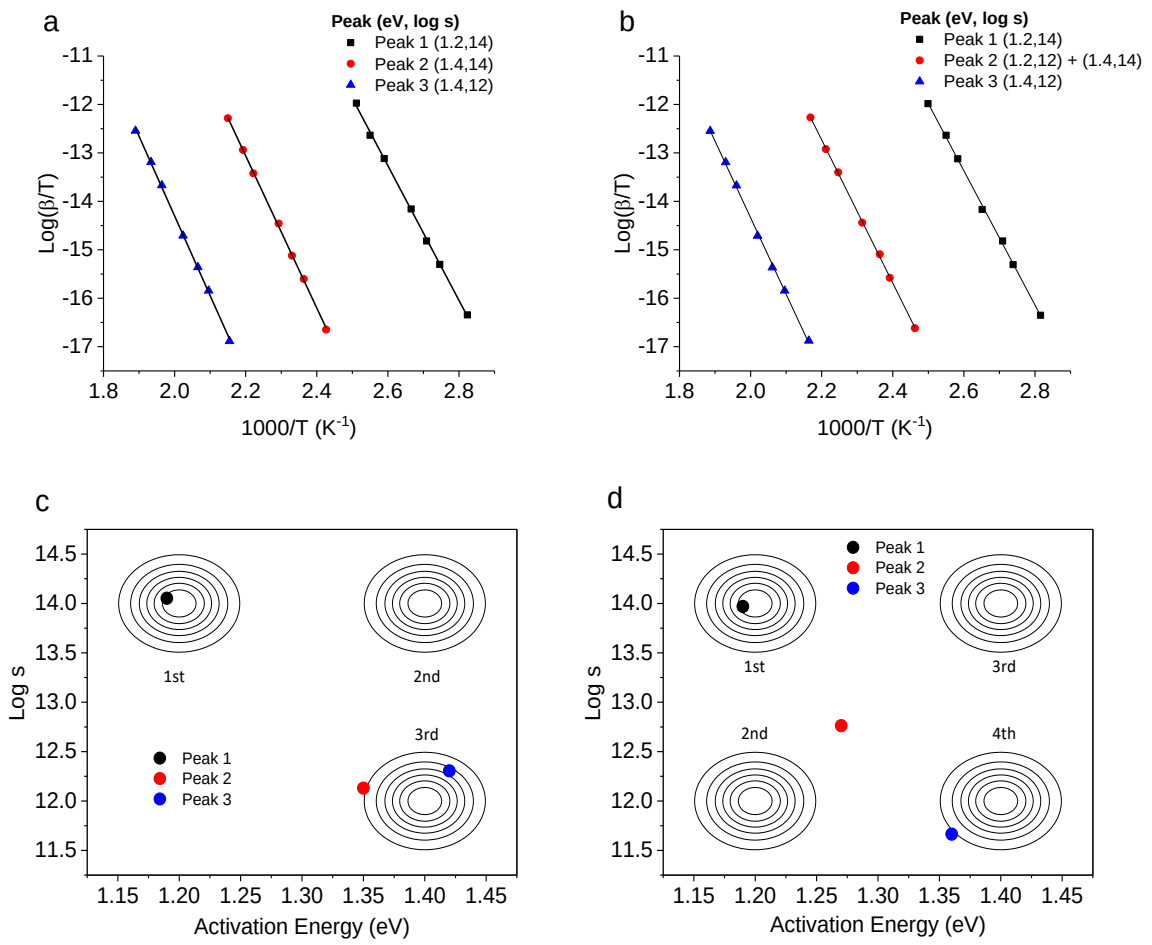

Figure 5-26. VHRM dataset for the (a) 3-trap distribution system and (b) 4-trap distribution system with corresponding results overlaid on the simulation inputs distributions for the (c) 3- and (d) 4-trap cases.

θ-datasets corresponding to the three- and four-trap parameter distribution systems were simulated for hold temperatures between 273 K and 550 K at for a hold time of 300 s. Hold temperatures were incremented by 2 K resulting in datasets of 127 and 112 curves for the three- and four-trap cases respectively. The datasets were analyzed using the IRM with the initial rise region corresponding to intensities below 5% of the lowest identifiable peak maximum and above the background (mean plus five times standard deviation of background). The initial rise region can only reliably produce the activation energy as the calculation of the frequency factor relies on knowledge of the true peak maximum, not possible when dealing with the cases at hand. Linear fitting was conducted using unweighted data.

Figure 5-27 shows the results of both the IRM and T_m-T_{stop} analysis for the three and four trap cases. The T_m-T_{stop} results for both cases suggest the presence of three approximately first-order peaks as indicated by the three distinct plateaus which are approximately constant. The uptick at the end of each plateau for peaks 1 and 2 are the result of the overlap between the peaks and the thermal depletion of the less thermally stable trapping centers. The uptick for the third plateau is a result of solely the depletion of the less thermally stable trapping centers. To confirm first-order behavior over either general or second-order, one would need to perform additional analysis such as dose response.

The IRM results in Figure 5-27 are to be compared with the blue dashed lines which correspond to the mean input activation energies. Regardless of the number of trapping centers or frequency factor, there are only two input energies of 1.2 eV and 1.4 eV each which a full width half maximum (FWHM), $2\sqrt{2\ln 2}\,\sigma = \sim 0.06\ eV$, and therefore, we would expect IRM analysis to produce energies between ~1.14-1.26 eV and ~1.34-1.46 eV. For both the three and four trap cases, a transition to a second plateau occurs.

For the three-trap case in Figure 5-27a, we observe a clear plateau in activation energy for hold temperatures between ~300 K and ~375 K corresponding to the first trap mean of 1.2 eV. Between ~375 K and ~425 K, the energies transition to a second plateau which corresponds to the input mean of 1.4 eV for both the 2nd and 3rd trap distributions. Both plateaus underestimate the input means, but fall within one FWHM of the input mean value. The results for the four-trap case in Figure 5-27b are similar to those of the three-trap case, but the transition region extends over a large range of hold temperatures. This is the result of the middle TL peak having two difference input means of 1.2 eV and 1.4 which spreads the IRM results over a wider range of energies. The increase in variability and uncertainty at the highest hold temperatures are the result of low (S/N) ratio.

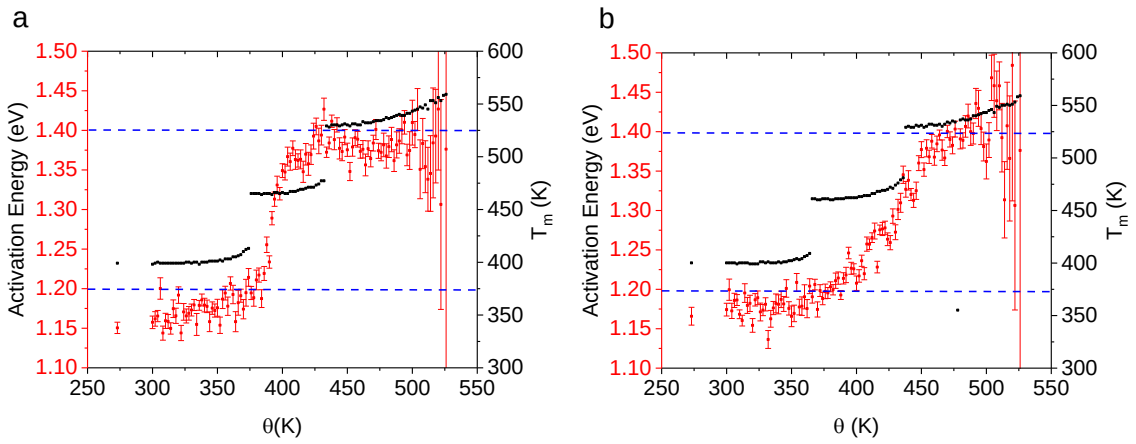

Figure 5-27. IRM (red data points) and T_m-T_{hold} (black data points) results for the (a) 3-trap and (b) 4-trap distribution systems. Error bars on the IRM results are propagated from the uncertainty in the slope calculation during fitting.

5.7 Variation in Linear Heating Rate

Up to this point, we have only considered the addition of Poisson noise in the attempts to simulate an experimental TL curve, but typical experimental systems can produce additional sources of uncertainty such as inconsistencies in the linear heating profile resulting from thermal lag. Inconsistencies such as these produce mismatches between the recorded temperature and the temperature experienced by the material and are, therefore, detrimental to curve fitting. For a typical TL reader, the user programs a linear heating rate by specifying the upper duration of heating (or upper T limit) and the rate. Let $T(t) = T_0 + \beta t$ be the programmed linear temperature profile sent by the controlling system and T' be the temperature profile experienced by the sample material. If no inconsistencies exist, then $T' = T$, which has been the case so far. When $T' \neq T$, the resulting dataset is simulated using the T' heating profile, but plotted against the programmed heating profile, T. Additionally, all curve used in the deconvolution method are simulated using the programmed heating profile of T.

To see how the two-dimensional deconvolution approach performs when applied to a simulated experimental system with inconsistencies in the heating profile, we consider two

different methods of introducing uncertainty into the linear heating profile. In the first case axis is shifted by a constant value, “constant shift”, and in the second case each individual temperature value is perturbed by a random value, “degree shift”. We recognize that many more variations, such as variations in heating rate, exist but we will limit ourselves to those already discussed.

The case of the “constant shift” is shown in Figure 5-28. Here, the shifted temperature is obtained from the expression $T_i^{'} = T + \mathcal{N}(0,1)$ where the subscript i denotes the temperature profile for the i^{th} curve in the dataset, to be referred to as “constant shift”. Thus, each curve within the “constant shift” dataset uses a purely linear profile offset by a single random value, Figure 5-28a. For the second case of the “degree shift” heating profile, we use an adjusted heating profile where each data point in T' randomly sampled from a normal distribution with a mean value corresponding to the programmed value and an estimated uncertainty of 0.25 K, expressed by the following expression, $T^{'}(t) = \mathcal{N}(T(t), 0.25)$. An example of this approach is demonstrated in Figure 5-28b, where each data point is randomly perturbed from the programmed value.

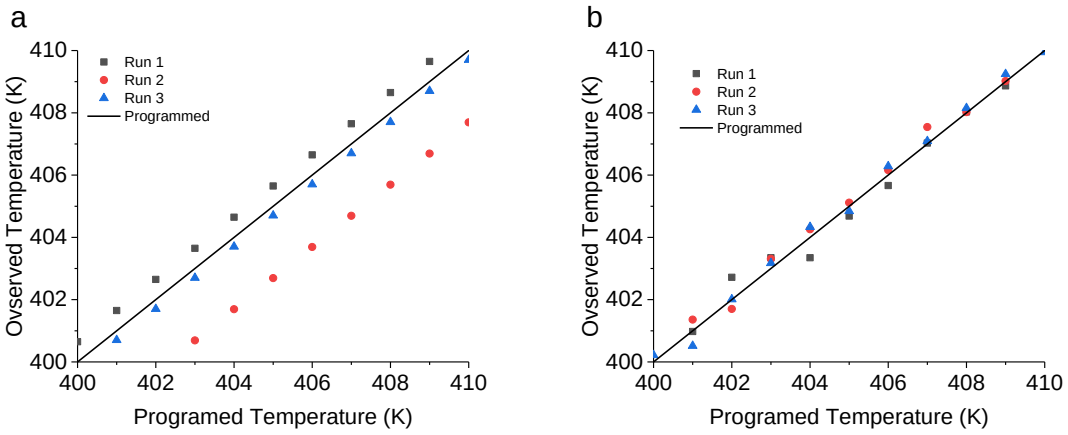

Figure 5-28. Demonstrations of the (a) constant shift and (b) degree shift for a linear heating rate of 1K/s. The programmed heating rate is shown as the black trace and the data points correspond to three different heating profiles.

Simulations were carried out using the 2-peak input model in Figure 5-4a using both the "constant shift" and "degree shift" temperature profiles as well as an unshifted temperature profile. A total of 31 curves were obtained for hold temperatures between 273 K and 500 K for a hold duration of 300 s. TL curve simulation and the subsequent two-dimensional deconvolution analysis follow the methodology already presented in this work. Figure 5-29 shows three simulated curve datasets obtained for the unshifted case and the two additional cases discussed in this section. To highlight the effect of each heating profile, Figure 5-29 shows the corresponding residuals between the simulated curve sets and an "ideal curve set" simulated without additive Poisson noise or changes to the linear heating profile.

Figure 5-29b shows the residuals for the unshifted heating rate case are at a maximum at the readout temperatures corresponding to the peak maxima. This is expected as the addition of Poisson noise adds scales with $\sqrt{I(T)}$ which is at a maximum at the peak maximum temperatures. Residuals for the "degree shift" case (Figure 5-29d) show that the maximum differences occur right before and after the peak maximum and are as much as five times greater than the unshifted case. The residuals for the "constant shift" (Figure 5-29f) were found to be approximately and order of magnitude greater than the other two cases and show no discernible pattern because of each individual curve being shifted randomly by a single constant value.

Figure 5-30 shows the deconvolution results for the datasets presented in Figure 5-29 above. Deconvolution results were obtained using the same resolution and ranges previously discussed in Section 5.3. No modifications were made to the uncertainty estimation, and therefore, we assumed all uncertainty within the system comes as a result of Poisson contributions only.

Figure 5-30a show the fitting results for the unshifted dataset and are consistent with previous analysis of the two-trap simulation input found in Figure 5-10b. Figure 5-30c shows the fitting results for the “degree shift” case and are characterized by a similar distribution to that of the unshifted dataset. This result suggests that the effect of the “degree shift” on curve shape is either too small to be detrimental to the deconvolution procedure or that the effect mimics the effect of adding Poisson noise and, therefore, is taken into account in some way during the uncertainty estimation.

Figure 5-30e shows the fitting results of the “constant shift” dataset. The trapping center distribution in Figure 5-30e shows the presence of multiple discrete peaks instead of the two expected Gaussian peaks used to simulate the dataset. Additionally, the plot of the simulated data in Figure 5-30f shows an approximate match in the overall depletion behavior (peak intensity), but each differs in peak location.

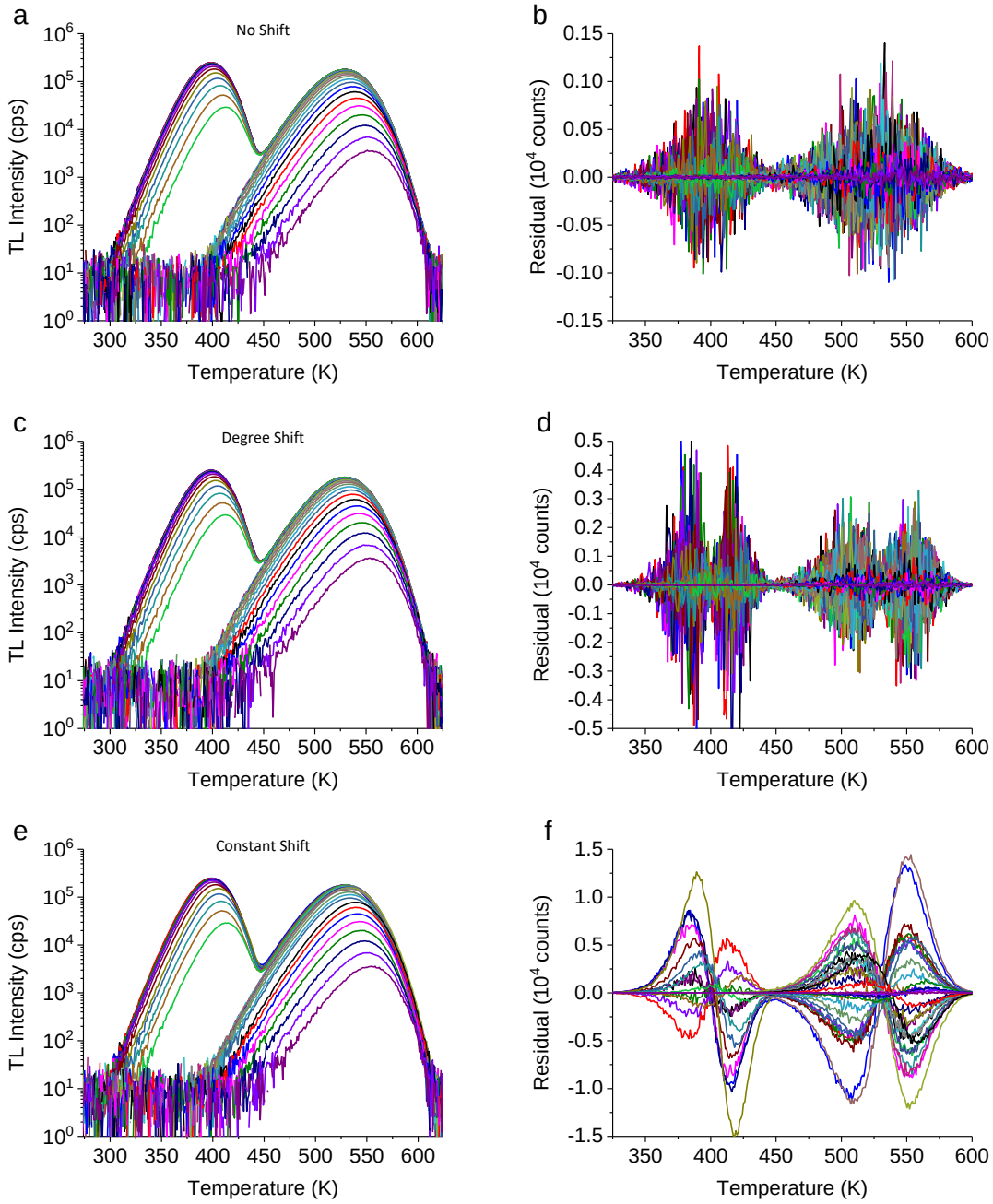

Figure 5-29. Datasets and residuals with the "ideal" case for the (a,b) unshifted (c,d) degree shift and (e,f) constant shift.

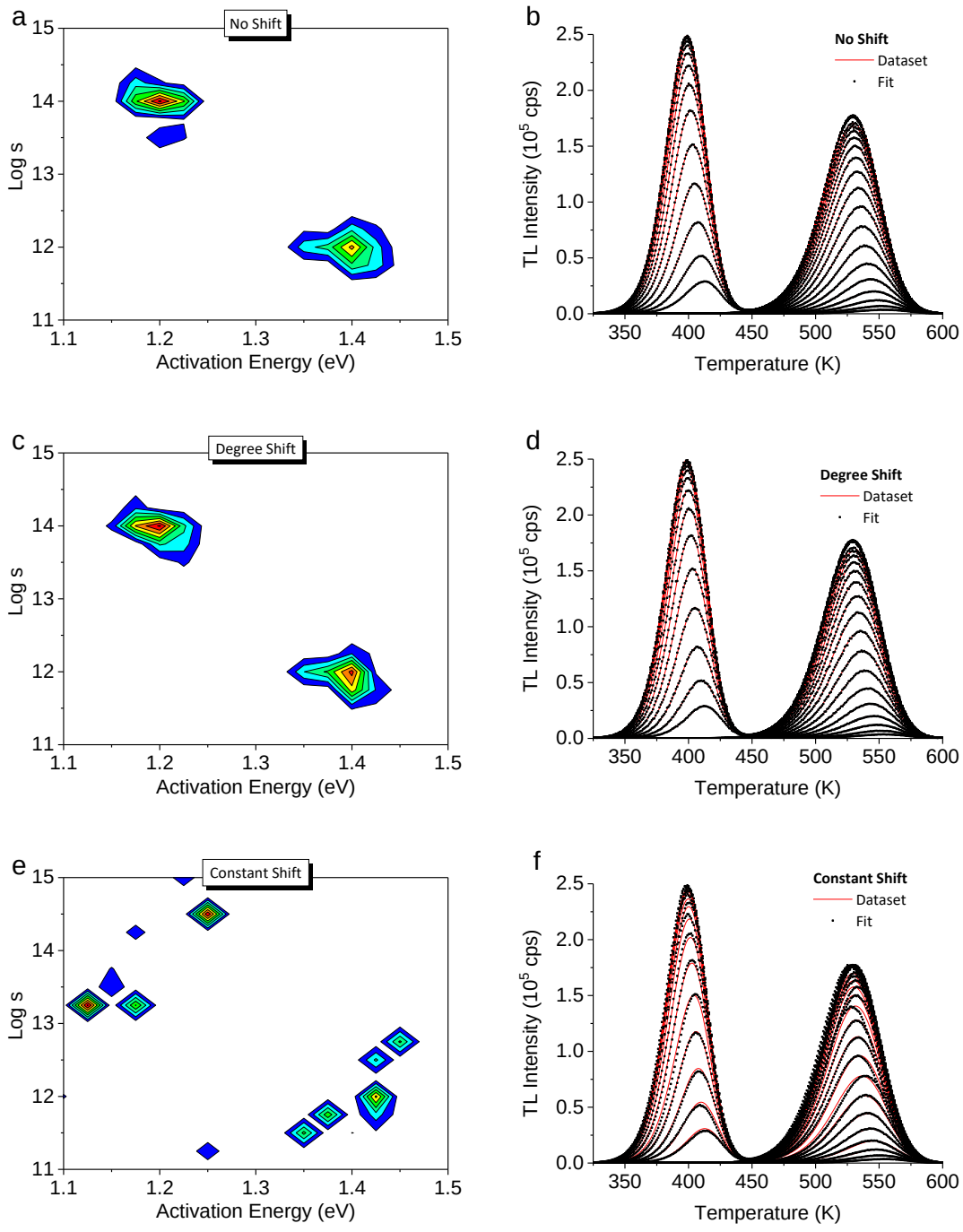

Figure 5-30. Two-dimensional deconvolution results for datasets simulated using (a) no shift, (c) degree shift, and a (e) constant shift in the linear heating profile. The models obtained from the deconvolution are plotted against the input dataset for the cases of (b) no shift, (d) degree shift, and a (f) constant shift in the linear heating profile.

5.8 Discussion

The data presented here attempts to provide a comprehensive understanding of the advantages and limitations of the two-dimensional deconvolution methods as applied to noise added step-annealed and varied heating rate datasets. While curve fitting using various functional forms of both first and general-order TL curves has seen heavy use in the attempt to characterize TL trap parameters, the two-dimensional deconvolution method presented by Whitley et al. (2002) has received minimal interest and, thus, its advantages and limitations are not well known. The success of the deconvolution method is reliant on distinct changes in a TL curve as a result of small changes in an experimental variable such as heating rate, or as we suggest, hold temperature.

We found, just as Whitley et al. (2002) did, that without the additon of Poisson noise both the θ-dataset can accurately obtain the input dataset (Figure 5-3). However, we did find that for the addition of noise the θ-dataset outperforms the β-dataset. This is due in part to the step-annealed dataset's stronger coupling between hold temperature and change in the TL curve shape than heating rate. Additonally, depending on the range of heating rates used, β-dataset curves are less distinct from each other and thus the deconvolution apporach is more sensitive when noise is added.

We found the two-dimensional method to be sensitive to various parameters including deconvolution method, S/N, and parameter space resolution. When presented with low signal, the background noise becomes a dominant component of the curve leading the deconvolution method to "fit the noise" producing many spurious trapping centers corresponding to TL peaks intended to account for these noise induced features. High signal with respect to background produces a nearly noiseless curve and both the heating rate and step-annealed datasets perform well. When dealing with the simulated TL curves (small dataset) with max intensities in

the 10^5 – 10^6 counts per degree range, both methods fail to reproduce the simulation inputs. It should be noted that these results are for simulated TL curves only, under experimental conditions TL intensities and noise levels will vary with the experimental system.

Perhaps, one of the major limitations of the two-dimensional deconvolution is the choice of parameter space resolution. We found that choices of fine grid spacing produced solutions spaces with groupings of individual trapping centers instead of the multinormal input distributions. Resolutions that were too coarse produced solution spaces with trapping center distributions, but were not at the appropriate locations. The effect of tuning this parameter allows for human bias and is seen as a major limitation of the approach. It is suggested on start with a coarse resolution and a large constraining dataset and work to finer gridding, keeping track of resolutions that produce consistent results and compare with additional approaches such as initial rise and methods of various heating rates when applicable.

We found that the two-dimensional deconvolution method performance was sensitive to noise and dataset size when dealing with step-annealed curves. For smaller curve sets (n = 7), the deconvolution method obtained the input distribution for the two-trap case, but was unsuccessful for the three- and four-trap cases. The expansion of the three-trap and four-trap cases to larger datasets (n=22 and n=33 respectively) improve the obtained distribution as compared to the input distribution and the n=7 results. The four-peak case still failed to obtain four distinct trap parameter distributions suggesting that both a larger dataset as well as high intensity are required to recover the input distribution as without noise both the heating rate and step-annealed (Figure 5-3) datasets can obtain the input distribution.

As noise will dominate low intensity TL peaks which are produced by the low occupancy traps found at the edges of the multinormal distribution, we cannot expect the two-dimensional deconvolution method to fully replicate the entire input distribution, but the poor performance

for the three- and four-trap cases (n = 7) despite each set containing distinctly different TL curves suggest noise is a dominating factor. The improvement of the results when using larger datasets (n = 22, n = 33) suggests that the effect of Poisson noise can be accounted for by further constraining the dataset. While one can easily produce many TL curves for either the heating rate or step-annealed datasets, not all curves will be sufficiently distinct from one another. Whitley et al. (2002) suggested using heating rates spaced at order of magnitude which requires precise heating equipment, a significant time investment, and limits the number of TL curves obtainable on a commercial TL reader. Furthermore, choosing smaller spacings than those used in this study produces curves that are similar both in position and shape which is further complicated when noise is present. A large number of step-annealed curves is easily obtained on most commercial TL readers and given the appropriate hold duration there exist a strong coupling between minor changes in hold temperature and annealed curve behavior. The down side of such an approach is that it requires accurate knowledge of the heating profile as well as the decrease in S/N ratio for high temperature peaks, as they will be fully depleted once they are resolved by the step annealing process.

The use of an extrapolation method was presented to help provide additional insight into the performance of the parameters obtained from the two-dimensional deconvolution. For small (n = 7), noise-added datasets, the contours demonstrated that the parameter distributions were the most accurate (low reduced-chi-squared metric) when applied to heating profiles most similar to those used to produce the constraining datasets. When using larger datasets, a larger range of heating profiles produced low reduced-chi-squared values suggesting that larger datasets are preferred to constrain the deconvolution. The results also indicate that if possible, the use of multiple, distinct heating profiles (e.g. hold times separated by order of magnitude) to produce appropriate datasets is preferred.

The results on the applicability of the traditional analysis methods (IRM and VHRM) demonstrate their limitations when dealing with complicated trap distributions. The IRM is only able to resolve activation energy and does a good job of identifying plateaus centered about the mean value of the multinormal distributions and within one FWHM, but the IRM is unable to resolve the underlying distributions nor the correct number of trapping centers (4-trap case). The VHRM is intended to be applied to well isolated TL peaks as an accurate recording of peak position is required making its use for peak directions here ill advised. The results in Figure 5-26 show that the method is able to approximate the mean value of the leading peaks parameter distribution, but it performs less well for subsequent peaks where there exists a high degree of overlap. The limitations of the traditional methods for highly complicated peaks highlights the potential utility of the two-dimensional deconvolution method for materials such as those used for temperature sensing.

Ultimately, the results presented within this work are the result of a purely mathematical solution based on the *a priori* assumption that all peaks within the simulated materials obey first-order kinetics. This approach ignores trap interaction, see Sakurai (2001), and tunneling effects, and it is therefore, limited with this regard. Additionally, we did not dedicate extensive time to the subject of the solution space resolution. The effect of this parameter is of additional concern with regards to its application to a material with an unknown trap distribution. The deconvolution relies on solution curves that are generated from a parameter space using an accurate heating profile and inconsistencies between the model and constraint dataset will result in incorrect results. An additional avenue of study would be the application of the two-dimensional deconvolution approach to simulated datasets obtained from many discrete trapping centers (e.g. >10). If the underlying traps produce peaks close in

proximity traditional curve fitting using first- or general-order fits will prove difficult and incorrect if the wrong number of peaks are identified in the TL curve of interest.

CHAPTER 6

KINETIC PARAMETER ANALYSIS OF NOVEL TEMPERATURE SENSING MATERIALS

In Section 2.3.3, we presented a discussion of novel TL materials LBO:Cu,Ag (LBO), MBO:Dy,Li (MBO), and CSO:Ce,Tb (CSO) for use in temperature sensing applications. Noticeably lacking from that discussion was a presentation of accepted values for trap parameters of these materials. A set of values was presented in Table 2-1 for LBO, but all but one study for peak 3 were obtained using a single method, GCDC, and assumed a discrete three-peak system. This is in contrast to the studies by Doull et al. (2014) which presented evidence for a more complex peak distribution. An accurate TL model is essential for the accuracy of thermal history reconstruction, and therefore, the goal of this study is to characterize the trap parameters of the novel TL materials. As an extension of this goal, we will investigate the materials for thermal quenching as the presence of this effect will skew the results of the analysis methods.

The investigation to obtain trap parameters for the novel materials was conducted using three different analysis methods: VHRM, IRM, and two-dimensional deconvolution. VHRM was used to obtain *E*-*s* values for each identifiable peak, while IRM results in *E* values only. The IRM was used to obtain E-T_{stop} results following the methods previously outlined in Section 3.4.2, including *E*-distributions from the "Van den Eeckhout" and search-method analyses. Two-dimensional deconvolution was used to obtained *E*-*s* distributions from step-annealing data previously used to obtain TL models of the same novel materials using two-dimensional deconvolution methods (Yukihara et al., 2014b).

In addition to the trap parameter analysis techniques, we studied the material for evidence of thermal quenching through analysis of the VHRM datasets. We looked at the change in the normalized TL curve area as a function of heating rate and employed TL models based on one-dimensional deconvolution models to predict each materials' response to changes in heating rate. The result of these efforts was used to determine if thermal quenching exists for a given material, but no effort to model the quenching parameters was made.

A thorough discussion of each material and the results of the various analysis method is presented at the end of each material subsection. The results of the quenching analysis suggest that both LBO and CSO suffered from thermal quenching. While this does not prohibit the use of these materials for temperature sensing, it does present difficulties in obtaining an accurate TL model for those materials. We attempted to apply the analysis method by Subedi et al. (2010) to obtain a correction function, but found the results to be poor and the use of the analysis would introduce more error then it would correct and have therefore left them out of the present study.

Analysis of MBO initially showed apparent thermal quenching, but analysis performed on a sample from a more recent synthesis shows no quenching, suggesting the older material degraded in storage or a variation in reagents used during synthesis was to blame. Trap parameters for MBO were found to be consistent among the methods investigated and present a set of parameters usable for building a temperature sensing TL model.

In conclusion, trap parameters were obtained for each of the novel materials and determinations of thermal quenching were made. MBO results showed consistency across all analysis method and did not display thermal quenching making it the most promising material for temperature sensing amount those investigated.

6.1 $Li_2B_4O_7$:Cu,Ag (LBO)

6.1.1 Various Heating Rate Method

VHRM was applied to a total of three LBO aliquots of (0.5 ± 0.1) mg from the control samples of the NSWC-2013 experiment. Sample sizes were chosen to minimize thermal lag between the heating element and TL material and were scattered to cover the base of the steel sample cup. Particle sizes were selected to be between 53 µm and 75 µm using sieves, but no efforts were undertaken to account for aggregation. TL curves were collected following a dose of ~10 Gy and a 120 s pause. Figure 6-1a shows the TL curves obtained from the LBO samples for various heating rates, with numbers to denote the approximate location of the TL peaks.

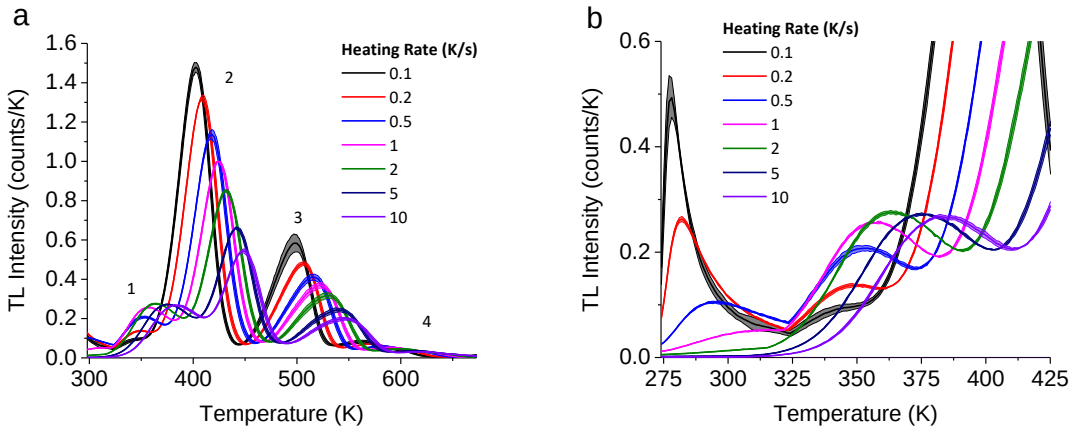

Figure 6-1. (a) TL curves obtained for the LBO samples for various heating rates. Each heating rate curve is the average of three aliquots and the shaded region indicates one standard deviation. (b) Zoomed-in section of (a) to better resolve the behavior of the low temperature peak.

The TL peaks in Figure 6-1a show an increase in peak position with increasing heating rate, but peaks 2 and 3 show a much larger decrease in TL intensity then one would expect from first-order TL peaks, see Figure 2-7. In addition to the intensity decrease, peak 3 displays a distinct change in peak shape, suggestive of thermal quenching. The TL emission data for LBO obtained by Doull et al. (2014) shows a broad emission for Cu^+. Broad band emissions are typically associated with the presence of thermal quenching of that luminescence center (Blasse

and Grabmaier, 1994). We will proceed presently with the VHRM and investigate the potential thermal quenching effects in the following subsection.

Figure 6-1b shows an enlargement to better visualize the behavior of peak 1 from Figure 6-1a. The normal behavior for a TL peak with increasing heating rate is for it to decrease in intensity while broadening to maintain the area. Such behavior is not evident for the first TL peak, which increases in intensity until the heating rates of (2 – 10) K/s. Figure 6-1b shows that, for readout temperatures below 50 °C, there is strong evidence for decay behavior from the low temperature TL peak for heating rates of (0.1 - 0.5) K/s, which is evidence for room temperature phosphorescence and is assumed to be the reason for the decreases in intensity and definition of the first TL peak.

Figure 6-2 shows the VHRM datasets, $1/T_m$ versus $\ln \beta/T_m^2$, for the LBO samples. Unweighted linear fits were obtained in *Origin 2017* for the VHRM datasets for each sample, and the slope and y-intercept were used to obtain the trap parameter values. The results from the varying heating rates analysis are provided at the end of the subsection with all other analysis methods (Table 6-1).

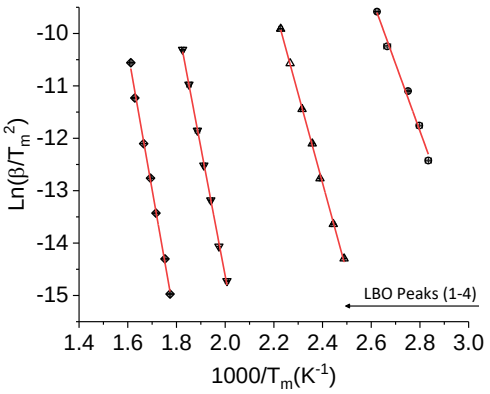

Figure 6-2. VHRM analysis data for the LBO samples. Unweighted linear fits for each peak are shown as traces. Data is the average of three aliquots where error bars represent one standard deviation.

6.1.2 Thermal Quenching

In the previous section, we suggested that the peak behavior from peaks 2 and 3 in Figure 6-1a was indicative of thermal quenching. First, we will investigate this possibility by studying the changes in TL curve area as a function of heating rate and modeling the expected TL curve changes using a simplistic one-dimensional deconvolution model.

Whole Curve Analysis

Figure 6-3 shows the total TL area as a function of heating rate obtained from the background subtracted TL curves used to obtain the VHRM datasets. Total TL area was normalized to the 0.1 K/s heating rate, as it is assumed to be the curve least effected by thermal quenching. A clear decrease in TL area is observed (Figure 6-3), indicating at least one TL peak suffers from thermal quenching for the heating rates investigated.

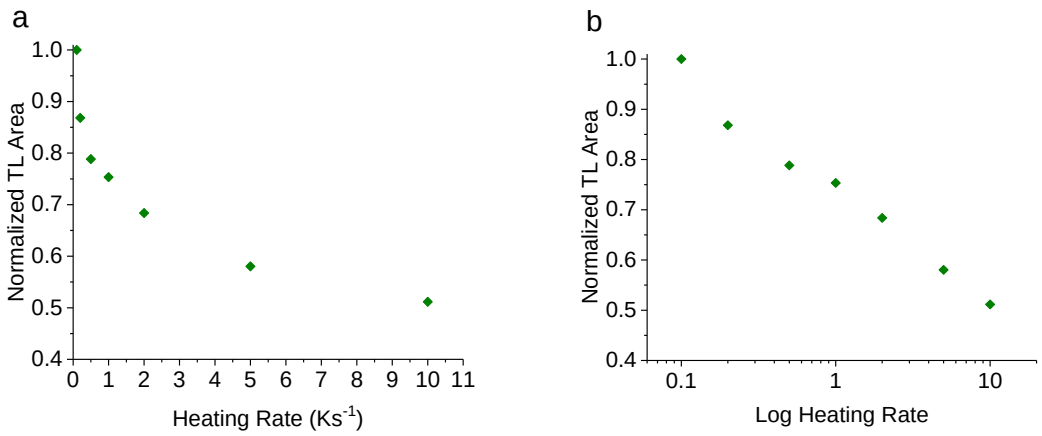

Figure 6-3. Normalized TL area for the LBO VHRM dataset in (a) linear and (b) linear-log scales.

TL Model Analysis

In addition to tracking the total curve area, we investigated the expected TL curve changes due to variations in heating rate using a TL model based upon the one-dimensional deconvolution method. We began by assuming the TL curve obtained at 0.1 K/s was

unquenched and obtained the underlying activation energy distribution using a one-dimensional deconvolution. Then, we modeled the unquenched TL curve at the heating rates used in Figure 6-1 to compare with the experimental data in Figure 6-1 for the < 1 mg samples.

Figure 6-4a shows the activation energy distribution obtained by performing a one-dimensional deconvolution on the 0.1 K/s heating TL curve from the VHRM dataset on a single aliquot of LBO. The deconvolution used 50 activation energies with peak maxima located at temperatures across the entire readout temperature axis for a resolution of ~ 0.02 eV in activation energy. Focusing our attention to TL peaks 2 and 3, we see the model undergo the expected decrease and broadening with an increase in heating rate, but the experimental data decreases at a much faster rate. Additionally, the experimental data shows major shifts in TL peak position and shape when compared to the simulated results. While this observation is not definitive, it is compelling evidence for the presence of thermal quenching.

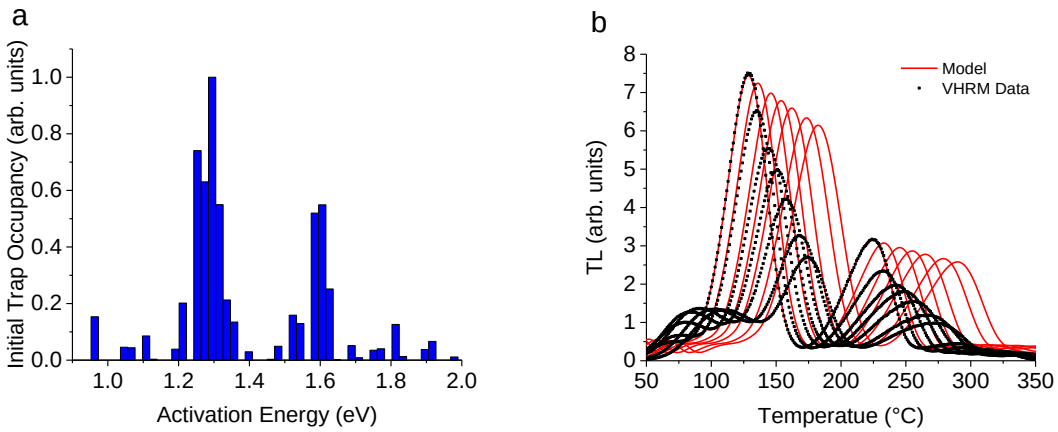

Figure 6-4. (a) TL model using the one-dimensional deconvolution method and a (b) comparison the VHRM dataset and a simulated VHRM heating rate dataset obtained using the TL model.

6.1.3 Initial Rise Method

The IRM was applied to data obtained for both NSWC-2013 and NSWC-2012 sample. The results for the NSWC-2013 data were obtained using a linear heating ramp, whereas those

for the NSWC-2012 data were obtained using a T_{hold} heating scheme and are presented separately within this section.

Linear Heating Ramp

For this analysis, we used a total of three aliquots of LBO with masses of (1.07 ± 0.06) mg from NSWC-2013 control samples. Particle sizes were the same as those used for the VHRM (53 µm < x < 75 µm). TL curves were collected following a ~10 Gy beta irradiation. A 120 s pause followed the irradiations and a longer pause of 180 s followed the linear heating ramp as an effort to reduce the effect of room temperature phosphorescence.

Figure 6-5 shows representative TL curves obtained from the step-annealing procedure (Section 3.4.2). From the curves, a total of five TL peaks could be identified with a possible sixth peak observed at a readout temperature of ~650 K (Figure 6-5b). A sequential depletion of each peak was observed with increase in stopping temperature, while each peak position was found to shift to higher temperatures with each increase in T_{stop}. The increase in peak position is thought to be the result of either 2nd order kinetics (McKeever, 1985), or highly overlapped first-order TL peaks (Kierstead and Levy, 1991). Dose response data collected by Doull et al. (2014) showed the main LBO peak (#2 in Figure 6-5) position to remain approximately constant with dose, suggesting first-order kinetics. Thus, the change in peak position we observed in Figure 6-5 suggests the presence of multiple first-order TL peaks. Doull et al. (2014) found peaks 1 and 3 to change shape with increase in dose, which the authors suggest to be the result of sensitization and does not preclude the existence of multiple overlapping peaks producing peaks 1 and 3. Figure 6-6 shows a representative IRM data set for the dataset presented in Figure 6-5 using the 5% intensity threshold.

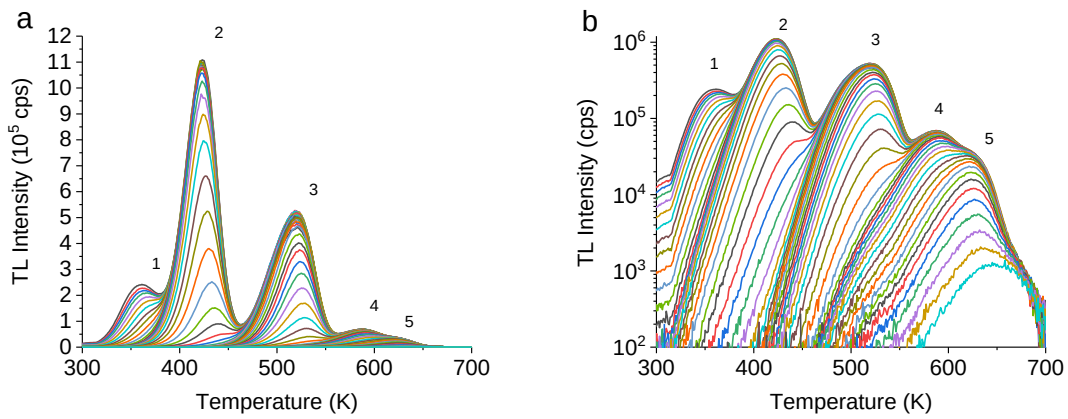

Figure 6-5. Step-annealed TL curves for a single aliquot of LBO originally placed in position 8. TL curves have been background subtracted and are shown in (a) linear and (b) log scale. Peak positions are indicated within each figure. Each color represents a different T_{stop} temperature.

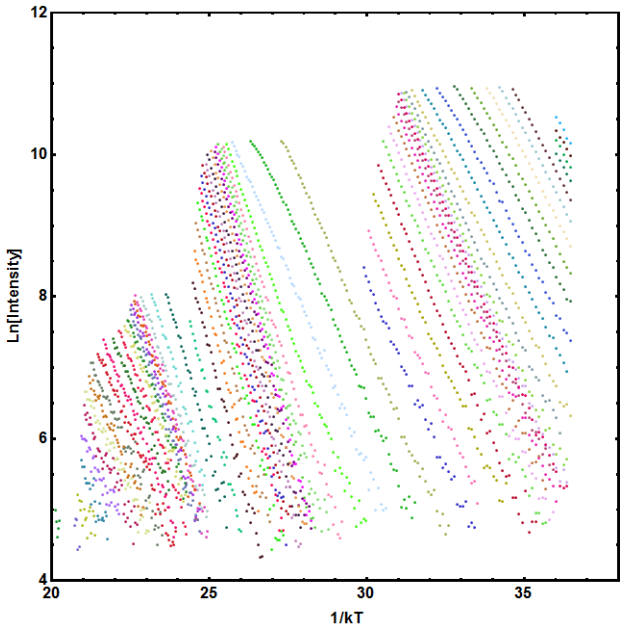

Figure 6-6. Analysis dataset for a single aliquot of LBO, "pos. 8". Data appears as diagonal bands with each change in color representative of a different T_{stop} temperature, which increases from right to left.

Linear fits of the IRM datasets were used to obtain activation energies for each T_{stop} temperature for each aliquot. The activation energy and peak position were obtained for each T_{stop} temperature. The averaged values across all three aliquots are presented as overlaid E-T_{stop} and T_m-T_{stop} plots in Figure 6-7a. The T_m-T_{stop} results suggest the presence of 5 distinct TL peaks as

indicated by the plateaus in Figure 6-7a. Three distinct plateaus were observed in the E-T_{stop} graph indicating the presence of three main peaks. Beyond the T_{stop} temperature of ~550 K, the system noise was too high producing poor linear fits, and therefore, no additional plateaus were identified despite the results of the T_m-T_{stop} plot suggesting additional peaks beyond the first three.

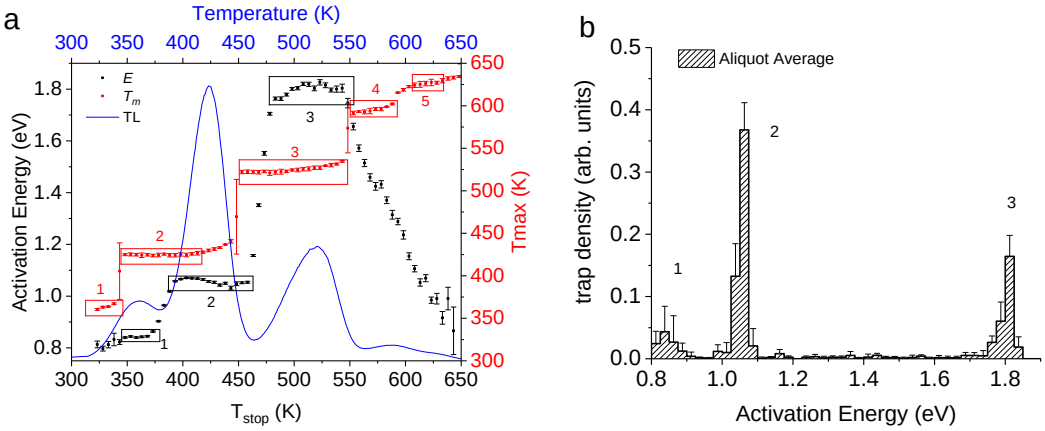

Figure 6-7. (a) IRM results for 5% method presented as overlapping E-T_{stop} and T_m-T_{stop} plots and as a (b) trap density distribution. The results, in both plots, were obtained as averages across three aliquots. Error bars represent one standard deviation. Numbers correspond to the TL peaks in Figure 6-5.

Additionally, we observed the flat portions of the T_m-T_{stop} plateaus did not coincide with the flat regions of the E-T_{stop} plateaus. The E-T_{stop} plateaus instead most closely lined up T_{stop} temperatures where the peak position had begun to trend towards to higher temperatures. These results were also observed in the simulations for highly overlapped peaks (Chapter 4).

Figure 6-7b shows the trap density distribution obtained using the "Van den Eeckhout" method to the IRM results in Figure 6-7a. Approximate peak positions are denoted by numbers 1-3 and correspond respectively to activation energies of ~0.84 eV, ~1.06 eV, and ~1.81 eV. These values line up with plateaus observed in Figure 6-7a as a result of the trap density distribution being weighted to the depletion in curve area. Activation energies between 1.1 eV and 1.7 eV correspond to T_{stop} temperatures above 550 K and the relatively low trap density

indicates these energies correspond to TL curves for which a negligible change in TL area was observed between successive T_{stop} temperatures.

Figure 6-8 shows the results of the search method as applied to the IRM data for the three LBO aliquots used in this study. The search method scans the region of the IRM data between the threshold intensity and the peak position for the combination of start and ending points that produces the lowest reduced chi-squared value. Small variances in sample size, distribution in sample holder, environment, and noise exist. Thus, we do not expect all aliquots to produce identical results, but we do expect trends to be present.

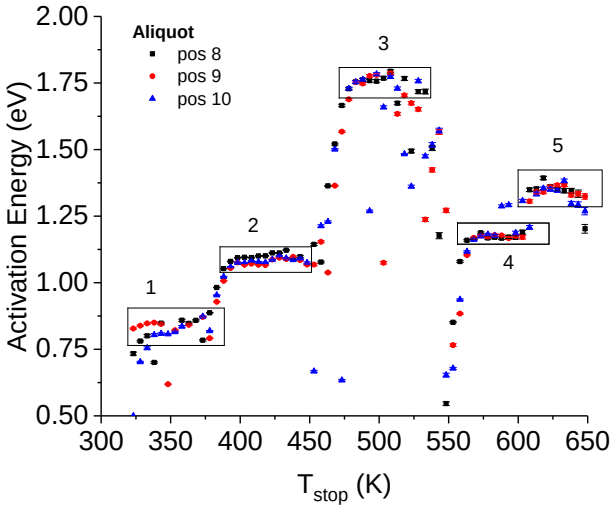

Figure 6-8. Search method results for three aliquots. Groupings of activation energies are indicated by numbered boxes and correspond to TL peaks. Numbers correspond to the TL peaks in Figure 6-5.

A total of 5 distinct plateaus were observed in Figure 6-8 and are indicated by numbered boxes. Placement and dimensions of the boxes were made using best judgement and are therefore to be treated with reservations, but no established method exist to correctly identify plateau regions for IRM results. The search method is able to identify a fourth peak (T_{stop} ~500-600 K) and a fifth peak (T_{stop} ~600-650 K) which correspond with the 4th and 5th T_m-T_{stop} plateaus in Figure 6-7a. The mean values of each activation energy value (without error bars) within a

given box in Figure 6-8 were used to compute a box average and standard deviation which are presented in Table 6-1.

Hold Temperature Results

Analysis in this section was conducted using material from control samples of the NSWC-2012 DTRA test. Results were obtained from the analysis of a single aliquot of LBO comprised of a few grains (<< 1 mg). The dopant concentration for these samples is 0.3% for each co-dopant, different than concentrations shown in the prior results. Step-annealed datasets, referred to as T_{hold}, were obtained according to the procedure outlined in Section 3.4.2. Data were obtained using a dose of ~10 Gy. Example analysis curves (Figure 6-9a) show the existence of an additional TL peak in the high temperature region, indicated by peak 3a and 3b. Figure 6-9b shows the difference between the NSWC-2012 (LBO:$Cu_{0.3\%}$,$Ag_{0.3\%}$) TL curve and the NSWC-2013 (LBO:$Cu_{0.4\%}$,$Ag_{0.1\%}$) TL curve. No information was available for grain size.

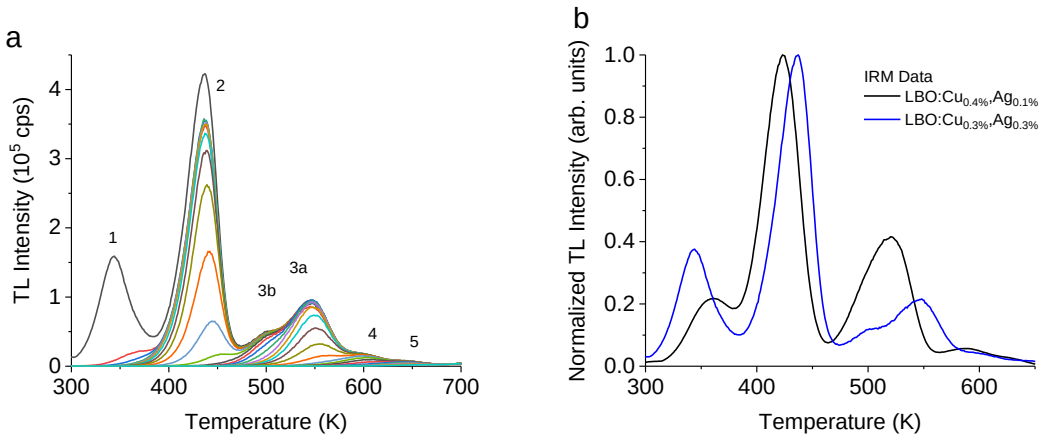

Figure 6-9. (a) TL curves obtained following a pre-heat to a set temperautre and a hold for 5 min and (b) a comparison between the TL curves for NSWC-2012 and NSCW-2013 as a result of different dopant concetrations.

Figure 6-10 shows the results of the IRM data analysis applied to the T_{hold} dataset in Figure 6-9a. E-T_{hold} results show three activation energy plateaus at ~ 0.8 eV, ~1.15 eV, and ~1.8 eV, which correspond roughly with the plateaus from the E-T_{stop} results. In contrast the

result for peak position, T_m, as a function of stopping or hold temperature vary by ~ 10–30 K, but still account for the same number of identifiable TL peaks (low temperature peak for T_{hold} not shown). The results suggest that the differences in dopant concentration are strongly reflected in the changes to TL curve shape and peak position but do not strongly affect the trapping center depths.

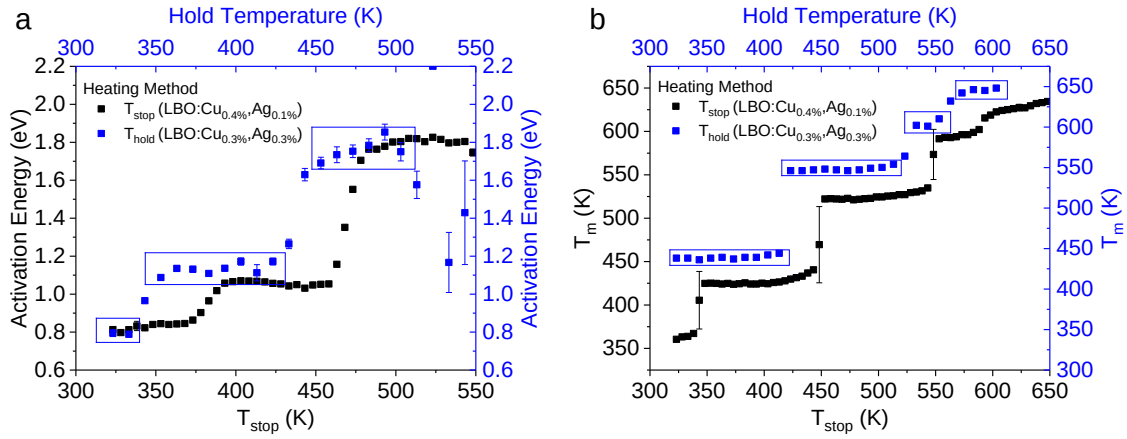

Figure 6-10. Comparison of the IRM results for the two different LBO samples shown as (a) E-T_{stop} and (b) T_m-T_{stop} plots. Error bars in (a) are given as fitting uncertainties for T_{hold} results and the uncertainty of a three-aliquot average for the T_{stop} results.

6.1.4 Two-dimensional Deconvolution

A subset of the dataset presented in Figure 6-9a was used to obtain a trap parameter distribution following the two-dimensional deconvolution method (Section 3.4.4). Following background subtraction, it was observed that the analysis curves displayed a constant vertical offset for the first 25 – 50 data points. Therefore, for all curves an additional background subtraction was conducted by subtracting the mean value of each curves first 30 data points (0°C – 30°C). The results of this additional background subtraction are shown in the analysis curves for the deconvolution procedure in Figure 6-11.

Figure 6-12 shows the results of the two-dimensional deconvolution for three different solution space resolutions. The solution space included activation energies from 0.8 eV to 2.9 eV

and frequency factors in log *s* from 8 to 20. The results in Figure 6-12 show no clear distribution and the results vary greatly with changes in the solution space resolution. Additionally, a larger number of the peaks in the solution space were found to have very high frequency factors, which is not consistent with any of the previous results. High frequency factor values produce very narrow TL peaks and their presence in the solution space indicates either an overfit or attempts to fit systematic noise.

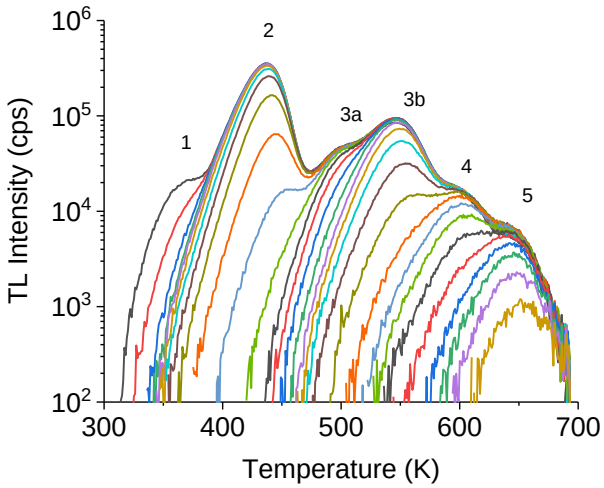

Figure 6-11. Analysis TL curves used for two-dimensional deconvolution. The dataset is comprised of 30 curves chosen for hold temperatures that resulted in large changes in total TL curve area.

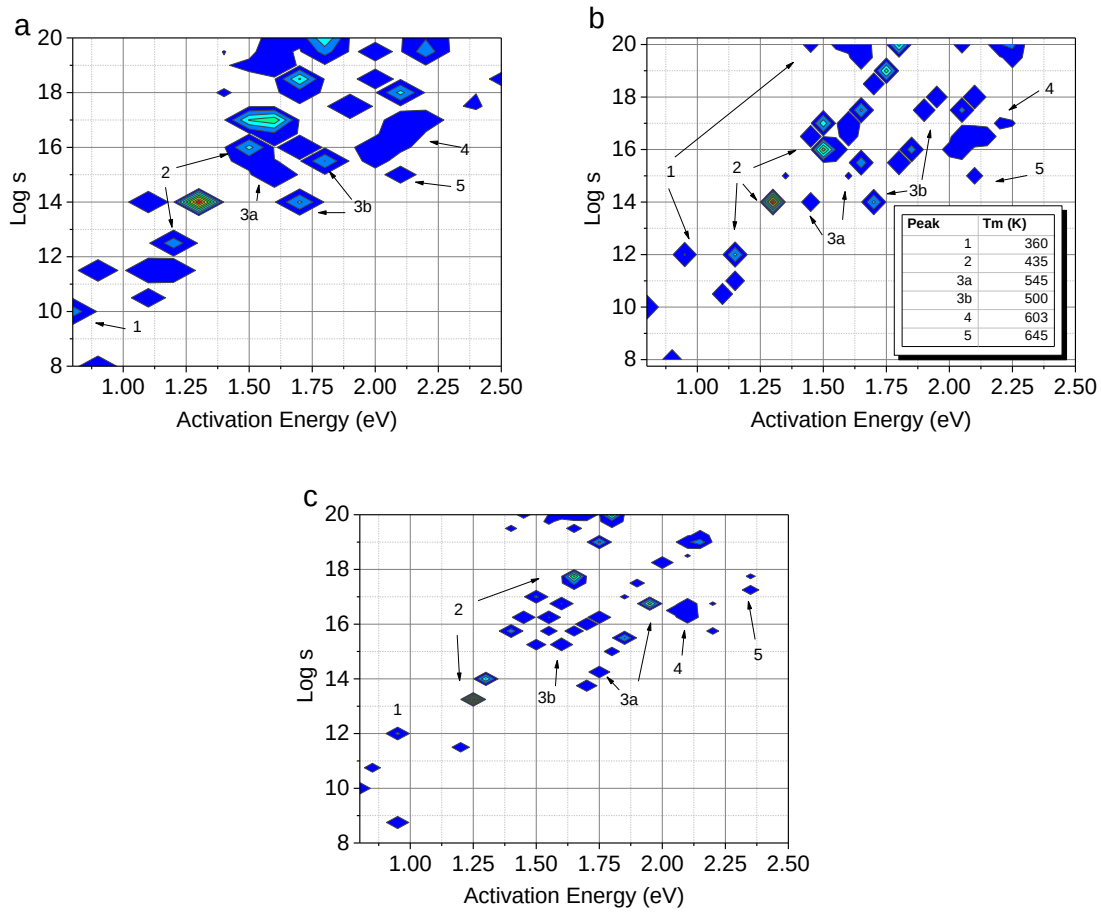

Figure 6-12. Trap distribution obtained from two-dimensional deconvolution using a solution space resolution of (a) ΔE =0.1 eV, Δlog s = 0.5 log s (b) ΔE = 0.05 eV, 0.5 log s and (c) ΔE = 0.05 eV, 0.25 log s. Trap distributions are matched with their corresponding TL peak position using Equation 2-9. Peak positions are displayed in the table of plot (b).

The results in Figure 6-12 do not suggest the underlying trap distribution to be of a known form, such as Gaussian, but rather a grouping of highly overlapped, discrete trapping centers. Additionally, we must point out that efforts to obtain a correct distribution of a thermally quenched dataset without correction will result in incorrect trap parameters, which in turn introduce error into the trap distribution results. Although these results are highly sensitive to solution space resolution, they provide a better fit to the dataset then the results in Yukihara et al. (2014b), suggesting that this model, while incorrect, is an improvement on the results of

the one-dimensional deconvolution (fixed log *s* = 14). This is easily seen by the presence of only the main TL peak having a frequency factor near the value of log *s* = 14.

6.1.5 Parameter Discussion

Table 6-1 displays the values for all the trap parameters obtained using the analysis methods in this section. Activation energies and peak positions obtained from IRM analysis were obtained as averages within a plateau region of interest signified by boxed data (e.g. Figure 6-8). The uncertainties were calculated following traditional uncertainty propagation methods (Taylor, 1997). All peak positions are presented for curves obtained using a 1 K/s heating rate.

Table 6-1. Summary of LBO trap parameters obtained using the analysis methods presented in this section. Uncertainties less than 10 meV in activation energy are not reported.

Peak	Parameter	VHRM	IRM (T_{stop})	IRM(Search)	IRM(T_{hold})
1	E(eV)	1.14 ± 0.06	0.846	0.82 ± 0.03	0.79 ± 0.01
	s (s^{-1})	2.4 x 10^{14}	-	-	-
	T_m (K)	357.5 ± 1.5	363.7 ± 0.5	-	-
2	E(eV)	1.47 ±0.01	1.06	1.09 ± 0.01	1.13 ± 0.01
	s (s^{-1})	2.4 x 10^{16}	-	-	-
	T_m (K)	424 ± 1	425.0 ± 0.5	-	439 ± 2
3	E(eV)	2.10 ± 0.03	1.80	1.75 ± 0.02	1.76 ± 0.02
	s (s^{-1})	1.9 x 10^{19}	-	-	-
	T_m (K)	523 ± 2	525.3 ± 0.5	-	548 ± 3
4	E(eV)	2.27 ± 0.03	-	1.18 ± 0.01	-
	s (s^{-1})	2 x 10^{18}	-	-	-
	T_m (K)	590 ± 1	595 ± 0.7	-	604 ± 5
5	E(eV)		-	1.34 ± 0.02	-
	s (s^{-1})	-	-	-	-
	T_m (K)		627 ± 1	-	645 ± 3

The values presented in Table 6-1 for peaks 2 and 3 do not agree with those found in literature (Table 2-1). Activation energies for peaks 2 and 3 are consistent for all methods except the VHRM, which are significantly larger than those obtained using the other analysis methods. We suggest this is the result of two factors: (1) individual TL peaks are the result of several overlapping peaks of varied trap depths and (2) thermal quenching of luminescence centers.

Doull et al. (2014) suggested that the main TL peaks were the result of a distribution or superposition of TL peaks based on step-annealed data, which showed changes in peak position despite evidence of approximately first-order kinetics. We found similar results for the peak position increase for both methods of step-annealing. We also used the VHRM trap parameters in Table 6-1 to simulate first-order TL peaks for a heating rate of 1 K/s. A comparison between the simulated TL curve and the 1 K/s curve from Figure 6-1a is shown in Figure 6-13. A clear difference can be seen between the simulated and experimental peak shapes and suggests more peaks are present then were accounted for in the analysis. Additionally, the results from two-dimensional deconvolution, though unreliable, suggest each main TL peak is comprised of a superposition of several discrete peaks.

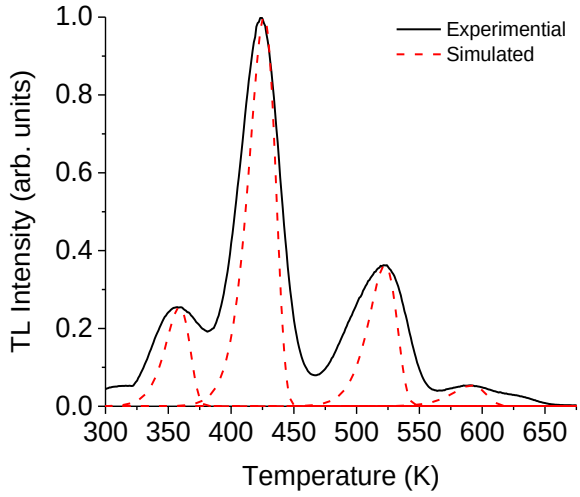

Figure 6-13. Comparison between simulated (using VHRM results) and experimental TL curves for LBO using a 1 K/s heating rate. Simulated TL peaks were normalized to the max intensity of the respective experimental TL peak.

Ultimately, the results do not present a usable TL model for temperature sensing. If LBO is to be used as a temperature sensing material, the issue of thermal quenching must be addressed and an accurate correction function obtained.

6.2 MgB_4O_7:Dy,Li (MBO)

6.2.1 Various Heating Rate Method

The VHRM was applied to a total of eight aliquots of MBO. Six aliquots were prepared from NSWC-2013 control material all with a mass of ~ 1 mg with three aliquots receiving a dose of ~ 5 Gy and the other three receiving a dose of ~ 10 Gy. Particle sizes (or aggregate size) were selected to be less than 125 μm. Initially, the ~ 10 Gy dose was used for consistency with the VHRM analysis of the other TL materials, but an additional dataset using the ~5 Gy was collected to avoid possible PMT saturation effects. A 2 min pause followed the irradiation of the sample. Two additional samples of ~ 1 mg of control material from a more recent detonation ("NM" tests) were also used for VHRM analysis. Data collection for the NM samples used a smaller dose of ~ 1 Gy in attempts to avoid sensitization effects. A total of seven heating rates between 0.1 K/s and 10 K/s were used for this study. For the NWSC-2013 datasets, the heating rates were incremented sequentially, but the NM samples used a randomized order (10, 1, 0.5, 2, 0.2, 5, 0.1) K/s. Figure 6-14 shows the results of the VHRM data collecting and analysis for the three NSWC-2013 (~5 Gy) samples and the two NM samples.

TL curves are presented as an average of the analysis curves. Figure 6-14a shows a large uncertainty in TL intensity for the two higher heating rates of 5 K/s and 10 K/s. The size of this error is larger than that found in the lower heating rates. This result is assumed to be the result of either inconsistent heating of the samples at the higher heating rates or material degradation. Furthermore, the NSCW-2013 samples show a strong decrease in main peak intensity but an increase in the second peak intensity. These results would suggest thermal quenching of the first TL peak and sensation of the second TL peak, but we do not expect

quenching of the Dy^{3+} luminescence center due to its line emission in TL emission data (Blasse and Grabmaier, 1994; Doull et al., 2014).

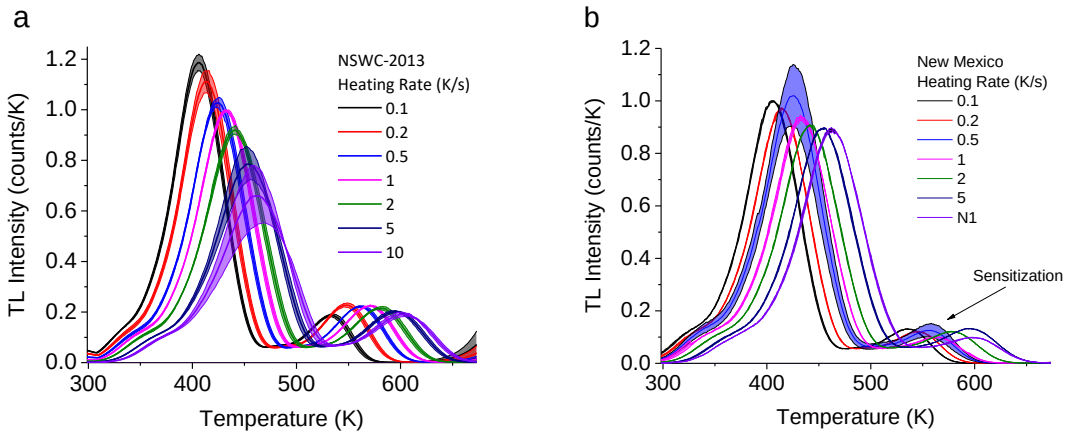

Figure 6-14. (a) TL curves obtained for NSWC-2013 aliquots using various heating rates. Each heating rate curve is the average of three aliquots and the shaded region indicates one standard deviation. (b) Average (two aliquots) TL curve data for the NM samples. Uncertainties represent a single standard deviation.

Additional data using a more recently synthesized material, NM sample, was collected to determine if the quenching result was real or an effect of material degradation in storage. The results of the VHRM data collection for the NM sample (Figure 6-14b) show a more reasonable decrease in the main peak intensity. Sensitization is still present for the second TL peak and is more prominent due to the randomization of the heating rate order. Attempts to correct for the sensitization were unsuccessful and are not discussed here. We have no explanation for the sudden increase in main peak intensity for the 0.5 K/s heating rate, and this effect was found for multiple samples but was random and could not be replicated and, therefore, is assumed to be the result of systematic error (e.g. incorrect dose, cup placement, etc.).

The data used for linear fitting are displayed in Figure 6-15. The data for both NM samples and NSWC-2013 samples follows a linear trend for both peaks. The result fitting results from Figure 6-15 are available in Table 6-2 and show relatively good agreement among all

samples for the activation energy of the first TL peak. The frequency factor for the NM samples is almost two orders of magnitude larger than that of the NSWC-2013 samples despite the similar activation energy and peak position. There is a large difference between the VHRM result for the NSWC-2013 data for the second TL peak for the ~ 5 Gy and ~10 Gy samples and is assumed to be the effect of sensitization, which results in both an increase in peak intensity as well as a shift to higher temperatures; see the dose response results from Doull et al. (2014) for more detail. We also see moderate agreement between the activation energies of peak 2 from the NM and NWSC-2013 samples when accounting for uncertainties. Furthermore, the frequency factor values are within an order of magnitude.

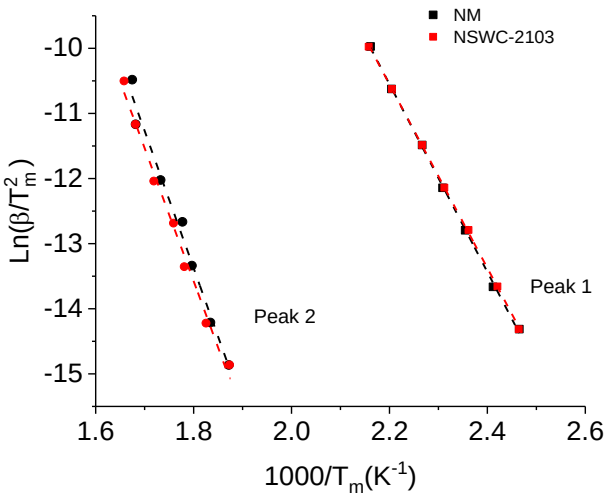

Figure 6-15. Representative VHRM data for the NSWC-2013 and NM samples with linear trend lines.

Table 6-2. MBO kinetic parameters obtained using the VHRM. Peak positions provided were obtained using the 1 K/s heating rate. A single sample was used to obtain the 10 mg result while the average and standard deviation of three samples are presented for 1 mg (both dose values).

Peak	Parameter	1 mg (NM)	1 mg (10 Gy)	1 mg (5 Gy)
1	E (eV)	1.24 ± 0.01	1.21 ± 0.05	1.23 ± 0.02
	s(s^{-1})	9.5 x 10^{14}	2 x 10^{13}	2 x 10^{13}
	T_m (K)	433	432 ± 2	434 ± 1
2	E (eV)	1.81 ± 0.01	1.75 ± 0.05	1.69 ± 0.07
	s(s^{-1})	1.2 x10^{13}	3.2 x 10^{14}	1.6 x 10^{14}
	T_m (K)	562 ± 2	568 ± 3	565 ± 2

6.2.2 Thermal Quenching

Initially, the NSWC-2013 VHRM data, found in Figure 6-14a, was thought to display evidence of thermal quenching for MBO. Subsequent VHRM data collection of the "newer" NM sample did not show the same drastic changes in peak intensity. Additionally, the agreement between the VHRM trap parameters from the NSWC-2013 and NM samples serves as a counter argument against thermal quenching as its effect would strongly change the activation energy values. To justify the observed decrease in TL peak intensity for the NWSC-2013 sample was due to material degradation or reagent contamination we conducted a thermal quenching study of both samples.

Whole Curve Analysis

Figure 6-16 shows a comparison between the total TL curve area of the NSWC-2013 and NM samples as a function of heating rate. The results for the NSWC-2013 samples display a strong decrease in TL area, resulting in a ~ 25% loss of total intensity over a two order of magnitude increase in heating rate. Over that same heating rate interval, we observe a slight increase (<1%) in total curve area for the NM samples. Except for the 0.5 K/s TL curve, all the curve areas for the NM sample are within 2% of the lowest heating rate curve.

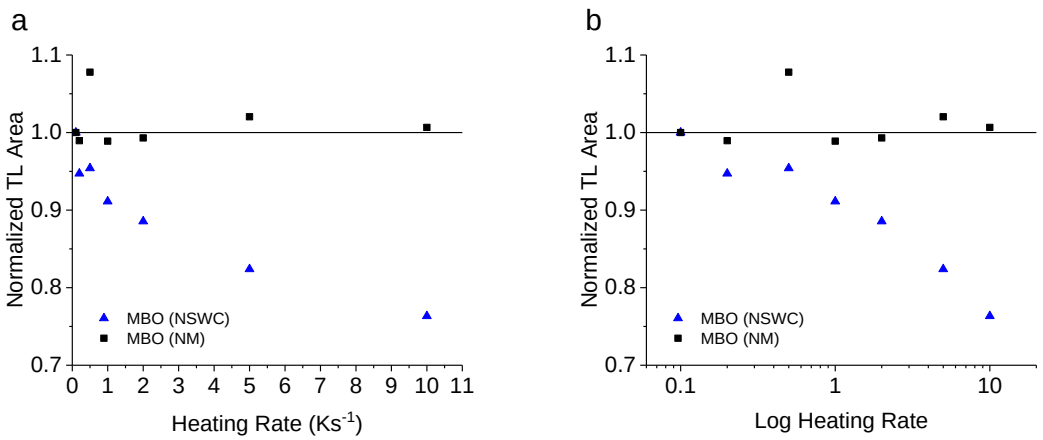

Figure 6-16. TL curve area as a function of (a) linear heating rate and (b) log heating rate for both the NWSC-2013 and NM samples. Areas are normalized to the lowest heating rate.

TL Model Analysis

TL models were obtained for the NSWC-2013 (~1 mg, ~ 5 Gy) samples and NM samples by a one-dimensional deconvolution of the lowest heating rate TL curve. A total of 30 activation energies (fixed $s = 10^{14} s^{-1}$) with a spacing of ~0.035 eV was used for the deconvolution. The energies were chosen such that the peak positions of the individual first-order peaks spanned the entire readout temperature axis (0°C to 400°C).

The TL model was used to predict the TL curve resulting from variations in heating rate for both materials using the heating rates for the VHRM dataset in the previous section. Figure 6-17 shows the results of the TL modeling of the NSWC-2013 and NM data sets. We clearly see a difference between the curve behavior between the two samples when focusing on the main TL peak. The NSWC-2013 sample shows a strong decrease in peak intensity, while the model predicts a gradual decrease with increase in heating rate. We do, however, see that the NSWC-2013 TL peak positions outpace the predicted data which is the opposite of what is expected for a thermally quenched peak. In contrast, the NM sample shows very good agreement with the model predictions for the main peak, but fails to capture the high temperature peak behavior

shown as an inset in Figure 6-17b, and is assumed to be a result of sensitization. These results suggest that NM sample does not suffer from thermal quenching, while the NSWC-2013 sample does. Both samples were synthesized according to the same methods described by Doull et al. (2014), but it is possible that there were differences in the reagent purity. Yukihara et al. (2014a) performed a comprehensive study of MgB_4O_7:Ln,Li and found evidence for a 550 nm broad band emission from Mn^{2+} resulting from an intrinsic defect or impurity introduced in the synthesis process. By using a higher purity reagent, they found the Mn^{2+} emission to disappear. If the Mn^{2+} center shows quenching and the Dy^{3+}center does not, then a possible explanation for the differences between the NSWC-2013 and the NM samples is the purity of the reagents used during the synthesis process. Additionally, due to the longer storage time of the NSWC-2013 as compared to the NM sample it is possible that material degradation also produced the differences in Figure 6-17, but further investigation is required.

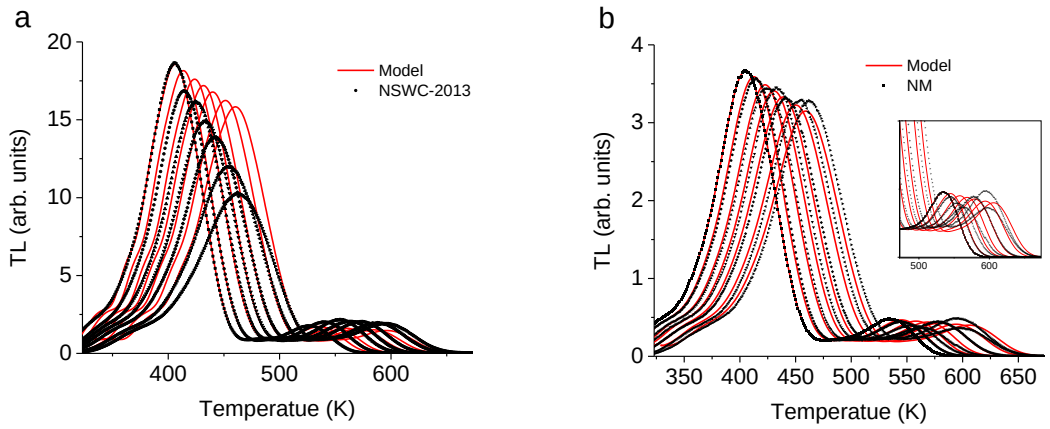

Figure 6-17. Comparisons between the simulated VHRM datasets and experimental VHRM datasets for a single (a) NSWC-2013 sample and a single (b) NM sample.

6.2.3 Initial Rise Method

Step-annealed TL curves for two different batches of MBO (NSWC-2012 and NSWC-2013 control samples) were obtained according to the methods described in Section 3.4.2. The NSWC-2013 data was obtained using a linear heating ramp to a set temperature, T_{stop}, while the

NSWC-2012 dataset was obtained using a fast-linear ramp to a set temperature, T_{hold}, and then held for 5 min. The IRM results presented and discussed in the following sections.

Linear Heating Rate

Three aliquots of ~1 mg of material (NSWC-2013) were used to collected step-annealed datasets. Datasets were collected using an irradiation of ~ 5 Gy beta to avoid saturation of the PMT. Figure 6-18 shows representative background subtracted step-annealed TL curves from a single aliquot of material. MBO has two well major TL peaks identified as peaks 1 and 2 in Figure 6-18. A more complex TL curve is observed when plotted on a log axis (Figure 6-18b). A strong (>10^2 counts) room temperature phosphorescent signal is observed for temperatures below 325 K and remains well into the depletion of peak one despite background subtraction.

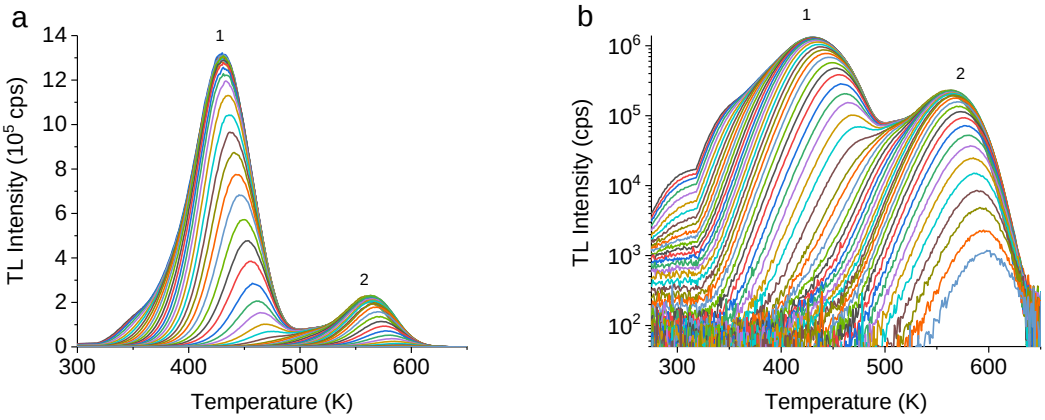

Figure 6-18. Step-annealed TL curves for a single aliquot of MBO originally placed in position 8. TL curves have been background subtracted and are shown in (a) linear and (b) log scale. Peak positions are indicated within each figure. Each color represents a different T_{stop} temperature.

Figure 6-18b shows a small shoulder of a low temperature TL peak with an estimated peak maximum between 325 K and 375 K. The shoulder appears to overlap with peak one and, therefore, must be fully depleted prior to the use of the IRM to peak one. We also observe a continuous movement of peak one's peak position to higher temperatures with increasing T_{stop} temperatures, also observed by Doull et al. (2014), which could suggest a continuous

distribution of peaks or a single TL peak with general order kinetics. The same behavior is seen for peak two, also. Figure 6-19 shows a representative IRM data set for the curves presented in Figure 6-18 using the 5% intensity threshold.

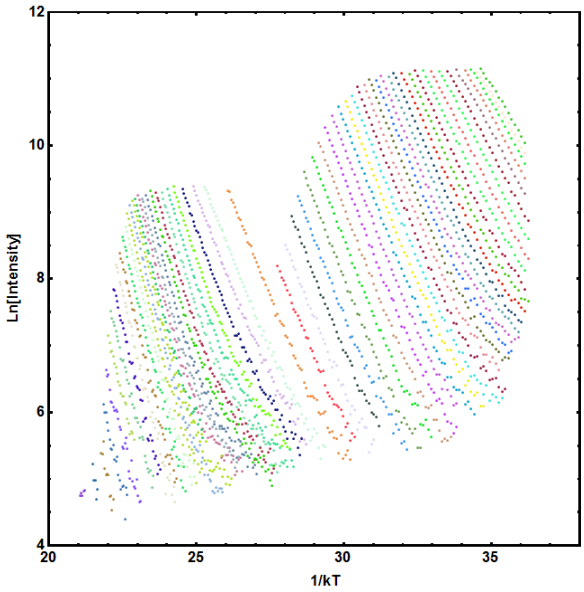

Figure 6-19. Analysis dataset for a single aliquot of MBO, "pos 8". Data appears as diagonal bands with each change in color representative of a different T_{stop} temperature, which increases from right to left.

Linear fits of the IRM datasets (Figure 6-19) were used to obtain activation energies for each T_{stop} temperature for each aliquot. In addition, the peak position for each step-annealed curve was also obtained. Figure 6-20a shows the IRM results as E-T_{stop} and T_m-T_{stop} plots. The T_m-T_{stop} results suggest the presence of two distinct TL peaks, but the linearly increasing "tail" at the end of each plateau suggest a superposition of multiple TL peaks make up each of the main two peaks identified in Figure 6-18 . Two distinct plateaus were observed in the E-T_{stop} graph indicating the presence of two main peaks, but as we previously saw for simulated Gaussian peak distributions in Chapter 4, this does not discount the existence of a supposition of TL peaks. Below T_{stop} temperatures of ~400 K, the activation energy value linearly increases, a result of high peak overlap between peak one and the low temperature shoulder.

As were the cases for LBO, we do not see an agreement between the plateau regions for T_m-T_{stop} results and the E-T_{stop} results. The E-T_{stop} plateaus instead most closely lined up T_{stop} temperatures where the peak position had begun to trend towards to higher temperatures, which we saw previously in the results of IRM analysis applied to simulated step-annealed data for highly overlapped peak distributions (Chapter 4). The plateaus in Figure 6-20a are denoted by the red and black boxes. The average peak positions and activation energies within each boxed region of interest are presented in Table 6-3.

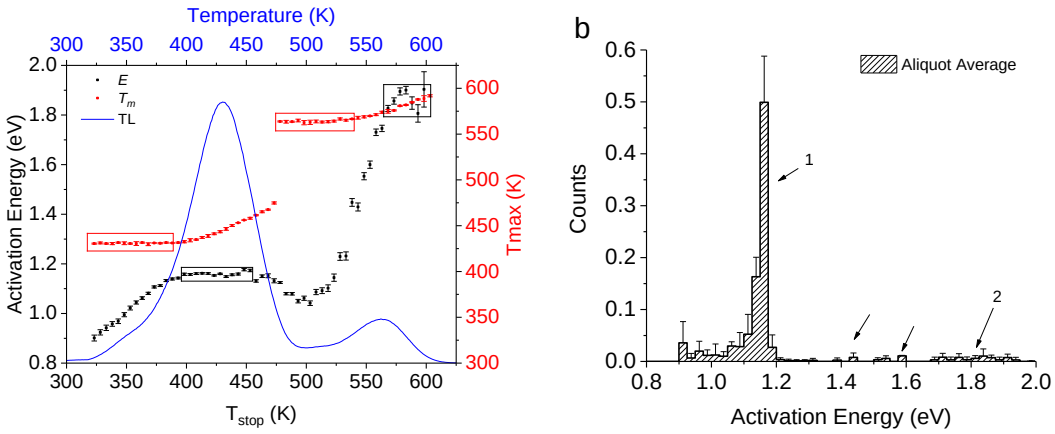

Figure 6-20. (a) IRM results for 5% method presented as overlapping E-T_{stop} and T_m-T_{stop} plots and (b) trap density distribution. All results were obtained as averages of parameters obtained for three aliquots. Error bars represent one standard deviation. Numbers correspond to the TL peaks in Figure 6-18.

Figure 6-20b shows the trap density distribution obtained using the "Van den Eeckhout" method to the IRM results in Figure 6-20a. Numbers 1 and 2 correspond to activation energies of ~1.16 eV and ~1.84 eV belonging to TL peaks one and two in Figure 6-18, respectively. Two additional energy peaks at ~ 1.45 eV and ~ 1.6 eV were found in Figure 6-20b (indicated by arrows) and may belong to the broad TL structure between the two main TL peaks.

Figure 6-21 shows the results of the IRM using the search method (Section 3.4.2). The activation energies obtained by the search method are representative of an IRM region that minimizes the reduced chi-squared fitting metric. These results are not meant to be taken as the

true energy values as the method will often selected portions of the initial rise region of the TL curve that do not meet the IRM criteria (Chapter 4). The results in do provide insight into the underlying peak structure and confirm the two-peak structure we have already determined for MBO using other analysis methods. The boxed regions correspond to the plateaus common across all three aliquots and are used to obtain peak activation energies (Table 6-3).

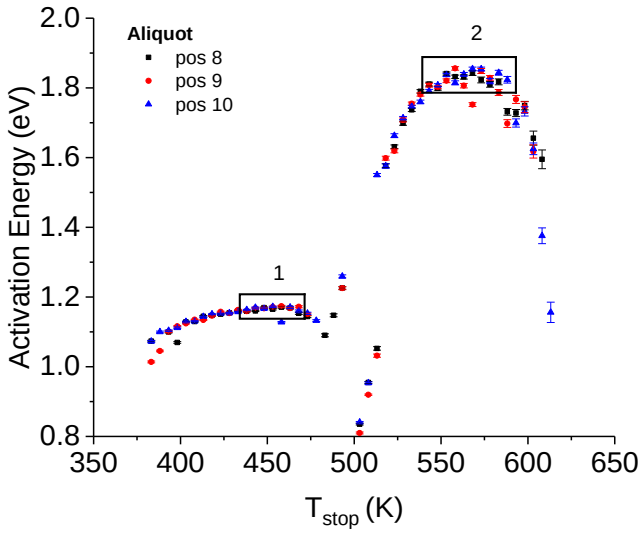

Figure 6-21. Search method results for three aliquots. Groupings of activation energies are indicated by numbered boxes and correspond to TL peaks. Numbers correspond to the TL peaks in Figure 6-18.

Hold Temperature Results

Analysis in this section was conducted using material from control samples of the NSWC-2012 DTRA test. Results were obtained from the analysis of a single aliquot of MBO comprised of a few grains of material (<< 1 mg, grain size unknown). Step-annealed datasets, referred to as T_{hold}, were obtained according to the procedure outlined in Section 3.4.2. T_{hold} temperatures ranged from ~ 323 K to ~653 K with a step size of 10 K. Irradiations of ~10 Gy beta were used in data collection. Background subtracted analysis curves are shown in Figure 6-22a. A comparison of the TL curves for the NSWC-2012 sample and a sample of the NWSC-2013 material are shown in Figure 6-22b. A small difference of ~5 K in peak 1's position is observed,

but we see a ~25 K difference in peak two position as well as a ~ 40% difference in relative intensity. The increased intensity for peak two of the NSWC-2012 TL curve suggests prior exposure to irradiation due to its known sensitization properties (Doull et al., 2014).

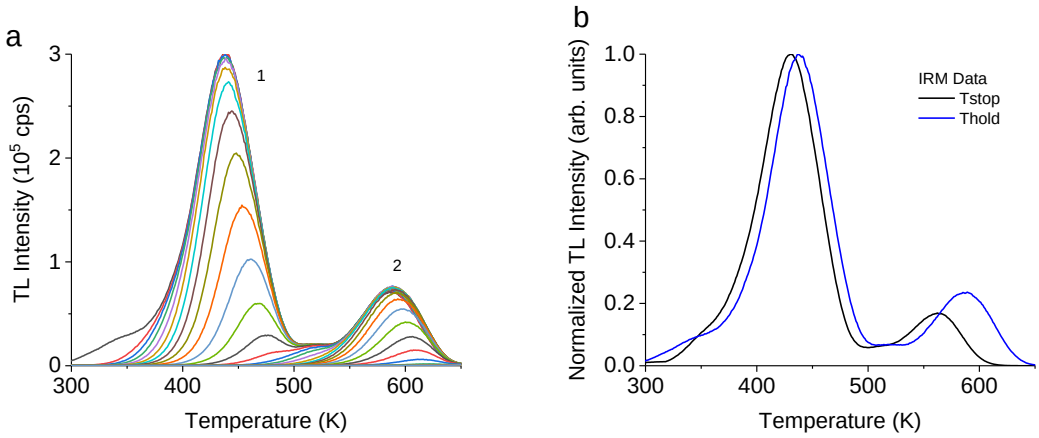

Figure 6-22. (a) TL curves obtained following a pre-heat to a set temperautre and a hold for 5 minutes and (b) a comparison between the TL curves for NSWC-2012 and NSCW-2013. Curves are normalized to max peak intensity.

Figure 6-23 shows the results of the IRM data analysis applied to the T_{hold} dataset of the NSWC-2012 samples. E-T_{hold} results (Figure 6-23a) indicate two activation energy plateaus at ~1.2 eV and ~ 1.9 eV, which roughly agrees with the plateaus of the NSWC-2013 samples. The T_m-T_{hold} analysis for both step-annealing datasets (Figure 6-23b) show two plateau regions. As previously observed in Figure 6-22b, the position of peak 1 was found to be similar between the different samples, and there is a larger difference in peak 2's position. The representative activation energies and peak positions of the plateau regions indicated by the boxed regions in Figure 6-23 are presented in Table 6-2.

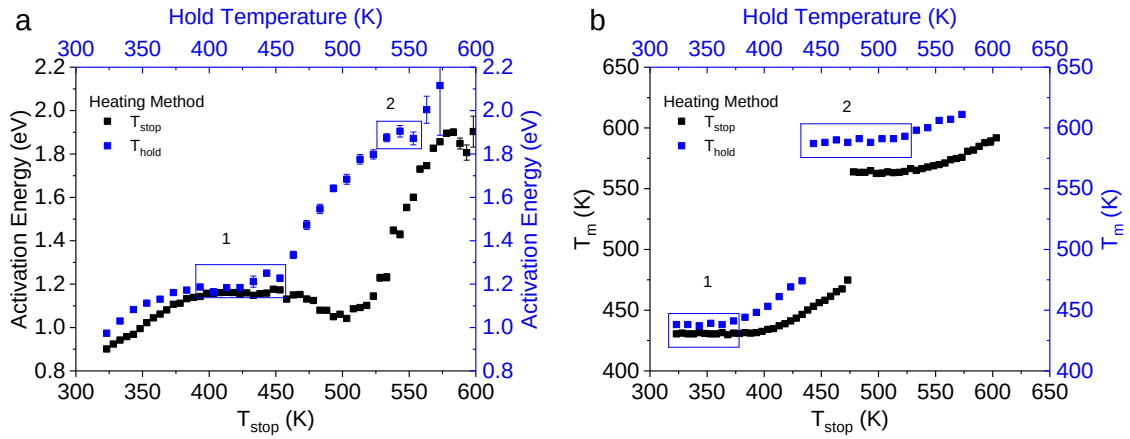

Figure 6-23. Comparison of the IRM results for the two-different step-annealing datasets: (a) *E*-T_{stop} and (b) T_m-T_{stop} plots. Error bars in plot (a) are given as fitting uncertainties for T_{hold} results and the uncertainty of a three-aliquot average for the T_{stop} results. Numbers correspond to the TL peaks in Figure 6-22a.

6.2.4 Two-dimensional Deconvolution

A subset of 26 curves of the 35 analysis curves in Figure 6-22a were used to obtain a trap parameter distribution following the two-dimensional deconvolution method (Section 3.4.4). Following background subtraction, it was observed that the analysis curves displayed a constant vertical offset for the first 25 – 50 data points. Therefore, for all curves, an additional background subtraction was conducted by subtracting the mean value of each curves first ~30 data points, or $T < 300$ K. The TL curves used for two-dimensional deconvolution analysis following the additional background subtraction are shown Figure 6-24.

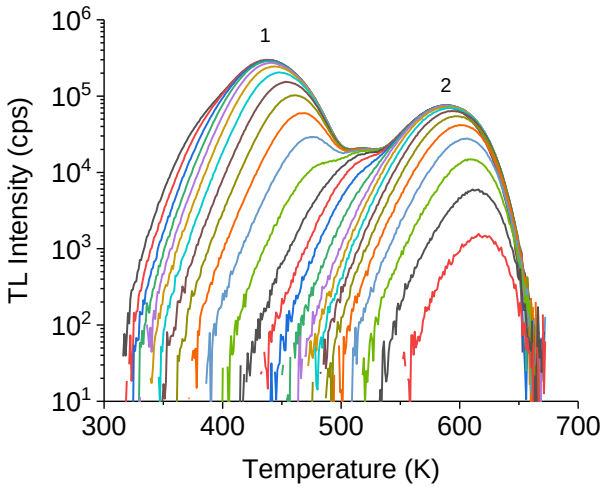

Figure 6-24. Analysis TL curves used for two-dimensional deconvolution. The dataset is comprised of 26 curves chosen for hold temperatures that resulted in large changes in total TL curve area.

We chose to use a solution space that included activation energies from 1 eV to 2 eV and *log s* values from 10 to 20, based on the results from the IRM and VHRM analyses already presented. We used four different resolutions, starting with a coarse step-size of 0.1 eV and 0.5 log s, and ending with a fine resolution of 0.025 eV and 0.25 log s.

The results of two-dimensional deconvolution method for all resolutions are shown as solution space contour plots (Figure 6-25). All results demonstrate two main trapping center groupings, one at ~1.3 eV and the other at ~ (1.8 – 1.9) eV. These groupings roughly correspond to peak 1 for the ~1.3 eV grouping, and peak 2 for the deeper traps. The consistency of the trapping centers across multiple resolutions is evidence the true trapping center parameters are near these values, but the trend of the solutions space from broad distributions to several discrete peaks does not allow for confidence in what those exact values are.

Figure 6-25d presents the solution space for the 0.025 eV and 0.25 log s resolution. This resolution was previously determined to be the best for the simulated datasets presented in Chapter 5. The results of the IRM and VHRM analyses are indicated by arrows and show good

agreement with deconvolution results for activation energy values, but there are large, factor of ten, differences in frequency factor.

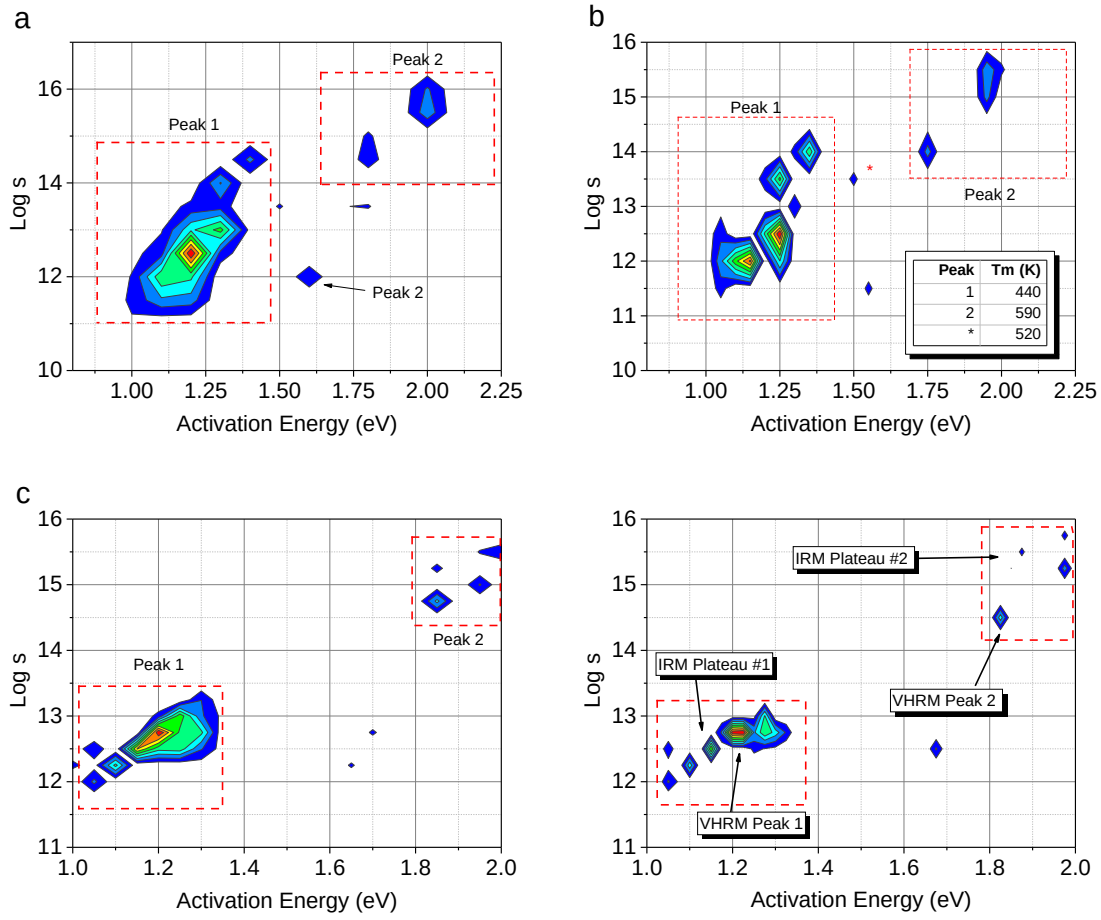

Figure 6-25. Trap parameter distribtions for soultion space resoultions of (a) ΔE = 0.1 eV and $\Delta \log s$ = 0.5 (b) 0.05 eV and $\Delta \log s$ = 0.5 (c) 0.5 eV and $\Delta \log s$ = 0.25 and (d) 0.025 eV and $\Delta \log s$ = 0.25. Trap distributions are matched with their corresponding TL peak position using Equation 2-9. Peak positions are displayed in the table of plot (b).

6.2.5 Parameter Summary

The results of the analyses method for each TL peak are shown in Table 6-3. VHRM results are for the NM sample only as it did not demonstrate thermal quenching. The IRM results were obtained from the boxed regions in Figure 6-20a, Figure 6-21a, and Figure 6-23. Values represent an average all values within the boxed regions and uncertainty propagation was conducted according the methods by Taylor (1997). Results for the two-dimensional

deconvolution are not included, but we refer the reader to Figure 6-25c where the result for Table 6-3 are indicated in the *E-log s* solution space.

Table 6-3. Summary of MBO trap parameters obtained using the analysis methods presented in this section. Uncertainties less than 10 meV in activation energy are not reported.

Peak	Parameter	VHRM (NM)	IRM (Tstop)	IRM(Search)	IRM(Thold)
1	E(eV)	1.24 ± 0.01	1.16	1.17	1.20 ± 0.01
	s (s^{-1})	9.5 x 10^{14}	-	-	-
	T_m (K)	433	430.8 ± 0.3	-	439 ± 1
2	E(eV)	1.81 ± 0.01	1.86 ± 0.01	1.818	1.88 ± 0.01
	s (s^{-1})	1.2 x 10^{13}	-	-	-
	T_m (K)	562 ± 2	564.1 ± 0.4	-	590 ± 2

The result for all MBO analyses confirmed the existence of two main TL peak structures. Peak 1 has an approximation peak position between 430 K and 440 K with peak 2 between 560 K to 565 K. The IRM results for the NSWC-2012 found a significantly higher peak position of 590 K, which we assume is due to pre-sensitization of the material prior to data collection. Nevertheless, all methods produced similar activation energies for both TL peaks; with peak 1 values between 1.16 eV and 1.25 eV, and peak 2 between 1.8 eV and 1.9 eV. These results are also in agreement with the two-dimensional deconvolution results.

The deconvolution results indicate the presence of many individual first-order TL peaks as suggested by Doull et al. (2014), but the values are much higher in activation energy then previously found by Souza et al. (2015). Evidence for a distribution of TL peaks was also found by reconstructing TL curves based on the VHRM results. We used the VHRM trap parameters in Table 6-3 to simulate first-order TL peaks for a heating rate of 1 K/s. A comparison between the simulated TL curve and the 1 K/s curve from Figure 6-14a are shown in Figure 6-26. A clear difference can be seen between the simulated and experimental peak shapes and suggests more peaks are present than were accounted for in the analysis.

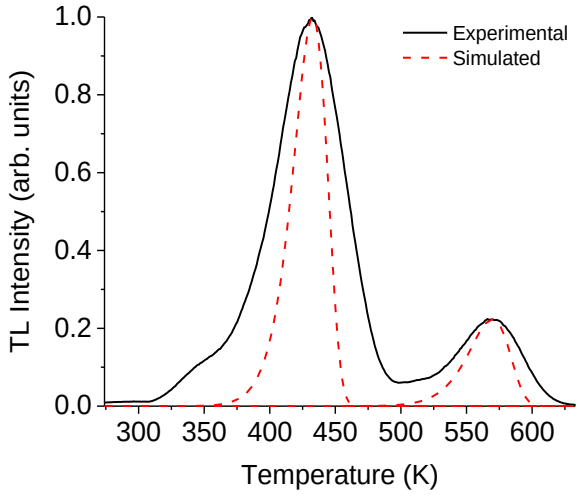

Figure 6-26. Comparison between simulated (using VHRM results) and experimental TL curves for MBO using a 1K/s heating rate. Simulated TL peaks were normalized to the max intensity of the respective experimental TL peak.

Our best estimates for the frequency factor for MBO are found in the VHRM and two-dimensional deconvolution. Both indicate a factor of ~ 100 difference with s_1 ~ 10^{13} s^{-1} and s_2 ~ 10^{15} s^{-1}. These results suggest the approximation of a common factor of 10^{14} s^{-1} was incorrect. However the results obtained for activation energies are not drastically off those found by Yukihara et al. (2014b).

The lack of thermal quenching for MBO and the consistency of trap parameters among the various analysis methods make this material suitable as a temperature sensing material, but we must caution users to account for issues concerning sensitization of the high temperature peak. Additionally, future studies of the material must be aware of the possibility of Mn contamination during synthesis (Yukihara et al., 2014a). Although we found it had no effect on the results, with any efforts to limit its effect on a TL curve, one must ensure that additional error is not introduced in the temperature reconstruction.

6.3 $CaSO_4$:Ce,Tb (CSO)

6.3.1 Various Heating Rate Method

TL curves were obtained at various heating rates for three aliquots of CSO (NSWC-2013) with mass of (0.6 ± 0.1) mg. Particle sizes were selected to be less than 125 µm, but no effort was undertaken to account for aggregates. A ~10 Gy dose was used in the irradiation of the material.

A set of seven heating rates were used to obtain the dataset in Figure 6-27a. We observed a strong decrease in peak intensity for TL peaks 3 and 4 as well as a drastic change to the shape of peak 4. Following background subtraction, plots of ln(β/Tm) versus $1/T_m$ were constructed for peaks 1, 3 and 4 (Figure 6-27b). The slopes and intercepts of the linear fits were used to obtain the activation energy and frequency factor values for the respective TL peaks and are presented in Table 6-4.

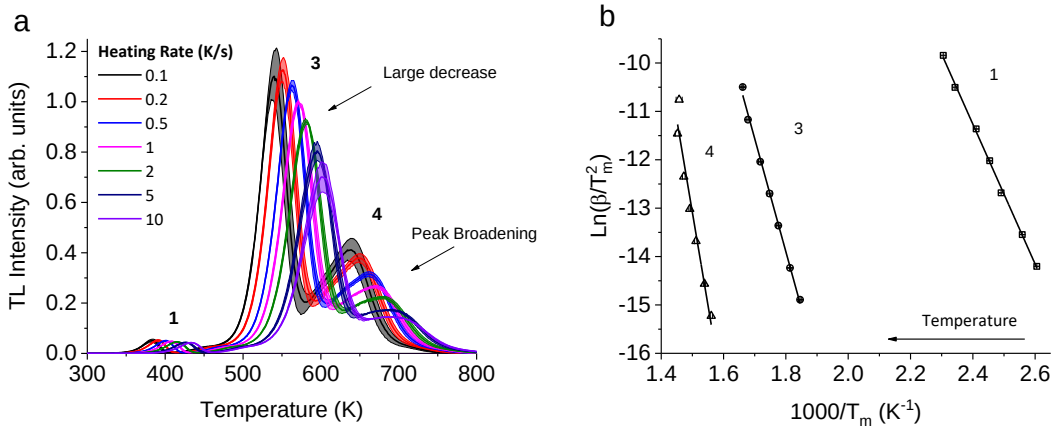

Figure 6-27. (a) TL curve obtained for CSO samples using various heating rates. Each heating rate curve is the average of three aliquots and the shaded region indicates one standard deviation. (b) VHRM datasets for each TL peak with linear trends.

6.3.2 Thermal Quenching

The substantial changes in peak intensity for peaks 3 and 4 could be the result of thermal quenching. To determine if thermal quenching is contributing to the observed curve changes, we studied the changes in TL curve area as a function of heating rate. A one-dimensional deconvolution model was used to predict the expected behavior of the TL curve from the lowest heating rate.

We will restate that all TL results for CSO were obtained using an optical filter to isolate the Ce^{3+} emission, but CSO also produced TL from the Tb^{3+} emission. Therefore, the analysis presented here is investigating the potential for thermal quenching of the Ce^{3+} recombination center only. Additionally, we have not investigated the effect of heating rate on Ce^{3+} emission band. Changes of the wavelength outside the filters range can also result in a reduction in TL intensity. We have not looked at the possibility of competition between the Ce^{3+} and Tb^{3+} recombination centers as the heating rate changes.

Whole Curve Analysis

Following background subtraction, the total TL curve area was obtained for each heating rate curve in Figure 6-27a. Each area was normalized to the lowest heating rate, 0.1 K/s, and plotted as a function of heating rate and log heating rate in Figure 6-28. The results show a slight increase in curve area from 0.1 K/s to 0.2 K/s but then, a quick decrease as the heating rate is increased to 10 K/s. These results suggest the potential for thermal quenching, but not for all TL peaks in the curve.

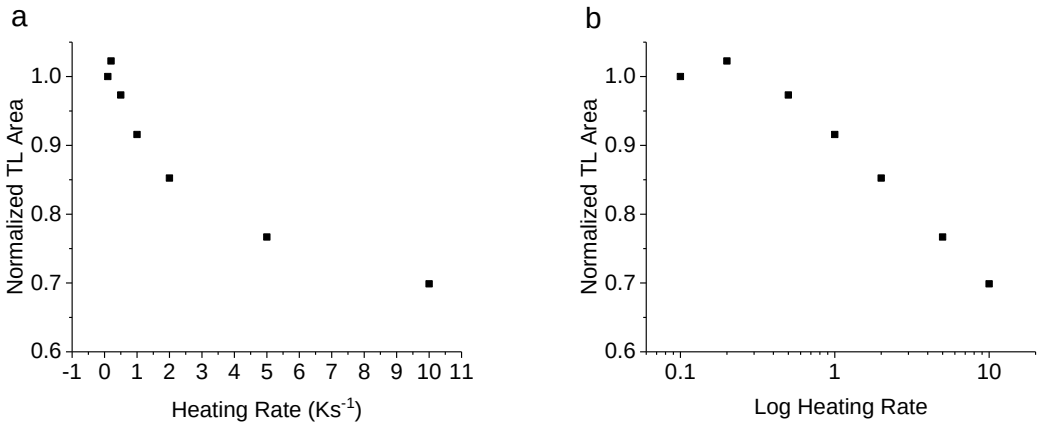

Figure 6-28. Normalized TL area for the CSO VHRM dataset in (a) linear and (b) log heating rate.

TL Model Analysis

TL models were obtained for both CSO VHRM samples by one-dimensional deconvolution of the TL curve for the 0.1 K/s heating rate. A total of 50 activation energies (fixed $s = 10^{14} s^{-1}$), with a spacing of ~0.034 eV, were used for the deconvolution. The energies were chosen such that the peak positions of the individual first-order peaks spanned the entire readout temperature axis (273 K to 873 K). The deconvolution used the non-negative least squares constraint to obtain a TL model as a distribution in activation energy.

The TL model was used to predict the TL curve resulting from variations in heating rate for both materials using the heating rates for the VHRM dataset in the previous section. The TL modeling results for CSO (Figure 6-29) are compared to the experimental data (mean values) from Figure 6-27. We see a clear difference between the curve behaviors between the two datasets when focusing on the main TL peak. As the temperature increases, the main peak of the experimental dataset decreases faster in intensity than predicted and the peak position lags the model results. A similar trend is also observed for peak 4, but the change in the peak shape is more drastic. These results, coupled with the whole curve analysis, suggest the reduction in TL

intensity is the result of thermal quenching, but it is not clear if all peaks suffer from this effect or not.

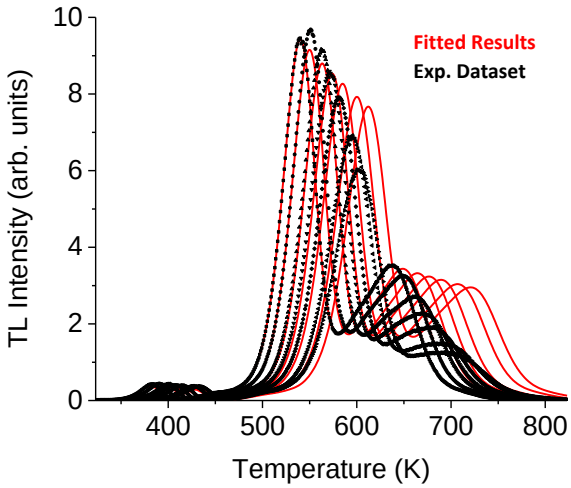

Figure 6-29. Comparison the CSO VHRM dataset and a simulated VHRM heating rate dataset obtained using the one-dimensional deconvolution TL model.

6.3.3 Initial Rise Method

Linear Heating Rate

The IRM was used to analyze step-annealed TL curve from CSO. Data were collect from samples of various masses: ~0.5 mg, ~5 mg and ~10 mg. Doses of ~ 10 Gy were used for the smaller sample sizes and a ~ 5 Gy was used for the 10 mg sample to avoid PMT saturation. Representative curves for each aliquot (Figure 6-30) show that sample size has a strong influence on the curve shape and peak positions. This is likely an effect of the increased thermal

mass leading to thermal lag. We therefore proceed using step-annealed data for the ~ 0.5 mg aliquot. Data for an additional ~0.5 mg aliquot were collected for IRM analysis.

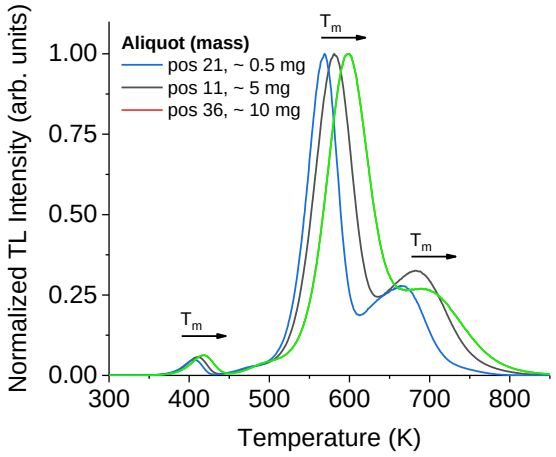

Figure 6-30. Representative TL curves from all three aliquots used in the IRM study.

Representative TL curves from the step-annealing dataset are shown in Figure 6-31. The CSO curve structure is comprised of four primary TL peaks (or structures) with a shoulder, peak 2, highly overlapped with the main TL peak, peak 3. Peak 5 is not well resolved in a linear scale of intensity.

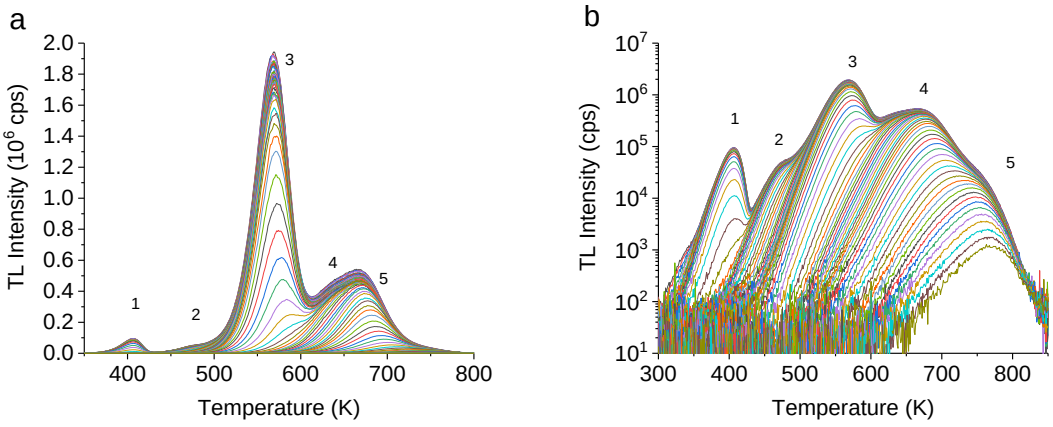

Figure 6-31. Step-annealing dataset for CSO position 21. TL curves are for T_{stop} of ~323 K to ~873 K. TL curves have been background subtracted and are shown with intensity on a (a) linear and (b) log scale. Approximate peak positions are indicated in each figure by numbers. Each color represented a different T_{stop} temperature.

Following background subtracting IRM datasets of *ln I* versus *1/T* were constructed for each aliquot. IRM datasets for position 21 is shown in Figure 6-32. Peaks 1 and 3 are clearly seen at horizontal axis (10^3/kT) values of ~ 35 and 25 respectively. The low temperature side of peak 2 can be seen at a value of ~27, but peaks 4 and 5 are not well resolved and appear as a continuous band.

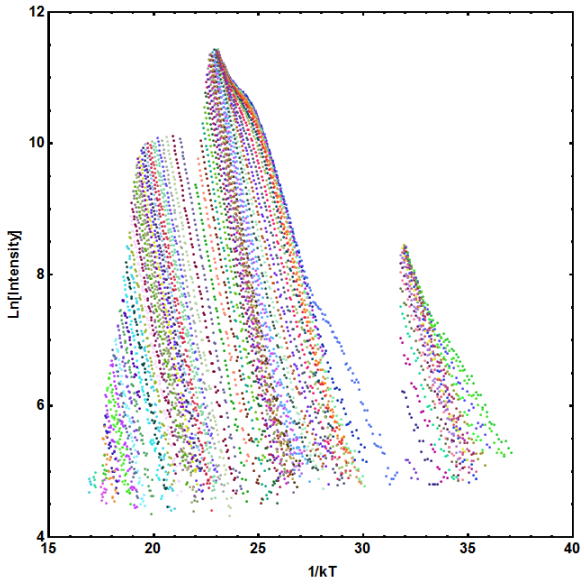

Figure 6-32. IRM Analysis dataset for a single CSO aliquot (pos 21). Data appears as diagonal bands with each change in color representative of a different T_{stop}, which increases from right to left.

Figure 6-33 shows the IRM results for the CSO samples. Characteristic trap parameter values for each peak were obtained using the boxed regions and are presented in Table 6-4. T_m-T_{stop} plots produced three plateaus corresponding to the most prominent TL peak: 1, 3 and 4. T_m-T_{stop} results also show a linearly increasing peak position after a T_{stop} of ~ 650 K, suggesting a continuous peak distribution instead of a single TL peak.

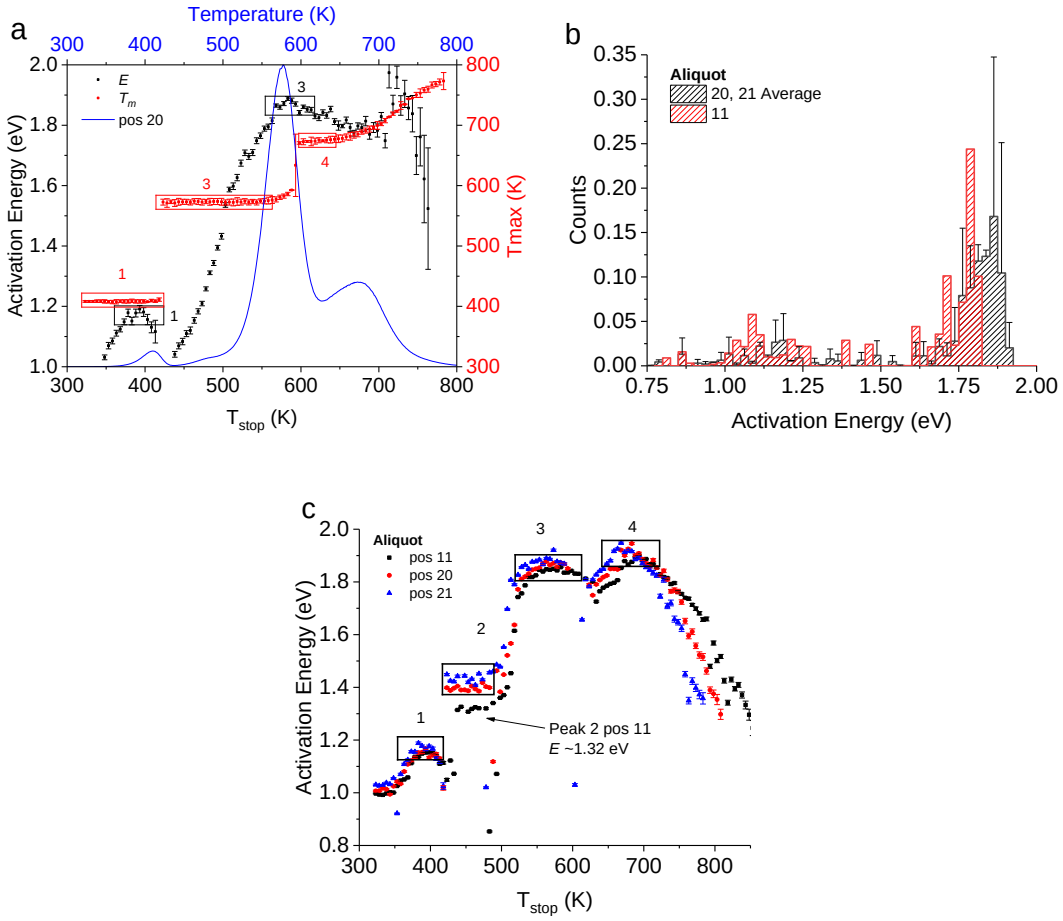

Figure 6-33. IRM results for 5% method presented as overlapping E-T_{stop} and T_m-T_{stop} plots for (a) positions (b) "Van den Eeckhout" trap density distribution and (c) search method results. IRM Results are presented as averages of parameters and error bars represent one standard deviation. Plateaus are indicated by numbered boxes and correspond to the TL peaks in Figure 6-31.

E-T_{stop} plots produced only two identifiable plateaus, indicated by the boxed regions in Figure 6-33a. One might be inclined to select additional plateau regions, but the lack of multiple well-defined T_m-T_{stop} plateaus suggests the energy values would not corresponding to singular TL peaks, but instead a portion of an energy distribution.

Application of the "Van den Eeckhout" method to the IRM results (Figure 6-33b) did not produce a well-defined activation energy distribution. A clear energy peak is found at ~ 1.85 eV, but it is not clear to which TL peak, or structure, it belongs to. We can conclude that the energy peak ~ 1.13 eV is the result of peak 1.

Figure 6-33c shows the results of the IRM search method analysis. Using this approach two additional plateaus in the $E\text{-}T_{stop}$ dataset were found, corresponding to peaks 2 and 4. These results show the importance of the search method, as previously hidden peak structures are now revealed. Additionally, the energy values ~ 1.4 eV for peak 2 and ~ 1.9 eV for peak 4 are present as small energy peaks in the "Van den Eeckhout" trap distribution.

Hold Temperature Results

IRM analyses in this section were conducted using material from control samples of the NSWC-2012 DTRA test. Results were obtained from the analysis of a single aliquot of CSO comprised of a few grains of material (<< 1 mg, grain size unknown). Step-annealed datasets, referred to as T_{hold}, were obtained according to the procedure outlined in Section 3.4.2. T_{hold} temperatures ranged from ~ 323 K to ~773 K with a step size of 10 K. Irradiations of ~10 Gy beta were used in data collection. Background subtracted analysis curves are shown in Figure 6-34a. A comparison of the TL curves for the NSWC-2012 sample and a sample of the NWSC-2013 material are shown in Figure 6-34b.

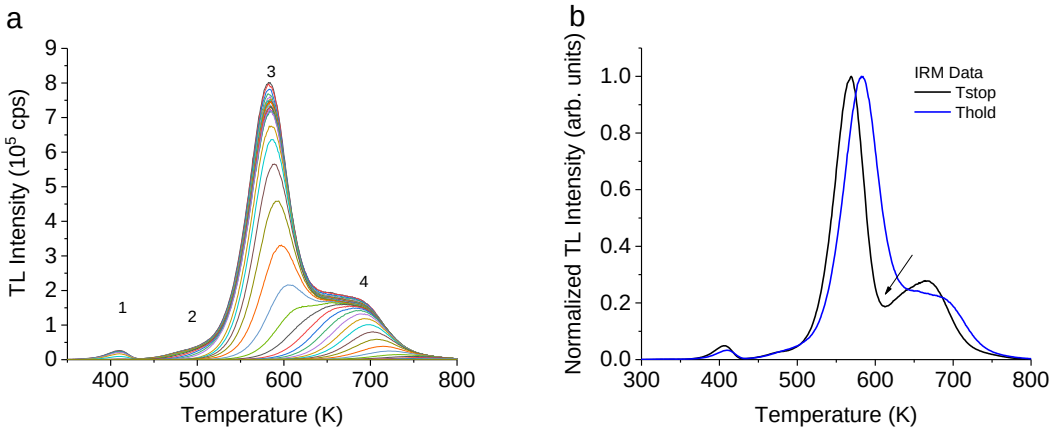

Figure 6-34. (a) CSO step-annealed TL curves obtained following a pre-heat to a set temperature and a hold for 5 min and (b) comparison between representative TL curves for NSWC-2012 and NSCW-2013 samples. Curves are normalized to max peak intensity.

A small difference of ~5 K in peak one's position ~15 K in peak three's positions were observed. We also see a large different in the TL curve structure following peak 3, indicated by the arrow in Figure 6-34b. To our knowledge, there are no differences in synthesis procedure or dopant concentrations between the NSWC-2012 and NSWC-2013 samples, and therefore, the reason for the TL curve discrepancies is unknown.

Figure 6-35 shows the results of the IRM data analysis applied to the CSO T_{hold} dataset. The E-T_{hold} results (Figure 6-35a) indicate two activation energy plateaus for peak 1 (~1.1 eV) and peak 3 (~1.8 eV). These plateaus are found at similar activation energies as those for the NSWC-2013 samples, despite the slight curve differences.

Figure 6-35b shows the results of the T_m-T_{hold} analysis for both step-annealing datasets. A total of four plateaus were identified and corresponding to TL peaks 1 and peaks 3-5. Figure 6-34b shows slight differences in peak 1 and peak 3 positions between the NSWC-2012 and NSWC-2013 materials and is also seen here. Also, we see small inflection points at T_{stop} values of ~625 K and ~700 K, which we assigned to peak 4 and 5, but these values should be treated as best estimates, as the plateaus are poorly defined. The representative activation energies and peak positions of the plateau regions indicated by the boxed regions in Figure 6-35 are presented in Table 6-4.

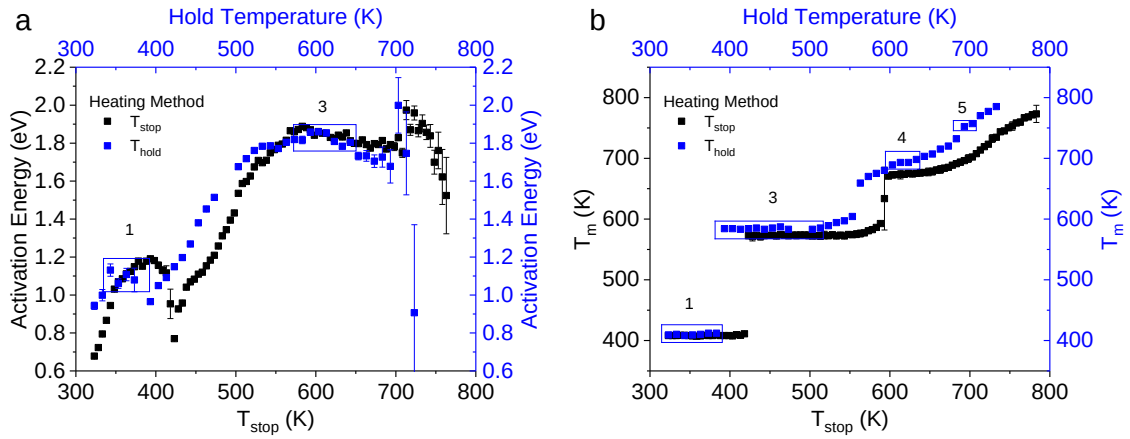

Figure 6-35. Comparison of the IRM results for the two different step-annealed datasets: (a) *E*-T_{stop} and (b) T_m-T_{stop} plots. Error bars in plot (a) are given as fitting uncertainties for T_{hold} results and the uncertainty of a three-aliquot average for the T_{stop} results.

6.3.4 Two-dimensional Deconvolution

A subset of 21 TL curves of the 45 analysis curves in Figure 6-22a were used to obtain a trap parameter distribution following the two-dimensional deconvolution method in Section 3.4.4. Following background subtraction, it was observed that the analysis curves displayed a constant vertical offset for the first 25 – 50 data points. Therefore, for all curves, an additional background subtraction was conducted by subtracting the mean value of each curves first ~30 data points, or $T < 300$ K. The TL curves used for two-dimensional deconvolution analysis following the additional background subtraction are shown Figure 6-36. The main TL peaks are identified, but peak 5 was is poorly resolved in the NSWC-2012 sample.

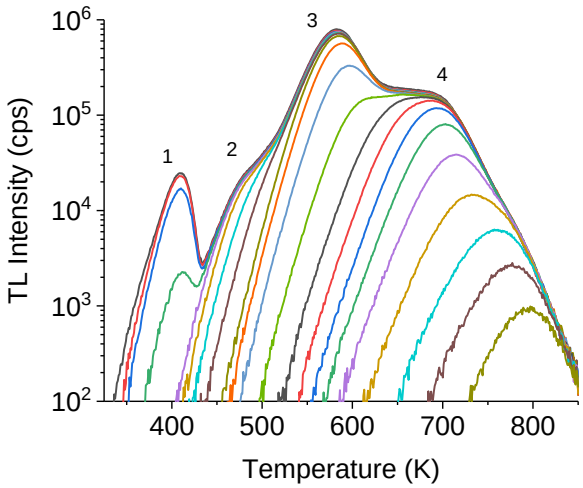

Figure 6-36. Analysis TL curves used for two-dimensional deconvolution. The dataset is comprised of 21 curves chosen for hold temperatures that resulted in large changes in total TL curve area.

We chose to use a solution space that included activation energies from 0.8 eV to 2.5 eV and *log s* values from 10 to 18, based on the results from the IRM and VHRM analyses already presented. We used three different resolutions starting with a coarse step-size of 0.1 eV and 0.25 log s, and ending with a fine resolution of 0.025 eV and 0.25 log s. The results of two-dimensional deconvolution for all resolutions are shown as solution space contour plots (Figure 6-37). A cutoff of 10% of the max distribution value was used to select the most prominent peaks, but some lower intensity peaks are hidden as a result. A single peak structure was found for all resolutions with an activation energy of ~ 1.9 eV and frequency factors between 14 log s and 15 log s and corresponds to peaks 3 and 4. Another peak common among the different resolutions was found at ~ 1.4 eV and 11.5 log s, which corresponds to a peak position of ~552 K, or the approximate location of peak 2.

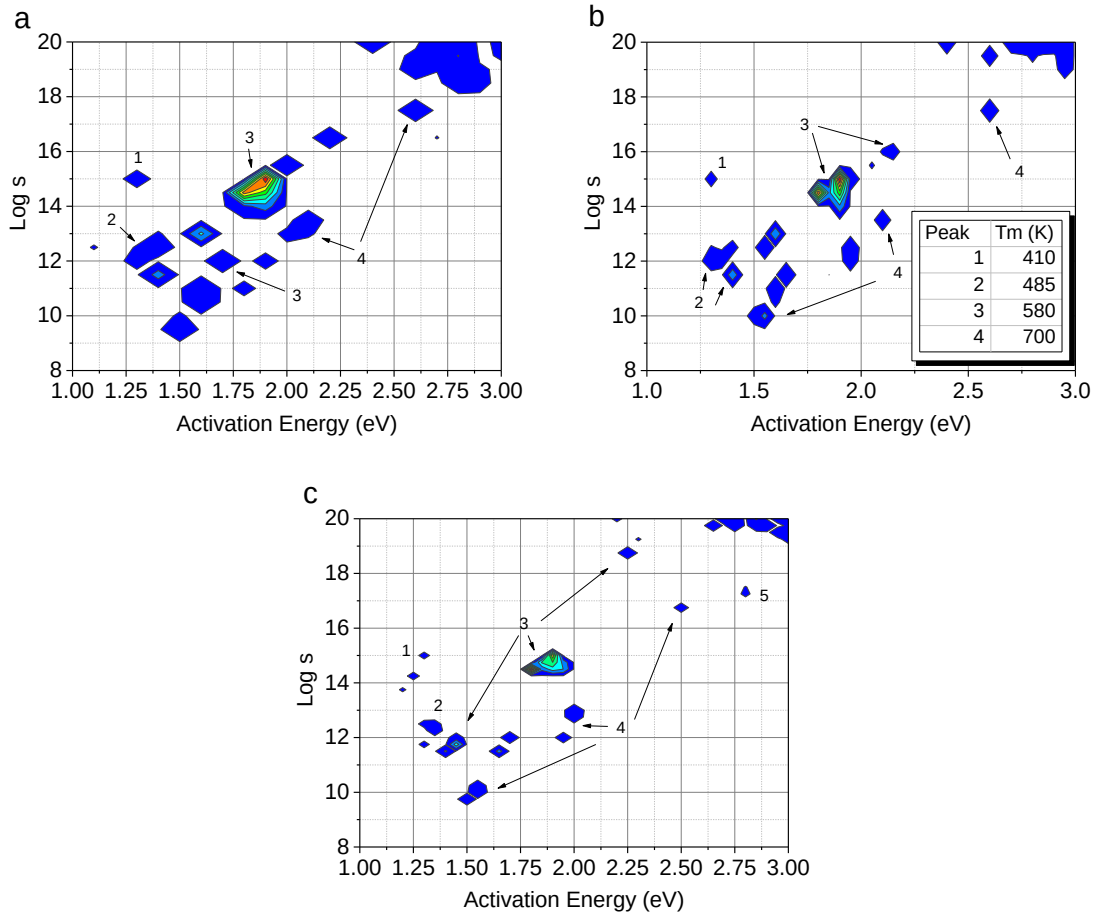

Figure 6-37. Trap parameter distributions for solution space resoultions of (a) ΔE = 0.1 eV and $\Delta \log s$ = 0.25 (b) ΔE = 0.05 eV and $\Delta \log s$ = 0.25 and (c) ΔE = 0.025 eV and $\Delta \log s$ = 0.25. Trap distributions are matched with their corresponding TL peak position using Equation 2-9. Peak positions are displayed in the table of plot (b).

6.3.5 Parameter Discussion

In this section we present a discussion of the results of the various TL studies within this section for CSO, although the evidence of thermal quenching suggests any values obtained are incorrect, as the datasets were not corrected prior to analysis. The results of the analyses methods for each TL peak are found in Table 6-4. The IRM results were obtained from the boxed regions in Figure 6-33a, Figure 6-33d, and Figure 6-35. Values represent an average of all values within the boxed regions and uncertainty propagation was conducted according the methods by Taylor (1997).

Table 6-4. Summary of CSO trap parameters obtained using the analysis methods presented in this section. Uncertainties less than 10 meV in activation energy are not reported.

Peak	Parameter	VHRM	IRM (T_{stop})	IRM(Search)	IRM(T_{hold})
1	E (eV)	1.24 ± 0.03	1.16 ±0.06	1.15	1.09 ± 0.02
	s (s^{-1})	3 x 10^{14}	-	-	-
	T_m (K)	407.5 ± 0.6	408.4 ± 0.5	-	410 ± 2
2	E (eV)			1.42	
	s (s^{-1})	-	-	-	-
	T_m (K)				
3	E (eV)	2.01 ± 0.03	1.86 ± 0.03	1.85	1.82 ± 0.01
	s (s^{-1})	5 x 10^{16}	-	-	-
	T_m (K)	573 ± 3	573 ± 1	-	584 ± 1
4	E (eV)	3.3 ± 0.2		1.90	-
	s (s^{-1})	5 x 10^{24}	-	-	-
	T_m (K)	670 ± 1		-	691 ± 7
5	E (eV)				-
	s (s^{-1})	-	-	-	-
	T_m (K)				755 ± 4

We found the application of the traditional analysis methods to CSO to be lacking. The IRM results, using the linear heating ramp, were unable to resolve the activation energy and position of many of the TL peaks, but the search method applied to the same data was able to identify approximate activation energies for peak 2 and peak 4. The activation energies using the VHRM do not agree with the IRM results and were between 0.1 eV and 0.15 eV above the other values for the same peaks. The VHRM analysis also produced abnormally high frequency factors, such as 10^{24} s-1 for peak 4, which would be unphysical. However, there is ample evidence that peak 4 (and peak 5) are part of a continuous distribution of peaks. This is the conclusion of the two-dimensional deconvolution trap distribution results, also. We used the VHRM trap parameters in Table 6-4 to simulate first-order TL peaks for a heating rate of 1 K/s to validate the parameter. A comparison between the simulated TL curve and the 1 K/s curve from Figure 6-27a are shown in Figure 6-38. A clear difference can be seen between the simulated and experimental peak shapes for peaks four and beyond. This is an issue, as one of the main benefits of CSO as a temperature sensing material its high temperature peaks, which allows it to

be applied to more extreme temperature environments. Not having an accurate TL model for those peaks introduces error into the thermal history reconstruction. Furthermore, the evidence of thermal quenching suggests that obtaining a correct TL model will prove difficult.

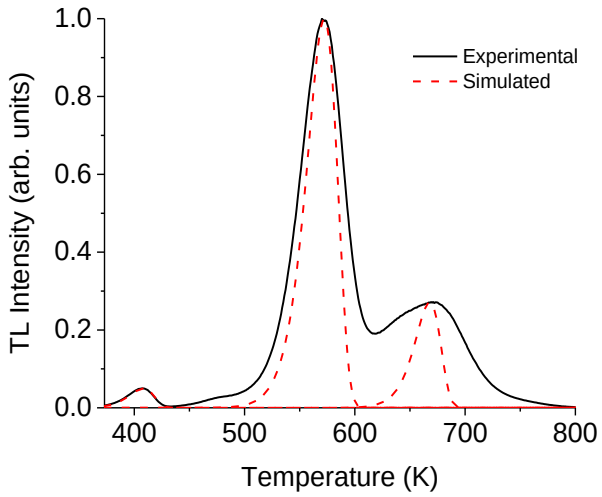

Figure 6-38. Comparison between simulated (using VHRM results) and experimental TL curves for CSO using a 1K/s heating rate. Simulated TL peaks were normalized to the max intensity of the respective experimental TL peak

CHAPTER 7

LIMITATIONS OF TL TEMPERATURE SENSING FOR USE IN AGENT DEFEAT TESTING

The objective of the studies presented in this chapter is to investigate various aspects of the TL temperature sensing methodology by means of numerical simulations to understand its limitations in its application as a temperature diagnostic for agent-defeat tests.

We apply the temperature reconstruction analysis to simulated TL data of samples containing particles heated to a distribution of temperatures to better understand the effect of "partially heated" samples. We employ heat transfer methods to determine a given TL material's response time to transient heating events and compare it with other timescale estimations (Section 2.4.4). Hydrodynamics simulations in FLAG were used to model the early time (~1 ms) blast wave environment of the NSWC closed-chamber, agent-defeat test (Daniels et al., 2015). The temperature profiles from the FLAG simulation are then used to model a TL particle's response to a realistic detonation environment. Additionally, we use a range of TL models to understand the temperature reconstruction method's sensitivity to changes in trap parameters. When appropriate the simulation results are compared with prior tests including those conducted at the UIUC shock tube facility, the Humble Ginkgo XIX test, and the NWSC closed chamber tests (Yukihara et al., 2015; Yukihara et al., 2016).

7.1 Multiple Particle Heating

7.1.1 Simple Temperature Distribution

Equation 3-22 was used to simulate the residual TL curves of the theoretical materials (E =1.35, 1.55, 1.75 eV, $s = 10^{12}$ s^{-1}) for two different constant heating profiles: 750 K for 1 ms and 950 K for 1 ms. We created three hypothetical samples which contain ratios (A:B) of 1:1, 2:1, and 1:2 by weight (or number of particles) from the theoretical material heated to 750 K or 950 K for a 1-ms duration. These combined samples are referred to as "mixtures" throughout this Chapter. We assume the mixtures are made up of TL particles of the same size and shape and all particles are uniformly irradiated. Therefore, the TL curve for a A:B mixture are obtained as the weighted summation of the two TL curves

$$I_{A:B}(T) = A \times I_{750K}(T) + B \times I_{950K}(T). \quad \textbf{7-1}$$

Figure 7-1a shows the TL curves one would expect to obtain from particles from each temperature exposure as well as a 1:1 mixture. Figure 7-1b shows the differences between the three mixing ratios when normalized to the high temperature peak.

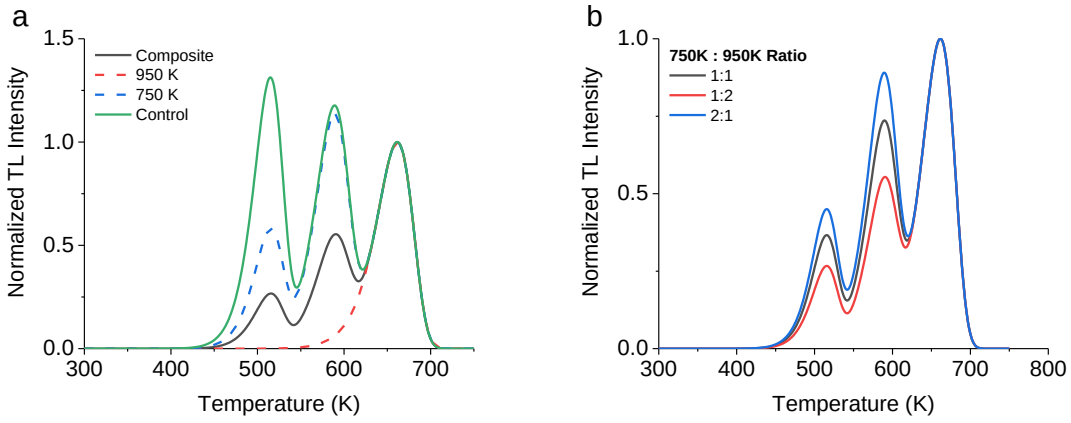

Figure 7-1. (a) TL curves obtained from particles exposure to either 750 K/1 ms, 950 K/1 ms, or an equal contribution, 1:1, of both thermal histories. (b) Comparison between different mixing ratios. All curves in plot (a) and (b) are normalized to the high temperature TL peak.

Thermal history reconstruction was conducted on the TL curves in Figure 7-1b. Equation 3-22 was used to generate TL curves assuming a constant heating profile for hold temperatures between 600 K and 900 K using a 1 K step size and a 1-ms hold time. Normalized model generated curves were compared to the mixture curves in Figure 7-1b using Equation 2-42, which produced a temperature profile for which the maximum value is the temperature that best describes the mixture curve data ("T_{best}"). The temperature history reconstruction for the mixture curve data is shown in Figure 7-2. The left column of Figure 7-2 shows the comparison between the "T_{best}" curve and the mixture curves, while the right column shows the temperature profile results.

The 1:1 ratio results indicate a strong agreement between the T_{best} and mixture curve for the two low temperature peaks but less so for the high temperature peak. The recovered temperature of 765 K is close to the 750 K, suggesting a bias of the thermal history reconstruction to the lower temperature range of the temperature distribution in the mixed sample. A second peak is present in Figure 7-2b at 840 K, indicating the presence of at least more than one temperature within the sample and is more than likely responsible for the poor agreement of peak 3 in Figure 7-2a. It is important to note that second η peak does not correspond to either heating temperature, 760 K or 950 K, suggesting the η peaks cannot be used to directly obtain the temperature distribution, but only to determine that more than one temperature is present in the sample. The 2:1 ratio results in Figure 7-2b-c also favors the lower temperature portion of the mixture as expected. The presence of multiple thermal histories is still evident in the temperature profile plot, as indicated by a "hump" at ~835 K, and a lack of agreement between the T_{best} and mixture curves for the high temperature peak. The 1:2 ratio data in Figure 7-2e-f also indicates the presence of multiple thermal histories as indicated by

two distinct peaks in the temperature profile plot and the evidence of partial heating seen at the low temperature peak in Figure 7-2e.

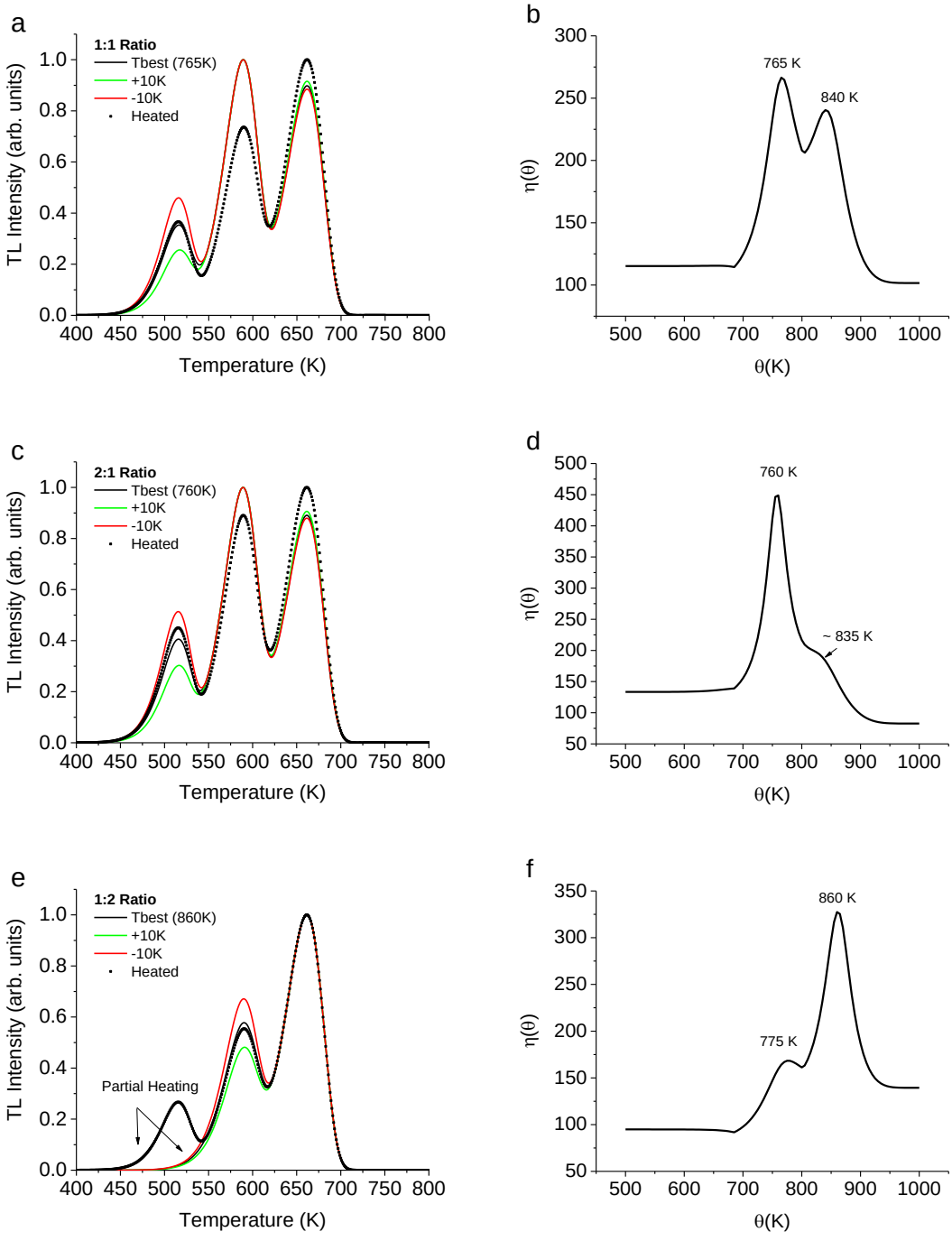

Figure 7-2. (a,c,e) Comparisons between the T_{best} and simulated ratio data and (b,d,f) the corresponding η profiles.

7.1.2 Realistic Temperature Distribution

The distributions of maximum temperatures provided in Figure 3-6a were used to obtain a more realistic temperature distribution of particles under agent-defeat testing conditions. The maximum temperatures were used to simulate an exponential decay temperature profile using Equation 3-23 for a decay constant of 50 ms, assuming a 1 s total heating time. Figure 7-3a shows all the exponential decay temperature profiles from Figure 3-6a.

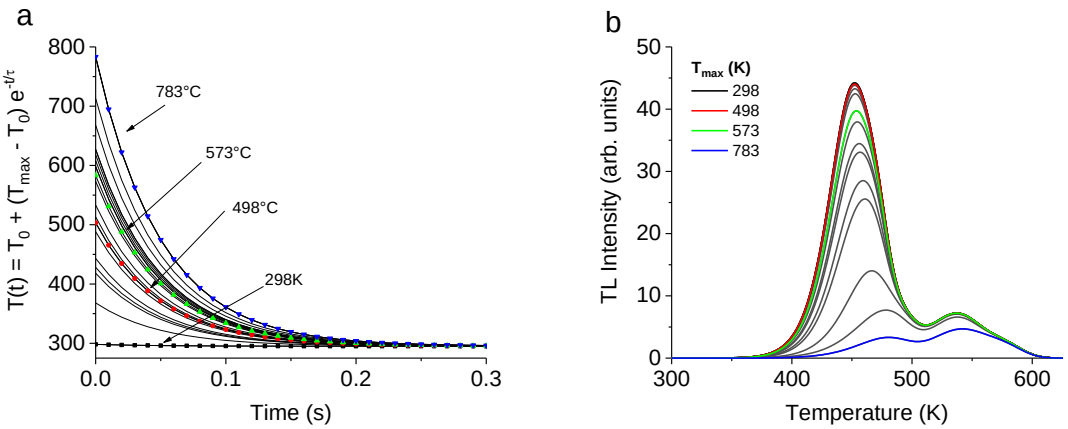

Figure 7-3. (a) Temperature profiles calculated using the data found in Figure 3-6a and (b) the corresponding residual TL curves.

The temperatures in Figure 3-6a were obtained from the thermal history reconstruction of individual MBO particles following a DTRA agent-defeat test by Armstrong (2017). The TL modeled used in the thermal history reconstruction was previously introduced in Figure 3-6b, and we will use the same model in this section. Then, Equation 3-22 was used to simulate the thermally depleted curves of MBO resulting from the heating functions in Figure 7-3a. The thermally depleted MBO TL curves are shown in Figure 7-3b. For purposes of this analysis, we assumed all particles are of equal size and mass and were exposed to the same uniform

radiation dose prior to use in agent defeat testing, but this is generally not the case for real materials.

Figure 7-4a shows a comparison between the summation of all the residual TL curves from Figure 7-3b and an unheated control curve. Figure 7-4a shows a small depletion of simulated heated TL curve as compared to the unheated control curve, as indicated by a decrease in the main peak (~450 K) intensity. Thermal history reconstruction was carried for the simulated heated TL curve in Figure 7-4a. Simulated heated TL curves were calculated using the MBO model and an exponential heating function with a 50 ms decay constant and a range of maximum temperatures between 373 K and 1273 K. Figure 7-4b shows a comparison between the T_{best} (573 K) curve and the simulated heated curve.

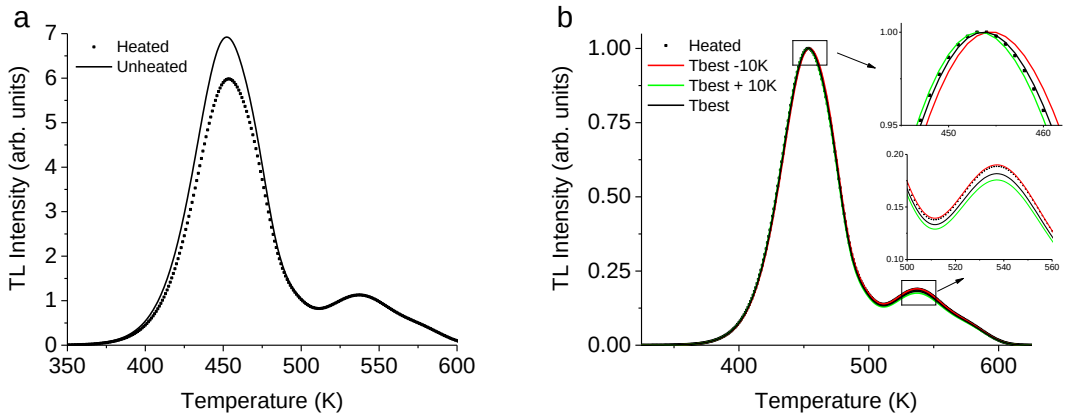

Figure 7-4. (a) Comparison between the simulated unheated ("control") and heated TL curves. The heated TL curve was obtained by summing the intensities of all the individual TL curves in Figure 7-3b. Both curves were normalized to the high temperature peak T_m ~ 540 K. (b) A comparison between the solution thermal history, T_{best}, the simulated heated curve and T_{best} ±10 K curves. T_{best} was 300°C (~573 K) assuming a 1 s heating and a decay constant of τ = 50 ms.

Figure 7-5a shows the temperature profile for the range of maximum temperatures investigated and strongly indicates the presence of a single thermal history can best explain the entire sample. The profile peak width at half maximum is ~ 20 K, and further suggests the sample was either heated using a single or a narrow temperature distribution centered about 300 °C. This result suggests the residual TL curve obtained from a sample comprised of particles

heated to a wide range of maximum temperatures (~ 500 °C range) can be explained by a single thermal history and suggests a flaw in the thermal history reconstruction method or the method for data collection. Figure 7-5b shows the depletion of the residual TL curve area as a function of maximum temperature. The T_{best} value obtained in Figure 7-5a results in less than a 10% depletion of curve area (~93%) and could be considered to have received insufficient heating (Yukihara et al., 2016). In fact, Armstrong (2017) found a total of 9 particles that were unheated in his original analysis.

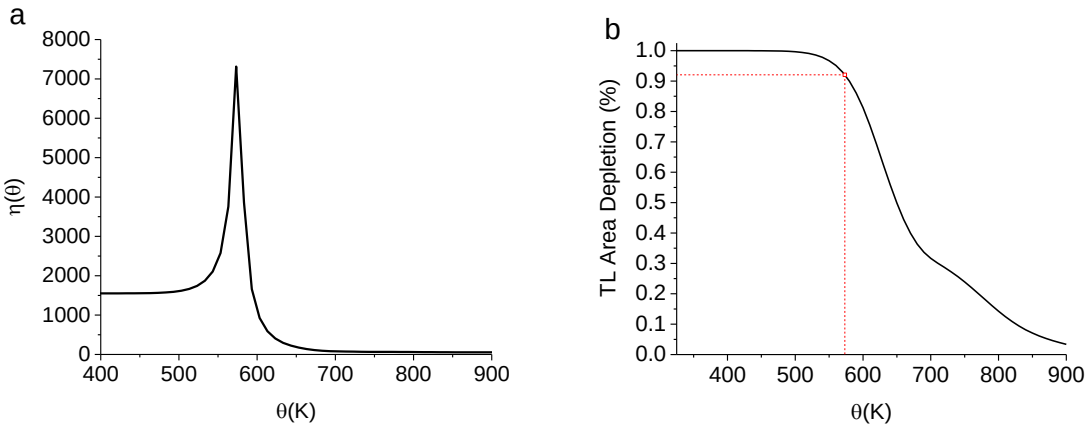

Figure 7-5. (a) Temperature profile curve for the curve in mixture curve in Figure 7-4a and (b) the depletion curve of TL area as a function of maximum temperature, grid lines indicate the position of the T_{best} value.

7.2 Single Particle Heating

In the previous section, we investigated the effect of mixtures of individual uniformly heated TL particles on thermal history reconstruction. Here, we consider single particles only and investigate the effect of thermal gradients within particle on the residual TL and resulting thermal history calculation.

Three particle diameters are used within this section: 25 µm, 50 µm and 100 µm. As was the case in the prior section, a hypothetical material was used, characterized by three first-order trapping centers with activation energies 1.35 eV, 1.55 eV, and 1.75 eV, and a common

frequency factor $s = 10^{12}$ s^{-1}. The initial trap occupancies for each trapping center are equal for all three traps and no noise is added to the TL curves. We used the thermal diffusivity constant for CSO in all calculations, $\alpha = 1.55 \times 10^{-7}$ $m^2 s^{-1}$ (Kontogeorgos et al., 2011).

7.2.1 Algorithm Validation

Figure 7-6 shows a comparison between the radial temperature profiles for a 50 μm particle in a 700 K heat bath using the FTCS solution and the analytic solution in Equation 2-50. The FTCS simulation use a ~0.5 μm spatial resolution and a ~0.4 μs time step. The FTCS results closely match the analytic solution indicating the numerical method is working correctly.

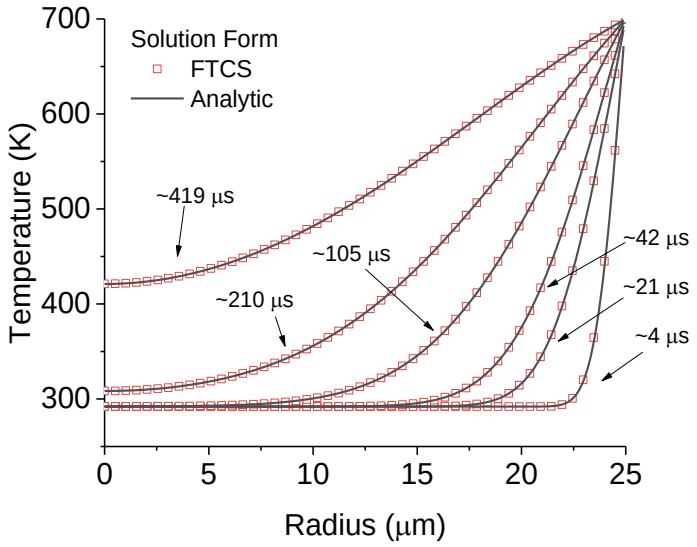

Figure 7-6. Comparisons of radial temperature profiles between the analytic and numeric solutions for a 50 μm CSO particle placed in a 700 K heat bath.

7.2.2 TL Thermal Response Time

Traditionally the characteristic time scale for particle heating is calculated using Equation 2-51, where the time scale is indicative of the time it takes the center of the particle to reach ~63% of the particle's surface temperature. Such a calculation is based on the existence of a time dependent temperature distribution within the particle. Since the trapping center

depletion is dependent on thermal exposure, it is reasonable to assume such a time scale would not be useful for identifying the response time of a TL temperature sensing particle. Alternatively, the uniform heating timescale (Equation 2-52) is expected to provide a better estimate for the TL response time of the particle, but needs to be verified. To obtain this new characteristic time scale, τ_c, for which the thermal history reconstruction temperature reflects the ambient gas or fluid temperature at the particle surface, we propose the following approach:

1. Divide the TL particle into *n* sub particles along the radius
2. Expose the TL particle to a set temperature for a set duration, t
3. Obtain the residual TL of each sub particle along the radius
4. Calculate the total residual TL and weight by geometric factor (e.g. $4\pi r^2 dr$)
5. Apply thermal history reconstruction assuming a constant heating for duration $\tau = t$
6. Check to see if reconstructed temperature is within 10 K of the set temperature
7. If not, increase exposure time, $t = t + \Delta t$ and return to Step 2, if so $\tau_c = t$.

We investigated three particle radius sizes, 12.5 µm, 25 µm, and 50 µm (25 µm, 50 µm, and 100 µm diameter particles). A set temperature of 700 K was used, and the heating duration was run for a simulation time of 100 ms. Radial temperature distributions were obtained using the method outlined in Section 3.6.2. The number of spatial data points was chosen to be equal to the integer value of the particle's diameter (e.g. 12.5 µm radius has 50 sub particles). This value was chosen to ensure thermal gradients within the sub particles themselves were minimal. The time step for the simulation depends on the particle size and was chosen to be sufficiently small enough to ensure computational stability, $\Delta t = \Delta x^2/4\alpha$. For example, a particle with a 12.5 µm radius has a spacing of Δx~0.52 µm and a time step of Δt~0.44 µs.

Figure 7-7a shows the radial temperature profile ($0 \leq r \leq 25$ µm) for the 50 µm particle at intervals of ~42 µs up to ~1.9 ms. The particle's surface temperature, at r = 25 µm, is fixed to the boundary condition of 700 K. The interior particle increases as a function of time with the core temperature, r = 0 µm, reaching ~690 K after ~1.8 ms.

Figure 7-7b shows the residual TL curves obtained for the 50 µm particle after ~1.9 ms. We compared the curves from three theoretical particles; an unheated particle (control), a uniformly heated particle (surface temperature = interior), and a simulated particle with thermal gradients within the interior obtained using the FTCS solution. The FTCS TL curve was used to calculate the thermal history, assuming a 1.9 ms heating duration and a constant heating profile. The FTCS curve returned a T_{best} of 681 K assuming a ~1.9 ms heating, while is ~ 20 K below the set temperature of 700K.

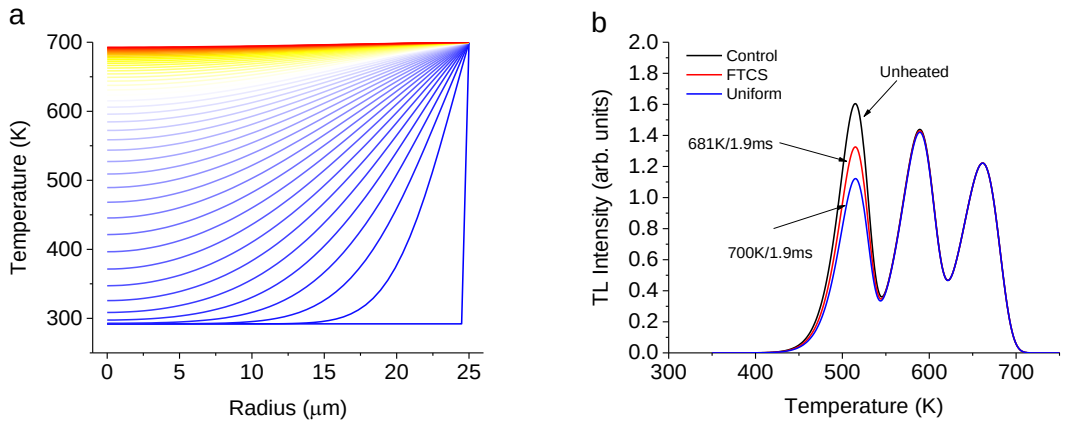

Figure 7-7. (a) Radial temperature profile of a 50 µm (diameter) particle placed in a 700K heat bath for 0.1 s. Contour lines are shown up to ~1.9 ms. (b) TL curve comparisons for a 50 µm particle subjected to no heating (control), radial uniform heating (predicted) and a non-uniform heating (FTCS).

Temperature distributions were obtained for each particle size (r = 12.5 µm, 25 µm, and 50 µm) at each time step. Using Equation 3-26, we calculated the total residual TL curves for each TL particle size at intervals of every 25-time steps. Then, each residual TL curve was used to perform a thermal history reconstruction assuming a constant heating profile and a heating duration equal to the simulation time step from which the TL curve was obtained. Each total

residual TL curve was used to obtain a reconstructed temperature (T_{best}) through the calculation of $\eta(\theta, \tau)$ using Equation 2-42 a temperature range between 600 K and 900 K (1 K step size) for a time scale, τ, equal to the simulation time from which the analysis curve was obtained.

Figure 7-8 shows the T_{best} values for the three particle sizes as a function of simulation run time (or exposure time). A horizontal line was placed at 690 K, ~98.6 % of the set temperature, and was chosen to be the critical threshold at which the particle was assumed to have been heated sufficiently such that its reconstructed temperature approximated the set temperature. The ±10 K threshold is arbitrary, but has been used by others as a basis to display the effect temperature changes on thermal history reconstruction results (Yukihara et al., 2014b; Yukihara et al., 2015; Yukihara et al., 2016). A better threshold metric should account for the possible sources of error within the thermal history reconstruction, as well as the desired accuracy of the thermal sensor itself and is left as future work.

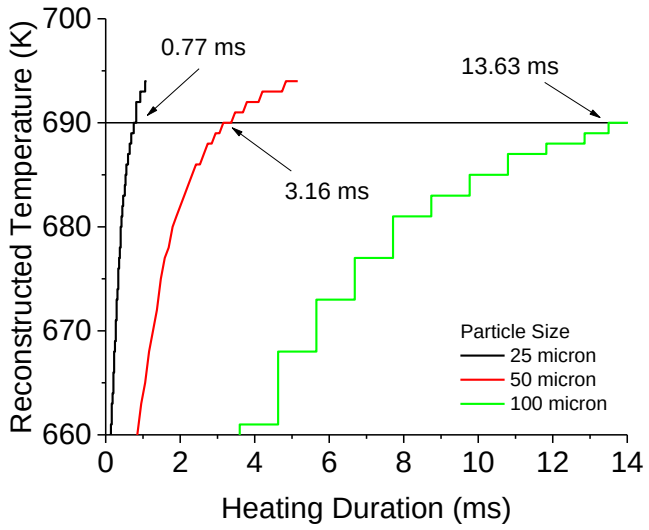

Figure 7-8. Reconstructed temperatures for various particle sizes as a function of exposure time to a 700 K heat bath. A horizontal line is placed at 690 K and the corresponding exposure time to reach this temperature is provided in the plot.

We found that the 25 µm, 50 µm, and 100 µm particles reached the critical temperature in ~0.8 ms, ~3.2 ms, and ~14 ms respectively. Calculation of the time constant found in Equation 2-51 produces characteristic heating times of ~0.10 ms, ~0.41 ms, and ~1.63 ms for the same particle diameters. There exists a very larger difference (~7-8 times longer) between the two sets of timescales, which suggests the new method for response time is superior for temperature sensing particles.

The use of the uniform heating time constant found in Equation 2-52 produced more reasonable heating times of ~0.5 ms, ~2.04 ms, and ~8.2 ms for the 25 µm, 50 µm, 100 µm particle sizes (diameters) respectively. These timescales correspond to a reconstructed temperature of ~697 K for each particle size. Equation 2-52 is based upon the time it takes the center of a spherical particle to reach 99.3% ($1-e^{-5}$) of the temperature difference between the particle and the surrounding environment which is ~697 K for a particle that starts at 292 K and is heated to 700 K. The simulation run times for Figure 7-8 were extended to obtain the heating duration required for the 25 µm and 50 µm particles to produce a reconstructed temperature of 697 K. We found heating times of ~2.3 ms and ~9.8 ms were required for the 25 µm and 50 µm particles respectively, and are still significantly longer than those predicted by Equation 2-52, suggesting the trapped charge lifetime (Equation 5-3) plays a significant role in the response time of the particle. By calculating the ratio of heating times to the smallest particle size, a trend of 1:4:16 is obtained for Equation 2-52 and 1:4.1:17.7 when using the new metric. This suggests that, while the response time is increased, the overall heating behavior obeys a similar scaling law.

7.3 FLAG Hydrocode Simulations

Hydrodynamics simulations were conducted according to the methods outlined in Section 3.6.3 to model the blast environment around individual TL particle sensors within a closed chamber agent-defeat test. The tracer particle temperature histories are used to model the residual TL curves from TL particle sensors within the same blast environment.

7.3.1 Tracer Particle Behavior

Nine massless tracer particles were placed within the simulation (Table 3-3) to track local gas temperature and position of a massless particle through the evolution of the simulation. Figure 7-9a shows the positions of the tracer particles in the two-dimensional plane through the evolution of the simulation. Tracers #1 and #4 travel the furthest from their initial position. Both particles follow the lead shock front, a region of high pressure gas from the detonation, into the containment wall and then move radially outwards with the gas as it fills the chamber. The remaining tracer particles follow unique paths dictated by the turbulent flow of the expanding gas within the chamber.

Figure 7-9b shows the temperature-time profiles of the individual tracer particles, or simple “tracers”. The profiles are all characterized by a large jump in temperature, signifying the arrival time of the lead shock front. After the arrival of the shock front, all tracers have their own unique temperature profile, dictated by the particles trajectory through the heated gas and the gases interactions with the chamber. Spikes in temperature arise from regions of increased pressure as the tracer moves through the system. Large jumps, such as those at 0.2 ms for tracer #4, are the result of the lead shock colliding with the chamber wall producing a so-called reshock as the reflect shock waves interact with the expanding gas.

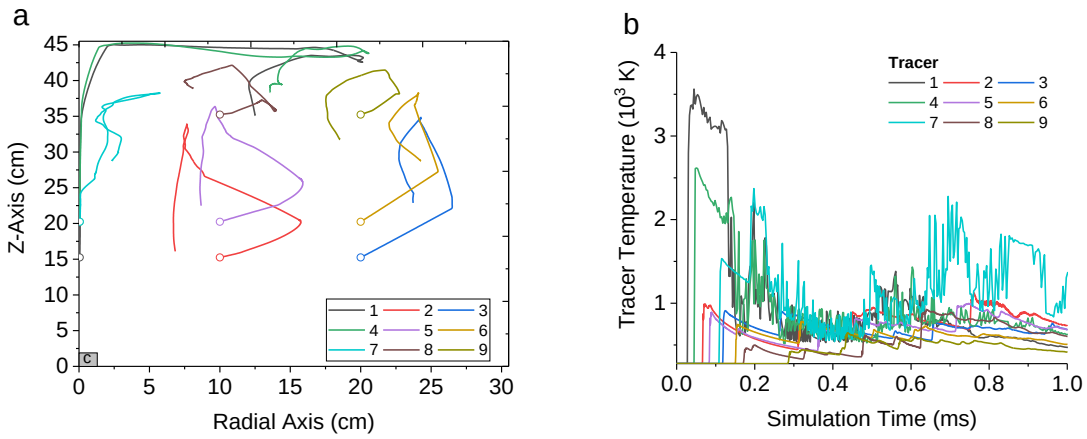

Figure 7-9. (a) Tracer positions over a 1 ms run. Initial positions are indicated by open data points. Tracers 1 and 4 represent the initial positions with regards to the NSWC test (Daniels et al., 2015), while the rest are to test effects of change the target agent location with regards to the HE charge. (b) Tracer temperatures as a function of simulation time. Tracers 1, 4, and 7 were sampled every four data points to reduce noise.

7.3.2 TL Particle Modeling

The tracer temperatures in Figure 7-9b were used as the boundary conditions to solve the one-dimensional heat equation as outlined in Section 3.6.3. The same trap parameters, E = 1.35 eV, 1.55 eV, and 1.75 eV and with a common frequency factor $s = 10^{12}$ s^{-1}, and thermal diffusivity constant used in the previous section are used again here. We only consider a 50 µm single particle size, as larger particles demonstrated no response to the heating (no curve depletion) and smaller particles were often fully depleted. This is not to say that larger particles would not be heated under these detonation conditions, but the short heating time, ~ 1 ms, was insufficient to produce changes to the residual TL curves.

Figure 7-10a shows the time-temperature profile at various radius positions and Figure 7-10b shows the corresponding residual TL curves. As the radius decreases, a dampening-like effect is observed for the temperature response. At the end of the simulation runtime, we see that multiple radii < 15 µm have reached similar temperatures. Following the methods outlined in Section 3.6, the residual TL curve for a single TL particle located at each radial position was

obtained. Representative TL curves for the temperature at the radii in Figure 7-10a are shown in Figure 7-10b.

Figure 7-11a shows the TL curves obtained in Figure 7-10b adjusted by Equation 3-26 to obtain the TL resulting from a shell at each radial position. The most intense curves were obtained near the center of the radii, ~12.5 µm, because the outer radii have been exposed to higher temperatures while the interior regions, which see lower temperatures, contribute a significantly smaller amount to the total TL.

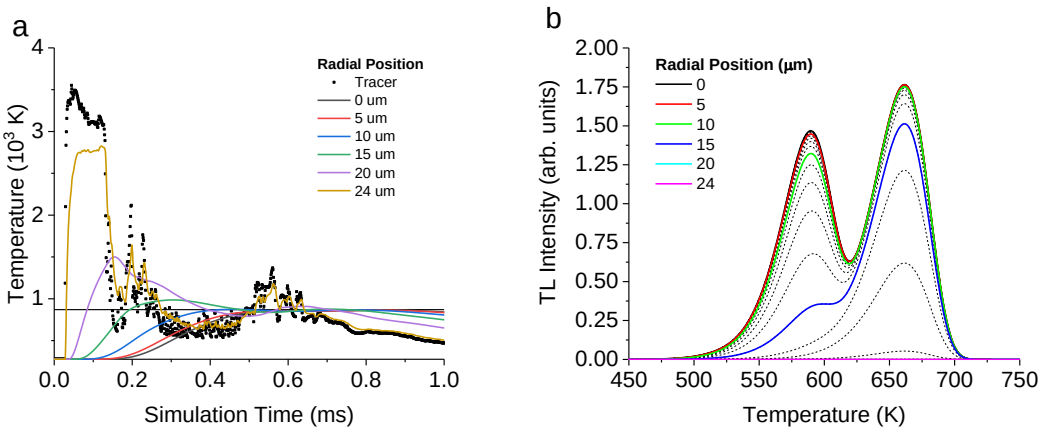

Figure 7-10. (a) Hydrocode simulation local gas temperature and radial temperatures of a 50 µm particle and (b) corresponding residual TL curves. The horizontal line in (a) corresponds to the reconstruction temperature of 870 K.

The total residual TL from the particle is obtained by summing over the residual TL at each interior radius using Equation 3-26. Figure 7-11b shows a comparison between the total residual TL and with the TL from an unheated particle. Then, the total residual curve is used for temperature reconstruction assuming a heating duration equal to the total run time of the hydrodynamics simulation.

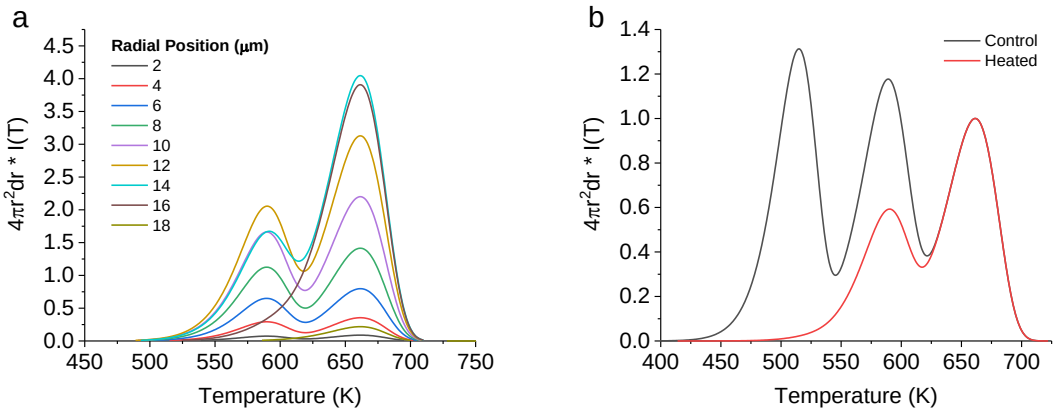

Figure 7-11. (a) Residual TL curves from shells at various radial positions and (b) comparison between the total control and total residual (heated) TL curves.

As shown in Figure 7-9a and Table 3-3, the tracer particles start at three different positions 0.05 cm, 10.0 cm and 20.0 cm measured radially outward from the center line. At each radial position, the tracers are placed 15.2 cm, 20.2 cm, and 35.2 cm from the high explosive (HE) charge along the z-axis. Temperature reconstruction results for each radial position group are shown in Figure 7-12 (0.05 cm), Figure 7-13 (10 cm), and Figure 7-14 (20 cm). The results are presented so that each row in the main figure corresponds to a single tracer. The row contains the tracer temperature profile, the residual TL curve and the T_{best} solution curve, and the solution profile, η(T), used to calculate the T_{best} value.

The results for the 0.05 cm group show the highest temperature exposure with reconstructed temperatures between 840 K and 900 K. As the total simulation run time was limited to 1 ms, we expected particles closest to the charge to report the highest temperatures as they spend a longer time exposed to the post denotation fireball. Evidence of partial heating was found for tracer #4, seen in Figure 7-12e and f. As the tracer temperature rises and falls, the particle heats and cools allowing for different temperature regions within the particle to develop, which in turn acts as a set of individual particles with a distribution of thermal histories,

see Section 7.1.1. Maximum tracer temperatures were found to be in the 2,000 K to 3,500 K range at the arrival of the lead shock (~ 0.1 ms duration).

The results for tracers placed at the 10 cm along the radial axis are found in Figure 7-13. The tracer temperatures for these particles were characterized by a large jump signaling the arrival of the lead shock, which was followed by an exponential-like decay as the simulation time increased. The maximum tracer temperature was found to be ~ 1,100 K. Thermal history reconstruction of tracers at this radial position resulted in temperatures between 700 K and 740 K. Evidence for partial heating was seen for tracer #2 in the depletion of the high temperature TL peak in Figure 7-13b despite the lack of depletion of the middle TL peak. Additionally, the solution profile shows a small shoulder (Figure 7-13c), which suggests the effect of particle heating was minimal.

The result for tracers placed at 20 cm along the radial axis are found in Figure 7-14. Reconstructed temperatures were found to be between 570 K and 700 K, but the profile curves for tracers #6 (Figure 7-14f) and #9 (Figure 7-14i) show no clear peak suggesting minimal to no heating took place. Tracer temperatures never went above 900 K and were characterized by steep jumps followed by a cooling period, similar to those found four the 10 cm group.

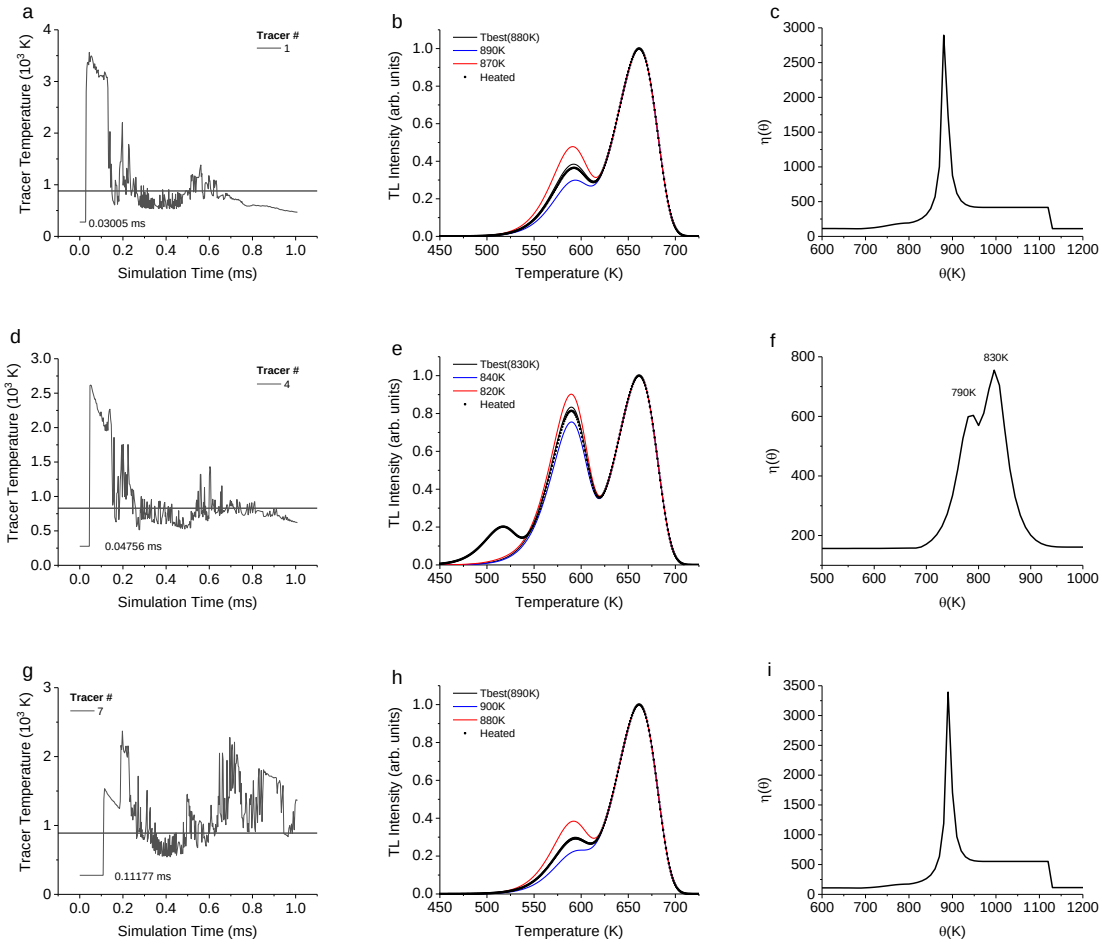

Figure 7-12. Simulation and temperature reconstruction results for tracers placed at 0.05 cm away from the charge along the radial axis at 15.24 cm, 20.24 cm, and 35.24 cm along the z-axis. The shock arrival time is listed in each tracer temperature plot. The horizontal grid lines in the tracer temperature plots correspond to the T_{best} temperature for the given tracer.

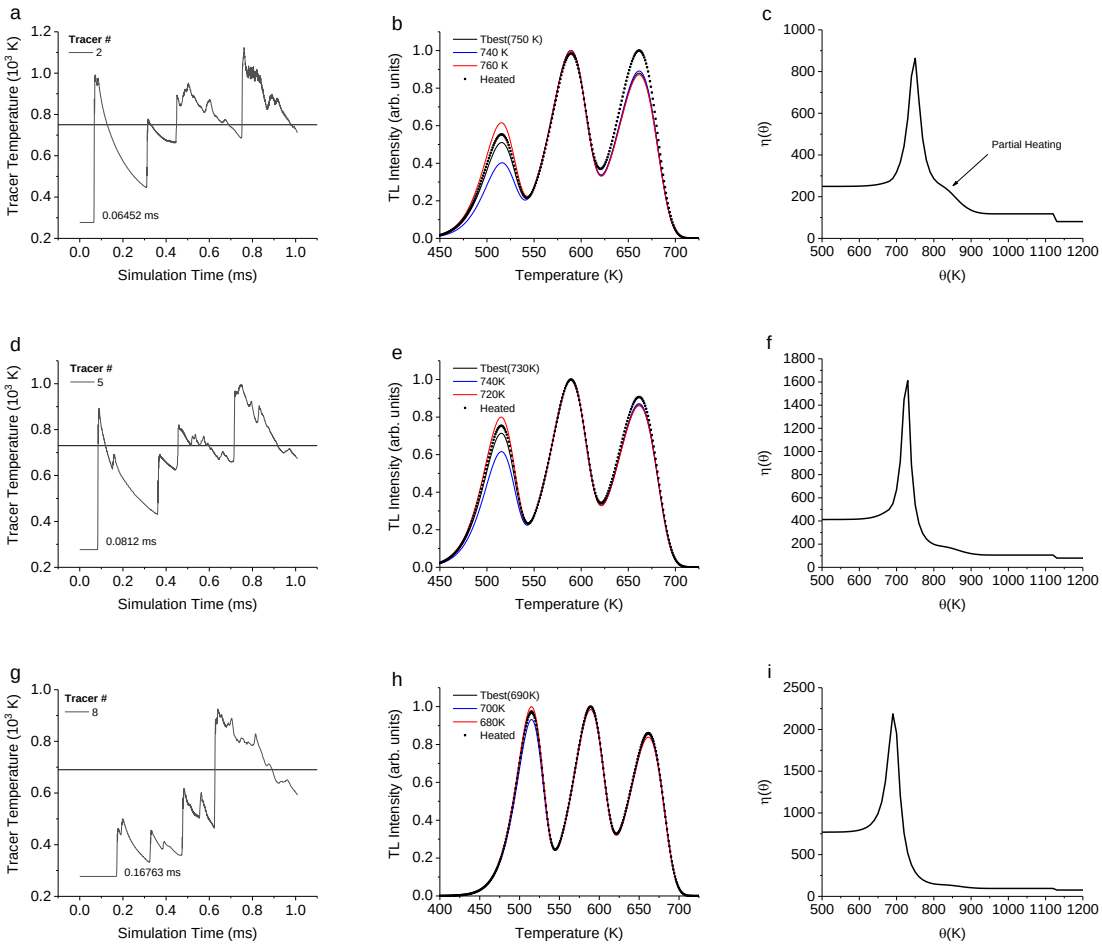

Figure 7-13. Simulation and temperature reconstruction results for tracers placed at 10 cm away from the charge along the radial axis at 15.24 cm, 20.24 cm, and 35.24 cm along the z-axis. The shock arrival time is listed in each tracer temperature plot. The horizontal grid lines in the tracer temperature plots correspond to the T_{best} temperature for the given tracer.

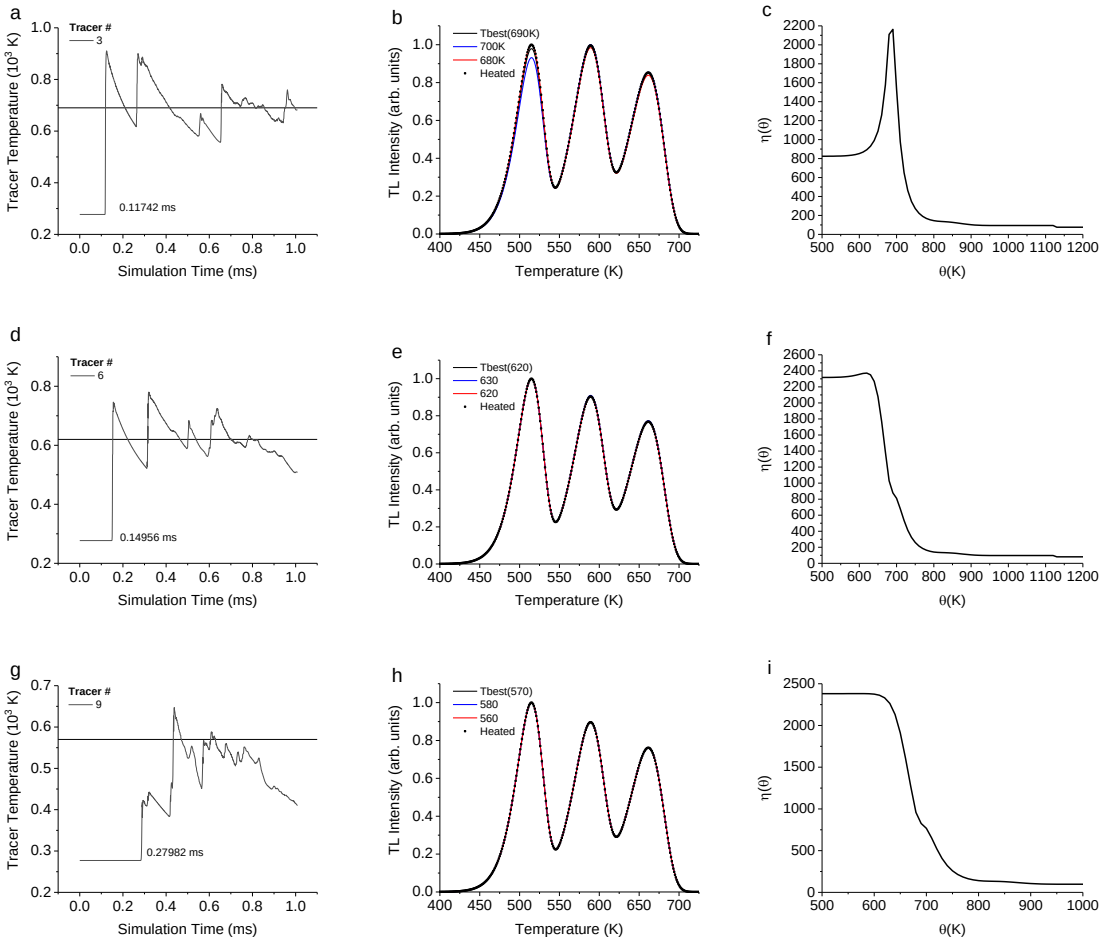

Figure 7-14. Simulation and temperature reconstruction results for tracers placed at 20 cm away from the charge along the radial axis at 15.24 cm, 20.24 cm, and 35.24 cm along the z-axis. The shock arrival time is listed in each tracer temperature plot. The horizontal grid lines in the tracer temperature plots correspond to the T_{best} temperature for the given tracer.

Figure 7-15 shows the reconstructed temperatures for each tracer as a function of the arrival time of the lead shock wave. Except for tracers #7 (r = 0.05 cm, z = 35.24 cm) and #8 (r = 10 cm, z = 35.24 cm), the particle temperature decreases with an increase in the shock arrival time. Previously, we found the characteristic response time of a 50 µm particle was ~ 3.16 ms, see Figure 7-8, ~ 3 times longer than the simulation run time used here. As the simulation run time was fixed to ~ 1 ms, the reduction of the particle temperature is most likely due the reduction in heating time. The outlier temperatures for tracer #7 and #8 suggest that initial particle placement does influence the final temperature, but the degree to which is effect is

important is not possible to determine from the results presented in this study. Additionally, we would expect longer simulation run times to result in all tracer particles having the same temperature as the system reaches thermodynamic equilibrium. This effect was already reflected in the convergence of individual tracer temperatures at the end of the simulation, in Figure 7-9b.

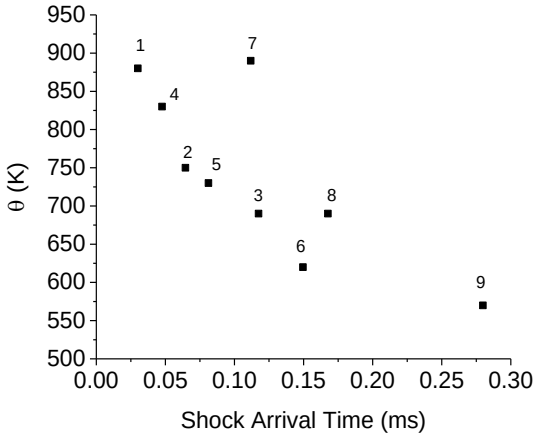

Figure 7-15. Reconstructed thermal history as a function of shock arrival time.

Influence of Trap Parameters

Traditionally, agent-defeat testing can utilize multiple types of TL particles (e.g. MBO and CSO) in the same test. Therefore, it is important to understand how changes to the underlying trap parameters effects the reconstructed temperature values.

To investigate the influence of trap parameters on the previous study, we selected temperature data from a single particle, tracer #1 in Figure 7-12a, to simulate the radial temperature profile for a two new sets of trap parameters. The first parameter set has three-trap centers and one recombination center. It is characterized by trapping centers which have a higher thermal stability than those investigated previously. The activation energies are 1.75 eV, 1.95 eV, and 2.15 eV all with a common frequency factor $s = 10^{12}\ s^{-1}$. The second set of trap

parameters has five trapping centers with activation energies 1.35 eV, 1.55 eV, 1.75 eV, 1.95 eV, and 2.15 eV and a common frequency factor $s = 10^{12}\ s^{-1}$. Again, a single recombination center is assumed.

Figure 7-16 shows the temperature reconstruction for both the new three- and five-trap theoretical TL materials. The three-trap system produced a T_{best} temperature of 948 K, much higher than the temperature of 880 K found using the old trap parameters in Figure 7-12c. We suggest the higher T_{best} value is a result of the more thermally stable trapping centers, which remains populated (though reduced) even at high temperatures. Although this may seem counter intuitive, consider a TL particle (or shell) close to the edge of the 50 µm particle. If the temperature is sufficiently high to fully deplete the entire TL curve, it will not contribute to the total residual TL curve. This will bias the residual LT curve to the interior shells, which see a lower temperature due to heat transfer, but if that same TL particle now has more thermally stable trapping centers, it will contribute to the residual TL curve and pass on that information during the thermal history reconstruction.

The five-trap system produced a T_{best} of 940 K, within 10 K of the new three trap system. Additionally, we found evidence of partial heating in Figure 7-16a suggesting that the more complex the trap system the greater chance for partial heating.

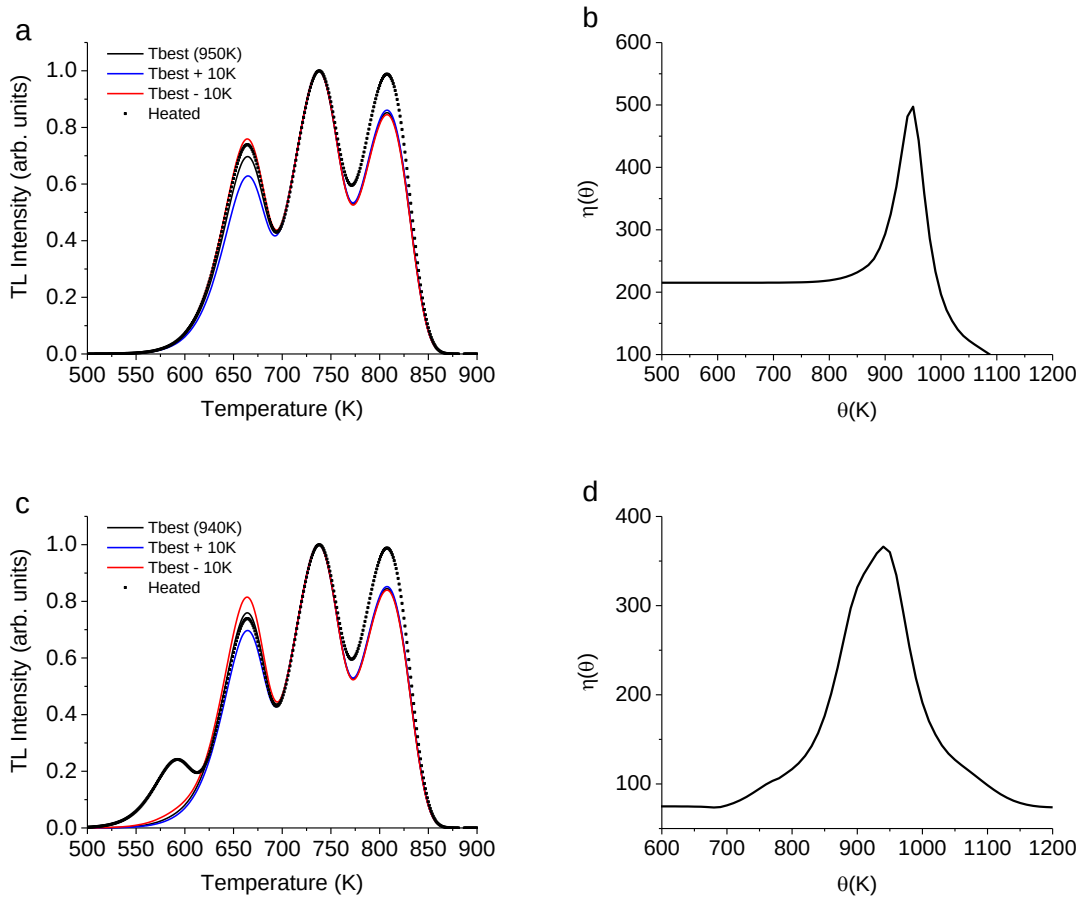

Figure 7-16. Analysis results for the 3-trap (1.75 eV, 1.95 eV, and 2.15 eV) and a 4-trap (1.35 eV, 1.55 eV, 1.75 eV, 1.95 eV, and 2.15 eV) models subjected to the temperature profile of tracer #1. (a,c) Heated curves with the best fit (T_{best}) and ± 10K solution curves and (b,d) η plots as a function of hold temperature θ.

Particle Heating of CSO

A TL model for CSO was obtained using the one-dimensional deconvolution model (Section 3.4.4) and applied to the TL curve from a CSO control sample (few grains) from the NSWC-2013 closed chamber detonation test. The TL curve was previously used to conduct thermal history reconstruction by Yukihara et al. (2015). The trap distribution for CSO, assuming a fixed frequency factor $s = 10^{14}\ s^{-1}$ is shown in Figure 7-17a. A total of 30 activation energies were used with a ~0.05 eV spacing. The NSWC-2013 tests used CSO sieved to particle sizes below 125 µm. We investigated the heating of two different particle sizes: 50 µm and 100 µm in

diameter. For each particle size, we obtained radial temperature profiles subject to the temperature boundary conditions provided by tracer #1 in Figure 7-12a.

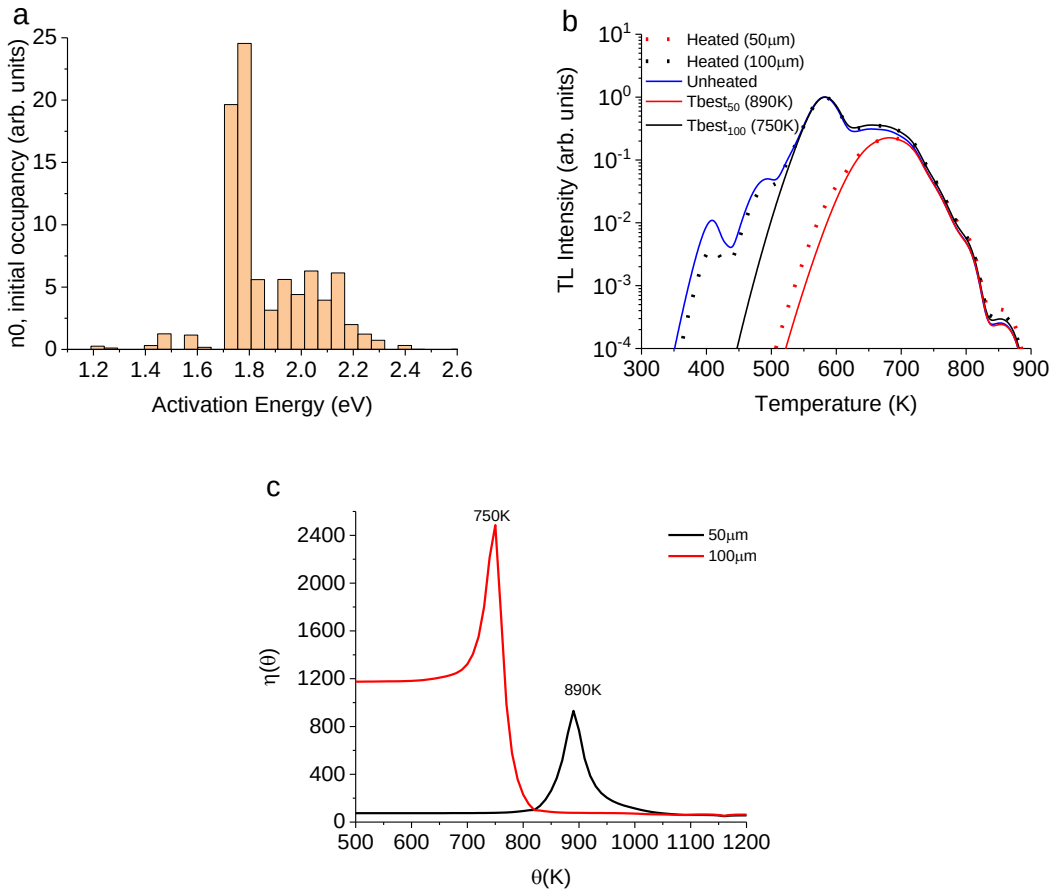

Figure 7-17. (a) CSO trap distribution obtained from the one-dimensional deconvolution assuming a fixed frequency factor $s = 10^{14}$ s^{-1}. (b) Comparisons between the simulated residual TL curves for the 50 μm and 100 μm CSO particles using temperature data from tracer 1 and (c) η plots as a function of hold temperature θ for each particle size.

Residual TL curves and T_{best} curves for each particle size are shown in Figure 7-17b. As expected, the curve for the 50 μm diameter particle shows a larger sensitivity to the heat exposure than that of the 100 μm diameter particle due to its smaller size. We found a reconstructed temperature of 890 K for the 50 μm diameter particle, consistent with the three-trap system results for tracer #1 (Figure 7-12), but below the results of the alternate trap systems (Figure 7-16). The reconstructed temperature for the 100 μm particle was found to be 750 K, significantly lower than the 50 μm particle. This result is of interest as both particle sizes

were likely to be present during the test as the particle selection was limited to below 125 µm. The 100 µm also shows a strong degree of partial heating as TL peaks one and two are still present for the simulated residual TL curve while the T_{best} curve shows both peaks fully depleted.

7.4 Discussion

The results presented in these studies aim to provide a basic understanding of several, previously ignored, factors that affect the use and accuracy of thermal history reconstruction based upon TL particle temperature sensors. These factors include the effect of multiparticle temperature distributions, thermal response time, and exposures to realistic thermal profiles.

Until recently, analysis of post-detonation test material has assumed the particles within each aliquot experience a similar thermal history. Armstrong (2017) found the exact opposite to be true, finding several hundred-degree differences in max temperature among individual MBO particles from a single aliquot material from the Humble Gingko XIX detonation test. When considering simple mixtures of TL particles exposed to two different temperatures, we found the thermal history reconstruction to be biased to the lower exposure temperature even when the mixture heavily favored the higher exposure temperatures. This finding is a direct result the temperature reconstruction method's dependence on sequential depletion of the TL curve. We also found the mixtures to reproduce the "partial heating" finding previously discovered in close chamber testing (Yukihara et al., 2015). It may be possible to infer a temperature distribution or uncertainty from the width of the T_{best} solution profile peak, see Figure 7-2d, but is left as a future study.

We found the same bias to lower temperatures when studying the temperature distribution of realistic MBO data from Armstrong (2017). Despite a broad range of maximum

temperatures, 300 K to 783 K, we found the sample to return a T_{best} of 543 K (300 °C), right in the middle of the temperature distribution in Figure 3-6a. The MBO sample used by Armstrong (2017) was obtained from site three in the source room, "SRC 3". Analysis of two aliquots from the same MBO sample using a one-dimensional deconvolution TL model and an exponential decay heating function (50 ms decay constant) resulted in similar temperatures of 566 K and 588 K (Yukihara et al., 2016). These results reinforce the conclusion that, when performing analysis of samples, one is averaging the results and therefore, underestimating the temperatures of many of the particles while overestimating the temperatures of others. This suggests one must conduct individual analysis of each TL particle within a sample, an extremely time intensive undertaking. It may be possible to use a deconvolution approach, but such an effort would require a "clean" regenerated TL curve from the sample itself. This is problematic as the detonation testing can mix TL sensitive materials into the analysis sample and materials such as MBO suffer from sensitization.

We developed a method for obtaining a characteristic heating timescale for an individual TL particle given its size and thermal diffusivity. The system we studied was the simplest and can easily be expanded to consider other heat transfer effects such as relative gas flows over the particle and radiative heat transfer. We found the response time for 50 µm TL particles to be ~ 3.16 ms, fast enough to measure sub second heating events, but not transient heating events (~ 1 - 10 µs) found in agent-defeat testing. This suggests a need for varied particle sizes for different testing environments and is of interest for future studies.

We had hoped this study would clarify the results from shock tube tests conducted at UIUC. A thorough discussion of the experimental system is presented by Guo (2015) and the results are summarized in the DTRA project report, Yukihara et al. (2016). The test essentially consists of 35 µm CSO TL particles loaded into the shock tube ~ 2.67 m from the collection

chamber at the end of the tube. A shock wave (~ planar wave) is propagated along the tube, followed by a high temperature region used to heat the TL particles. The NASA CEA program takes velocity and pressure inputs from the shock wave to calculate post-shock temperatures. From the shock velocity, it was estimated that exposure times lasted between 2 ms and 5 ms, well within the response time for 35 μm CSO particles. Estimated temperatures of the shocked gas were found to be much higher than the temperatures obtained by thermal history reconstruction of heated CSO particles. From the results presented on TL response time in Section 7.2.2 and hydrocode simulations in Section 7.3.2, we suspect the difference was not due to slow response time. The NASA CEA program provides a single temperature, but we suspect the thermodynamic environment in the post-shock wave region to not be uniform in temperature for the duration of the particle heating, which in turn would result in the temperature underestimation by the TL particles.

The FLAG hydrodynamic simulations provided insight to the behavior of TL particles in agent defeat testing such as the DTRA NWSC closed chamber test. Tracer results show that a particle's initial position has a strong influence on its path through the fireball, and therefore, the temperature its experiences. Tracer temperatures were not found to resemble the constant or exponential decay heating functions typically used in thermal history reconstruction (Talghader et al., 2016), which will produce an incorrect estimation of the temperature history experience by the particle. However, we also found the particles to be unaffected by the transient temperature behavior, which suggest that the constant and exponential functions may capture the longer time scale temperatures of the blast environment after the main shocks and reflected shocks have dissipated.

The ~ 1 ms simulation run time was considerable shorter than the estimated ~ 0.1 s heating time by Yukihara et al. (2015), who found temperatures of CSO for LBPX to be ~ 667 K.

The initial position for tracer #1 reflects the original position of ~ 2 g of sample material during the tests. We found a temperature of 890 K for tracer #1 in Figure 7-12a-c, and ~750 K (~100 µm) when using the CSO TL model, both are considerably higher than the published result, especially when considering the differences in heating time. The exact reason for these differences in temperature are not known, but there are major factors we have not yet addressed such as the explosive formulation and effect of particle aggregation. We have used PBX 9501 as a surrogate for the unknown LPBX formulation, which if less energetic would produce lower temperatures and account for the overestimation in temperature. The most basic effect of particle aggregation is the creation of larger effective particle size and can occur post material preparation (e.g. sieving) as was a problem in laboratory tests with TL materials (Yukihara et al., 2014b). The effect of aggregation is also known issue when modeling temperature induced spore death for bio-agents such as anthrax and has the effect of greatly reducing the rate heat transfer (Zhu et al., 2012).

We also found that, when allowing for heat transfer across a particle, trap parameters have a drastic effect on the thermal history reconstruction temperatures. A comparison between two three trap models resulted in a ~ 70 K increase in temperature when substituting a less thermally stable trap for a more thermally stable trap. If the TL particle is found to be uniformly heated ($Bi < 0.1$), then the TL model will play a negligible role in the temperature calculation, but if thermal gradients are present then the TL model, along with the heat transfer properties of the material will play a significant role in temperature determination.

CHAPTER 8

CONCLUSIONS

In this work, the step-annealing method and two-dimensional deconvolution analysis methods were investigated for their accuracy and validity as applied to complex TL curves. The insight and methods obtained from those studies were applied to the TL trap parameter analysis of the novel temperature sensing materials: LBO, MBO, and CSO. Analysis of trap parameters including the VHRM as well as a study into thermal quenching of the TL curves from these materials. Known issues for TL temperature sensing, including partial heating and TL particle response time were investigated using numerical simulations based on hypothetical and realistic datasets. The DTRA NSWC closed chamber test (Yukihara et al., 2015) was modeled using the LANL FLAG code. The simulation looked at early, ~ 1 ms, blast wave environment for TL particles following the detonation of a PBX 9501 charge. Temperatures obtained from tracer particles were used to inform heat transfer simulations of TL particles to understand their response to transient temperature profiles and to provide context for previous test results.

The results presented in Chapter 4 showed the IRM utility as part of a researcher's tool box for understanding a material's underlying *E*-distribution, but it also reveals the method's limitations. Precise recovery of the input *E*-distributions used in this study was not possible, but this approach can provide a reasonable estimation of the *E*-distributions, if paired with additional analysis method such as trap density distributions proposed by (Van den Eeckhout et al., 2013) and the *E*-histograms.

The E-T_{stop} and trap density distributions showed the IRM approach underestimated the simulation input activation energies in a variety of cases: (a) when using weighted LLS fitting; (b) when the TL intensity is low; (c) for strongly overlapped peaks; (d) in the high-energy range of the E-distributions. In all these cases, the underestimation occurs due to the difficulty is isolating a region of the initial rise in which $n \sim n_0$, either because the intensity is low, and the initial rise is too noisy, or because the "initial rise" region of the apparent peak consists of several peaks.

In his work, the trap density distribution method proposed by Van den Eeckhout et al. (2013) was applied to experimental data only and was not investigated for the case of simulated datasets, and therefore, the extent of its limitations were unknown. We have implemented that approach here and shown that despite the presence of noise, this method provided reasonable estimations of the E-distributions, although the exact distributions could not be recovered in all cases. An arbitrary E-distribution, represented by the uniform distribution, could not be recovered by the method. We only investigate the trap density method for E-distributions, and therefore its efficacy for E-s trap distributions is not known. However, the success for E-distributions suggest promise for this technique as applied to temperature sensing materials.

The influence of noise was seen to be most impactful for low intensity TL peaks, typically found at high T_{stop} temperatures. The IRM is one of the most utilized methods for the determination of the kinetic parameters in TL materials, making it important to continue investigating its applicability and developing more reliable protocols. We suggest a route of future work in protocols that seek to increase the S/N for low intensity TL peaks. This can be achieved with a protocol that varies the radiation doses as the pre-heating is applied to increase the signal. Other methods to selectively isolate TL peaks, such as optical bleaching Biderman et al. (2002), should also be explored. Nevertheless, such alternative methods are material dependent and cannot be generalized.

The two-dimensional deconvolution study served as an extension and discussion of the work by Whitley et al. (2002) on simulated TSC data to that of realistic TL data. It was previously known that a recovery of the exact trap distribution was not possible for ideal curves (noiseless), but the inclusion of Poisson noise was found to decrease accuracy of this approach for step-annealed datasets and make it inapplicable to varied heating rate datasets.

The study demonstrated that the two-dimensional deconvolution technique can approximate the input distribution when using noiseless step-annealed data as was previously demonstrated for varied heating rate data (Whitley et al., 2002). Additionally, it was found that the technique can also approximate the input distribution for moderate S/N when applied to a two-trap distribution dataset of 7 curves. A larger dataset of 22 curves was needed to approximate the three-trap distribution, and the four-trap distribution failed for the 33-curve dataset. We found the technique to fail to recover the input distribution when using a noise added varied heating rate dataset for both the three and four-trap distributions.

Results from the two-dimensional deconvolution analysis were sensitive to numerous factors including (a) solution space resolution; (b) dataset size; (c) uniqueness of curves within the dataset; and (d) TL curve intensity (S/N). The choice of an optimal solution space resolution remains an open question, but the other cases are easily controlled by the individual running the experiment and analysis.

The two-dimensional deconvolution approach applied to step-annealed data resulted in reasonable estimations of the two-trap and three-trap distributions studied here and was unable to obtain a reasonable estimation for the four-trap distribution. The method requires a large and varied constraining dataset. Results of the extrapolation of the recovered trap distributions models to a broad range of heating profiles suggest promise for this technique as applied to temperature sensing materials. Even in cases where the exact distribution was not

recovered, Figure 5-14, the extrapolated result, Figure 5-15, suggested the model was approximate for heating times within an order of magnitude.

Traditional analysis methods or VHRM and IRM as well as the two-dimensional deconvolution method were used to obtain trap parameters for LBO, MBO, and CSO. In addition, the total curve and individual peak areas were obtained as a function of heating rate and peak position to determine if thermal quenching was present in these materials. The results for LBO and CSO showed a drastic decrease in total TL area and TL peak areas, a known thermal quenching effect. The evidence of thermal quenching means the trap parameters obtained should be treated with caution as they are likely incorrect as they were obtained from uncorrected TL data. To fully determine if thermal quenching is present, we suggest a study on the effect of temperature on the luminescence lifetimes for CSO and MBO, similar to those performed by (Akselrod et al., 1998b) for α-Al2O3:C.

TL characterization of LBO resulted in activation energies of ~ 1.06 – 1.13 eV for peak two and ~ 1.75 – 1.8 eV for peak three when using IRMs. Similar activation energies were found for the LBO:$Cu_{0.4\%}$,$Ag_{0.1\%}$ and LBO:$Cu_{0.3\%}$,$Ag_{0.3\%}$ concentrations. Activation energies obtained from the VHMR were ~ 0.3 eV higher than those obtained using the IRM. Sufficiently small sample sizes were used in these studies, so this result should not be the effect of thermal lag but could be a result of thermal quenching, which would skew the peak position to lower temperatures then expected at higher heating rates. There is also the possibility of each TL peak being comprised of multiple sub TL peaks. Trap density distribution for the IRM results do show each peak as having a narrow band of activation energies for each peak and the reconstructed TL peaks from the VHRM data in Figure 6-13 indicates there are additional TL peaks needed. Attempts to apply the two-dimensional deconvolution failed to produce well resolved peak

structures. Ultimately, more work needs to be conducted on LBO prior to its reliable use as a TL temperature sensing material.

TL characterization of MBO produced consistent results among all analysis methods used in the study. Two main TL peaks were evident at ~ 430 K and ~560 K with a small peak structure present between them. The 2nd TL peak showed significant sensitization, left as an outstanding study to be addressed prior to further use of this material in temperature sensing.

The ~430K MBO TL peak has an activation energy between 1.16 eV (IRM) and 1.24 eV (VHRM) while the higher temperature TL peak has an energy between ~1.81 eV (VHRM) and 1.88 eV (IRM-T_{hold}). These energy values were also found to be consistent with the solutions space distribution for the two-dimensional deconvolution method. The best results were obtained for the ΔE = 0.025 eV and $\Delta \log s$ = 0.25 resolution, which was the main resolution used for simulated datasets in Chapter 5, also. The frequency factors from the VHRM analysis were found to differ from those in the deconvolution by several orders of magnitude. One probable reason is that the deconvolution results found the main peak to be the result of multiple peaks centered at ~1.15 eV, ~1.21 eV, and ~1.27 eV. Despite the limitations of MBO having emission in the visible spectrum, it is well suited for application to temperature sensing.

TL parameter analysis for CSO was not successful in determining consistent values across the analysis methods used. The activation energies for the VHRM were found to be ~0.1 eV, ~0.15 eV, and ~ 1.4 eV higher than the IRM for peaks one, three and four (IRM search method) respectively. The difference for peak three could be the result of a continuous distribution of activation energies similar to that found in Figure 6-33b. The difference for peak four are suggested to be the result of the complex underlying peak distribution, which could not be determined by the traditional IRM approach alone. An inspection of Figure 6-38 shows just how poorly the VHRM result for peak four matches with the full TL curve. The two-dimensional

deconvolution was unable to provide result with well-defined energies and was found to be sensitive to solution space resolution. The VHRM results provide evidence for thermal quenching for all peaks but the low temperature, ~407 K, TL peak. This peak was found to be the result of a single trapping center and was found to not be affected by thermal quenching. Although this material was expected to serve as the primary temperature sensing material due to its high temperature TL peaks and UV emission, the issues with thermal quenching and the inability to obtain an accurate TL model make its use difficult.

Thermal history reconstruction analysis of simulated samples comprised of TL particles heated to various temperatures were found to display the same partial heating features previously seen in experimental TL curves from detonation tests (Daniels et al., 2015; Yukihara et al., 2014b; Yukihara et al., 2015; Yukihara et al., 2016). The results indicated a temperature bias to the TL particles heated to the lowest temperature as a result of their higher intensity TL curve and the thermal reconstruction efforts to account for the presence of partially heated TL peaks. Analysis of realistic temperature distributions for MBO provided results that were consistent with whole sample analysis by Yukihara et al. (2016) suggesting prior results may be drastic underestimates of the highest particle temperatures within the individual samples. Future use of TL temperature sensors must develop a protocol or analysis method to obtain the full distribution of temperatures within a given sample.

We developed a method for obtaining a characteristic heating timescale for an individual TL particle given its size and thermal diffusivity. The time scales obtained for typical TL particles suggests the particles are insensitive to early transient behavior in agent-defeat tests and sensitive to the longer scale > 1 ms heating behavior. This value will change given different environments such as forced convection, $Bi < 0.1$, and is, therefore, just a first step.

Thermal history reconstruction for particles in the FLAG hydrodynamic simulations found the particles to be unaffected by the transient temperature behavior, suggesting that the constant and exponential functions may be valid over sufficient heating time scales.

The results suggested, that for Bi>0.1, the temperature reconstruction method is strongly sensitive to trapping parameters. Variations in the thermal stability of a trapping center produced ~ 70 K change in the reconstructed temperature value. This result suggests the use of TL particles where thermal gradients are possible will result in incorrect thermal histories.

In conclusion, a robust investigation of the heat transfer effects for TL materials is required to determine if the technology is still viable. For cases where Bi<0.1, one must still be aware of samples containing multiple thermal histories, and a protocol to analyze such samples is required for TL materials to serve as a useful diagnostic. We found MBO to be the most promising material based upon the ability to full characterize the material and the lack of thermal quenching. The consistency of the trap parameters between the traditional methods and the two-dimension deconvolution method suggests a new method for characterization of control samples prior to thermal history reconstruction. Although the studies for the IRM and two-dimensional deconvolution methods were aimed at an application for the temperature sensing materials, the findings are applicable to analysis of their TL curves and should prove useful in understanding complex TL curves.

REFERENCES

Ã–zisik, M.N. and Özışık, M.N., 1993. *Heat conduction*. John Wiley & Sons.

Agersnap Larsen, N., Bøtter-Jensen, L. and McKeever, S.W.S., 1999. *Thermally stimulated conductivity and thermoluminescence from Al_2O_3:C*. Radiation Protection Dosimetry 84, 87-90.

Aitken, M.J. and Thompson, J., 1968. *Determination of heat penetration in archaeological remains*. In: Thermoluminescence of Geological Materials, D.J. McDougall (Ed.). Academic Press, London.

Akselrod, M., Agersnap Larsen, N., Whitley, V. and McKeever, S., 1998a. *Thermal quenching of F-center luminescence in Al 2 O 3: C*. Journal of Applied Physics 84, 3364-3373.

Akselrod, M.S., Agersnap Larsen, N., Whitley, V.H. and McKeever, S.W.S., 1998b. *Thermal quenching of F-center luminescence in Al_2O_3:C*. Journal of Applied Physics 84, 3364-3373.

Akselrod, M.S., Akselrod, A.E., Orlov, S.S., Sanyal, S. and Underwood, T.H., 2003. *Fluorescent Aluminum Oxide Crystals for Volumetric Optical Data Storage and Imaging Applications*. Journal of Fluorescence 13, 503-511.

Armstrong, P., 2017. *Thermoluminescent Microparticles used as Harsh Environment Temperature Sensors Characterized using MEMS Devices*. THE UNIVERSITY OF MINNESOTA.

Asay, B.W., Son, S.F., Dickson, P.M., Smilowitz, L.B. and Henson, B.F., 2005. *An investigation of the dynamic response of thermocouples in inert and reacting condensed phase energetic materials*. Propellants, Explosives, Pyrotechnics 30, 199-208.

Aşlar, E., Meriç, N., Şahiner, E., Kitis, G. and Polymeris, G.S., 2017. *Calculation of thermal quenching parameters in BeO ceramics using solely TL measurements*. Radiation Measurements 103, 13-25.

Barbina, V., Contento, G., Furetta, C., Malisan, M. and Padovani, R., 1982. *Preliminary results on dosimetric properties op MgB4O7:Dy*. Radiation Effects 67, 55-62.

Benoit, P.H., Sears, D.W.G. and McKeever, S.W.S., 1991. *The natural thermoluminescence of meteorites: II. Meteorite orbits and orbital evolution*. Icarus 94, 311-325.

Betts, D.S., Couturier, L., Khayrat, A.H., Luff, B.J. and Townsend, P.D., 1993. *Temperature distribution in thermoluminescence experiments. I. Experimental results*. Journal of Physics D: Applied Physics 26, 843.

Biderman, S., Horowitz, Y., Oster, L., Einav, Y. and Dubi, Y., 2002. *Glow curve analysis of composite peak 5 in LiF: Mg, Ti (TLD-100) using optical bleaching, thermal annealing and computerised glow curve deconvolution*. Radiation protection dosimetry 101, 69-72.

Blasse, G. and Grabmaier, B.C., 1994. *Luminescent Materials*. Springer, Heidelberg.

Bohun, A., 1954. Czech. J. Phys. 4.

Booth, A.H., 1954. Canad. J. Chem. 32.

Bos, A.J.J., 2006. *Theory of thermoluminescence*. Radiation Measurements 41, Supplement 1, S45-S56.

Bosacchi, A., Bosacchi, B., Franchi, S. and Hernandez, L., 1973. *Optical properties of a 'quasi-disordered' semiconductor: ZnIn2S4*. Solid State Communications 13, 1805-1809.

Bosze, E.J., Hirata, G.A. and McKittrick, J., 2011. *An analysis of $Y_2O_3:Eu^{3+}$ thin films for themographic phosphor applications*. Journal of Luminescence 131, 41-48.

Bøtter-Jensen, L., McKeever, S.W.S. and Wintle, A.G., 2003. *Optically Stimulated Luminescence Dosimetry*. Elsevier, Amsterdam.

Brown, J.T., 2007. *Comparison of Ignition Characteristics of Pure and Coated Aluminum Powder in a Shock Tube Facility*. University of Illinois at Urbana-Champaign.

Bull, R.K., McKeever, S.W.S., Chen, R., Mathur, V.K., Rhodes, J.F. and Brown, M.D., 1986a. *Thermoluminescence kinetics for multipeak glow curves produced by the release of electrons and holes*. J. Phys. D: Appl. Phys. 19, 1321-1334.

Bull, R.K., McKeever, S.W.S., Chen, R., Mathur, V.K., Rhodes, J.F. and Brown, M.D., 1986b. *Thermoluminescence kinetics for multipeak glow curves produced by the release of electrons and holes*. Journal of Physics D: Applied Physics 19, 1321.

Burton, D., 2007. *Lagrangian Hydrodynamics in the FLAG Code, LA-UR-07-7547*.

Carrera, M., Zandomeni, R.O., Fitzgibbon, J. and Sagripanti, J.L., 2007. *Difference between the spore sizes of Bacillus anthracis and other Bacillus species*. Journal of Applied Microbiology 102, 303-312.

Chen, R. and Haber, G.A., 1968. *Calculation of glow curves' activation energies by numerical initial rise methods*. Chemical Physics Letters 2, 483-485.

Chen, R., 1969. *On the calculation of activation energies and frequency factors from glow curves*. Journal of Applied Physics 40, 570-585.

Chen, R. and Winer, S.A.A., 1970. *Effects of Various Heating Rates on Glow Curves*. Journal of Applied Physics 41, 5227-5232.

Chen, R. and McKeever, S.W.S., 1997. *Theory of Thermoluminescence and Related Phenomena*. World Scientific Publishing Co., Singapore.

Chen, R. and Pagonis, V., 2011. *Thermally and Optically Stimulated Luminescence: A Simulation Approach*. John Wiley & Sons Ltd., Chichester, West Sussex, UK.

Christodoulides, C., 1985. *Errors involved in the determination of activation energies in TL and TSDC by the initial rise method*. Journal of Physics D: Applied Physics 18, 1665.

Chruścińska, A., 1994. *The fractional thermoluminescence: some aspects concerning the experimental data analysis*. Journal of Luminescence 62, 115-121.

Chvoj, Z., 1977. *Some remarks on the analysis of thermoluminescence glow curves*. Czechoslovak Journal of Physics B 27, 957-958.

Cohen, I., Bar-Kohany, T., German, U. and Ziskind, G., 2014. *Optimization of the temperature profiles due to a nitrogen jet impinging on a TLD detector*. Radiation Measurements 70, 48-51.

Colyott, L., Akselrod, M. and McKeever, S., 1996. *Phototransferred thermoluminescence in alpha-Al2O3: C*. Radiation protection dosimetry 65, 263-266.

Crockett, S., 2018. *SESAME Database*. http://www.lanl.gov/org/padste/adtsc/theoretical/physics-chemistry-materials/sesame-database.php (accessed on 2018).

Crowe, C.T., Schwarzkopf, J.D., Sommerfeld, M. and Tsuji, Y., 2011. *Multiphase flows with droplets and particles*. CRC press.

Danczyk, J. and Suresh, K., 2012. *A Methodology for FEA over Tangled Meshes*. University of Wisconsin.

Daniels, A., Stamatis, D., Lightstone, J.M., Milby, C. and Svingala, F.R., 2015. *Evaluation of thermal sensing materials in closed chamber detonations*. In, International Detonation Symposium (July 13-18, 2014). San Francisco, CA.

Densmore, J.M., Homan, B.E., Biss, M.M. and McNesby, K.L., 2011. *High-speed two-camera imaging pyrometer for mapping fireball temperatures*. Applied Optics 50, 6267-6271.

Dobaczewski, J., Nazarewicz, W. and Reinhard, P.G., 2014. *Error estimates of theoretical models: a guide*. Journal of Physics G: Nuclear and Particle Physics 41, 074001.

Doull, B.A., Oliveira, L.C. and Yukihara, E.G., 2013. *Effect of Annealing and Fuel Type on the Thermoluminescent Properties of $Li_2B_4O_7$ Synthesized by Solution Combustion Synthesis*. Radiation Measurements 56, 167-170.

Doull, B.A., Oliveira, L.C., Wang, D.Y., Milliken, E.D. and Yukihara, E.G., 2014. *Thermoluminescent properties of lithium borate, magnesium borate and calcium sulfate developed for temperature sensing*. Journal of Luminescence 146, 408-417.

Garlick, G.F.J. and Gibson, A.F., 1948a. *The Electron Trap Mechanism of Luminescence in Sulphide and Silicate Phosphors*. Proc. Phys. Soc. 60, 574-590.

Garlick, G.F.J. and Gibson, A.F., 1948b. *The Electron Trap Mechanism of Luminescence in Sulphide and Silicate Phosphors*. Proceedings of the Physical Society 60, 574.

Glumac, N., Krier, H., Bazyn, T. and Eyer, R., 2005. *Temperature measurements of aluminum particles burning in carbon dioxide*. Combustion Science and Technology 177, 485-511.

Gobrecht, H. and Hofmann, D., 1966. *Spectroscopy of traps by fractional glow technique*. Journal of Physics and Chemistry of Solids 27, 509-522.

Gordon, S. and McBride, B.J., 1994. *Computer program for calculation of complex chemical equilibrium compositions and applications*. National Aeronautics and Space Administration, Office of Management, Scientific and Technical Information Program.

Gotlib, V.I., Kantorovich, L.N., Grebenshicov, V.L., Bichev, V.R. and Nemiro, E.A., 1984. *The study of thermoluminescence using the contact method of sample heating*. Journal of Physics D: Applied Physics 17, 2097.

Gottiparthi, K., Schulz, J. and Menon, S., 2014. *On the neutralization of bacterial spores in post-detonation flows*. Shock Waves 24, 455-466.

Gunawidjaja, R., Myint, T. and Eilers, H., 2011a. *Stabilization of tetragonal phase in ZrO_2:Eu by rapid thermal heating*. Chemical Physics Letters 515, 122-126.

Gunawidjaja, R., Myint, T. and Eilers, H., 2011b. *Correlation of optical properties and temperature-induced irreversible phase transitions in europium-doped yttrium carbonate nanoparticles*. Journal of Solid State Chemistry 184, 3280-3288.

Guo, S., 2015. *Turbulent interactions with normal shocks and their effects on aluminum particle burn time*. Masters of Science, University of Illinois at Urbana-Champaign.

Gut, A., 2009. *An intermediate course in probability*, 2nd ed.. ed. Dordrecht
New York : Springer, Dordrecht
New York.

Haake, C.H., 1957. *Critical Comment on a Method for Determining Electron Trap Depths*. J. Opt. Soc. Am. 47, 649-652.

Hansen, P.C., 1992. *Numerical tools for analysis and solution of Fredholm integral equations of the first kind*. Inverse problems 8, 849.

Hemam, R., Singh, L.R., Prasad, A.I., Gogoi, P., Kumar, M., Chougaonkar, M., Singh, S.D. and Sharan, R., 2016. *Critical view on TL/OSL properties of Li2B4O7 nanoparticles doped with Cu, Ag and co-doping Cu, Ag: Dose response study*. Radiation Measurements 95, 44-54.

Heyes, A.L., Seefeldt, S. and Feist, J.P., 2006. *Two-colour phosphor thermometry for surface temperature measurements*. Optics & Laser Technology 38, 257-265.

Heyes, A.L., 2009. *On the design of phosphors for high-temperature thermometry*. Journal of Luminescence 129, 2004-2009.

Hoogenstraaten, W., 1958. *Electron traps in zinc-sulphide phosphors*. Research laboratory of NV philips.

Hornyak, W., Chen, R. and Franklin, A., 1992. *Thermoluminescence characteristics of the 375 C electron trap in quartz*. Physical Review B 46, 8036.

Hornyak, W.F. and Franklin, A.D., 1988. *Single level isothermal TL-decay (with energy level distribution and retrapping)*. International Journal of Radiation Applications and Instrumentation. Part D. Nuclear Tracks and Radiation Measurements 14, 81-89.

Hornyak, W.F. and Chen, R., 1989. *Thermoluminescence and phosphorescence with a continuous distribution of activation energies*. Journal of Luminescence 44, 73-81.

Horowitz, Y.S., 1983. *Thermoluminescence and Thermoluminescent Dosimetry*. CRC Press, Boca Raton.

Horowitz, Y.S. and Yossian, D., 1995. *Computerised glow curve deconvolution: application to thermoluminescence dosimetry*. Radiation Protection Dosimetry 60, 1-114.

Ignatovych, M., Fasoli, M. and Kelemen, A., 2012. *Thermoluminescence study of Cu, Ag and Mn doped lithium tetraborate single crystals and glasses*. Radiation Physics and Chemistry 81, 1528-1532.

Jaque, D., Maestro, L.M., Escudero, E., Martín-Rodríguez, E., Capobianco, J.A., Vetrone, F., Juanrranz de la Fuente, A., Sanz-Rodríguez, F., Iglesias-de la Cruz, M.C., Jacinto, C., Rocha, U. and García Solé, J., 2013. *Fluorescent nano-particles for multi-photon thermal sensing*. Journal of Luminescence 133, 249-253.

Jetté, F.X., Higgins, A.J., Goroshin, S., Frost, D.L., Charron-Tousignant, Y., Radulescu, M.I. and Lee, J.J., 2011. *In-situ measurements of the onset of bulk exothermicity in shock initiation of reactive powder mixtures*. Journal of Applied Physics 109, 084905.

Kathuria, S. and Sunta, C., 1979. *Kinetics and trapping parameters of thermoluminescence in LiF TLD-100-dependence on dose*. Journal of Physics D: Applied Physics 12, 1573.

Kathuria, S. and Sunta, C., 1982. *Order of kinetics for thermoluminescence in LiF TLD-100*. Journal of Physics D: Applied Physics 15, 497.

Kearney, S.P., Lucht, R.P. and Jacobi, A.M., 1999. *Temperature measurements in convective heat transfer flows using dual-broadband, pure-rotational coherent anti-Stokes Raman spectroscopy (CARS)*. Experimental Thermal and Fluid Science 19, 13-26.

Kierstead, J.A. and Levy, P.W., 1991. *Validity of repeated initial rise thermoluminescence kinetic parameter determinations*. International Journal of Radiation Applications and Instrumentation. Part D. Nuclear Tracks and Radiation Measurements 18, 19-25.

King, G.E., Guralnik, B., Valla, P.G. and Herman, F., 2016. *Trapped-charge thermochronometry and thermometry: A status review*. Chemical Geology 446, 3-17.

Kitis, G., Papadopoulos, J.G., Charalambous, S. and Tuyn, J.W.N., 1994. *The Influence of Heating Rate on the Response and Trapping Parameters of Alpha-Al2O3:C*. Radiation Protection Dosimetry 55, 183-190.

Kitis, G., Furetta, C., Prokic, M. and Prokic, V., 2000. *Kinetic parameters of some tissue equivalent thermoluminescence materials*. Journal of Physics D: Applied Physics 33, 1252.

Kitis, G., Chen, R. and Pagonis, V., 2008. *Thermoluminescence glow-peak shape methods based on mixed order kinetics*. physica status solidi (a) 205, 1181-1189.

Kitis, G., Pagonis, V. and Tzamarias, S.E., 2017. *The influence of competition effects on the initial rise method during thermal stimulation of luminescence: A simulation study*. Radiation Measurements 100, 27-36.

Kittel, C., 2004. *Elementary statistical physics*. Courier Corporation.

Kivits, P. and Hagebeuk, H.J.L., 1977. *Evaluation of the model for thermally stimulated luminescence and conductivity; reliability of trap depth determinations*. Journal of Luminescence 15, 1-27.

Koch, J.D., Piecuch, S., Lightstone, J.M., Carney, J.R. and Hooper, J., 2010. *Time-resolved measurements of near infrared emission spectra from explosions: Pure pentaerythritol tetranitrate and its mixtures containing silver and aluminum particles*. Journal of Applied Physics 108, 036101.

Kontogeorgos, D., Mandilaras, I. and Founti, M., 2011. *Scrutinizing gypsum board thermal performance at dehydration temperatures*. Journal of Fire Sciences 29, 111-130.

Kumar, M., Alagu Raja, E., Prasad, L.C., Popli, K.L., Kher, R.K. and Bhatt, B.C., 2005. *Studies on automatic hot gas reader used in the countrywide personnel monitoring programme*. Radiation Protection Dosimetry 113, 366-373.

Kumar, R., Saurav, S., Titov, E., Levin, D., Long, R., Neely, W. and Setlow, P., 2011. *Thermo-structural studies of spores subjected to high temperature gas environments*. International Journal of Heat and Mass Transfer 54, 755-765.

Lapraz, D., Prevost, H., Iacconi, P., Guigues, C., Benabdesselam, M. and Briand, D., 2002. *On the luminescence properties of $CaSO_4$:Ce*. Radiation Protection Dosimetry 100, 365-368.

Larsen, N.A., 1999. *Dosimetry based on thermally and optically stimulated luminescence*.

Lawson, C.L. and Hanson, R.J., 1974. *Solving Least Squares Problems*. Prentice-Hall, Inc., Englewoods Cliffs, New Jersey.

Levi, M.A., 2004. *Agent Defeat Weapons*. The National Academy of Sciences http://www.brookings.edu/~/media/research/files/testimony/2004/4/27technology-levi/levi20040427.pdf (accessed on July 16, 2015).

Lewis, W.K. and Rumchik, C.G., 2009. *Measurement of apparent temperature in post-detonation fireballs using atomic emission spectroscopy*. Journal of Applied Physics 105, 056104.

Lewis, W.K., 2012. *Time-resolved spectroscopy studies of aluminized explosives: Chemical dynamics and apparent temperatures*. Journal of Applied Physics 111, 014903.

Lewis, W.K., Rumchik, C.G. and Smith, M.J., 2013. *Emission spectroscopy of the interior of optically dense post-detonation fireballs*. Journal of Applied Physics 113, 024903.

Lilley, E. and Taylor, G., 1981. *Order of kinetics for thermoluminescence in LiF TLD-100*. Journal of Physics D: Applied Physics 14, L13.

Lilley, E. and McKeever, S., 1983. *On the order of kinetics for thermoluminescence in LiF (TLD-100)*. Journal of Physics D: Applied Physics 16, L39.

Lyamayev, V.I., 2006. *A low-cost microcontroller-based measurement system for a fractional glow technique*. Measurement Science and Technology 17, N75.

Mah, M.L., Manfred, M.E., Kim, S.S., Prokić, M., Yukihara, E.G. and Talghader, J.J., 2010. *Measurement of rapid temperature profiles using thermoluminescent microparticles*. IEEE Sensors Journal 10, 311-315.

Mah, M.L., Armstrong, P.R., Kim, S.S., Carney, J.R., Lightstone, J.M. and Talghader, J.J., 2013. *Sensing the thermal history of high-explosive detonations using thermoluminescent microparticles*. IEEE Sensors Journal 13, 1742-1747.

Mah, M.L., 2017. *Fire and Ice: Thermoluminescent Temperature Sensing in High-Explosive Detonations and Optical Characterization Methods for Glacier Ice Boreholes*. University of Minnesota.

Majumdar, A., 1993. *Microscale Heat Conduction in Dielectric Thin Films*. Journal of Heat Transfer 115, 7-16.

Mandowski, A., Bos, A.J.J., Mandowska, E. and Orzechowski, J., 2010. *Monte-Carlo method for determining the quenching function from variable heating rate measurements*.

May, C.E. and Partridge, J.A., 1964. *Thermoluminescent Kinetics of Alpha-Irradiated Alkali Halides*. The Journal of Chemical Physics 40, 1401-1409.

Mazumder, S. and Majumdar, A., 2001. *Monte Carlo study of phonon transport in solid thin films including dispersion and polarization*. Journal of Heat Transfer 123, 749-759.

McKeever, S.W.S., 1980. *On the analysis of complex thermoluminescence. Glow-curves: Resolution into individual peaks*. physica status solidi (a) 62, 331-340.

McKeever, S.W.S., 1985. *Thermoluminescence of Solids*. Cambridge University Press, Cambridge.

McKeever, S.W.S., Moscovitch, M. and Townsend, P.D., 1995. *Thermoluminescence Dosimetry Materials: Properties and Uses*. Nuclear Technology Publishing, Ashford.

Medlin, W., 1961. *Decay of phosphorescence from a distribution of trapping levels*. Physical Review 123, 502.

Milby, C., Stamatis, D., Carney, J., Horn, J. and Lightstone, J., 2012. *Efficacy of Energetic Formulations in the Defeat of Bio Agents*. In: Central States Section of the Combustion Institute Spring Technical Meeting 2012 - Combustion Fundamentals and Applications, Dayton, Ohio, USA, The Combustion Institute, 861-868.

Mishra, A.K., Wang, J. and Huang, L., 2014. *Thermal Sensitive Quantum and Phonon Confinements for Temperature Mapping in Extreme Environments*. The Journal of Physical Chemistry C 118, 7222-7228.

Mittani, J.C., Prokić, M. and Yukihara, E.G., 2008. *Optically stimulated luminescence and thermoluminescence of terbium-activated silicates and aluminates*. Radiation Measurements 43, 323-326.

Myint, T., Gunawidjaja, R. and Eilers, H., 2012a. *Fast pyroprobe-heating-induced structural changes of Y_2O_3:Eu precursors and their optical signatures*. Journal of Physical Chemistry C 116, 1687-1693.

Myint, T., Gunawidjaja, R. and Eilers, H., 2012b. *Spectroscopic properties of nanophase Eu-doped ZrO_2 and its potential application for fast temperature sensing under extreme conditions*. Journal of Physical Chemistry C 116, 21629-21634.

Nadasi, E., Varjas, T., Prantner, I., Virag, V. and Ember, I., 2007. *Bioterrorism: warfare of the 21st century*. Gene Ther. Mol. Biol 11, 315-320.

Nanjundaswamy, R., Lepper, K. and McKeever, S.W.S., 2002. *Thermal quenching of thermoluminescence in natural quartz*. Radiation Protection Dosimetry 100, 305-308.

Nicholas, K.H. and Woods, J., 1964. *The evaluation of electron trapping parameters from conductivity glow curves in cadmium sulphide*. British Journal of Applied Physics 15, 783.

Pagonis, V., Mian, S. and Kitis, G., 2001. *Fit of First Order Thermoluminescence Glow Peaks using the Weibull Distribution Function*. Radiation Protection Dosimetry 93, 11-17.

Parfiabovitch, I.A., 1954. J. Exp. Theor. Phys. S.S.S.R. 26.

Patra, G.D., Singh, S.G., Tiwari, B., Sen, S., Desai, D.G. and Gadkari, S.C., 2013. *Thermally stimulated luminescence process in copper and silver co-doped lithium tetraborate single crystals and its implication to dosimetry*. Journal of Luminescence 137, 28-31.

Pekpak, E., Yilmaz, A. and Özbayoglu, G., 2011. *The effects of synthesis and doping procedures on thermoluminescent response of lithium tetraborate*. Journal of Alloys and Compounds 509, 2466-2472.

Pender, L.F. and Fleming, R.J., 1977a. *Numerical analysis of thermoluminescence data for a quasi-continuous activation energy distribution (glass-rubber transition analysis)*. Journal of Physics C: Solid State Physics 10, 1561.

Pender, L.F. and Fleming, R.J., 1977b. *Thermoluminescence in polystyrene*. Journal of Physics C: Solid State Physics 10, 1571.

Piters, T.M. and Bos, A.J.J., 1994. *Effects of non-ideal heat transfer on the glow curve in thermoluminescence experiments*. Journal of Physics D: Applied Physics 27, 1747.

Placido, F., 1980. *Thermoluminescence test for fire-damaged concrete*. Magazine of Concrete Research 32, 112-116.

Press, W.H., Teukolsky, S.A., Vetterling, W.T. and Flannery, B.P., 1993. *Numerical Recipes in FORTRAN; The Art of Scientific Computing*. Cambridge University Press.

Prokić, M., 1980. *Development of highly sensitive $CaSO_4$:Dy/Tm and MgB_4O_7:Dy/Tm sintered thermoluminescent dosimeters*. Nuclear Instruments and Methods 175, 83-86.

Puchalska, M. and Bilski, P., 2006. *GlowFit—a new tool for thermoluminescence glow-curve deconvolution*. Radiation Measurements 41, 659-664.

Randall, J. and Wilkins, M.H.F., 1945a. *Phosphorescence and electron traps II. The interpretation of long-period phosphorescence*. Proc. R. Soc. Lond. A 184, 390-407.

Randall, J.T. and Wilkins, M.H.F., 1945b. *Phosphorescence and Electron Traps. I. The Study of Trap Distributions*. Proceedings of the Royal Society of London. Series A, Mathematical and Physical Sciences 184, 365-389.

Randall, J.T. and Wilkins, M.H.F., 1945c. *Phosphorescence and Electron Traps. II. The Interpretation of Long-Period Phosphorescence*. Proceedings of the Royal Society of London A: Mathematical, Physical and Engineering Sciences 184, 390-407.

Ranz, W. and Marshall, W.R., 1952. *Evaporation from drops*. Chem. Eng. Prog 48, 141-146.

Rawat, N.S., Kulkarni, M.S., Tyagi, M., Ratna, P., Mishra, D.R., Singh, S.G., Tiwari, B., Soni, A., Gadkari, S.C. and Gupta, S.K., 2012. *TL and OSL studies on lithium borate single crystals doped with Cu and Ag*. Journal of Luminescence 132, 1969-1975.

Rohatgi, A., 2018. *WebPlotDigitzer*. https://automeris.io/WebPlotDigitizer/ (accessed on 2018).

Romet, I., Aleksanyan, E., Brik, M.G., Corradi, G., Kotlov, A., Nagirnyi, V. and Polgár, K., 2016. *Recombination luminescence of Cu and/or Ag doped lithium tetraborate single crystals*. Journal of Luminescence 177, 9-16.

Rozenfeld, R., Bar-Kohany, T., Weinstein, M., Abraham, A., German, U., Alfassi, Z. and Ziskind, G., 2011. *Thermal behaviour of a LiF crystal mounted in a TLD card and heated by jet impingement*. Radiation Measurements 46, 1432-1435.

Rudlof, G., Becherer, J. and Glaefeke, H., 1978. *Behaviour of the fractional glow technique with first-order detrapping processes, traps distributed in energy or frequency factor*. physica status solidi (a) 49, K121-K124.

Sakurai, T. and Gartia, R.K., 1997. *Evidence of continuous trap distribution in the glow curve of a Brown microcline*. Journal of Applied Physics 82, 5722-5727.

Sakurai, T., 2001. *Fatal defect in computerized glow curve deconvolution of thermoluminescence*. Journal of Physics D: Applied Physics 34, L105.

Sakurai, T., Shoji, K., Itoh, K. and Gartia, R.K., 2001. *Origin of the exponential distribution of traps in glass*. Journal of Applied Physics 89, 2208-2212.

Sanaye, S., Dhabekar, B., Kumar, R., Menon, S., Shinde, S., Rao, T.G. and Bhatt, B., 2003. *Energy transfer process in CaSO4: Tb, Ce phosphor*. Journal of luminescence 105, 1-8.

Schulman, J.H., Kirk, R.D. and West, E.J., 1965. *Use of lithium borate for thermoluminescence dosimetry*. In: Proceedings of the International Conference on Luminescence Dosimetry, Stanford University.

Singh, T.S.C., Mazumdar, P. and Gartia, R., 1988. *On the determination of activation energy in thermoluminescence by the initial rise method*. Journal of Physics D: Applied Physics 21, 1312.

Souza, J., Ferrari, V. and De Freitas, L., 1993. *TL peak structure of MgB4O7: Dy*. Radiation protection dosimetry 47, 239-242.

Souza, L.F., Antonio, P.L., Caldas, L.V.E. and Souza, D.N., 2015. *Neodymium as a magnesium tetraborate matrix dopant and its applicability in dosimetry and as a temperature sensor*. Nuclear Instruments and Methods in Physics Research Section A: Accelerators, Spectrometers, Detectors and Associated Equipment 784, 9-13.

Spencer, J.Q. and Sanderson, D.C.W., 1994. *Mapping thermal exposure by luminescence thermometry*. Radiation Measurements 23, 465-468.

Spencer, J.Q.G. and Sanderson, D.C.W., 2012. *Decline in firing technology or poorer fuel resources? High-temperature thermoluminescence (HTTL) archaeothermometry of Neolithic ceramics from Pool, Sanday, Orkney*. Journal of Archaeological Science 39, 3542-3552.

Subedi, B., Kitis, G. and Pagonis, V., 2010. *Simulation of the influence of thermal quenching on thermoluminescence glow-peaks*. physica status solidi (a) 207, 1216-1226.

Subedi, B., Oniya, E., Polymeris, G.S., Afouxenidis, D., Tsirliganis, N.C. and Kitis, G., 2011. *Thermal quenching of thermoluminescence in quartz samples of various origin*. Nuclear Instruments and Methods in Physics Research Section B: Beam Interactions with Materials and Atoms 269, 572-581.

Sun, H., Yu, M., Sun, X., Wang, G. and Lian, J., 2013. *Effective temperature sensing by irreversible morphology evolution of ultrathin gold island films*. Journal of Physical Chemistry C 117, 3366-3373.

Sunta, C., Kulkarni, R., Piters, T., Ayta, W.F. and Watanabe, S., 1998. *General order kinetics of thermoluminescence-a comparison with physical models*. Journal of Physics D: Applied Physics 31, 2074.

Sunta, C.M., Ayta, W.E.F., Chubaci, J.F.D. and Watanabe, S., 2005. *A critical look at the kinetic models of thermoluminescence - II. Non-first order kinetics*. Journal of Physics D: Applied Physics 38, 95-102.

Sunta, C.M., 2015. *Unreveling thermoluminescence*. Springer.

Takenaga, M., Yamamoto, O. and Yamashita, T., 1977. *Lithium borate activated with copper and silver for TLD*. Journal of the Atomic Energy Society of Japan 19, 543-549.

Talghader, J.J. and Mah, M.L., 2012. *Luminescent thermometry for sensing rapid thermal profiles in fires and explosions*. In: Optical, Acoustic, Magnetic, and Mechanical Sensor Technologies, K. Iniewski (Ed.). CRC Press, 79–106.

Talghader, J.J., Mah, M.L., Yukihara, E.G. and Coleman, A.C., 2016. *Thermoluminescent microparticle thermal history sensors*. 2, 16037.

Tanguay, V., 2009. *Combustion of reactive metal particles in high-speed flow of detonation products*. McGill University.

Taylor, G.C. and Lilley, E., 1978. *The analysis of thermoluminescent glow peaks in LiF (TLD-100)*. Journal of Physics D: Applied Physics 11, 567.

Taylor, J.R., 1997. *An Introduction to Error Analysis The study of Uncertainties in Physical Measurements*, Second Edition ed. University Science Books, Sausalito, California.

Toshiaki, O., 2000. *Characteristic Time Required to Achieve Uniform Temperature in Thermal Conduction of N -Dimensional Sphere Heated from Surface*. Japanese Journal of Applied Physics 39, 6111.

Van Beek, J.D., Meier, B.H. and Schäfer, H., 2003. *Inverse methods in two-dimensional NMR spectral analysis*. Journal of Magnetic Resonance 162, 141-157.

Van den Eeckhout, K., Bos, A.J., Poelman, D. and Smet, P.F., 2013. *Revealing trap depth distributions in persistent phosphors*. Physical Review B 87, 045126.

Wang, D., Doull, B.A., Oliveira, L.C. and Yukihara, E.G., 2013. *Controlled synthesis of $Li_2B_4O_7$:Cu for temperature sensing*. RSC Advances in press.

Wang, J. and Huang, L., 2011. *Thermometry based on phonon confinement effect in nanoparticles*. Applied Physics Letters 98, 113102.

Wang, S., Westcott, S. and Chen, W., 2002. *Nanoparticle luminescence thermometry*. Journal of Physical Chemistry B 106, 11203-11209.

Weizman, Y., Horowitz, Y. and Oster, L., 1999. *Investigation of the composite structure of peak 5 in the thermoluminescent glow curve of LiF: Mg, Ti (TLD-100) using optical bleaching*. Journal of Physics D: Applied Physics 32, 2118.

Whitley, V.H., Agersnap Larsen, N. and McKeever, S.W.S., 2002. *Determination of ionization energies and attempt-to-escape factors using thermally stimulated conductivity*. Radiation Protection Dosimetry 100, 147-152.

Wintle, A.G., 1975. *Thermal quenching of thermoluminescence in quartz*. Geophysical Journal of the Royal Astronomical Society 41, 107-113.

Yukihara, E.G., Whitley, V.H., Polf, J.C., Klein, D.M., McKeever, S.W.S., Akselrod, A.E. and Akselrod., M.S., 2003. *The effects of deep trap population on the thermoluminescence of Al_2O_3:C*. Radiation Measurements 37, 627-638.

Yukihara, E.G., Milliken, E.D. and Doull, B.A., 2014a. *Thermally stimulated and recombination processes in MgB_4O_7 investigated by systematic lanthanide doping*. Journal of Luminescence, submitted.

Yukihara, E.G., Coleman, A.C. and Doull, B.A., 2014b. *Passive temperature sensing using thermoluminescence: laboratory tests using $Li_2B_4O_7$:Cu,Ag, MgB_4O_7:Dy,Li and $CaSO_4$:Ce,Tb*. Journal of Luminescence 146, 515-526.

Yukihara, E.G., Coleman, A.C., Bastani, S., Gustafson, T., Talghader, J.J., Daniels, A., Stamatis, D., Lightstone, J.M., Milby, C. and Svingala, F.R., 2015. *Particle temperature measurements in closed chamber detonations using thermoluminescence from Li2B4O7:Ag,Cu, MgB4O7:Dy,Li and CaSO4:Ce,Tb*. Journal of Luminescence 165, 145-152.

Yukihara, E.G., Talghader, J.J., Jacobsohn, L.G. and Ballato, J., 2016. *Luminescence Materials as Nanoparticle Thermal Sensors*. Oklahoma State University Stillwater United States.

Yukihara, E.G., Coleman, A.C., Biswas, R.H., Lambert, R., Herman, F. and King, G.E., 2017. *Thermoluminescence Analysis for Particle Temperature Sensing and Thermochronometry: Principles and Fundamental Challenges*. Submitted

Yunus, C.A. and Afshin, J.G., 2011. *Heat and mass transfer: fundamentals and applications*. Tata McGraw-Hill, New Delhi, India.

Zhou, W., Orr, M., Jian, G., Watt, S., Lee, V. and Zachariah, M., 2015. *Inactivation of bacterial spores subjected to sub-second thermal stress*. Chemical Engineering Journal 279, 578-588.

Zhu, T., Kumar, R., Titov, E. and Levin, D., 2012. *Analysis of Fractal-Like Spore Aggregates in Direct Simulation Monte Carlo*. Journal of Thermophysics and Heat Transfer 26, 417-429.

VITA

ADAM CARRIGAN COLEMAN

Candidate for the Degree of

DOCTOR OF PHILOSOPHY

DISSERTATION: THERMOLUMINESCENCE TEMPERATURE SENSING: AN INVESTIGATION OF METHODOLOGICAL AND PRACTICAL LIMITATIONS OF THE TECHNIQUE

MAJOR FIELD: PHYSICS

BIOGRAPHICAL: PERSONAL

Born in Bryn Mawr, Pennsylvania on August 5, 1985

EDUCATION

MASTER OF SCIENCE 2012
San Diego State University, San Diego, CA

BACHELOR OF ARTS 2008
Claremont McKenna College, Claremont, CA

EXPERIENCE

TEACHING ASSISTANT 2015 – 2018
Oklahoma State University, USA

RESEARCH ASSISTANT 2013 – 2015
Oklahoma State University, USA